UNIVERSITY OF LEEDS

School of Chemical and Process Engineering

PhD Thesis

"*Study on the dynamic behaviour of colloidal particles in bidisperse settling suspensions and at gas-liquid interfaces*"

Hangyu Chen

Acknowledgements

My deepest thanks are extended to my supervisors, Dr Timothy N. Hunter, Prof. Michael Fairweather, and Dr Xiaodong Jia. I am not an expert in laboratory experiments when I arrived, but Dr Timothy Hunter helped me a lot and explained everything I need patiently, then, he analysed and supervised my research conscientiously and responsibly. Dr Timothy Hunter gave me the greatest academic support. I would also like to thank Dr Thomas C. Sykes who helped me a lot when I was struggling with sedimentation simulation models.

I would like to thank my family, for their tolerance, understanding and support, without their funding support I would not be able to continue my PhD.

I would like to specially thank Dr Xiaodong Jia and his enterprise Structure Vision Ltd. He helped me very much with the LBM-DEM coding and gave me a very good experience in the structure and modification of CFD software. The models are all included in the DigiFlow and DigiDEM modes of the DigiPac software. Without his help, I would not do my project smoothly.

I would like to thank all the staff and students at the Colloidal Group and the Chemical and Process Engineering laboratories, for providing both technical and administrative assistance when required. I would also like to thank all supervisors and students in the Colloidal Group that helped me in my research and daily life and let me enjoy the great afternoon tea meeting every week.

I would lastly like to thank my friends for supporting me through the good times and the bad alike and letting me enjoy the long period of overseas study life. I especially would like to thank my beautiful girlfriend Yu Cao, who support me when I feel down and encourage me when I need and whose love made this all possible.

Contents

Abstract

Colloidal particles are significant materials in industrial processes that attracts increasing interest across a wide range of fields, from food colloids to cosmetics, novel material producers, and mineral flotation. The sedimentation and adsorption of colloids are two important applications. Although they have been studied for many years, theories still lack systematically explanation and models need to be improved to satisfy the engineering and scientific demand. Bidisperse and polydisperse colloidal systems are relatively more complex than monodisperse system which has been well studied but is not normally directly applicable in industrial processes. It is simple to consider qualitatively that size and mixing ratios will influence systems stability and their sedimentation in particular, however, there are a lack good theoretical explanations and models incorporating bidisperse suspensions in stability and settling analysis. Adsorption of colloids at liquid interfaces is another common but significant problem, which relates to the three-phase contact line at very small scales. Again, it is easy to appreciate qualitatively that the wettability of colloids will significantly affect the adsorption process. Nevertheless, results need to be further investigated to understand the kinetic details and to propose dynamic adsorption models.

To investigate the sedimentation problems, research was undertaken to study the bidisperse sedimentation process and propose a suitable model that can simulate bidisperse sedimentation that may also be easily extended to polydisperse systems. Colloidal silica spherical particles with different sizes (100, 500, and 800 nm) are used to prepare suspensions in different size ratios and mixing ratios as materials. Firstly, the size distributions of colloids are checked with two devices based on different techniques (LUMiSizer® and Zetasizer®). Then, the sedimentation results are recorded using an analytical centrifuge (LUMiSizer®) and compared with classical empirical theories to investigate the hindrance effect with volume fraction changes under centrifugal forces. The

influence of size ratios and mixing ratios on bidisperse sedimentation are thereforce quantified for various total volume fractions, with secondary particle-fluid effects shown to be particularly important in some mixing ratios. Furthermore, a 1D bidisperse sedimentation model is proposed to simulate the settling of bidsiperse colloidal particles with different size ratios and mixing ratios which considered interparticle interactions and the mixture viscosity colloids. The results of the simulation were compared with the experimental data with generally less than 10 % deviation and can be easily extended to polydisperse systems.

The same original silica spherical particles (800 nm) are used in adsorption experiments. Silica particles are esterified with alcohol to achieve different wettability and marked as SiO-butane and SiO-hexane. Size distributions and zeta potentials are well checked after the esterification. The adsorption networks of colloids with 4-Methyl-2-pentanol (MIBC) subphase are investigated with the Langmuir-Blodgett trough, while the surface tension change during the adsorption process was recorded using a pendant drop tensimeter with a sealed cuvette. The effective diffusion constant and adsorption rate are calculated based on fitting pendent drop data to modified short-time model and long-time approximation models, which critically enabled quantification of the influence of wettability and concentration on adsorption rate. Then, to further investigate the adsorption, an LBM-DEM coupling model is established to investigate the single colloidal particle adsorption process. Several coupling problems are solved, and a novel adhesive force scheme is proposed to better describe the adsorption process with a clear three-phase contact line. The simulation results clearly illustrate the adsorption process of single colloids with different wettability from the bulk to fluid interfaces and finally reaches a stable state. The adsorption rate with different hydrophobicity was then simulated. Simulation results were shown to have the same trend as the experimental data but different in the value magnitudes, because experiments include hundreds of thousands of particles rather than a single particle in the simulation.

Publications & Declaration

The candidate confirms that the work submitted is his/her own, except where work which has formed part of jointly authored publications has been included. The contribution of the candidate and the other authors to this work has been explicitly indicated below. The candidate confirms that appropriate credit has been given within the thesis where reference has been made to the work of others.

Published and peer reviewed in PhD:

1. Hangyu Chen, Xiaodong Jia, Michael Fairweather, Timothy N. Hunter. Characterizing the sedimentation of bidisperse colloidal silica using analytical centrifugation, Advanced Powder Technology,34 (2): 103950, DOI:10.1016/j.apt.2023.103950.
All data was generated by Hangyu Chen. Other co-authors are acknowledged for support regarding data analysis and for manuscript review.

2. Hangyu Chen, Thomas C. Sykes, Xiaodong Jia, Michael Fairweather, Timothy N. Hunter. Simulation of bidisperse colloidal suspension sedimentation using a modified 1-D model, Physics of Fluid, in preparation.
All data was generated by Hangyu Chen. Thomas Sykes is acknowledged for initial support with the simulation code. Other co-authors are acknowledged for support regarding data analysis and for manuscript review.

Data from Paper #1 is contained within Chapter 4 and data from Paper #2 is contained within Chapter 5.

The right of Hangyu Chen to be identified as the author of this work has been asserted by him in accordance with the Copyright, Designs and Patents act 1988.

Signed:

Covid Statement

The PhD project of the author was severely delayed by the Covid-19 which caused the university and laboratory closures from the start of 2020 to 2021. The university was fully closed to experimental work for 6 months, with very restricted access for further 6-9 months and sickened many lab members and research group members. This delay directly influenced author's study especially pertaining to the experimental data characterisation in Chapter 5 & 6. The author was not able to investigate the concentration profiles of settling suspensions experimentally because the lab was closed, and the time is not enough. The author was not able to complete absorption studies on smaller particles to investigate the effect of sedimentation on results. The communication between the author and the computing source and co-supervisors were also influenced, which delayed the improvement of simulation model and results. Otherwise, the 3D simulation model can be further improved. However, with the serious delays, the author managed to work through them without any additional time on the thesis submission. The further work that the author could do if I had had the time is included in the 'future work' which can be a reference for further research.

Nomenclature

LBM – Lattice Boltzmann method

DEM – Discrete element method

vdw – Van der Waals

ele – Electrostatic

A_H – Hamaker constant

K – Debye-Huckel parameter

N_A – Avogadro constant.

R – Gas constant

T – Kelvin temperature

t - Time

U_0 – Terminal velocity

ρ - Density

μ – Dynamic viscosity

v – Kinematic viscosity

ϕ – Volume concentration

g – Gravity acceleration

d – Diameter

r - Radius

γ – Interface tension

θ – Angle

E – Energy

f_α – Density distribution function at α direction

e_α – Lattice speed at α direction

τ – Relaxation time

c_s^2 – Lattice sound speed

ω – Weight factor

$\mathbf{u}$ – Velocity vector

$\mathbf{M}$ – Transform matrix

$\mathbf{\Lambda}$ – Diagonal matrix

Re – Reynolds number

Kn – Knudsen number

λ – Mean free path

L – Length

a – Centrifugal acceleration

D – Diffusion coefficient

k_B – Boltzmann's constant

U – Energy potential

C – Molar concentration

Π – Surface pressure

P – Pressure

$\mathbf{I}$ – Identity matrix

$\mathbf{F}$ – Force vector

ψ – Effective density

1. Introduction

1.1 Colloidal Particle Sedimentation and Adsorption Processes

Particle sedimentation in suspensions is ubiquitous phenomenon, which is caused by the density difference between the bulk phase and particles. With the acceleration or gravity force, particles' buoyancy force cannot hold the particles in their positions, and they move towards the accelerated direction, and then the sedimentation occurs. Likewise, Particle adsorption at liquid-gas interfaces is an important process in nature and engineering (Noskov 1996). For example, in floatation, particles are selectively attached to the surface of bubbles, forming aggregates that rise to the top of the unit and are separated (Ge et al. 2020). When particles are close enough to the interface and attached, particles tend to be captured by the bubble interface. As a result, particle-bubble interactions and adsorption are significant.

To understand dynamic settling and adsorption behaviour of particles, it is prudent to first take an overview of the fundaments of both sedimentation and adsorption (Guo et al. 2003), including their mechanism, and importance to science and engineering.

A colloidal dispersion is a mixture in which one substance of microscopically dispersed insoluble particles is suspended throughout the substance fluid. Colloidal particles are small solid objects that are suspended in a fluid phase and the size ranges from a few nanometres to several microns. Their small size means the particles can be suspended in the fluid by thermal motion for enough time to observe, provided the buoyancy mismatch between the particles and the fluid is not very large and no additional force (e.g., centrifuges) are applied. Colloidal particles may also assemble at the interface between two fluids (Binks 2017), including liquid-fluid and fluid-gas interface. Colloidal particles with different wettability can also be used for foaming or defoaming processes (Thareja et al. 2008, Reguera et al. 2015). Colloidal particles are also common materials in industries such as the food industry (Dickinson 2013),

paints (Bartlett et al. 2012), mineral flotation processing (Jodin et al. 2004), and recovery of materials (Struis et al. 2013).

In terms of studying colloidal dynamics, the sedimentation of colloidal suspension is a good starting point and has been intensively studied for years (Siano 1979, Bloesch and Burns 1980, Concha and Bürger 2002), where sedimentation theory is used to predict the efficiency of industrial processes or product shelf-life. The balance between the buoyancy and frictional force drives the particle separation rate from the fluid (Vesaratchanon et al. 2007). Sedimentation leads to the separation of the continuous and dispersed phases, resulting in the formation of a particle sediment bed. Similarly, phase separation can also occur when the dispersed phase is less dense than the continuous phase, with the dispersed phase rising to the top which was usually named creaming. For long shelf time particles, the whole particle settling time can be months, thus, centrifugal forces were used to accelerate the settling and the result can be easily converted to a normal gravity scale (Antonopoulou et al. 2018). Analytical centrifuge has become a common way to study and record the detail in mono and polydisperse systems.

The terminal velocity of particles in suspension can be calculated with the Stokes settling rate equation. Based on the terminal velocity, various hindering settling velocity models have been proposed, and possibly the most well-known theory is the Richardson and Zaki (R-Z) model (Richardson and Zaki 1954) which describes the relationship between the particle settling rate and the volume fraction of suspensions. However, the R-Z model shows large deviations when it is extended to bidisperse and polydisperse. There are also alternative models, such as the Bachelor model (Batchelor 1972) and Al - Naafa and Selim (A-S) model (Al‐Naafa and Selim 1992), who modified settling factors using different coefficients to better discribe the hindrance effect. However, Bachelor's model is only restricted to a diluted concentration and the A-S model generally overpredicts the settling velocities and shows a

larger deivation at the lower interface. They are all emperical models with the need to choose exponent coefficients or other artificial coefficients to satisfy the equations.

In addition to empirical models, there are also mathematical treatments of sedimentation which relate the settling velocities to the properties of suspensions. In particular, Kynch's one-dimensional monodisperse zonal sedimentation model (Kynch 1952) is regarded as the first truly numerical model for the sedimentation and separation of particle fractions forming incompressible cakes. It has been further extended by various authors (e.g., Davis and Russel (Davis and Russel 1989) who included Brownian diffusion for colloidal particles, and van Deventer *et al*., who incorporated aggregate densification (van Deventer et al. 2011)). There are also other complex simulations using Masliyah-Lockett-Bassoon (MLB) model (e.g.,(Berres and Bürger 2003, Tory and Ford 2004)), force coupling method (FCM) (Abbas et al. 2006), effective-medium model (Koo 2008) or effective voidage model (Dutta and Bhattacharyya 2009) to predict the settling velocities of two interfaces but cost more computation time. 1D simulation models are very useful and efficient to predict the particle settling velocity and the concentration change. There are mainly two kinds of 1D simulation models, particle-based and the continuum-based approaches. The comparison of them was discussed by Bargiel and Tory (Bargie and Tory 2010). Now, most settling prediction models are time-consuming or ignore the particle Brownian motion and particle-particle interactions, where particles are treated as rigid objects. However, in the work of Antonopoulou et al (Antonopoulou et al. 2018) particles interparticle interactions are captured through the modelling of DLVO theory, which may be extended to bidisperse and polydisperse systems.

For nanoparticles, suspended in the liquid phase is common due to the size and usually can be easily separated with liquid-gas interface separation technology such as flotation. The dynamics of nanoparticle-bubble interactions especially the dynamic of adsorption when

particles contact with the bubble interface is a very complex scientific area, which is difficult to study directly. It is obviously important in floatation processes, as well as in the formation of particle stabilised foamed chemical products. For the particle adsorption processes, there are mainly three steps (Xing et al. 2017): drainage, film rupture, and contact until stable. There are also two theories that described the small particle adsorption at the liquid-gas interface with the diffusion-controlled model and the mixed kinetic-diffusion model (Eastoe and Dalton 2000) which can predict the adsorption process with the variation of dynamic surface tensions (DSTs). The contact angle of adsorbed particles is also an important factor in the adsorption process and directly influences the stability of adsorption and the detachment energy (Zhang et al. 2017). For very small nano particles, they behave dynamically more like surfactants, but for larger colloids, they do not really change the surface tension directly, but generate surface deformation and cause an ‘apparent’ surface tension variation (Manga et al. 2016).

Colloidal particle adsorption is a quite small-scale simulation, and continuity assumption is limited in some cases. Bidisperse sedimentation is significantly influenced by particle mixing ratios and sizes, which is more complicate for polydisperse systems. However, for colloids, the detail information in the settling process is hard to obtain and demand to investigate. Single colloidal particle adsorption behaviour is quite hard and expensive to obtain. The small size of colloids makes it nearly impossible to track the adsorption. However, the adsorption at liquid interface is quite important in industrial process especially the application with different wettability which is a significant influence factor. Knowing the particle adsorption with different wettability is a burning question.

1.2 LBM and DEM Simulations

As a mesoscopic method, the lattice Boltzmann method (LBM) has developed into a promising numerical technique for simulating multiphase flow. Unlike the traditional

computational fluid dynamic methods (CFD) (such as the volume-of-fluid (Hirt and Nichols 1981), level-set methods (Sussman et al. 1998)) which solve the conservation equations of macroscopic properties (i.e. mass, momentum, and energy) numerically but need to follow the continuity assumption and restricted in mesoscopic and microscopic scale, LBM shows good performance in both scales. Conventional fluid dynamic methods used N-S equations (Li et al. 2001) to solve the fluid flow problems. LBM has been used as an alternative to N-S equations in small-scale simulations (Yang et al. 2018). The LBM shows many advantages including simplicity and high efficiency in program parallelization and ease in dealing with complex boundaries, and its kinetic nature allows simple incorporation of microscopic physics without the constraints of molecular dynamics simulations on length and time scales (Aidun and Clausen 2009). LBM has been extensively used to simulate liquid-gas two-phase flows and gas-solid two-phase flows. There are many multiphase models in LBM such as the colour model (Gunstensen et al. 1991), free energy model (Swift et al. 1995), mean field model (He et al. 1998) and pseudopotential model (Shan and Chen 1993). The pseudopotential model is also known as the Shan-Chen model which uses a pseudopotential between fluid nodes to generate a multiphase which is one of the simplest schemes to code, thus, attracting researchers.

The discrete element method (DEM) (Cundall and Strack 1979) is widely used to investigate the constitutive mechanical behaviour of materials such as rock, soil, aggregates, and powders. In this method, Newton's equation of motion is solved for individual particles (Cundall and Strack 1979). In DEM, the granular system is modelled as an assemblage of geometrically simplified objects or elements (particles). The particle-particle interaction in DEM is evaluated through contact law. DEM has been successfully combined with traditional CFD schemes to simulate fluid-granular interaction behaviour (Sl et al. 2021, Fei et al. 2022). Since both the LBM and DEM are basically explicit, they are highly compatible from the

computation and implementation points of view (Feng et al. 2007). The information exchange between LBM and DEM is also important and mainly the forces and solid object movement. There are mainly four coupling methods: Simple bounce-back (Ladd et al. 1994, Ladd 1994), Interpolated bounce-back (Bouzidi et al. 2001, Chun and Ladd 2007), Immersed moving boundary method (IMB) (Noble and Torczynski 1998, Owen et al. 2011), and immersed boundary method (IBM) (Peskin 1972, Ladd 1994). They have their own advantages and disadvantages in different situations. With both advantages of LBM and DEM, the particle movement at the multiphase interface can be achieved.

However, there are problems when coupling the LBM and DEM methods such as the multiphase force exchange and the calculation treatment on moving objects. The adhesion force between LBM and DEM is still an unfixed problem which seriously restricts multiphase coupling and the industrial use of these models.

1.3 Aims & Objectives

From the above, it is evident that there are still unknown problems in colloidal particle sedimentation, especially for bidisperse and polydisperse system, as well as complexities in understanding the influence of particle wettability on adsorption kinetics at liquid-gas interfaces. Thus, in this thesis, the main aims are shown as follows:

1. Study the bidisperse experimentally to investigate the influence of size ratio and mixing ratio on the settling process and hindrance effects. Compare settling data for a range of system to current analytical settling models.

2. Propose a bidisperse 1D mathematic simulation model that can be used to predict the settling of the bidisperse systems and track the concentration evolution of species, to better describe the bidisperse sedimentation system in both gravity and centrifugal conditions. Simulations will be validated against completed experimental data.

3. Experimentally study wettability influences on nano particle adsorption dynamic at air-water interfaces, including the packing network structure of adsorbed monolayers.

4.Try to propose a new combined LBM-DEM numerical method that can be used to simulate the process of nanoparticle adsorption at the liquid-gas interface and realise the influence of different particle wettability. Again, the proposal is to validate against experimental data collected in the thesis, as well as other test cases.

1.4 Thesis Summary

While ubiquitous in nature, industrial engineering and chemical consumer products, a complete understanding of the dynamics of nanoparticle suspensions is lacking. While predicting their gravitational behaviour within liquid suspensions is possible with a number of modelling approaches, aspects such as particle polydispersity and dynamic particle-fluid interactions are complex, resulting often in poor correlations to experimental data. Nanoparticle adsorption at interfaces is also extremely difficult to model, requiring knowledge of individual particle adsorption rates, and secondary network reorganisation.

To help develop robust approaches to predict nanoparticle dynamics, this thesis considers a number of key aspects of nanoparticle sedimentation and adsorption. Specifically, the sedimentation of bidisperse nanoparticle mixtures is explored, as the most fundamental case of polydispersity, both from an experimental perspective and through an innovative 1D simulation. Then, the adsorption of nanoparticles at an air-water droplet surface is explored, and the effects of contact angle on network structure and adsorption rate are measured. Lastly, an LBM and DEM coupling framework is established to numerically simulate the particle adsorption process with the different particle wettability to get a better understanding of the particle adsorption at the liquid interface.

This thesis aims to study the process of silica colloidal particles sedimentation and adsorption at the liquid-gas interface and used flotation as an example to deconstruct the mechanisms. Experiment and simulation were both considered the gain a comprehensive understanding of the role of particle size and wettability on the whole process. The following contains a summary of the thesis structure:

Chapters 1&2 introduction and literature review encompass the introduction of the study and literature review. Chapter 1 contains an introduction of general colloidal sedimentation and particle adsorption processes, as well as a brief introduction to LBM and DEM in simulation work. Chapter 2 comprehensively details former researcher's important sedimentation experiments and improvement of colloidal suspension systems and adsorption studies. The important influence factors are discussed such as particle size and hydrophobicity. The development of LBM and DEM are also listed in detail, and the applicability in multiphase flows highlighted. They have been proved as useful tools in fluid flow simulation studies.

Chapter 3 preparation of study. Describes the experimental systems and material particles that were used throughout the thesis studies and outlines a number of general experimental procedures. It includes the characterisation of the nanoparticle and the esterification method used to alter the particle hydrophobicity. The contact angles of esterified silica wafers are also checked.

Chapter 4 & 5 sedimentation experiment and simulation. The bidisperse sedimentation experiment results are shown in Chapter 4. The Mixture of 100:500 and 500:800 silica particle dispersions are measured previously using Zetasizer and LUMiSizer. The size distribution data and settling velocities of upper and lower interfaces are then analysed and compared to empirical models. 1D bidisperse sedimentation simulation is introduced in Chapter 5, which is based on Davis-Russel's model (Davis and Russel 1989). Improvements

to the 1D model are incorporated and the results also compared with the empirical models and experiment data.

Chapter 6 adsorption experiments. Particle network structure and adsorption experiments are conducted with a Langmuir trough and pendant drop surface tension instruments, for particle with variable wettability at an air-water interface. The results are analysed using a modified short-time approximation model and a modified long-time approximation model, to obtain adsorption kinetics assuming diffusion dominated interactions.

Chapter 7 LBM -DEM simulations. The methodologies of LBM and DEM are shown in Chapter 7 and some improvement schemes proposed and verified with case study examples. Then, single particle adsorption simulations are completed at an air-water interface, and simulated data compared qualitatively with experiments from Chapter 6.

Chapter 8 Conclusions and Recommendations.

2. Literature Review

Outline

Particle sedimentation and liquid-gas interface adsorption are common phenomena in many industrial processes, such as flotation and coating, while they are important more fundamentally to science and engineering. There are many previous research and useful methods that have great potential to study these problems. To better describe the studies, his literature review is divided into a number of sections: Section 2.1 covers the stability of particle suspension and DLVO theory; Section 2.2 focuses on particle sedimentation and experimental methods such as using analytical centrifuge on bidisperse and polydisperse systems; Section 2.3 describes a number of empirical and analytical models that used to simulate sedimentations; Section 2.4 covers topics of particle adsorption at the liquid interface using experimental methods and simulation models. Section 2.5 introduces LBM models and the coupling with DEM to solve multiphase fluid flow which shows good performance at mesoscopic scales.

2.1 DLVO Theory of Particle Stability in Suspensions

Colloidal dispersions play a significant role in a wide range of applications and the stability of colloids in the liquid has been studied for many years (Churaev and Derjaguin 1985, Churaev 1995, Heurtault 2003, Liang et al. 2007, Ueno et al. 2008, Iijima and Kamiya 2009). To start the study, suspensions are assumed to be in a stable state and the particles and bulk fluid are not easily separated which may need a couple of techniques or theories to support. In colloidal systems, particles dispersed in water and any liquid of high dielectric constant usually develop a surface charge, and there are two charging mechanisms (Liang et al. 2007) for it. One is by the ionization or dissociation of surface groups, and another is by the adsorption of ions from solution. Hence, an individual particle immersed in the liquid will be

surrounded by an electric double layer. There are two models for the compact part of the double layer, as shown in Fig.2-1 (A and B). The model shows in Fig.2-1 (A) allows for a plane of adsorbed ions (partially dehydrated) on the particle surface (the centres of which form the locus for the inner Helmholtz plane (IHP)) followed by a plane occurring at the distance of closet approach of the hydrated counterions (the outer Helmholtz plane (OHP)). Fig. 2-1(B) shows another type of surfaces, such as proteins, where there are few or no adsorbed ions at all, the modified Gouy–Chapman model, where the OHP is located at the plane of closest approach of the hydrated counterions is probably more appropriate.

There is also a comparison of two popular models of the electric double layer, namely, the diffuse layer and the basic Stern model for a plate surface shows in Fig.2-1 (C and D). The diffuse layer model assumes a negligible ionic size and the basic Stern model considers a finite ionic size by introducing a plane of closet approach.

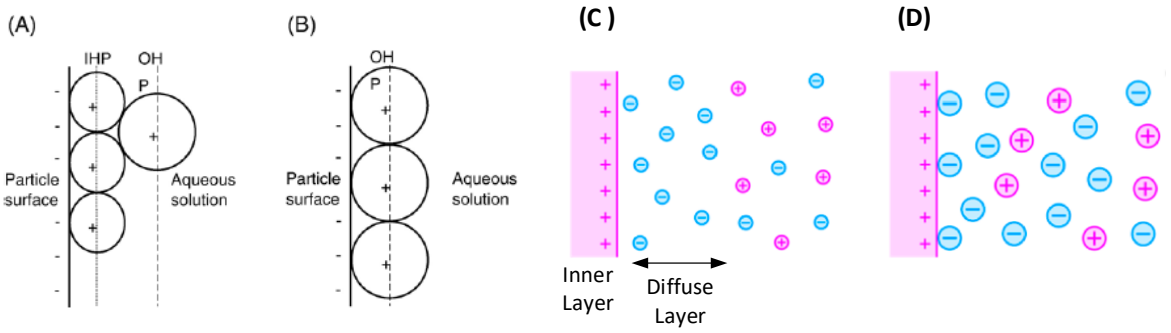

Figure 2-1 Models for compact part of the double layer (Liang et al. 2007), (A) Gouy-Chapman-Grahame-Stem (triple layer) model and (B) modified Grouy-Chapman model. (C) the diffuse layer model. (D) the basic Stern model (Trefalt et al. 2016).

The well-known Derjaguin-Landau-Verwey-Overbeek (DLVO) (Verway and Overbeek 1948, Derjaguin and Landau 1993) theory is a classical explanation for colloidal particle suspension stability in the fluid bulk, which is the algebraic summation of van der Waals attractive force, f_{vdw} and electrostatic repulsive force, f_{ele}. For two spherical particles (Peng et al. 2010), *i* and *j*, the forces can be expressed as Eq.(2.1, 2.2):

$$f_{vdw} = -\frac{A_H (4r_i r_j)^3}{6}[\frac{s_{ij}}{[s_{ij}{}^2 - (r_i + r_j)^2]^2 \times [s_{ij}{}^2 - (r_i + r_j)^2 + 4r_i r_j]^2}] \quad (2.1)$$

$$f_{ele} = 64\pi\varepsilon_r\varepsilon_0\kappa(\frac{RT}{zF_c})^2 \times \tanh(\frac{zF_c\zeta_i}{4RT}) \times \tanh(\frac{zF_c\zeta_j}{4RT}) \times \frac{r_i r_j}{r_i + r_j} e^{-\kappa h_{ij}}, \quad (2.2)$$

where A_H is the Hamaker constant, $A=\pi^2 C\rho_i\rho_j$, where C is related to materials. The Hamaker constant for a given system is notoriously difficult to obtain experimentally (Leong and Ong 2003). There are many values for the Hamaker constant of silica-water-silica systems, for example, 0.7×10^{-20} and 3.8×10^{-20} (Rhodes 2008, Kes et al. 2009). s_{ij} is the centre-to-centre distance between the two particles and r is particle radius. ε_r is the dielectric constant of the medium, ε_0 is the permittivity of vacuum, $8.8541878128(13)\times10^{-12}$ F.m^{-1}(CODATA 2019), and z is the valence of the background electrolyte. For H^+, z is +1, while for Ca^{2+} it is +2. F_c is the Faraday constant, while ζ_i is the zeta-potential of the particles, and h_{ij} is surface separation distance. It is worth to mention that the formula above can only be applied when the range of interactions and the separation distance h_{ij} are much less than the radius of the particle. Also, κ is the Debye-Huckel parameter which is also the inverse Debye length and can be expressed as Eq. (2.3):

$$\kappa = \sqrt{\frac{z^2 e^2 \rho_\infty}{\varepsilon_0 \varepsilon_r k_B T}} or \kappa = \sqrt{\frac{2N_A e^2 I}{\varepsilon_0 \varepsilon_r k_B T}} \quad (2.3)$$

Where e is the elementary charge, $1.602176621e^{-19}$(Newell and Tiesinga 2019), ρ_∞ is the number density of ion i in the bulk solution. N_A is Avogadro Constant. I is 1000 * salt Molar, mol/m^3. R is the gas constant, T is Kelvin temperature. An electric double layer is a phenomenon that plays a fundamental role in the mechanism of the electrostatic stabilization of colloids. Colloidal particles gain negative electric charge when negatively charged ions of the dispersion medium are adsorbed on the particle surface (Park and Seo 2011). With the

value of attractive and repulsive forces, we can calculate the double layer stability, by considering the interaction potential versus distance, as exampled by (Antonopoulou et al. 2018) shown in Fig.2-2.

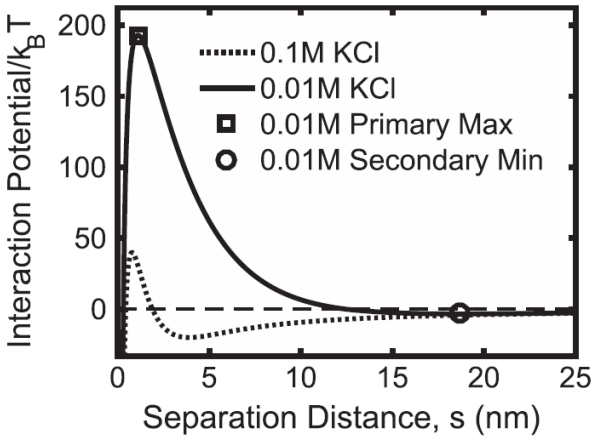

Figure 2-2 DLVO-computed interaction potential normalised by thermal energy for silica in 0.01M and 0.1M KCl suspensions, using a Hamaker constant of 2.5 × 10-20 J for the silica-water-silica system(Antonopoulou et al. 2018).

However, with the continuing studies of colloids (Liang et al. 2007), DLVO theory has been found to fail in the explanation of various experimental observations where non-DLVO interactions are also needed to be considered. Non-DLVO forces including solvation forces, hydrophobic forces and steric forces are still out of the realm of DLVO theory. However, for certain well-described particle systems, DLVO interactions are still the dominating force for stability in colloidal dispersions. In the current thesis, I propose to use well-stabilised silica nanoparticle systems, which can be described using DLVO theory, to ensure stable nanoparticle dispersions in the thesis work.

2.2 Particle Sedimentation

A great number of studies have been reported over the years on characterising complex colloidal sedimentation (e.g.,(Vesaratchanon et al. 2007, Padding and Louis 2008)) and prediction of the settling rate (e.g.,(Cao et al. 2015, Antonopoulou et al. 2018)). For industrial processes and products, perhaps the greatest challenge in predicting sedimentation and separation is that systems are not always monodisperse. In fact, bidisperse and polydisperse

suspensions are more common. Bidisperse suspensions can be regarded in many ways as the 'simplest' case of polydisperse systems, allowing investigations into the underlying mechanisms of multi-sized particle settling. For example, Richardson and Zaki (Richardson and Zaki 1954) proposed a simple formula based on monodisperse suspensions and applied it to polydisperse systems, using the total volume fraction of particles. The terminal velocity of a single particle is expressed as Eq. (2.4):

$$U_0 = \frac{d^2(\rho - \rho_c)\mathrm{g}}{18\mu_c} \tag{2.4}$$

Where d is the diameter of the dispersed phase, ρ is the dispersed phase density (kg/m^3), g is the acceleration (m/s^2), ρ_c and μ_c are the density and viscosity of the continuous phase, respectively. The hindrance effect was proposed by Richardson and Zaki (Richardson and Zaki 1954), and the sedimentation velocity is described by the following Eq.(2.5):

$$\frac{U}{U_0} = (1-\phi)^n \tag{2.5}$$

Where U is the sedimentation velocity and U_0 is the Stokes' velocity, ϕ is particle volume concentration and n is the sedimentation coefficient.

In the industrial processes, particle suspensions are more likely to be bidisperse or polydisperse rather than monodisperse, and R-Z model shows low performance in those no-mono system cases. Other investigations have shown, nonetheless, that this formula did not match well with experiments of large differences in size or density (Davis and Gecol 1994), although further modifications to power-law models for sedimentation of bidisperse and polydisperse dispersions have been proposed (Mirza and Richardson 1979, Krishnamoorthy 2010). Empirical models have not always proved to be accurate in bidisperse sedimentation, especially for large particles (Cheung et al. 1996). While the sedimentation of polydisperse

systems is more complex than bidisperse, it is known to be strongly influenced by the size distribution of particles (Zimmels 1983). Therefore, the use of multiple particle size ratios in investigations will aid in understanding the interaction between different size classes. It has also been reported that the mixing ratio of particles influences the relative viscosity of species in bidisperse sedimentation (Chong et al. 1971), which is not something that is fully taken into account in most analytical sedimentation models.

While significant theoretical and experimental work exists on bidisperse settling, as outlined, considerable questions remain about their sedimentation dynamics and, in particular, the interactions between one size fraction on the settling of another. Especially for fine colloidal systems, more understanding is required of the effect of size and concentration ratios on sedimentation, and whether changes in specific ratios significantly affect particle drag or enhance particle wake effects. Such changes may also modify the accuracy of common sedimentation models that are widely used industrially for predicting behaviour.

The bidisperse suspension system is more complex than monodisperse due to different species mixture and interparticle interactions. Some researchers studied non-colloidal particles, and some are trying to explain the sedimentation process with simulation models. Colloidal particles are usually having a diameter of approximately 1 nm to 1 micrometre, for particles larger than 1 micrometre we marked them as non-colloidal particles. Non-colloidal suspensions were studied by Cheung and co-workers (Cheung et al. 1996). They proposed a model to calculate the bidisperse suspension interfaces and they also mentioned when large particles settled the small particles will reach a steady-state velocity.

There is much research that focuses on modifying the R-Z-like model to predict the particle sedimentation in a dilute or concentrated situation or bidisperse and polydisperse system. The Richardson-Zaki model (Richardson and Zaki 1954) is very popular but does not shows good

performance in bidisperse and polydisperse systems. Alternatively, Bachelor (Batchelor 1972) derived a linear relationship between the mean fall velocity of a particle and the concentration for diluted monodisperse suspensions, where the coefficient of the equation has been further discussed and modified by other authors (e.g., (Batchelor and Wen 1982, Al‐Naafa and Selim 1992)). In a diluted bidisperse sedimentation system, Al-Naafa and Selim (Al‐Naafa and Selim 1992) studied the sedimentation of mono and bidisperse for uncharged rigid spheres. They also proposed formulas to predict the settling velocities for bidisperse particles which are shown in Fig.2-3. The results showed good agreement with the experimental data, with some overprediction in dilute concentrations. The upper interface mainly consists of particles with smaller settling rate and the lower interface is the mixture of both species.

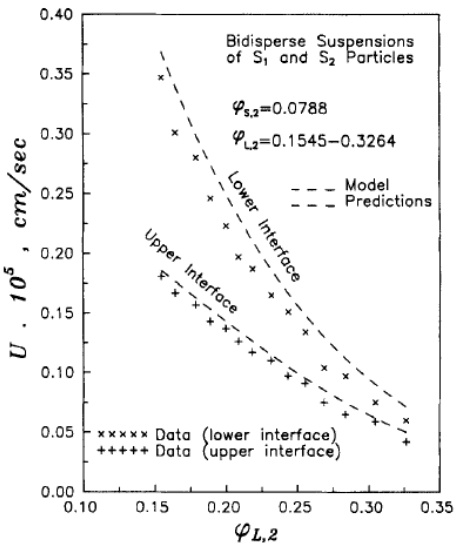

Figure 2-3 Hindered settling data for a bidisperse suspension of particles (Al‐Naafa and Selim 1992).

There is much research that has experimentally studied the bidisperse sedimentation suspension. To observe the sedimentation of particle suspensions, many effects have been considered, but it is very difficult to clearly record the particle movements because of the large number in suspension. There are some studies that used picture analysation to track and record the interface of sedimentation thus getting the sedimentation information (Davis and

Acrivos 1985, Krishnamoorthy et al. 2007, Spruijt and Biesheuvel 2014, Hernando et al. 2015). However, most of them cannot obtain of the detail the concentration, and only focus on the settling rate (Krishnamoorthy et al. 2007), the interface position (Spruijt and Biesheuvel 2014) and the sediment bed (Hernando et al. 2015) or roughly quantitively check the sedimentation (Davis and Acrivos 1985). Furthermore, this technology is not very suitable for polydisperse suspensions, because it is hard to distinguish particles from other species.

Another potential complexity with studying fine colloidal systems is that separation occurs naturally over extended periods of time that are difficult to measure accurately, and subject to other forces, in particular, Brownian motion (Padding and Louis 2008) that counters the gravitational movement. To overcome the challenges of low settling rate systems, centrifugal sedimentation is a simple but useful intensified solid-liquid separation method. Within the high-value chemicals industry, centrifugal separators are a very common method to accelerate settling processes, either for solids waste management (Chu and Lee 2001, Usher et al. 2013) or as an investigative technique to study products which are formulated for long shelf lives (Mao et al. 2001, Sviatskii et al. 2016, Meng et al. 2017). Torsten et al (Detloff et al. 2006) used an analytical centrifuge – LUMiSizer with STEP^{TM} – Technology checked particle sedimentation with the light extinction curves which has shown in Fig.2-4. The settling rate and size distribution can be calculated from the light extinction change verse time that recorded as shown in Fig.2-4 (right).

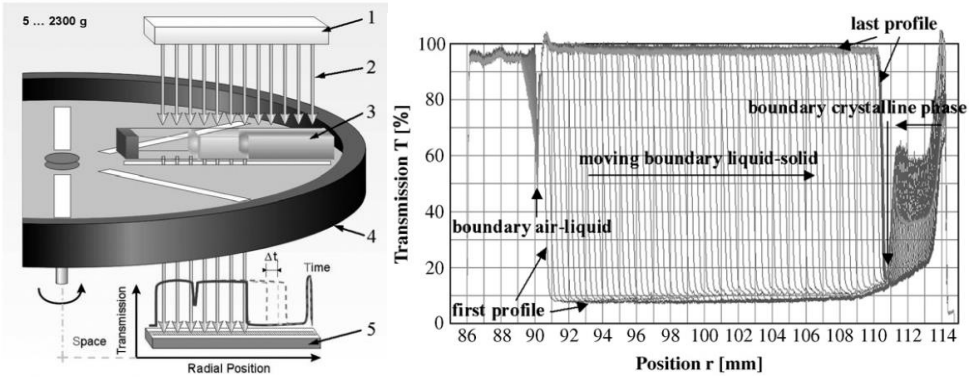

Figure 2-4 Measurement scheme of the analytical photocentrifuge (left). Transmission profiles of monodisperse SiO_2 280 nm at 2000 rpm(right)(Detloff et al. 2006).

Since it is tedious to record and analyse the particle suspension sedimentation with the camera and picture analysation, the light scattering method becomes an efficient way to get the settling rate based on the intensity change of particle suspension vs time. For a monodisperse system, the light intensity vs time profile is smooth and has an 's' shape curve (Davis and Birdsell 1988). The curve can be more zigzag for bi/polydisperse system (Cheung et al. 1996). In particular, laser-based centrifugal analysers can simultaneously track interfacial settling rates of multicomponent systems, using scanning light transmission data. Modern instruments have been developed into very useful tools to investigate colloidal suspensions, allowing illumination across their entirety by having detectors that can measure light extinction profiles instantaneously with micrometre scale resolution (Sobisch and Lerche 2018). It is reported that even very small changes in dispersion state can be detected. Lerche (Lerche 2019) has characterised both mono and polydisperse systems ranging from nano to micro-sized with the same instrumentation, showing the high reliability of centrifuge data and analysis methods. Analytical centrifuges can also measure the size distribution of suspensions, where results have been shown to be more accurate than dynamic light scattering (DLS) devices (Chiu et al. 2011), especially for bidisperse and polydisperse nanoparticles (Braun et al. 2011), and have been used to separate bidisperse charged nanoparticle suspensions (Xu et al. 2020). Furthermore, particles in different species show clearly on the intensity vs position curve in most cases (Ullmann et al. 2017), and the settling

rate can be easily calculated with different levels of intensities of known particles which has been shown in Fig.2-5. The intensity data shows 3 species of particles with different intensity levels, and it is easy to calculate the settling rate of each species when tracking the data change with positions.

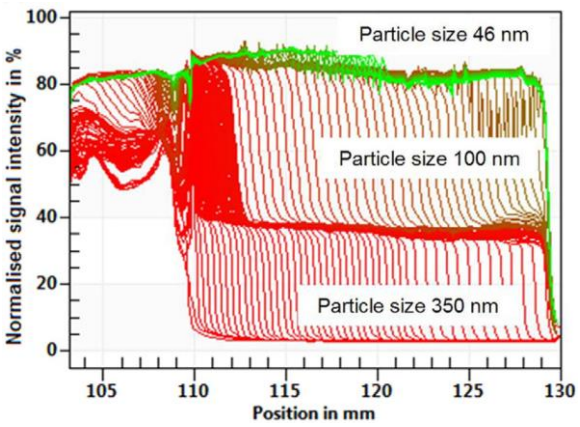

Figure 2-5 Cuvette-type analytical centrifugation results with 3 particle sizes (Ullmann et al. 2017).

Centrifugal sedimentation for concentrated bidisperse colloidal suspension has been studied by Cao and co-workers (Cao et al. 2015). They used polymethylmethacrylate (PMMA) particles of different sizes with equal densities. There are two types of sedimentation for bidisperse system names settling independently and collectively which is shown in Fig.2-6. It was found that the sedimentation coefficient decreased with decreasing porosity and increasing ratio of the volume of small particles to the volume of total particles. Then, a model was developed for describing the relation between the sedimentation coefficient and porosity in the centrifugal sedimentation of a bidisperse suspension.

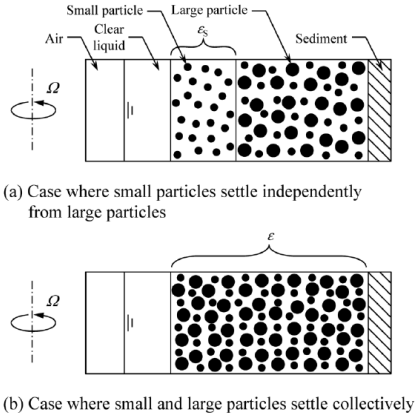

Figure 2-6 Two types of centrifugal sedimentation behaviours in bidisperse suspension(Cao et al. 2015).

With a number of advantages, the analytical centrifuge also has drawbacks as it is based on light transmission. If the light transmission is disturbed by other species or the solution in suspension, a large deviation or missing data may occur which is captured by the author's research in the later Chapter 4.

Within the high-value chemicals industry, centrifugal separators are a very common method to accelerate settling processes; either for solids waste management (Chu and Lee 2001, Usher et al. 2013, Shiels et al. 2018) or as an investigative technique to study products which are formulated for long shelf lives (Mao et al. 2001, Sviatskii et al. 2016, Meng et al. 2017). Furthermore, centrifugal sedimentation may lead to enhanced Reynolds number-dependent wake effects (Yin and Koch 2007), as well as Drafting-Kissing-Tumbling (DKT) events (Dash and Lee 2015, Zaidi et al. 2015) that can lead to a modified drag force acting on trailing particles in a moderate Re number which has been shown in Fig.2-7. This phenomenon has been verified by simulations (Yin and Koch 2007) and has been found to be even more prevalent in dilute suspensions (Hu and Guo 2019). Therefore, the use of analytical centrifuges for studying sedimentation must be made with care, to take account of other particle-fluid dynamic effects, which would not be evident under earth gravity.

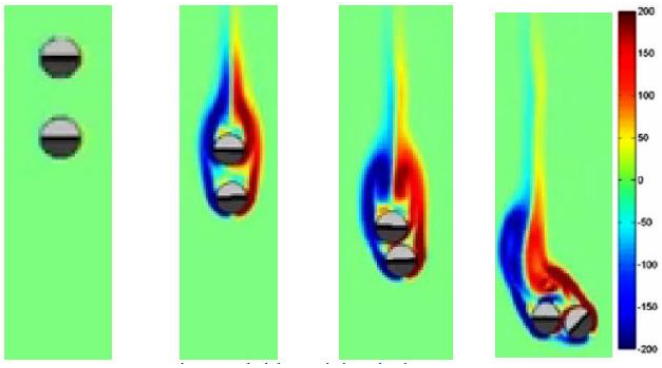

Figure 2-7 Fluid vorticity during DKT (Zaidi et al. 2015).

2.3 Particle Sedimentation Simulation Models

Empirical models, such as the R-Z model (Richardson and Zaki 1954), modify the terminal velocity of single particles using some hindrance functions to slow the predicting settling rate and fit the experimental data. However, the influence of a number of particle factors on the overall settling rates has been modelled and simulated by researchers in more detail. The important influence factors such as mixing ratio, bidisperse fluid viscosity, and particle-particle interactions are not only simply estimated as empirical functions but can be modelled explicitly. Usually, models are based on concentration analysation, which focuses on the concentration change of particles or particle-based systems with the mass of particle movement (Bargie and Tory 2010).

Tory and Ford (E. et al. 2004) used the Masliyah-Lockett-Bassoon (MLB) (Lockett and Bassoon 1979, Masliyah 1979, Bürger et al. 2002) equation to predict polydisperse settling velocities. The concentration changes of the various species in each layer represented the mean velocity of each species. They used a stochastic model to incorporate the spatial and continuous temporal variability of particle velocities and finally produced a hydrodynamic diffusion that replaces shocks with concentration gradients. However, in the MLB model, interparticle interactions are ignored and a stochastic substitute is used to simulate the behaviour of polydisperse suspensions, which generates noise like a volume fraction curve. It also ignores the different mixing ratio concentration effects in bidisperse and polydisperse

systems. The interfaces that represent the particles did not form immediately, but with an 'induction period' which also increased the deviation. The result of the stochastic model is shown in Fig.2-8 which illustrates the volume fraction change of two species at different height during the sedimentation.

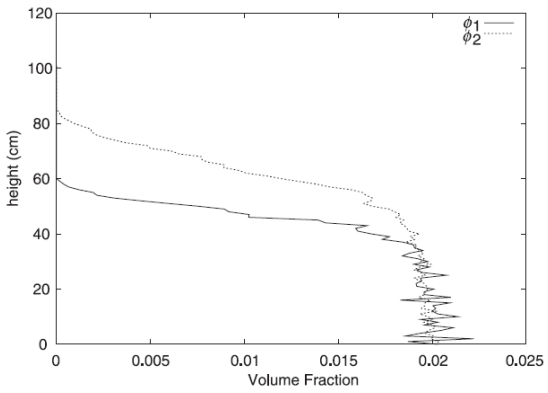

Figure 2-8 Solid profiles for the stochastic model at t =50 and Stokes velocity ratio α = 0.7 (E. et al. 2004).

Waston et al (Watson et al. 2005) introduced a simple force and flux balance model for sedimentation and creaming in high volume fractions. They extended the model from a monodisperse version to a polydisperse and the settling data can be extracted from the concentration change of each species. The model also gives a satisfactory qualitative description of real emulsion creaming data. However, it also implies that the effective droplet radius is larger than the measured droplet radius, or that the effective background viscosity is reduced. The model may generate a larger deviation on sedimentation simulations, especially for fast sedimentation cases. The concentration profiles vs time in the monodisperse system is shown in Fig.2-9.

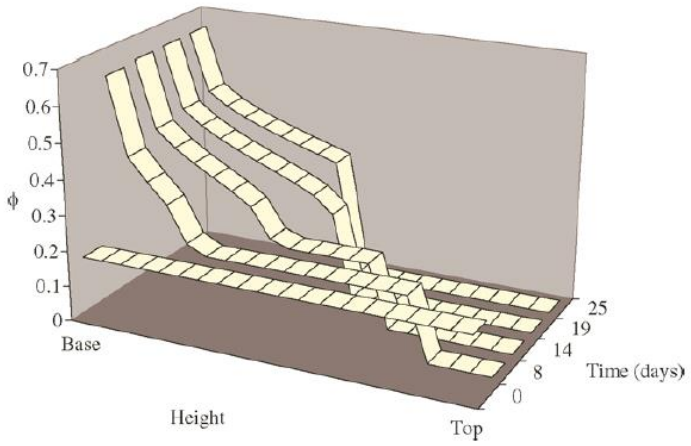

Figure 2-9 Model sedimentation profile for a 17.85% dispersion of 1.1μm diameter latex spheres calculated using monodisperse sedimentation model(Watson et al. 2005).

There are also researchers that trying to use a more complex and direct model to simulate the settling process and the dynamic of sedimentation (Abbas et al. 2006). Abbas et al used a force coupling method (FCM) based on a low order multipole expansion of the velocity disturbance induced by the presence of particles to describe the particle settling with gravity and showed a great agreement. DLVO theory can also be added to their model. The simulation approach is based on the solution of the three-dimensional Stokes equations forced by the presence of the dispersed phase. The multi-body hydrodynamic interactions are achieved by a low order multipole expansion of the velocity perturbation. The role of the different contributions of force coupling methods (FCM) on the relative trajectories is shown in Fig.2-10. Different marks represent the trajectories of particles with forces in a shear flow which has been described detailly in the figure. Particles are driven continuously to approach each other. The limit region of overlapping is materialized by the thin dashed line. The particles overlap when only the monopole and the dipole forces are applied. It can obtain very detailed information about single particles but is computationally intensive.

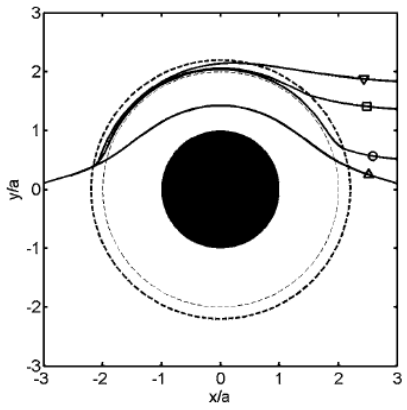

Figure 2-10: Relative trajectory of the centres of two equal spheres in a shear flow (Abbas et al. 2006) △ : FCM alone, o: Monopole + dipole + lubrication force. □ : Monopole + dipole + repulsion + lubrication force. ▽ Monopole + dipole + repulsion force.

Vesaratchanon et al (Vesaratchanon et al. 2007) summarized the progress of the development of colloidal sedimentation models for monodisperse, bidisperse and polydisperse nanoparticle dispersions until 2007. The limitations of various models were discussed and the factors such as particle concentration, particle charge, polydispersity in size, and electrolyte concentration were considered.

More recently, Koo (Koo 2009) utilized and compared four effective-medium models (marked as EM models) that determine hindered settling velocity of equal-sized particles in a viscous fluid. He found that the EM-IV model is the most suitable for predicting both the effective viscosity and the sedimentation velocity in the aspect of simplicity and accuracy which means is the most effective method. The comparison of settling velocity for four methods is shown in Fig 2-11.

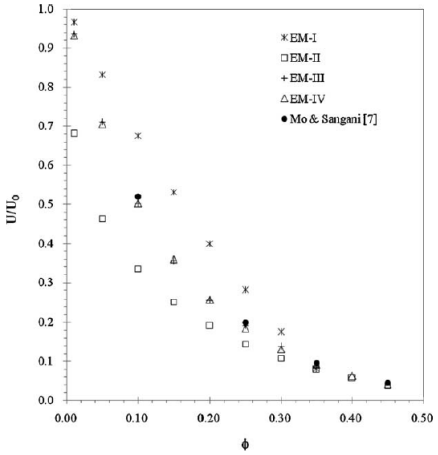

Figure 2-11 Normalized hindered settling velocity U/U_0 as a function of concentration(Koo 2009).

An effective voidage model that includes the influence of particle-particle interaction was used by Dutta and Bhattacharyya (Dutta and Bhattacharyya 2009) to predict the slip and interface velocities of sedimenting zones for bidisperse solid-liquid systems. The model assume that the thickness of the liquid envelops surrounding a 'test particle' is the same as that of the surrounding average particles leading to over-prediction of the effective voidage experienced by the smaller particles. They described the sedimentation zones of the bidisperse mixture which are shown in Fig.2-12. The model visualizes that particle in the bed surrounded by particles of 'average size' but influenced by an effective voidage difference from the average voidage. They predicted velocities of the upper and lower interfaces and compared them with former models and showing better agreement and giving good insight into the treatment of particle fluid environment.

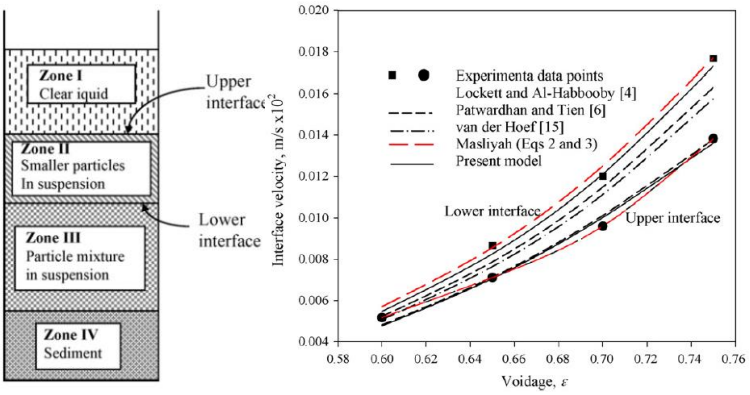

Figure 2-12 The different zones of sedimentation of a binary mixture of solid particles (left) and compassion of experimental and predicted interface velocities (right) (Dutta and Bhattacharyya 2009).

Suspension viscosity models (Zhang and Acrivos 1994) are one of the most popular continuum-based models to predict the settling velocity of particles with the advantage of reducing the velocity to zero at the maximum volume fraction (unlike the classic R-Z model, which has realistic boundary condition for high volume fractions). Particles in suspension do not sediment alone but move and are hindered by surrounding particles, where the effect of hindrance increases as the particle volume fraction increase. Usually, sedimentation literature neglects particle interactions (Lockett and Al-Habbooby 1974, Ackerson et al. 1999, Genovese 2012) for convenience and based on the hard-sphere assumption, which means there is no restriction on the minimum separation distance between two colloidal particles. However, the assumption may not be suitable (Antonopoulou et al. 2018) for highly charged colloidal particles. Effective volume fraction and effective diameter have been used to describe interparticle interactions and depletion interactions, respectively. Particles in suspension do not sediment alone but are also hindered by surrounding particles. An effective volume fraction is defined based on the effective particle size and an exclusion volume around the particle. To describe colloidal suspensions, Metin (Metin 2012) has demonstrated the use of effective particle size and taking into account the interparticle interactions using an effective maximum volume fraction. This method can be applied in the monodisperse sedimentation model and can be extended to bidisperse models.

The bidisperse sedimentation has been studied for years, but in those studies, particles usually are not colloidal particles (Cheung et al. 1996, Cao et al. 2015) and in some research, the Brownian motion can be ignored (e.g.,(Abbas et al. 2006, Koo 2011, Hernando et al. 2015)). Furthermore, many researchers use simulations (Tory and Ford 2004, Koo 2008) to try to illustrate the mechanism of bidisperse sedimentation because the experiment is more difficult and the interface of bidisperse suspensions is hard to track. Therefore, there is still a need for

an accurate bidisperse settling model that can predict particle behaviours in complex multicomponent systems and track the detailed change of concentrations.

Some important attempts at simulating bidisperse sedimentation have been made by previous researchers, however. For example, Dorrell and Hogg (Dorrell and Hogg 2010) simulated bidisperse suspension sedimentation using a modified MLB model. Their work generalised the pioneering study of Kynch (Kynch and G. 1952) to mixtures of particle size and density and calculated the evolving state of the suspension. They showed how to classify the settling behaviour in one of four regimes, depending on the governing parameters that could be extended to mono, and poly disperse suspensions. They first found an ungraded region at the base of the deposit, then the size of the ungraded region, which was then normalised with respect to final deposit depth and grew as the total initial volume fraction was increased. However, they still used a monodisperse effective viscosity function in an R-Z model within their calculation. Examples of volume fraction changes for a bidisperse suspension are shown in Fig.2-13.

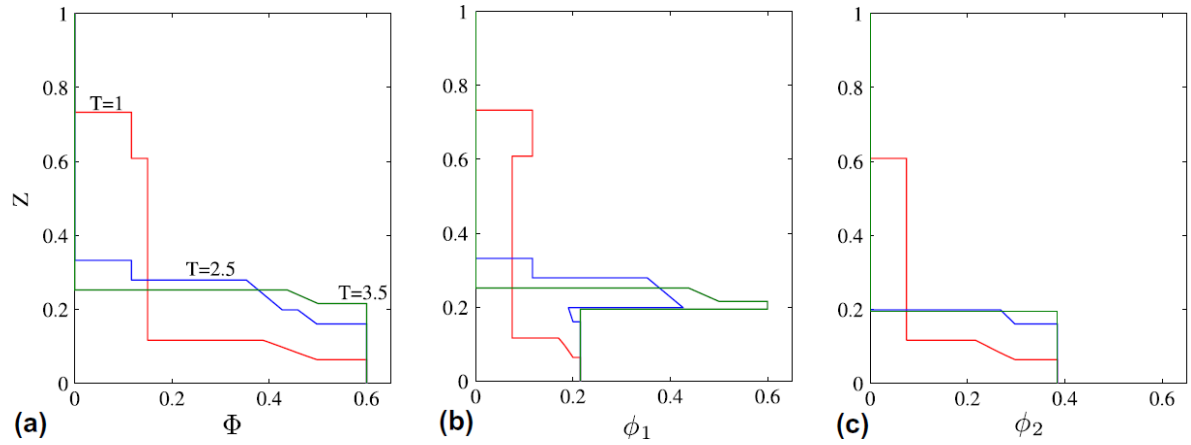

Figure 2-13 (a) The total volume fraction,Φ(Z,T), (b) volume fraction of species 1 ,Φ_1(Z,T), (c) volume fraction of species 2, Φ_2(Z,T) as functions of dimensionless height at T=1.0,2.5 3.5 Times (Dorrell and Hogg 2010).

A new differential model for the relative viscosity of bimodal suspensions was proposed by Qi and Tanner (Qi and Tanner 2011) which is a viscosity-based model. They proposed that

the bimodal suspension has a dominant large particle composition and that the small particles fill the empty spaces between the large particles. Thus, the model can be based on the theory of monodisperse suspensions and become the link between monodisperse and bidisperse systems. The example of calculated relative viscosity is shown in Fig.2-14.

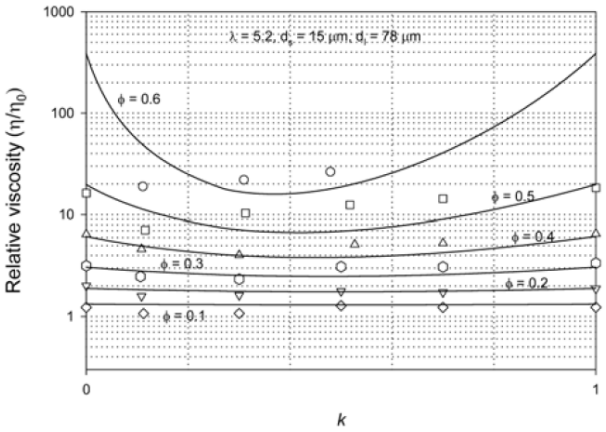

Figure 2-14 The calculated results compared to experimental data. k is the volume fraction of small particle. Lines: calculated results by using model(Qi and Tanner 2011); Symbols: experimental measurements given by Polinski et al (Poslinski and A. 1988).

In the research of Chiavassa and Marti et al (Chiavassa et al. 2016), they developed a hybrid finite difference WENO scheme that only uses the characteristic information of the Jacobian matrix of the system in the regions, where singularities exist or are starting to develop, and simulated polydisperse sedimentation. The results are shown in Fig.2-15. Although it solved part of the computation cost problem, the calculation cost is still large and not suitable for colloidal particles with a Brownian diffusion effect.

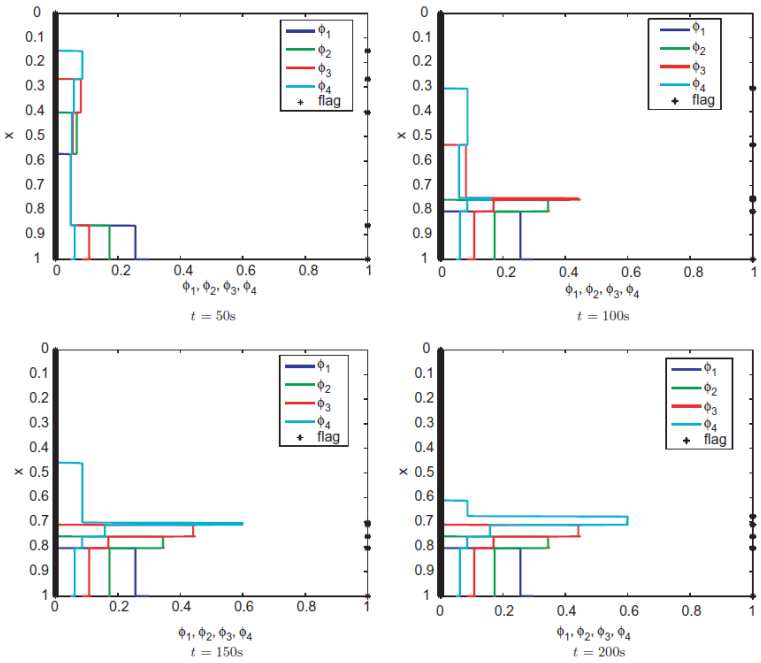

Figure 2-15 Time Evolution of the numerical solutions of a four multicomponent system and flag vector of test 1 computed with t= 300 s and N =16000 CELLS(Chiavassa et al. 2016).

Boscarino et al (Boscarino et al. 2016) used a linearly Implicit-explicit (IMEX) Runge-Kutta (RK) method to simulate polydisperse sedimentation, yielding good results which show very good agreement at the diffusion problems. However, this model, by contrast, focuses too much on the diffusion of particles and does not consider particle-particle interactions to a significant degree. So, it may be suitable at a very fine particle scale where diffusion dominated the behaviour of particles. A part of the resultant simulation is shown in Fig.2-16.

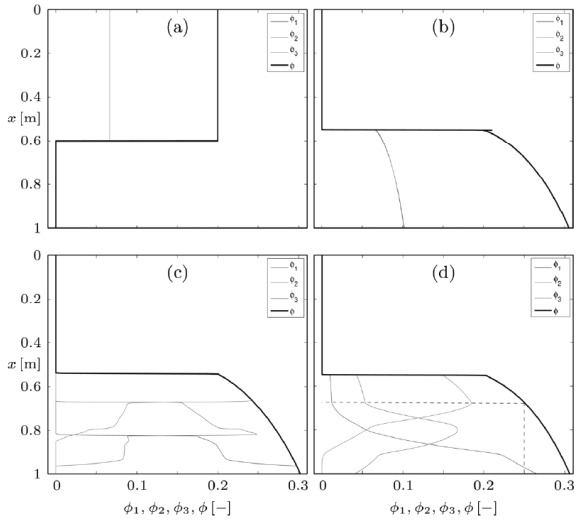

Figure 2-16 Model results (a) initial condition, (b,c,d)numerical solution with linearly implicit strongly-stability preserving (LI-SSP3) (4,3,3) scheme with x = 1/16000 m for solving (b) Model A, (c) Model B and (d) Model C at simulated time T =60000s (Boscarino et al. 2016).

To understand the sedimentation behaviour of colloidal suspensions, monodisperse is always a good starting point. Antonopoulou et al (Antonopoulou et al. 2018) proposed a one-dimensional model for sedimentation using an effective maximum volume fraction, with an extension for sedimentation under centrifugal force. The different volume factions of suspensions have different hinderance effect for particle sedimentation thus particles have different separation velocities from the bulk fluid to the sediment bed. An adaptive finite difference solver was used to obtain more accurate results. They provide that the maximum volume fraction accurately captures interparticle interactions with DLVO theory and can be used to predict the settling velocity of particles, which is a good insight for viscosity-based models. The result of separation velocity in different volume fractions is shown in Fig.2-17.

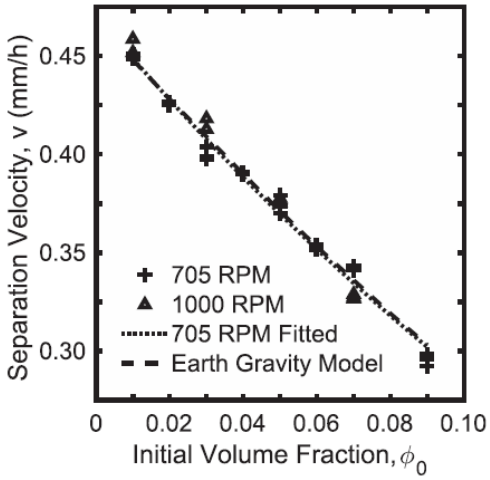

Figure 2-17 Separation velocities for different initial volume fractions and comparison with experimental data (Antonopoulou et al. 2018).

Since colloidal particles are small and related Peclet numbers are usually larger than 1 which means the Brownian motion can be important. The trend of research generally switched from simple 1D models to particle-based complex 3D simulation models which is more directly simulated the sedimentation and behaviour of particles but also more computational consuming. Padding and Louis (Padding and Louis 2018) employed stochastic rotation dynamic (SRD) to describe the solvent, and a molecular dynamic (MD) scheme to propagate the colloids. They found the thermal fluctuations may remain important up to a very large

Peclet number and hydrodynamic interactions are important for low Peclet numbers. Afra et al (Afra et al. 2019) used a lattice Boltzmann-discrete element method (LBM-DEM) to simulate freely falling particles on sedimentation behaviour and tracked the drafting, kissing and tumbling (DKT) process of particles has been realised. However, their model is only restricted to a small number of particles and a single fluid phase. Liu and Wu (Liu and Wu 2019) improved the coupling of LBM-DEM and included particle adhesive force, while they also improved the immersed moving boundary coupling method between LBM and DEM with low grid resolution to simulate more particles. Despite this, LMB-DEM methods are still extremely computationally intensive for simulating multi-particle sedimentation and related problems (as further explored in Section 2.5) especially if polydispersity is accounted for. Therefore, I believe there is still a critical requirement to develop relatively computationally efficient 1D models of particle settling, where effects of bidisperse sizes and particle interactions can be explicitly incorporated. It is clear that the use of modified viscosity models provides a potential route forward, and this method is chosen for investigation in the PhD project.

2.4 Particle Adsorption at Fluid-Fluid Interfaces

2.4.1 Thermodynamics and Wettability Influences of Particle Adsorption

When a fresh interface is formed with a surfactant solution, surfactant molecules can diffuse from the bulk to the interface, and then adsorb at the fluid interface (Eastoe and Dalton 2000). Like surfactants, solid particles can also adsorb at liquid interfaces. Thermodynamics favours the adsorption process, which results in the reduction of surface or interfacial tension (Bizmark et al. 2014). For nanoparticle adsorption, the size of colloids is one of the most important factors because it decides the relative magnitude of forces and other factors like collision probability. The surface charge is also an important factor when adsorption occurs. When charged colloidal particles are adsorbed at liquid interfaces (like air-water interface and

oil-water interface), their energy and dynamic change will be more complex than neutral particles or low-charged particles. Once adsorbed at the interface, the particle diameter and equilibrium contact angle at the interface determine the strength of adsorption (Manga et al. 2016). In this thesis, we mainly focus on the wettability effect of particles.

In the work of Eastoe and Dalton (Eastoe and Dalton 2000) small nanoparticle adsorption rates at the liquid-gas interfaces can be revealed by the variation of dynamic surface tensions, where there are mainly two models: the diffusion-controlled and the mixed kinetic-diffusion models. The former mainly describes adsorption when the liquid-gas interface is dilute, and particles are free to adsorb with no hindrance which is dominated by the diffusion effect. However, the mixed kinetic diffusion model, is more complex than the former one and needs to consider the adsorption barriers that prevent adsorbing. For adsorbed colloidal particles, they may be the potential barriers to unabsorbed particles and behave like surfactant. The study in surfactant can also reveal some mechanism of small colloidal particles. The theories use surfactant molecular as an example shown in Fig.2-18.

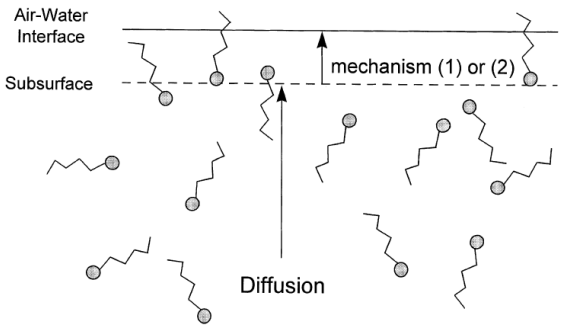

Figure 2-18 Transport of monomer to the interface(Eastoe and Dalton 2000). Once the monomer has diffused to the subsurface it will either instantaneously be adsorbed at the interface in accordance with the diffusion-controlled model (1) or will have to pass through a potential barrier to adsorb (2).

The Contact angle which can represent the strength of hydrophobic interactions is one of the most important factors that can influence adsorption. Contact angles of particles are directly linked to their wettability, which is influenced by the surface energy. The contact angle effect is shown in Fig.2-19, as discussed by Aveyard and Clint (Aveyard and Clint 1995). It also represents the trend that particles' contact line moves to an energetically stable state at the

interface, which means desorption is easier or harder to occur. With Young's equation, we can get the relationship between interface tension γ_{sa} solid-air, γ_{aw} air-water, and γ_{sw} solid-water as Eq. (2.6):

$$\gamma_{sa} - \gamma_{sw} = \gamma_{aw} \cos\theta \tag{2.6}$$

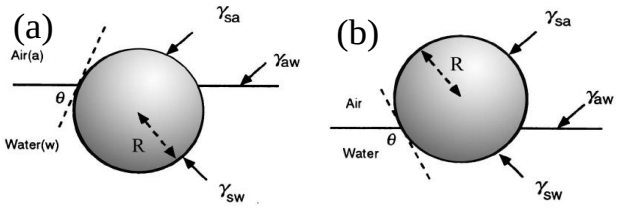

Figure 2-19 Effects of contact angles (Aveyard and Clint 1995). (a) hydrophilic, contact angle <90 ° , (b) hydrophobic, contact angle >90 ° .

The reduction of surface energy (ΔE) is associated with the adsorption of a single spherical particle to its radius and wettability. With some former studies (Lin et al. 2003, Lin et al. 2005, Bizmark et al. 2014, Dugyala et al. 2016), the understanding of fundamental aspects of colloidal particle adsorption at the fluid interface has not kept pace with applications (Bresme and Oettel 2007). Measurement of the contact angle of nanoparticles at the fluid interface, and the account of the possible effects of line tension on the measurement, is still a significant challenge (Isa et al. 2011, Kaz et al. 2012). As a result, the magnitude of the adsorption energy, which has potentially important consequences for the equilibrium structure of interfacial assemble and the kinetics of their formation, cannot be accurately predicted. Colloidal particle adsorption at the fluid interface is thermodynamically favoured, but the process can be kinetically limited, a situation arising when a significant energy barrier to adsorption exists. Hydrophobic particles show more stability on the fluid-gas interface and the detachment energy is larger comparing to neutral particles, see Eq. (2.7). The calculation of desorption energy ΔE for the rigid particle is defined (Levine et al. 1989) as Eq. (2.7):

$$\Delta E = -\pi r^2 \gamma_0 (1 - |\cos\theta|)^2 \tag{2.7}$$

With r being the radius of the particles, γ_0 is the pure solution interfacial tension and θ being the three-phase contact angle of the particles at the interface.

Wettability of particle not only influences the adsorption of the particle itself but affects the adsorption possibility of other particles. In the mixed diffusion-kinetic adsorption mechanism(Eastoe and Dalton 2000), particles are not only controlled by the diffusion but need to overcome any potential energy barrier and be in the correct orientation for adsorption, then, there should be an 'empty site' in the interface that allows particle strike. The wettability of particles can significantly influence the surface energy barrier and the occupied surface area on the interface.

The stability of particle-laden foams is important in industrial processes like froth flotation. Stability is determined by many factors, similar to adsorption because the discussion of stable interfaces must happen after successful adsorption. In Bournival and co-workers' article (Bournival et al. 2015), the effects of particles on bubble surfaces are summarised. They used the example of froth floatation to illustrate the problem. There are many factors like particle hydrophobicity, size, shape, and concentration. From the hydrophobicity results, only the foam film was investigated, and it is shown that the bridging of interfaces by particles, without de-wetting, can significantly improve bubble stability. When it comes to particle sizes, the agglomeration of the particles creates coagula of different size as well as shapes, and it also influences the expansion and equilibrium position of the three-phase line of contact. In the study of Aveyard et al (Aveyard et al. 1994) who also investigated the stability of aqueous foams, the structure of three-phase interaction changed with contact angle on the interface of foams was summarised, as shown in Fig.2-20. Usually, increasing the concentration of particles leads to increases in stability. It is found that foams can be stabilized for long periods by adsorption of solid particles on the gas-liquid interface.

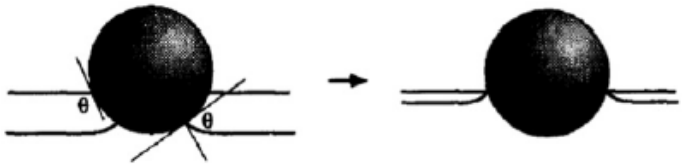

Figure 2-20 Destabilization of a thin liquid film by the de-wetting of a hydrophobic particle (Θ >90º) (Aveyard et al. 1994).

It is obvious that soft and hard colloidal particles have different characters when adsorption occurs. In the research of Style and co-workers' (Style et al. 2015), soft particles were determined to be better emulsifiers than hard particles, because they may stretch and deform at fluid interfaces. Soft particles have much higher adsorption energies than hard particles. The explanation is that the deformation of soft particles can increase adsorption energies and it is governed by competition of bulk elasticity and surface tension. From the result, it is clear that when surface tensions favour the complete spreading of the particles at the interface, plastic deformation can lead to unusual fried-egg morphologies, as presented in Fig.2-21. Another interesting result they obtained is that when deformable particles have surface properties that are very similar to one liquid phase, adsorption can be extremely sensitive to small changes in their affinity for the other liquid phase.

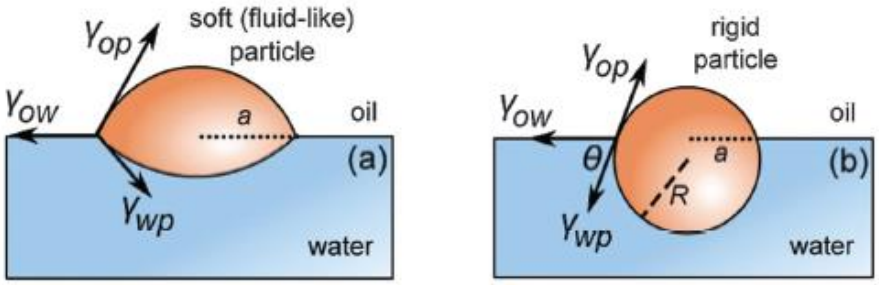

Figure 2-21 Schematic of the interface of a soft particle (left) and rigid particle (right)(Style et al. 2015).

After particles successfully touched the liquid interface, the stability of adsorption becomes important. The attachment and detachment energy have been studied by Anjali et al (Anjali and Basavaraj 2016). Here, the effect of size, shape and surface chemistry of particles are all

taken into consideration, and they used the gel trapping technique (GTT) to measure them. They systematically investigated the wettability of non-spherical particles (cube, peanut and spherocylindrical) adsorbed at the interface formed by two immiscible fluids and calculated the detachment energies. Results are shown in Table.2-1. It is suggested that the three-phase contact angles vary with the particle surface properties and interfacial tensions.

Table 2-1 Three phase contact angles of peanut shaped and spherocylindrical and cuboidal particle at air-water and decane-water interfaces (Anjali and Basavaraj 2016).

Particle type and shape	Aspect ratio	Contact angle, θ (°)	
		Air-water	Decane-water
Hematite – Peanut	2.3	43 ± 3	50 ± 4
Hematite – Peanut	2.2	45 ± 3	50 ± 3
Hematite – Spherocylinder	1.6	42 ± 2	48 ± 3
Hematite – Spherocylinder	2.6	44 ± 2	51 ± 3
Hematite-Silica - Core-shell spherocylinder	2.3	55 ± 4	–
Silica shells - Spherocylinder	2.3	57 ± 4	–

Recently, Xu and Liu (Xu et al. 2022) investigated the silica nanoparticles at the oil-water interface with different contact angles and found that wettability is important for particle adsorption at the interface. For colloid adsorption, a very common and robust interface is the gas-liquid interface, for example, droplets and bubbles. Usually, the adsorption at the liquid-gas interface is regarded as an irreversible process because it needs very large energy to get desorbed (Kumar et al. 2013) which is shown in Fig.2-22 and the energy varies with particle contact angles (Kumar et al. 2013, Davies et al. 2014).

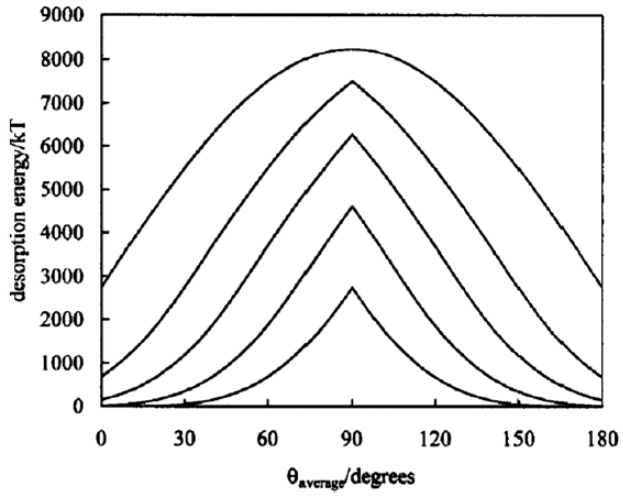

Figure 2-22 Variation of desorption energy with area weighted contact angle for particles ($\alpha = 90^o$ and γ_{OW} = 0.036N m^{-1})(Kumar et al. 2013).

The detachment energy of adsorbed particles varies with particle contact angle and directly influences the stability of adsorption. The contact angle of particles is a significant influence factor for the adsorption at the liquid interface and directly influences the adsorption process, thus, in this thesis, the author investigated the contact angle influence on the whole particle adsorption process.

2.4.2 Kinetics of Particle Adsorption

In some natural processes of adsorption such as the flotation process, sedimentation is the first step for the occurrence of adsorption. Particles drive by gravity or buoyancy then move to the interface and when they are close enough finally adsorption occurs. Researchers have studied them for many years and want to figure out their theory and mechanism especially when they adsorb at interfaces (Paunov et al. 2002). Liquid-Liquid interface such as the oil-water interface studies has been studied with many methods such as colloidal probe technique (Preuss and Butt 1998), gel-trapping technique (GTT) (Dong et al. 2017), film calliper method (Horozov et al. 2008) and cryogenic scanning electron microscopy (Cryo-SEM) (Isa et al. 2014).

For particle adsorption at the liquid interface, the simplest case is the adsorption of the single spherical particle at fluid-fluid interfaces. Ballard et al (Ballard et al. 2018) studied not only

the single spherical particle but also non-spherical particle adsorption at the liquid interface which is shown in Fig.2-23. They explored the effects that a variation of the morphology and surface chemistry of a particle can have on its stability to adhere to a liquid interface, from a thermodynamic as well as a kinetic perspective.

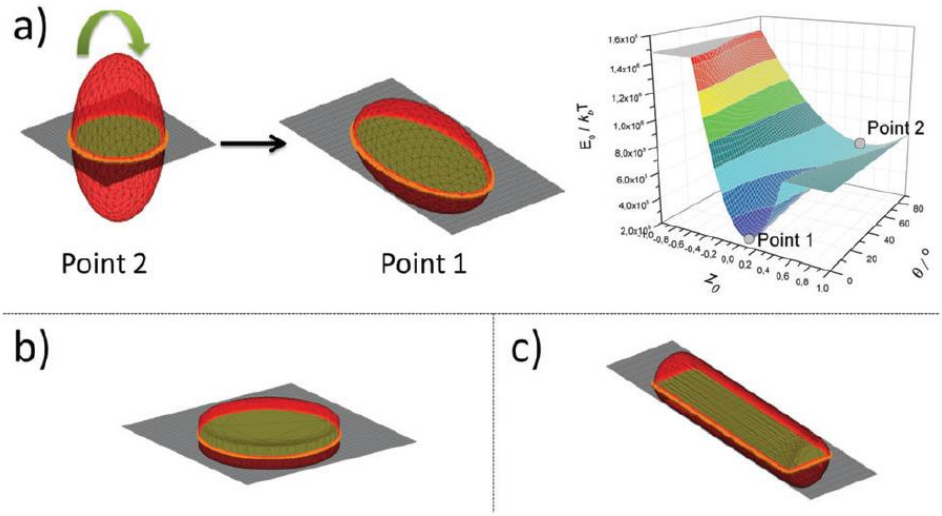

Figure 2-23 Schematic showing the adsorption of aspherical particles at fluid interfaces (Ballard et al. 2018). (a) Nonspherical particles have multiple orientations for similar distances from the interface resulting in a 3D adsorption free energy landscape giving the adsorption energy E_0 as a function of both particle height (z_0) and orientation angle(θ). (b and c) Cylindrical particles can lie in an end-on on upright configuration depending on the aspect ratio.

The particle-bubble collision is important in the adsorption process before the stable state of particle adsorption, to investigate it, Dai et al (Dai et al. 2000) provided a review of various models between particles and bubbles. Derjaguin and Dukhin (Derjaguin and Dukhin 1993) published a theory that clarified the bubble-particle interaction process by a three-zone model, as shown in Fig.2-24. which is also included in the article of Dai and co-workers. In Dai and co-workers' article (Dai et al. 2000), different models were also mentioned such as the Langmuir-Blodgett model, the Sutherland model, the Gaudin model and the Flint-Howarth model et al. They generated from different assumptions and hydrodynamic conditions, and most of them were tested by experimental data. They also divided three zones around a bubble with rising velocity, which is dominated by different forces. Zone 1 is a region far away from the bubble interface and dominated by hydrodynamic forces. While in Zone 2, the

liquid flow around the rising bubble surface creates a tangential stream, and diffusional and electrophoretic forces control the motion of particles. In Zone 3, surface force becomes the main force. while qualitatively, we might know interaction occurs in three zones, the actual interaction within Zone 3 is very difficult to measure, especially with nanoparticles. Hence, there is still significant uncertainty on the statistical likelihood of adsorption occurring in particles. Also, the complicating factor of hydrodynamic effects in a dynamic foam column adds further complexities. Therefore, it will be proposed in this work to consider adsorption on static droplets, where we can simplify interaction to the interfacial Zone 3.

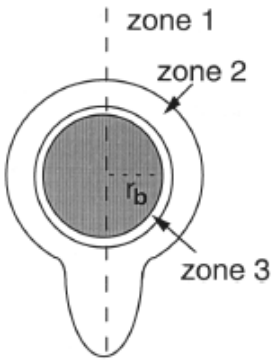

Figure 2-24 Three zones around a bubble (Derjaguin and Dukhin 1993).

Kaz et al (Kaz et al. 2012)studied the adsorption and the dynamic of binding, interestingly, they show that the adsorption of polystyrene microspheres to a water-oil interface is characterized by a sudden breach and an unexpectedly slow relaxation. The experiment results are shown in Fig. 2-25. In their continue research, particles do not reach equilibrium even after long time, and the relaxation appears logarithmic in time, suggesting that complete equilibration may take months. They show the contact-line pinning is a good pointcut to study the particle adsorption. After their study, Wang et al (Wang et al. 2017) also studied the effect of contact-line pinning on the adsorption of nonspherical colloids and they conclude that the dynamics of colloidal particles adsorbing to a liquid interface are not determined by minimization of interfacial energy and viscous dissipation alone.

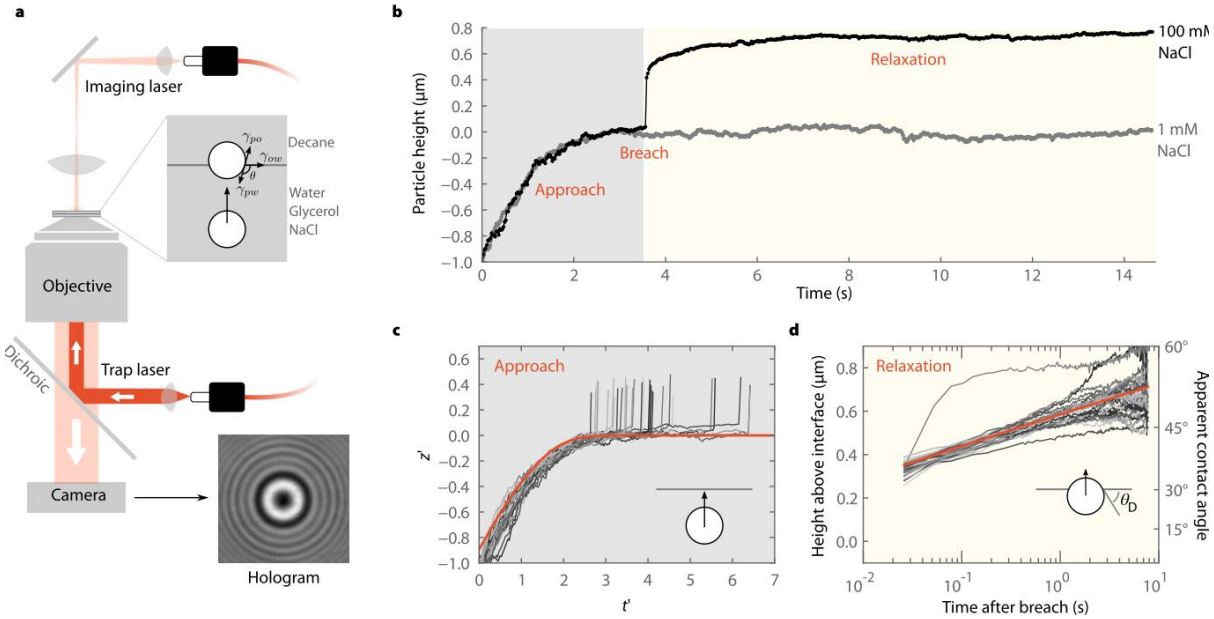

Figure 2-25 Holographic microscopy reveals dynamics of particle approaching and breaching an interface (Kaz et al. 2012). (a) Laser light gently pushes a colloidal sphere upward to a water-oil interface, while a second laser illuminates the sphere from above. (b) Typical trajectories for 1.9-μm- diameter polystyrene sphere at low and high salt concentrations. (c) The approach to the interface is governed by a balance of drag and radiation pressure. (d) A semi-log plot of position versus time after breach shows that the relaxation is approximately logarithmic.

Morgan et al (Morgan et al. 2021) successfully used a Langevin model to investigate the adsorption dynamics of ellipsoidal colloids at a liquid interface, which was coupled with a finite element model. The Langevin equation (Langevin 1908) is a stochastic differential equation describing how a system evolves when subjected to a combination of deterministic and random forces. The adsorption trajectory is found by solving the Langevin equation for the particle at the liquid interface. The model can reproduce the monotonic variation of particle orientation with time which is observed experimentally and can quantitatively model the absorption dynamics for some experimental ellipsoidal systems. They proved that the Langevin model can capture the adsorption trajectory. However, their model is mainly focused on particle movement for one adsorption and is not perfect on the detail of dynamics at the gas-liquid interface. Adsorption trajectories of the particle are shown in Fig.2-26.

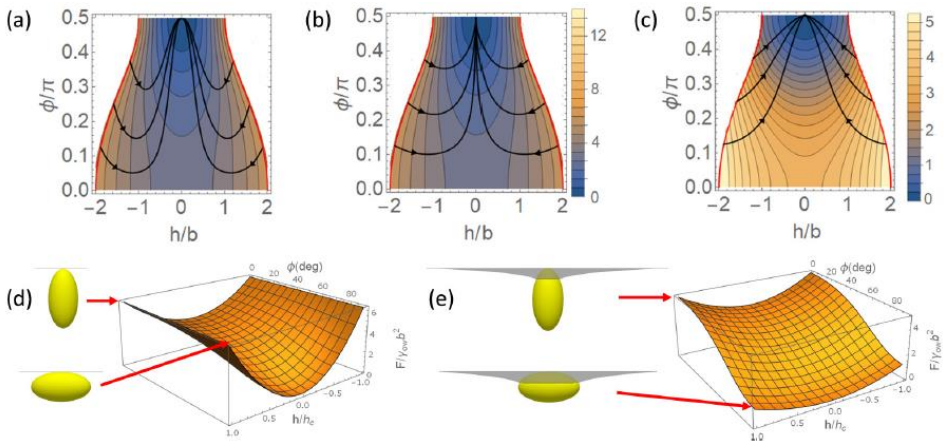

Figure 2-26 (a-c) adsorption trajectories in the plane (black line) for ellipsoids with contact angle 90º, (d) (e) free energy landscape represented as a three-dimensional plot of free energy vs h/h_c and ϕ and system configuration at $h=-h_c$ for ellipsoids in the vertical or horizontal orientation for (d) flat interface case and (e) deformed interfaces case (Morgan et al. 2021).

The steps of bubble-particle attachment have been described by Xing et al (Xing et al. 2017) which is schematically shown in Fig.2-27. In their description, there are mainly three steps of attachment, first is the drainage of wetting film to a critical thickness, and then, the film rupture and the contact line formed. Finally, the contact line expanded to be stable. However, they also pointed out that macroscopic experiments are not able to provide information on forces and evolution of film drainage. Particles may collect at the bottom of the bubble if they are not detached.

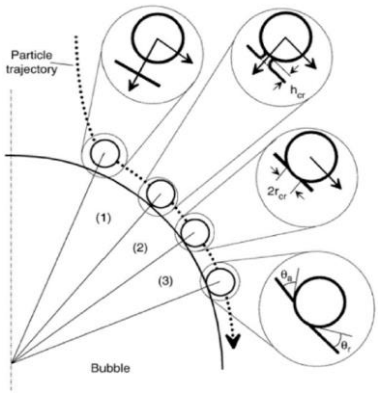

Figure 2-27 Steps of bubble-particle attachment (Xing et al. 2017).

2.4.3 Structure and Flow of Colloidal Monolayers

Lee et al (Lee et al. 2006) compared stability differences upon particle modification with chemical and physical treatment. The monolayer behaviour of silica particles and the packed

structure of particulate films were determined by the chain length of modifying agents. Silica particles treated with octanol, dodecanol and butanol and cationic surfactants of various chain lengths were used. The schematic illustration of the situation of silica particles floating at the air-water interface is shown in Fig.2-28. For a particle chemically grafted by hydrocarbon chains, the alkyl groups distribute uniformly on the surface and the particle has a different characteristic from that of an amphiphilic molecule. such particles stay at the air/water interface, the particle–water interaction is weak, and the particles tend to aggregate due to the higher particle–particle interaction.

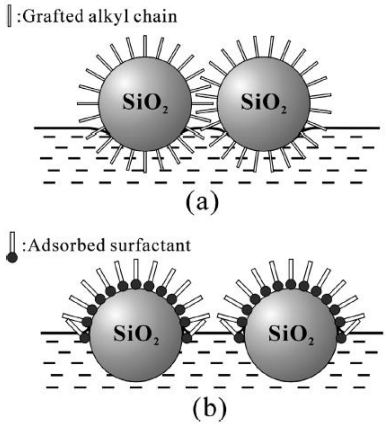

Figure 2-28 schematic illustration of the situation of silica particles floating at the air/ water interface. The surface of silica particles is chemically grafted by alkyl chain (a), or modified by adsorption of surfactant (Lee et al. 2006).

Form the study of Bournival and co-workers (Bournival et al. 2015), it is reported that the section of the particles in the air phase gives rise to an augmented van der Waals attractive potential energy due to the much lower relative dielectric constant of air compared to water. A dipole is formed from the DLVO theory is also used to calculate the interaction potential energy of adsorption, which is shown in Fig.2-29.

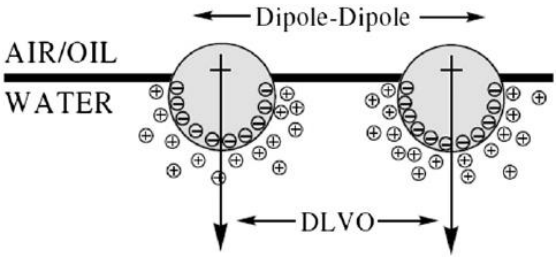

Figure 2-29 Dipole-dipole formation and interaction (non-polar phase) and DLVO forces (polar phase) of particles adsorbed at an interface (Bournival et al. 2015).

Langmuir-Blodgett trough is a good tool to study the networking of particles at the liquid-gas interfaces, the interfacial structures were inferred by measuring the surface-pressure behaviour of monolayer arrays. This technique is one of the methods to manipulate materials in the molecular level (Hussain 2009) and is commonly used in nanotechnology (Timothy et al. 2009, Othman and Radiman 2016) and molecular electronics (Hussain and Bhattacharjee 2009). Rey et al (Rey et al. 2018) demonstrated the complex assembly of particle phases with spherical colloidal particles adsorbed at the air/water interface, that was altered with molecular amphiphiles. They also investigated the interfacial behaviour of colloidal particles in the presence of different amphiphiles on a Langmuir trough. The results of colloidal in different phases and Langmuir trough surface pressure are shown in Fig.2-30. They directly measured the monolayer structure change with the surface pressure.

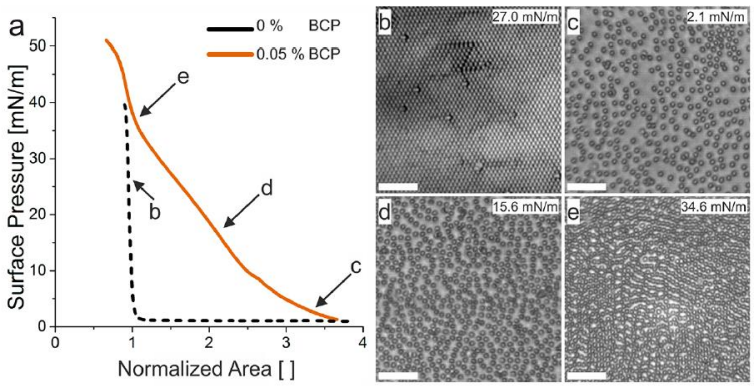

Figure 2-30 Phase diagram (Rey et al. 2018)of a mixture of colloids (d = 600 nm) with BSA: (a) normalized compression isotherms for different concentrations of BSA. (b-e) Representative images of the different phases observe(b) hexagonal close-packed phase, (c) square phase, (d) chain phase, and (e) single colloids.

Bizmark et al (Bizmark et al. 2014) used dynamic surface tension measurements to track the adsorption of ethyl cellulose nanoparticles at the gas-fluid interface. They used a modified

short-time adsorption model with *Early-Time* dynamic surface tension data and a separate *Long-Time* model to understand data towards equilibrium, to calculate the adsorption energy barrier and adsorption rate of nanoparticles. The surface tension is not simply linear relationship with time but versus $t^{0.5}$ and $t^{-0.5}$ which shows the early and late progress of adsorption are different. The result of early time data and the linear fitting results are shown in Fig.2-31.

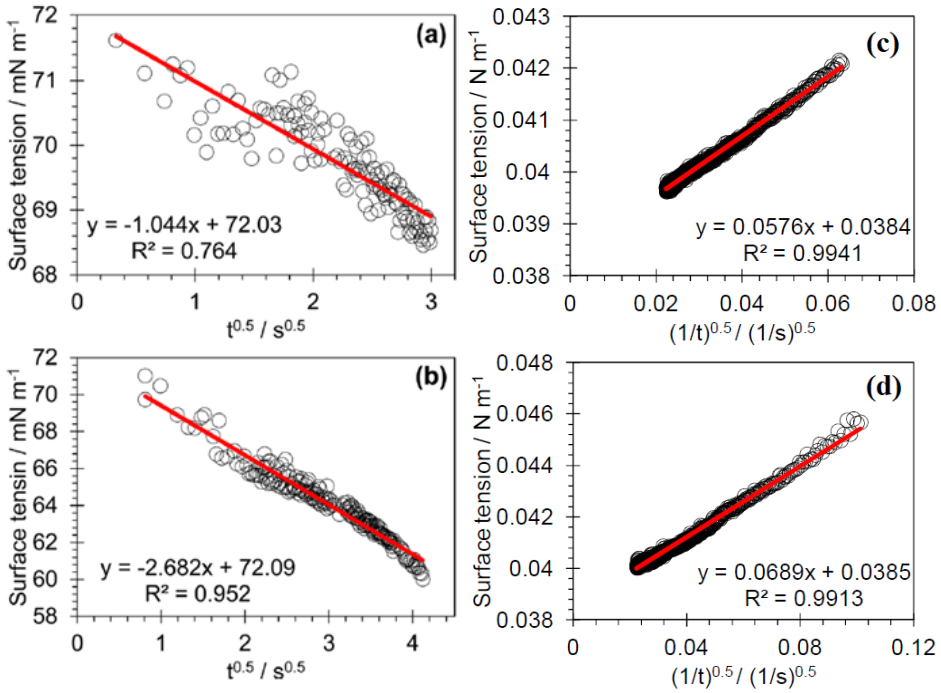

Figure 2-31 A exemplary plot of early time DST data of (a) 89.1 nm (b) 42 nm EC nanoparticles at a bulk concentration of 0.8g L^{-1} against $\sqrt{t}$. Exemplary plot of late-time DST data of (c) 89.1 nm (d) 42 nm EC nanoparticles at a bulk concentration of 0.8g L^{-1}. (Bizmark et al. 2014).

They also calculated the interaction energy in DLVO and indicate that with strong electrostatic repulsion the hydrophobic interactions are not strong enough to overcome electrostatic repulsion. Similar research was undertaken by Dugyala et al (Dugyala et al. 2016) who also used dynamic surface tension measurements to record the surface tension to study the adsorption kinetics of nanoparticles (nano-silica). They also used early time surface tension data and a modified short-time model to calculate the energy barrier as shown in Fig.2-32.

Despite a few examples of research into the use of surface tension measurement to measure the adsorption rate, there is still significant questions as to how particle hydrophobicity affects the adsorption rate, and whether dynamic surface tension measurements can still be used to model adsorption dynamics for larger nanoparticles that are fully irreversibly adsorbed (and hence, do not act like surfactant). To investigate particle adsorption, Langmuir trough and dynamic surface tension measurements such as pendant droplet methods are used to research the particle networking and measure the adsorption rate. They show good performance and are easy to be applied. Therefore, they are chosen to investigate the adsorption process in this thesis. There are also good adsorption models such as the Langevin model that investigated the particle adsorption process, considering the particle movement and three-phase contact lines, but it is still a challenging problem to describe a good simulation model to realise the whole process.

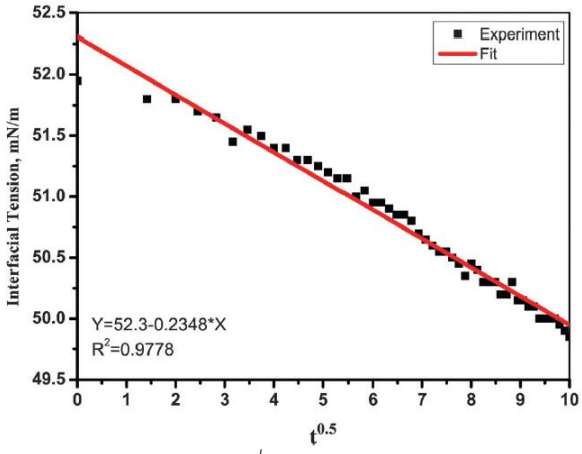

Figure 2-32 Plot of early time surface tension vs. √t data (from 0 to 100s) for suspension containing 1 wt % particles and 01 M NaCl concentration (Dugyala et al. 2016).

Yuan and co-workers (Yuan et al. 2018) reviewed the experimental and theoretical studies on spontaneous nanoparticle adsorption on the bubble interfaces. They found that when bubbles exist in the mixture, nanoparticles tend to spontaneously aggregate at the bubble interface, forming a layer of 'colloidal armour', as schematically shown in Fig.2-33. It makes the bubble interface partially rigid and less mobile, and it will also influence the drag forces. Particles have no room for adsorption. It will cause the flow separation and a slanted wake

region behind the nanoparticle-adsorbed bubble at a small Reynolds number. Interactions between nanoparticles, such as the electrostatic double layer force and steric repulsion force, can significantly resist the approach of two bubbles and hinder the rapture of the liquid film.

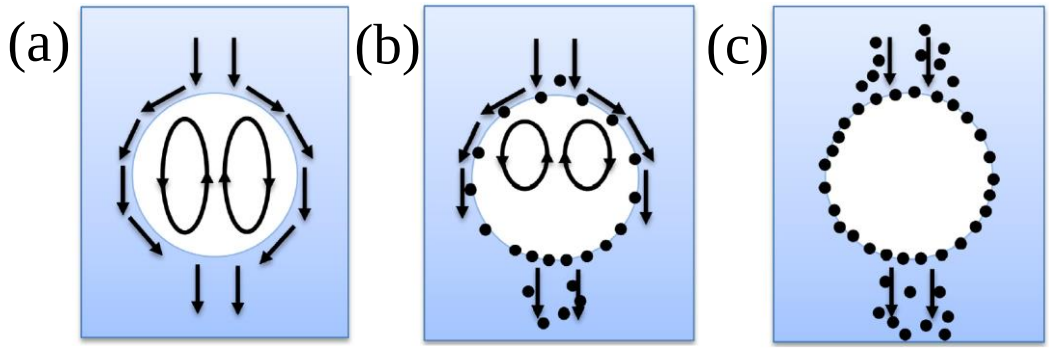

Figure 2-33 Particle adsorption with bubble rising and layer of 'colloidal armour'(Yuan et al. 2018).

Liascukiene et al (Liascukiene et al. 2018) characterised the adsorption of micron-scale particles onto the interface of a bubble flowing in a colloidal aqueous suspension within a microfluidic channel. In their research, particle sizes, concentration and the mean velocity of the colloidal suspension were investigated as parameters. They used PIV to observe the results, which are shown in Fig.2-34. The figure shows the bubble become more 'colloidal armour' like with the adsorption of particles and shows the difference with particle sizes. From the results, it is suggested that the bubble velocity is in fact slower than the mean flow in reality. Then they also found that the presence of adsorbed particles does not influence the speed of the bubble. Two complementary mechanisms to cover the bubble interface are identified.

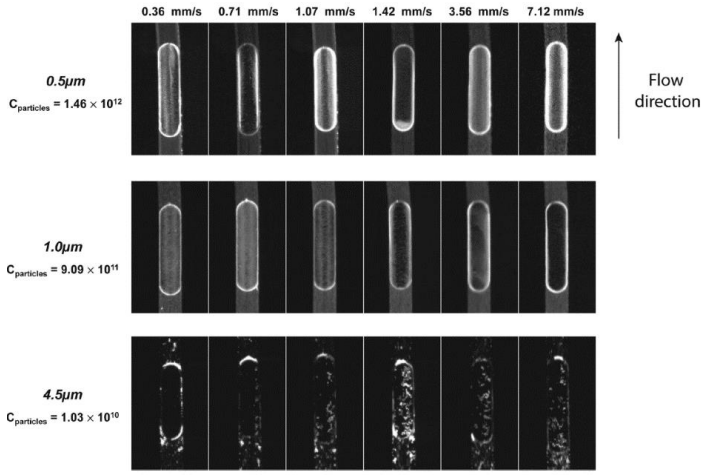

Figure 2-34 Bubble coverage in the channel (Liascukiene et al. 2018).

2.5 LBM and DEM Methodologies

Simulation methods can be useful tools to reveal and explain complex phenomena. As mentioned in the article of Bournival et al and the study of Yuan and co-workers (Bournival et al. 2015, Yuan et al. 2018), experimental data sometimes is hard to obtain especially at the scale of colloidal particles. Simulation of colloidal particle adsorption at gas-liquid interfaces is necessary for obtaining further information on the whole process, including detail one the motion of particles and fluids. In general, computational fluid dynamics (CFD) is used to simulate the evolution of fluid and particles, For example, the most popular method to solve fluid flow problems is the Naiver-stokes equation (Chorin 1968) based method, which is based on the continuity hypothesis. CFD is usually used when the internal flow data is hard to obtain, and the real structure is too complex to conduct the experiment. Numerical simulation can make it easier to investigate every detail of fluid and particles. However, for simulation methods, such as direct numerical simulation (DNS) (Moser et al. 1999), cases like complex structures and a large number of particles would be extremely computationally demanding. In the research of colloidal particles, the research scale is very small and the *Kn* number is relatively high, which means the continuity hypothesis is limited. The adsorption process of particles has not been fully recovered and a suitable method is still requiring investigation to

describe the adsorption process that is both accurate for the particle and fluid phases. Therefore, it is needed to use a proper multiphase simulation model to describe the adsorption behaviour with colloidal particles.

2.5.1 Fundamentals of LBM-DEM methods

Lattice Boltzmann method (LBM) is a mesoscopic numerical method which is suitable to solve problems on the scale of colloidal particles. Because of the length scale of colloids, conventional numerical simulation methods have limitations. This method is based on the discrete Boltzmann equation and can be used on a small scale without a continuity hypothesis. It was derived from the Lattice Gas Automata (LGA) (Frisch et al. 1986) and has been developed for many years (Gunstensen et al. 1991, Chen et al. 1992, Shan and Chen 1993, Ladd 1994, Martys and Chen 1996). LBM is widely used due to an important simplification model in the collision operator, which is named the Bhatnagar-Gross-Krook (BGK) model (Bhatnagar et al. 1954). It used a simple term on the right side of the equation to describe the collision of two nodes which greatly simplified the process of collision and make it easier to understand. The Lattice Boltzmann equation (LBE) is expressed as Eq. (2.8):

$$f_\alpha(\mathbf{x}+\mathbf{e}_\alpha c\triangle t, t+\triangle t) - f_i(\mathbf{x},t) = -\frac{1}{\tau}[f_\alpha(\mathbf{x},t) - f_\alpha^{eq}(\mathbf{x},t)] \tag{2.8}$$

Where f_α is the density distribution function of the fluid, f_α^{eq} is the equilibrium distribution function. $\mathbf{e}_\alpha c$ is the lattice speed in α direction, and the velocity c is decided by the lattice spacing Δx and time step Δt (both of them are usually equal 1 in the lattice system), the square of the lattice sound speed is $c_s^2 = 1/3$.Here, also, τ is the dimensionless relaxation time, which is related to viscosity in the BGK model. The left hand of LB equation represents the streaming step, and the right-hand side stands for the collision part. LBM uses distribution functions to represent the property of each node and the macroscopic properties can be calculated form them. The process of fluid flow is realised by the collision and streaming of

distribution functions. For the velocity model, D2Q9 square and D3Q19 cubic model are commonly adopted (Chen et al. 2014). The nodes of D2Q9 and the schematic of the distribution function are shown in Fig.2-35.

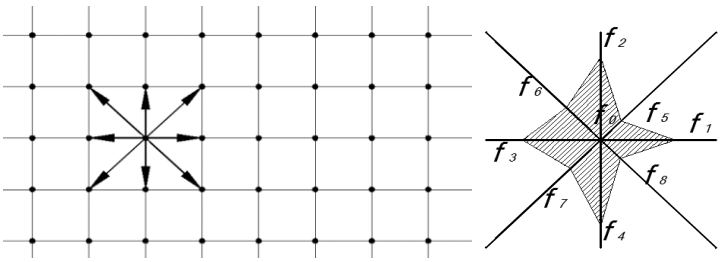

Figure 2-35 Lattice grids (left) and distribution function (right).

For D2Q9 model, the equilibrium distribution functions f_α^{eq} can be calculated as Eq. (2.9):

$$f_\alpha^{eq} = \omega_\alpha \rho[1+\frac{3}{c^2}(\mathbf{e}_\alpha \cdot \mathbf{u})+\frac{9}{2c^4}(\mathbf{e}_\alpha \cdot \mathbf{u})^2-\frac{3}{2c^2}\mathbf{u}^2] \tag{2.9}$$

Where ω_α is the weight factor and given by ω_0 = 4/9, $\omega_{1\text{-}4}$ = 1/9, and $\omega_{5\text{-}8}$ = 1/36. The fluid density ρ and velocity **u** can be obtained as Eq. (2.10 and 2.11):

$$\rho = \sum_\alpha f_\alpha \tag{2.10}$$

$$\rho\mathbf{u} = \sum_\alpha f_\alpha \mathbf{e}_\alpha \tag{2.11}$$

velocity is related to the relaxation time by Eq. (2.12):

$$\upsilon = c_s^2(\tau - 0.5)\triangle t \tag{2.12}$$

For the widely use of the BGK model, researchers found that there is also some limitation of this model. They also are looking for a more stable model that can replace the BGK model. Then another LB model came into focus again and drew a lot of attention (d'Humières 2002, Du et al. 2006, Premnath and Abraham 2007) because the BGK model is too simple and only has one parameter to adjust the whole equation. This parameter can adjust the dynamic

viscosity of fluid but other parameters such as bulk viscosity and the parameters for energy flux and momentum are also changed (d'Humières 2002). Thus, the stability of BGK is influenced by only one parameter, which is not suitable for simulation stability.

In Du and co-works (Du et al. 2006) research, it is found that the incompressible Multiple-relaxation-time (MRT) -LB model showed better numerical stability. The results are checked with cavity flow and double shear flow, and both results are better in the MRT scheme. Thus, in this thesis, MRT scheme LBM are used to improve the stability of model. The main idea of the MRT scheme is that the advection is mapped onto the momentum space by a linear transformation and the flux is still finished in the velocity space. The transfer matrix **M** that transforms the distribution function from velocity space to momentum space is different from velocity models. The evolution equation of MRT-LB model with extra forces can be expressed as Eq. (2.13):

$$f_\alpha(\mathrm{x}+\mathrm{c}_\alpha\,\delta t, t+\delta t) - f_\alpha(x,t) = -(\mathbf{M}^{-1}\Lambda\mathbf{M})_{\alpha\beta}[\,f_\beta - f_\beta^{eq}\,] + \delta t F_\beta \tag{2.13}$$

Where **M** is the transform matrix and **Λ** is a diagonal matrix that represents different relaxation times. The scrip α means velocity space and β means matrix space.

Single phase LBM is a good alternative for N-S equations on a mesoscopic scale and is also useful on the macroscopic level. With curved boundary conditions, it is easy to simulate curved real shape objects (Wang et al. 2014). Tao and Guo (Tao and Guo 2015) studied low-speed flow over a microscale airfoil and simulated at different angles to check the pressure field and fluid flow changes. They showed LBM is suitable in the transitional flow regime in which the effect of the Knudsen layer should be considered. Knudsen number (*Kn*) (Toschi and Succi 2005) can be used to represent the physical length scale and check the hydrodynamic scale of a problem which is shown in Eq.(2.14):

$$Kn = \frac{\lambda}{L} \tag{2.14}$$

Where λ is the mean free path of fluid and L is the representative physical length scale. In the case that Kn number larger than 0.1 the flow becomes transition flow, N-S equations are limited. Part of the results is shown in Fig.2-36.

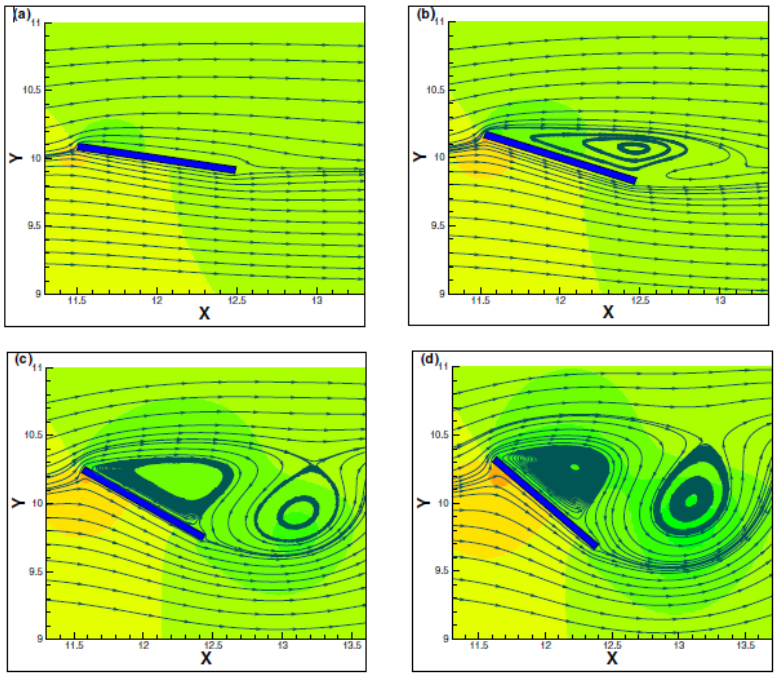

Figure 2-36 Pressure field, and instantaneous streamlines of the flow pass an inclined flat airfoil of 5% thickness ratio (Tao and Guo 2015). (a) Re = 135.7, θ = 10°; (b) Re = 135.7, θ = 20°; (c) Re = 135.7, θ = 30°; (d) Re = 135.7, θ = 40°.

LBM is also popular in solving porous media problems since the boundary condition is relatively simple and easy to apply. Cheng et al (Cheng et al. 2019) simulated non-Darcy flows associated with high Reynolds numbers in porous media. They found that at elevated velocities, the internal core effect in a large channel will lead the flow to be more homogenous and less tortuous, while in a porous model with complicated pore space, the steady eddy and reversal flow resulting from drag force will make the flow paths more torturous. LBM can accurately reveal the internal fluid flow in porous media which is shown in Fig.2-37.

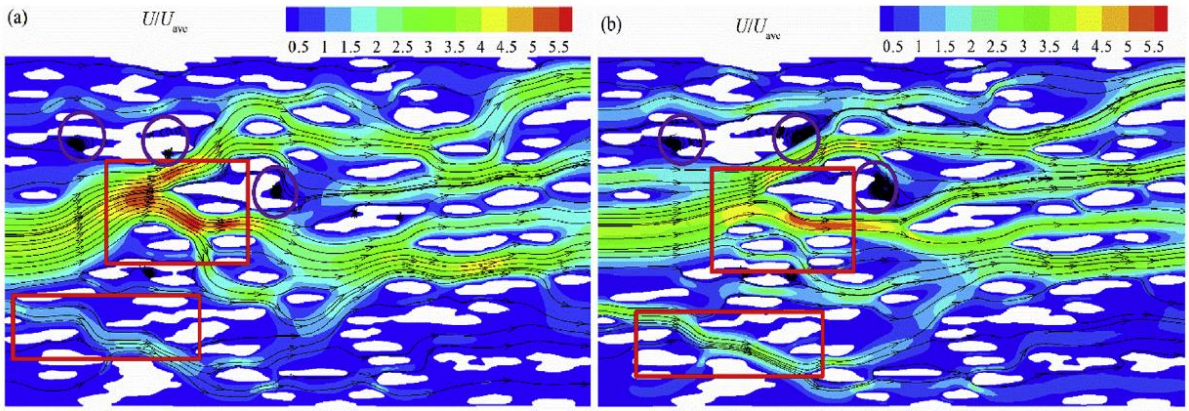

Figure 2-37 Plot of velocity distribution with R4 at specific points, with the legend being denoted by U/U_{ave}, where U_{ave} is the average velocity through the entire porous medium; (a) the Darcy regime ($Re = 5.7\times10^{-3}$) and (b) the non-Darcy regime ($Re = 6.68$) (Cheng et al. 2019).

The single-phase model is the most widely used model in LBM, but it cannot simulate problems that include interfaces like bubbles in the water. There are mainly four multiphase models (Chen et al. 2014). The first one is called Rothman-Keller (RK) model (Gunstensen et al. 1991) which uses colour gradients to separate and calculate the interaction at the multiphase, and it is also called the colour model. Then is the pseudopotential model proposed by Shan and Chen (Shan and Chen 1993), and it is also called S-C model. In this model, a pseudopotential is introduced to account for the nonlocal particle interactions. Another one is the free energy model proposed by Swift (Swift et al. 1995). In the free energy model, phase effects are directly introduced into the collision. The final one is proposed by He et al (He et al. 1998) and called the mean-field method (Shao et al. 2013) where a proper force term was derived for multiphase behaviour. Among the four methods, the pseudopotential model is more attractive due to its simplification and physical meaning. The non-ideal equation of state (EOS) (Yuan and Schaefer 2006) was used to achieve different fluid characters and a high-density ratio between the liquid and the gas phase. Then, Li et al (Li et al. 2012, Li and Luo 2013, Li et al. 2014) and Hu et al (Hu et al. 2013) further improved the multiphase model and finally suitable to simulate multiphase problems in real cases. The single droplet of the single component multiphase results is shown in Fig.2-38.

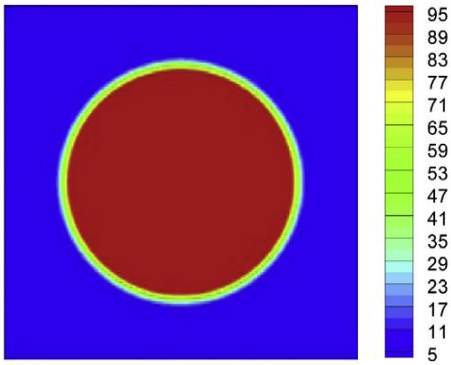

Figure 2-38 Single droplet density profile for pseudopotential single component multiphase model(Li and Luo 2014).

Kupershtokh's (Kupershtokh et al. 2009) force method was proposed to solve the unstable problem in large density ratio between liquid and gas phases. This improvement in the single component model improved the density ratio obviously to 10^9 and also can avoid higher pseudo current which can make the model more stable. In the same year, Li et al (Li and Luo 2013) proposed a new scheme to adjust surface tensor in the multiphase model. They added a source item into the evolution equation which is related to the pressure tensor. In this model, the surface tensor can be adjusted without changing the density ratio, and it also adjusts the force term in the MRT scheme and make a better thermodynamic consistency. This method is also simpler to adjust the stability. Single bubble or bubble rising can be easily achieved as Fig. 2-39. For problems that are fluid laden with particles, there are also some methods that can be used that are based on LBM or combined with DEM. Chen (Chen et al. 2014) et al summarised the improvement of LBM in the multiphase model and compared the drawbacks of each model.

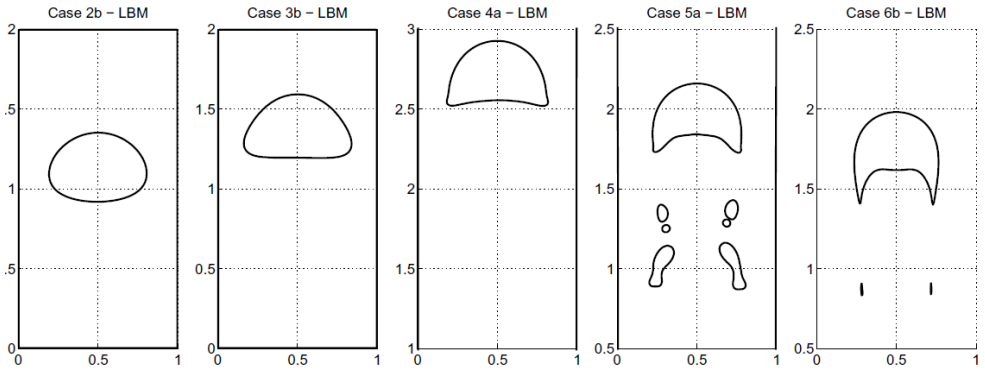

Figure 2-39 Interfacial profile of rising bubbles simulated with LBM in different time steps(Kupershtokh et al. 2009).

In the development of the pseudopotential model, there are many important developments that give this model capability to simulate multiphase flow in high-density ratio. Bao and Schaefer (Bao and Schaefer 2013) improved the pseudopotential model in the multi-component fluid, and the multi-component model in his research can simulate multi-component problems in the high-density ratio (10^2). The multi-component result is shown in Fig.2-40.

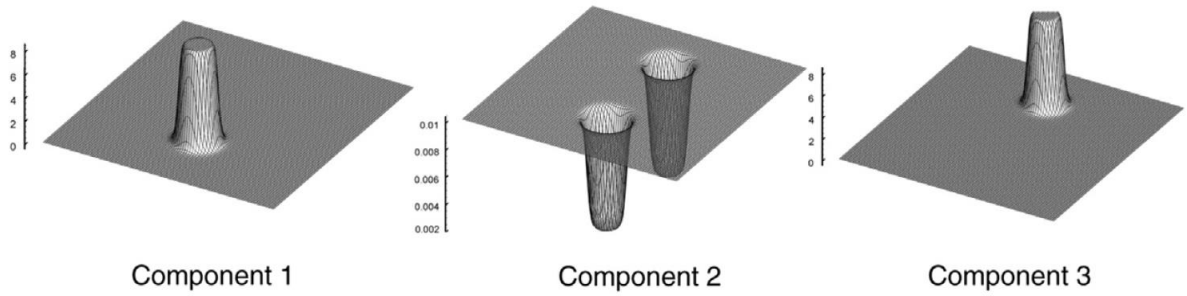

Figure 2-40 Density distribution of each component for a three-component system(Bao and Schaefer 2013).

The dynamic behaviour of multiphase flow in a gas-liquid-solid mixture system plays an important role in various applications of petroleum industries, chemical industry, food industry and water treatment. Colloidal particle adsorption is important in industries such as printing and cosmetic, but the adsorption behaviour is complex and hard to observe due to its small size. Simulation is a way to study the behaviour, but researchers still usually use

empirical theories to do the study and ignored the detail of the interface and the particle movement. The three-contact line problem is the most important part of the study.

However, it is still challenging to simulate gas-liquid-solid three-phase flow with the LBM and one of the challenges is to deal with the three-phase contact line on solid particles and the large density ratio of multiphase.

There is also an alternative model that uses LBM-PSM to simulate the gas-liquid-solid problem which treated the solid particles as a special fluid particle with a very large viscosity (B et al. 2013).In the coupled LBM-DEM schemes, the interactions between fluid and solid particles are treated by the immersed boundary method (Suzuki and Inamuro 2011) or the momentum exchange method (Ladd et al. 1994), which can enforce a no-slip boundary condition between fluids and solids according to the conservation law of momentum. The momentum exchange method has also been developed to better fit the moving particles with a Galilean invariant momentum exchange scheme (Wen et al. 2014). Chen (Chen et al. 2013) developed immersed boundary conditions and proposed a sharp-interface immersed boundary method to reduce the spurious-pressure oscillations for moving particles with fresh nodes. However, most of the above studies on LBM-DEM coupled methods are limited to single-phase flow. Coupling the multiphase LBM and DEM requires an algorithm of LBM-DEM to simulate the co-evolution between the fluid-fluid interface and the fluid-solid interface because the two types of interfaces must not penetrate each other (Fei et al. 2022). Ding and Xu (Ding and Xu 2018)proposed a multiphase fluid-solid coupling algorithm of LBM-DEM to simulate the debris flow with a free-surface model. However, such a model neglected the flow information of the gas phase. Yka et al (Yka et al.) developed a numerical method to simulate 3D three-phase flow to investigate leaked gas behaviour in unconsolidated sandy seabed sediments. However, mass conservation was not ensured.

As a pioneering work, Ladd (Ladd 2006) applied LBM where liquid particles bounce back at half-way along the link which connects fluid nodes with solid boundary nodes mimicking. This method creates a numerical oscillation of the fluid-solid interface force. Then, Habte and Wu (Habte and Wu 2017) presented a numerical simulation based on a combined LBM, Immersed Boundary Method (IBM) and Hard Sphere Molecular Dynamic (HSMD) scheme. In their method, sedimentation that involves 7200 particles can be simulated which is shown in Fig.2-41. LBM can also combine with other numerical methods like DEM (Peng et al. 2010), usually in the combined model, LBM is used to describe fluid and other methods are used to simulate particles and particle forces.

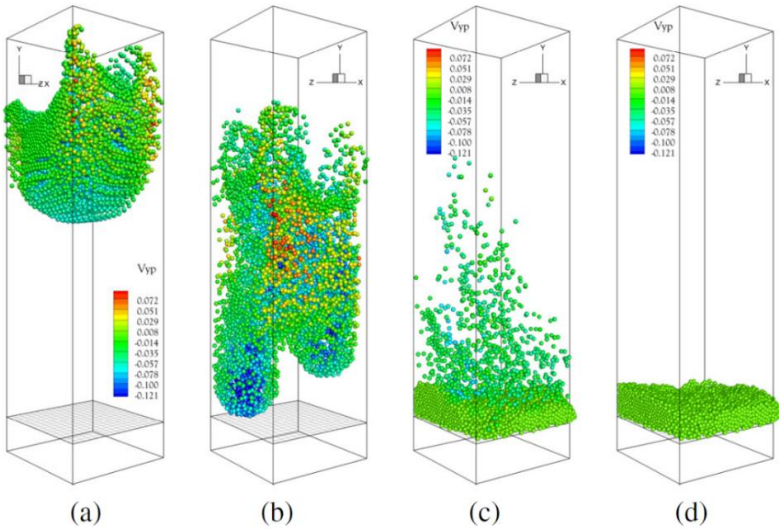

Figure 2-41 Visualization of 7200 identical hard spheres settling in a viscous fluid within a cuboid in different time steps(Habte and Wu 2017).

LBM can also be used in the scale that includes Brownian motion (Nie and Lin 2009, Mynam et al. 2011, Satoh 2012, Wang et al. 2012). If the radius of particles that are suspended in the fluid is small enough, they will cause Brownian motion (molecular motion, that causes random diffusive motion). Colloidal particles will also undergo particle diffusion like Brownian motion in the fluid and move randomly. In the simulation of nanoscale, Brownian motion is an important factor that influences the motion of particles.

There are many methods to include Brownian motion in simulation. The most popular method is the Monte Carlo method (MC). It is powerful but computational time consuming because it needs to track each particle. It does not have a real-time scale and can only conduct short-time simulations. Although some of those problems have been solved by some researchers. In Hac and co-workers' (Hac et al. 2005) research, the Monte Carlo method showed the capability to simulate the particles in mixed fluids and diffusion in real timescale. But in this article, no specific methods were mentioned, just the result and capability which agree with the experiments. In Ruiz and co-workers' article (Ruiz Barlett et al. 2009), two different MC methods were compared. It showed the kinetic Monte Carlo method is better than the fixed time step Monte Carlo method and showed the errors and explanations of MC.

2.5.2 Applications to Nanoparticle Dynamics and Interfacial Systems

A model named the LB-CA model was proposed in Wang and co-workers' article (Wang et al. 2012). It is a method that uses LBM for two-phase flows, where the gas is described by LBM, but the solid particle is described by the cellular automation (CA) probabilistic approach. And it can combine drag forces, Brownian diffusion (like MC), and ex-forces. The LBM used is still the standard BGK-LBM but combined with a cell automation probabilistic model for particle transport. This transport in a fluid depends on the combined effect of the fluid-particle interaction, gravity and buoyancy, Brownian diffusion, and electrostatic force. The trajectories of particles are shown in Fig.2-42.

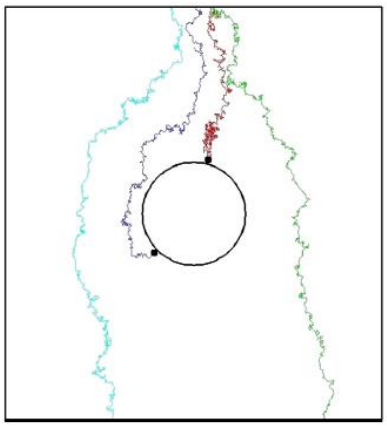

Figure 2-42 Typical particle trajectories in Brownian-diffusion-dominated cases(Wang et al. 2012).

Maxwell et al (Maxwell et al. 2012) used a 3D DEM simulation to analyse the kinetics of the collision of multiple particles against a stationary bubble and the sliding of the particle over the bubble interface. The particle packing arrangements of multiple particles on the surface of the bubble have been successfully simulated with micron-size particles and studied the hydrophobicity influences. The simulation results are shown in Fig.2-43. However, in their study, the particle size is beyond the size of colloids and the bubble is assumed that not be influenced by the particles.

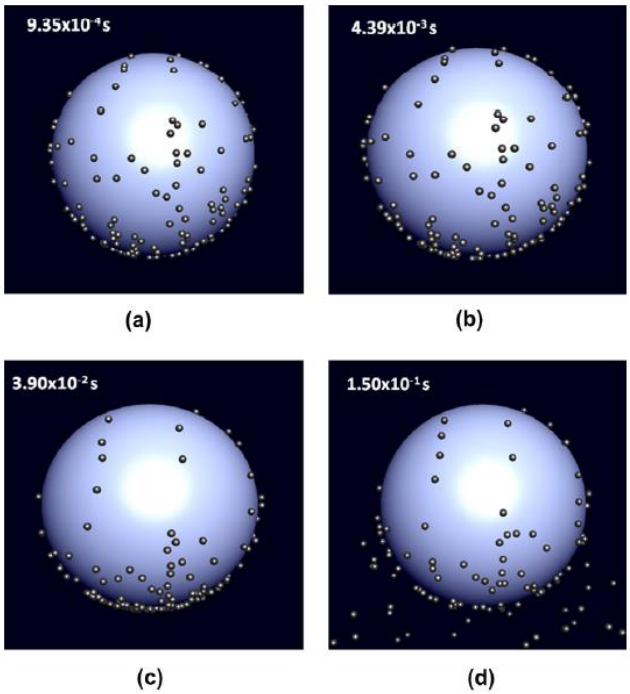

Figure 2-43 Side View of the monodisperse system for the value of hydrophobic constant of (a) $K_1 = 10^{-9}$ N m; (b) $K_1 = 10^{-10}$ N m; (c) $K_1 = 10^{-11}$ N m; (d) $K_1 = 10^{-12}$ N m (Maxwell et al. 2012).

In the research of Peng et al (Peng et al. 2010), they applied the DEM computational technique to simulate the aggregation behaviour of Nano-sized particles, with the aim of obtaining an insight into nanoparticles aggregation driven by random Brownian diffusion and externally induced electrophoresis motion. Results are shown in Fig.2-44. This method can be used to simulate nano-size particles and also the Brownian motion with the change of different key factors such as volume fraction, pH and frequency.

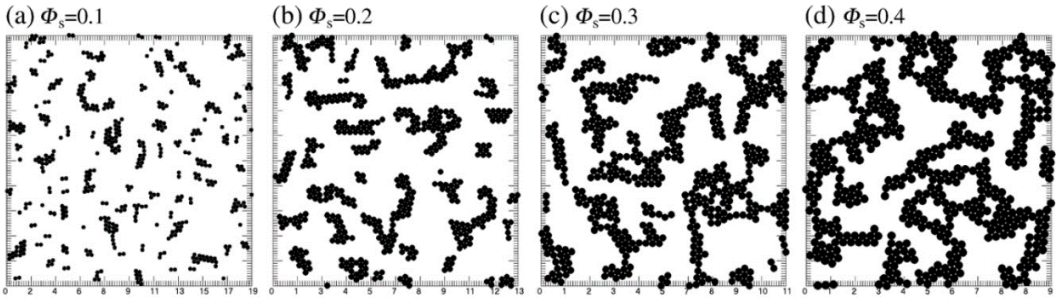

Figure 2-44 Aggregate structure in different volume fractions in pH=9 (Peng et al. 2010).

A two-dimensional mass conserving lattice Boltzmann method (LBM) was developed for multiphase flows with solid particles suspended within the liquid and vapour phase by Joshi and Sun (Joshi and Sun 2009). The capillary interactions between two suspended particles on a liquid-vapour interface were achieved. The relationship and force exchange between two phases and particle forces are the first link in this study. Particles are spontaneously accumulated around the liquid-vapour interface and inhibit coarsening of the interface, which is shown in Fig.2-45. However, the large pseudo-current problem around the interface was also reported.

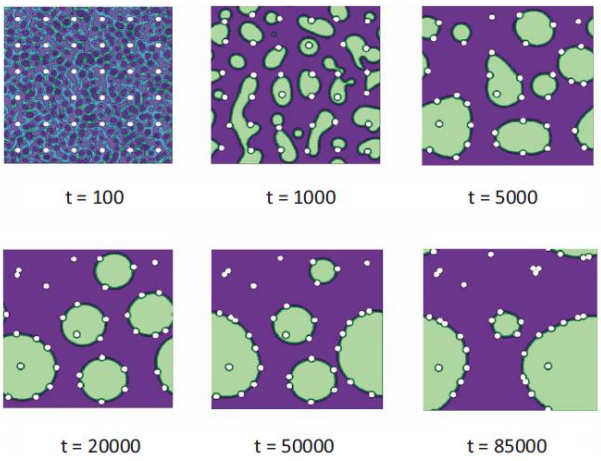

Figure 2-45 LBM simulation of spinodal decomposition in the presence of suspended particles (Joshi and Sun 2009).

Liang et al (Liang et al. 2013) introduced a pseudo-solid model (PSM) in the framework of the lattice Boltzmann method for multi-component fluids. Self-assembly of colloidal particles partially immersed in a fluid layer on the substrate was carried out. A typical phenomenon in the fluid layer due to the lateral capillary force, namely the attraction of two colloidal particles with the same affinity is numerically demonstrated, while the influence of particle distance and surface tension was investigated. Fig.2-46. shows a schematic representation of the phenomenon that a neutrally wetting colloidal particle with surrounding fluid can suspend at the fluid-fluid interface due to the fluid interface tension.

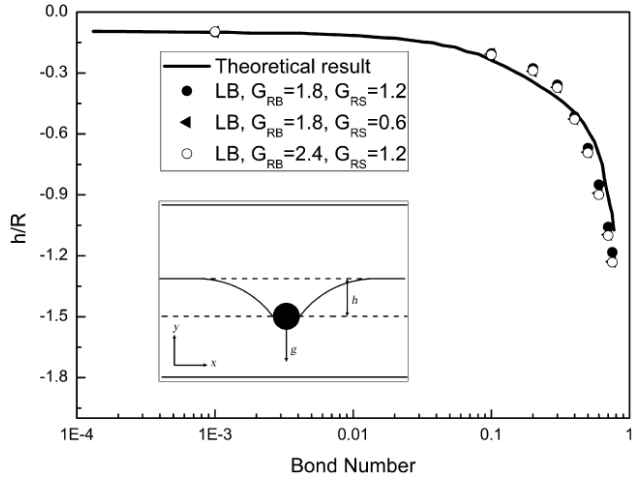

Figure 2-46 The normalized equilibrium displacement of h/R of a single particle below an initially flat interface as a function of Bond number (Liang et al. 2013).

In this thesis, we chose a combination of Shan and Chen single-component multiphase (SCMP) model with DEM to describe the particle suspension and adsorption to the liquid-gas

interface. The pseudopotential model has been developed for years to improve the ability to simulate multiphase flow (Li et al. 2012, Hu et al. 2013, Chen et al. 2014). There are only several studies that coupled LBM and DEM or with other solid movement, equations to solve the moving object with the multiphase model. Joshi and Sun (Joshi and Sun 2009) coupled LBM single component multiphase model and Newton's law to investigate the particles moving and adsorption on the interface of a droplet and successfully realised particles suspended at the liquid-vapour interface. However, they also pointed out that the pseudo current caused by the multiphase cannot be ignored. Liang et al (B et al. 2013) proposed a novel modelling approach for colloidal particles called the pseudo-solid model (PSM) and coupled with LBM for multi-component fluids. It can describe the movement at the liquid-vapour interface and a lateral capillary force was introduced to realise the capillary force. Chen et al (Chen et al. 2015) tried a multicomponent multiphase model to simulate the particle motion at the liquid-vapour interface. They solved some problems that cause unphysical movement and density profiles and proposed a principle that a force coupling shows follows when calculating the exchange force between the fluid and the solid object. However, the multicomponent multiphase model is computationally time consuming and not very suitable to simulate a large-scale case. In this study, the pseudopotential model was used in LBM to couple with DEM and simulate the multiphase effect.

It is worth mentioning that the coupling of LBM and DEM explicit schemes necessitates matching of their respective critical time steps (Owen et al. 2011). Stability criteria require the DEM time step to be less than a critical value, however, in the LBM the time step is implicitly dependent on other solution parameters such as the relaxation time. Consequently, it is needed to guarantee consistency of time steps in DEM and LBM.

2.6 Summary

Sedimentation and adsorption processes are significant in industry and research studies. In terms of sedimentation, there is much research on the sedimentation of colloidal particles and models, but the mechanism of bidisperse and polydisperse systems is still not fully recovered. The influence of factors such as particle mixing ratios, particle size, and particle-particle interactions are still to be fully understood. Empirical settling models such as the R-Z model (Richardson and Zaki 1954) and the Batchelor model (Batchelor 1972) are restricted in their ranges and ignored some influence factors, thus, losing accuracy in some cases and cannot reveal the true phenomena. Although particle-based simulation models can also show good performance, they can be very computationally costly. Continuity models (Bargie and Tory 2010) such as viscosity-based simulation models (Zhang and Acrivos 1994, Antonopoulou et al. 2018) are a better alternative to simulate the mass particle settling and track the concertation changes, thus, other factors can also be considered and reflected on the changes of concentrations, and velocities are easy to obtain. The interparticle interaction is also an unignorable factor, especially for polydisperse systems or wide-size distribution systems. There is a need to develop the bidisperse and polydisperse settling model with those important considerations and be efficient.

Likewise, our understanding of colloidal nanoparticle adsorption at liquid-gas interface is still lacking, in terms of the kinetic process of adsorption and the influence of factors, such as particle hydrophobicity and fluid flow. Experiments are continually conducted to find out the mechanism of colloidal particle adsorption. However, due to small scale of colloids, experiment data is usually expensive and lacks details. Langmuir trough (Rey et al. 2018) and dynamic surface tension measurement (Bizmark et al. 2014, Dugyala et al. 2016) have been proved to be a good tool to study the adsorption interface structure and predict the adsorption rate, however, as yet, they have not been rigorously applied to study nanoparticles

of variable hydrophobicity. To better study the adsorption process, many kinds of models are proposed and developed in recent years. In the small scale of colloidal particle adsorption. LBM shows good performance in multiphase problems on mesoscopic scales which include most colloids. DEM has been used to couple with some other methods and studied particle adsorption problems formerly (Maxwell et al. 2012). LBM and DEM are two powerful simulation methods and have been proved as high accuracy tools with the coupling methods to combine the fluid flow work by LBM and particle movement work by DEM. They have the potential to simulate particle movement and multiphase fluid flow problems and are suitable for particle adsorption studies.

3. Characterisation of Experimental System

3.1 Introduction

To study the sedimentation and adsorption of particles, the most common material silica is chosen to be the basis particulate material of particles. Silica is easy to acquire in large quantities across a range of sizes in relatively monodisperse form. To know the detail of the system and develop a theory that is experimentally practical and industrially relevant, it is important to characterise the particle parameters. As silica is highly hydrophilic (Su et al. 2006) it is necessary to modify its surface for particles to attain an intermediate wettability, allowing attachment to the air-water interfaces and form a layer (Kharrat et al. 2014). The wettability of particles is an important factor in the adsorption process. To be able to consider a range of systems that may be encountered in industry, it is determined that the particles should be modified to attain 3 different hydrophobicity including the original SiO_2. The detail of measurements and devices are introduced in this chapter.

3.2 Particles and Esterification.

The colloidal silica particles used are Angstrom Sphere® silica powder, with nominal quoted mean sizes of 100, 500 and 800 nm (Fiber Optic Center Inc., USA). The particle densities (ρ_p) were measured as 2.2 g/cm^3 for the 100 nm silica particles and 1.92 g/cm^3 for the 500 nm and 800 nm particles, using a Pycnomatic ATC gas pycnometer (Thermo Electron, USA). The density results are close to expectations for silica particles (Hyde et al. 2016).

Additionally, ultra-high-resolution scanning electron microscopy SU8230 (Hitatchi, Ltd.) was used as a further method to confirm average particle sizes and particle morphology. To enhance the electrical conductivity, dry silica particles from the manufacturer were placed as a monolayer under high vacuum conditions and coated with a layer of carbon on a standard SEM stub. Images are shown in Fig. 3-1. Energy-dispersive X-ray spectroscopy (EDS) was

also used to ensure samples were pure silica particles without any contamination. The SEM size distribution is shown in Fig.3-1.

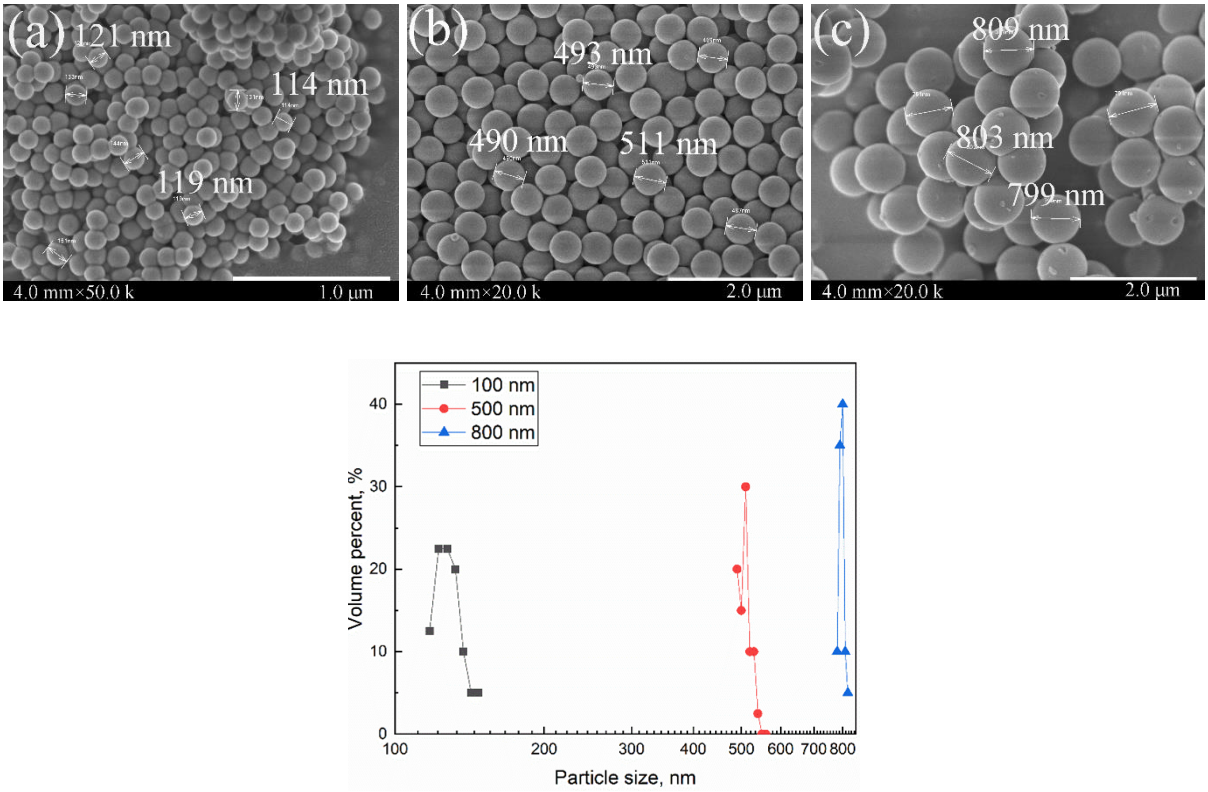

Figure 3-1 Scanning electron micrographs of silica nanoparticles, with nominal mean sizes of (a) 100 nm (50.0k magnification), (b) 500 nm (20.0k magnification), (c) 800 nm (20.0k magnification). The size distributions of three particles were calculated from the SEM images with minimum 40, 50 and 35 counted particles for 100, 500 and 800 nm, respectively.

Suspensions used in the sedimentation experiment were prepared by adding silica powder to a 1×10^{-4} M potassium chloride (KCl) background electrolyte solution, using KCl crystalline powder (Fluka Chemie GmbH, Germany) and ultrapure Milli-Q^{TM} water, with a resistivity of 18.2MΩ cm at 298 K (Millipore, USA). The suspensions were placed in an ultrasonic bath (XUBA3, Grant) for 15 min prior to characterisation without heating. Samples were then further dispersed using an ultrasonic probe, Sonic Dismembrator (Fisher Scientific) at 80% amplitude for 5 min. The purpose of the ultrasonic bath and probe is to fully homogenise the suspensions before any measurements were taken.

Two different size ratios were investigated, comprising nominal 500 and 800 nm silica particles (with a relative mean size ratio of 1.6) as well as 100 and 500 nm particles (with a relative mean size ratio of 5). Bidisperse nanoparticle suspensions (500: 800 nm and 100:500 nm) were prepared in three relative mixing ratios on a volume basis (1:2, 1:1, 2:1). The total volume fractions of the bidisperse suspensions ranged from 0.001 to 0.03 for the mixture of 100 nm and 500 nm particles, and from 0.0005 to 0.05 for the mixture of 500 nm and 800 nm particles. It is noted that while the actual particle size distributions are confirmed through detailed characterisation for simplicity, the species are labelled as per the manufacturer specifications throughout (100, 500 and 800 nm sizes). A Zetasizer® Nano ZS dynamic light scattering analyser (Malvern Panalytical Ltd., UK) was used to confirm the size distribution of the silica particles. Dispersions at 1000 ppm concentration were firstly prepared using the procedure outlined above. For the measurements, 3 samples were analysed over 120 s measurement time and 3 runs for each sample. Autocorrection functions are fitted using the Zetasizer® "general purpose mode" for the monodisperse systems and "multiple narrow modes" for the bidisperse suspensions. The zetapotential of silica particles are shown in Fig.3-2. The zeta potential of 100 nm particles is not measured by the author but used the data measured by Elliott et al (Elliott et al. 2018) who used the same material in this thesis, thus, the data is not shown in the figure.

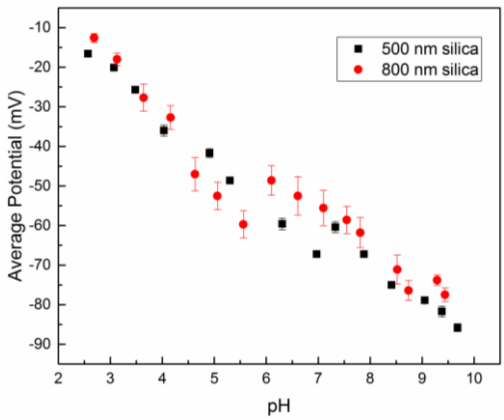

Figure 3-2 Zeta potential for SiO_2 in background electrolyte (1×10^{-4} M KCl).

Phase separation of both monodisperse and bidisperse suspensions is monitored using a LUMiSizer® analytical centrifuge (LUM GmbH, Germany). The LUMiSizer® (Lerche 2019) enhances sedimentation by exposing sample dispersions to a centrifugal acceleration greater than earth gravity. The analysis uses a method called 'Space and Time resolved Extinction Profile' (STEP®) technology, which is an updated approach from classical static light scattering (Sobisch and Lerche 2018). The centrifuge rotation rate can be altered from 0 to 4000 rpm and the effective detection zone ranges from 105 to 130 mm. In the LUMiSizer®, a light source pulses near-infrared (865 nm) light through the side of each sample cell at user-specified times. The light intensity is normalised prior to each run. A 25 mm 2048 element CCD-line detects the intensity of transmitted light across the length of the sample, yielding transmission profiles that can be converted to interface sedimentation, using appropriate transmission thresholds. The transmission profiles are recorded every 10 s throughout each run. Each sample is sealed and placed horizontally in the analyser, along the radial axis, with the top of the sample nearest to the centre of rotation. The base of the sample is determined to be at a radial distance of 129.3 mm from the centre of rotation. The centrifugal acceleration, *a*, is given by Eq. (3.1):

$$a = (2\pi n)^2 r \tag{3.1}$$

where *n* is the number of centrifuge revolutions per second and *r* is the radial position in the centrifuge, with *r* = 0 at the centre of rotation. The height of the sample cell in the centrifuge in this study is 20 mm. Due to the position of the sample in the centrifuge, *r* is given by Eq. (3.2):

$$r = r_{\max} - x \tag{3.2}$$

where r_{max} is the radial position (m) at the base of the sample and *x* is the position. As the particles sediment towards the end of the tube, the acceleration does slightly increase with the

settling interface. The particle size distribution from LUMiSizer and Zetasizer are compared in Fig.3-3.

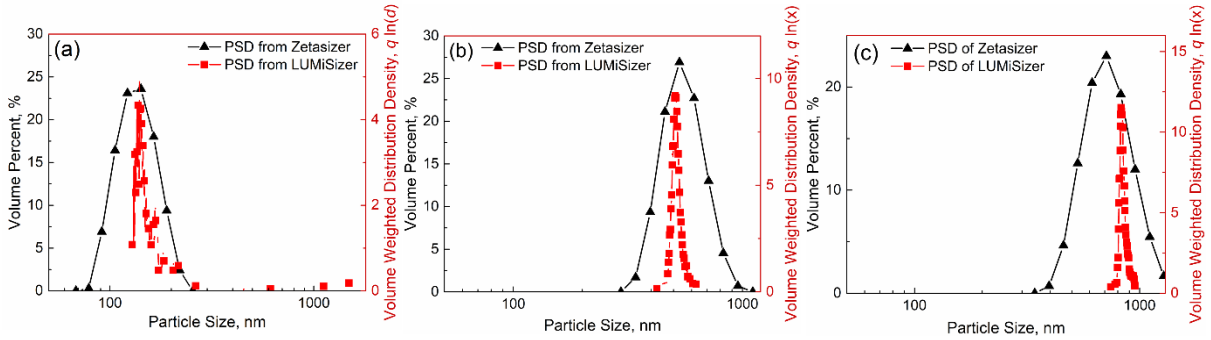

Figure 3-3 Particle size distributions of the three nano-silica dispersions, as measured by the Zetasizer® as a volume distribution (black, left-hand axis), and the LUMiSizer® as a volumetric differential distribution (red, right-hand axis). Particles have nominal sizes of (a) 100 nm, (b) 500 nm, and (c) 800 nm.

From the monodisperse PSD results, all three types of silica particles are measured to be close to their manufacturer defined sizes, especially for the 500 and 800 nm particles, while their polydispersity indexes from DLS are 0.031, 0.012 and 0.07 for the nominal 100, 500 and 800 nm particles respectively, confirming that the suspensions are all nearly monodisperse (San Chan and Don 2013). Interestingly, results also suggest that sizes measured from the LUMiSizer® are both closer to the manufacturer specifications, and with much smaller distributions than through DLS (which can be visually observed in Fig. 3-3 for all three particle types). Similar results have been found by Chiu and co-workers (Chiu et al. 2011), for example, who compared size distributions of organic/inorganic coatings from analytical centrifuge and DLS, also reporting that the analytical centrifuge produced more accurate PSDs. The limitations of DLS measurements for particle size have also been discussed by Anderson *et al.* (Anderson et al. 2013), who suggested that DLS is not very suitable for measuring particles with broad size distributions, while they also found that the analytical centrifuge was one of the best techniques to study non-monodisperse particle systems.

The main reason for the distribution broadening is the relative influence of larger particles on scattered intensity (where $I \propto d^6$ in the Rayleigh regime)(Behra et al. 2019)) meaning that only a few larger particles or aggregates can skew the data or increase the error in the autocorrelation inversion (Anderson et al. 2013). While the larger particles in this study would be strictly outside of the Rayleigh limit, the issues of peak broadening are reduced, but remain. In this case, also, the particles are towards the upper measurable limit by DLS, due to their small Brownian diffusions. Additionally, DLS measurements may be affected by any associated bound ion or electrical double layers, due to their effect on Brownian diffusion (and thus measured for hydrodynamic diameter) which is most prevalent when they are of the same size order as the particles themselves (Schumacher and van de Ven 1987). In fact, it is evident from Fig.3-3 that the DLS overestimates the smallest 100 nm particles more so than the 500 or 800 nm particles, where the relative double layer effects will be more significant.

Importantly, the LUMiSizer® matched the SEMs estimations of the nominal 100 nm particles, which are also measured to give a mean size of ~115-120 nm. Additionally, the LUMiSizer® detected a small degree of aggregation, as evident in the distribution in Fig 3-3(a), which visually affected the transmission profiles to those expected from a true monodisperse system (see Appendix. Fig.A1) although this did not significantly affect the mean sizes. To further probe the influence of any aggregation of the fine particles, 100 nm distributions are analysed at 1000 and 4000 rpm using a 0.005 volume fraction for comparison, with results presented in the Appendix, Fig. A2, along with the related velocity distributions. Similar to the 0.001 volume fraction data presented in Fig. 3-3, there is evidence of a particle aggregation peak (which is more noticeable in terms of velocity, as related to size squared) although, again, the aggregates don't affect the detection of the primary mean.

In this study, the wettability of silica particles would be modified. The colloidal silica particles used are Angstrom Sphere® silica powder, with nominal quoted mean sizes of 800

nm (Fibre Optic Centre Inc., USA). The particle densities (ρ_p) were measured as 1.92 g/cm^3 for 800 nm particles, using a Pycnomatic ATC gas pycnometer (Thermo Electron, USA) three times and used the average value.

To modify the silica surface, particles are subjected to an esterification reaction with straight long chain alcohol producing a covalently bonded alkane coating. The esterification method is considered to bond as a pure monolayer (Ossenkamp et al. 2002) with no secondary or polymerization reactions (Trau et al. 1992), thus, the particle size change can be ignored. Furthermore, using different length alcohol chains readily allows consistent wettability modification of large quantities of particles without relying on exact reagent concentrations or environments. The general esterification reaction (Ossenkamp et al. 2002) is shown schematically in Fig.3-4, where the reaction occurs at the free surface silanol groups as shown in Eq.(3.3):

$$SiOH + HOR_xH_y \longrightarrow SiOR_xH_y + H_2O \tag{3.3}$$

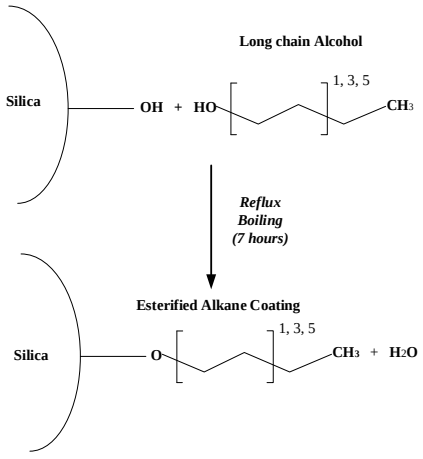

Figure 3-4 Schematic representation of esterification reaction used to hydrophobise the silica particles.

In the effect, the reaction is an "esterification type" water condensation, where under continued high-temperature conditions, the alcohol group condenses with the surface

hydroxyl group (Franks et al. 2000), bonding the alkane chain via the terminal oxygen atom to the silica and producing a water by-product.

To hydrophobise the silica particles to differing extents, 2 different long chain alcohol are used: 1-butanol, 1- hexanol, giving a resultant alkane coating of 4 and 6, respectively. Before the reaction, suspensions of silica particles with alcohol were sonicated and well disperse to make sure there is no aggregation. A heat insulation mantle is covered on the surface of the flask to let it reach the designed temperature and save energy. The reaction is completed as follows. 8 g of 800 nm silica particles were reacted with 100 g of the given alcohol and boiled/ condensed in a 500 mL insulated conical flask under reflux for a period of 7 hours. The mixture is magnetically stirred to inhibit coagulation. A $CaCl_2$ filled drying tube is mounted on top of the condenser to reduce moisture ingress from the surrounding environment, but it is not very necessary. Because the moisture will generate in the flask anyway. The diagram and picture of the esterification setup are shown in Fig.3-5.

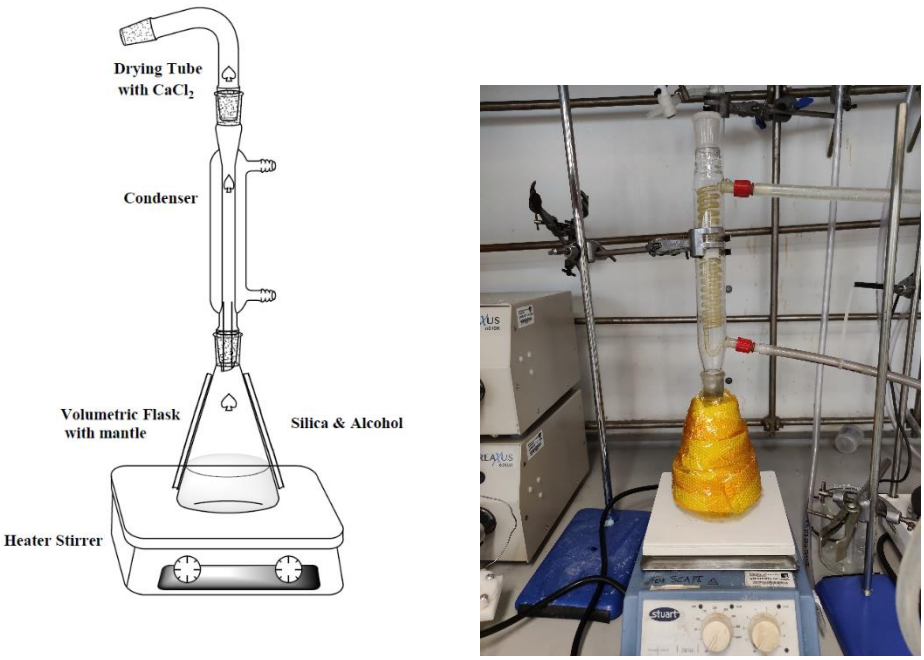

Figure 3-5 Silica particle reflux setup (left) and real reaction device in the laboratory (right).

The grafted particles were centrifuged (in a Thermo Scientific 40 mL tube centrifuge, USA) at 5000 rpm for a period of 8 mins and the supernatant was removed, before redispersing the

particles in acetone. The samples were centrifuged again (at 5000 rpm for 8 mins), the was supernatant removed, and the particles re-dispersed in fresh acetone. The process was completed one more with ethanol ensuring the complete removal of excess reagent alcohol (Hansen et al. 2001). The particles were then air-dried in a laminar flow cabinet and stored in a desiccator for no longer than 2 months. For the purpose of easy description, the resulting particles from esterification with butanol and hexanol are labelled as SiO-butane, and SiO-hexane, respectively.

It is not convenient to directly measure the contact angle of silica nanoparticles, thus, silica wafers are used to detect the contact angle changes due to the esterification. The same treatment is used to the polished silica wafers made of the same material as silica particles. The contact angles of treated silica wafers are measured 5 times each and used as particle contact angles. The measured contact angle of the silica wafer increases with alcohol chain length. The following pictures are measured with KSV camera, and the original and esterified silica wafers are shown in Fig.3-6. and the contact angle results are shown in Table 3-1. The distribution of particle size, for the 800 nm particles, after esterification is shown in Fig.3-7, where it is observed that the esterification does not considerably alter the distributions, indicating particle stability is maintained.

Figure 3-6 Static contact angles for original and esterified silica wafers. (a) Origin SiO2, (b) SiO-butane, (c) SiO-hexane.

Table.3-1. Contact angles of silica wafer treated with alcohols.

Particle	Original SiO_2	SiO-butane	SiO-hexane
Contact angle, °	25.3	46.6	68.5
Deviation, °	0.03	0.1	0.05

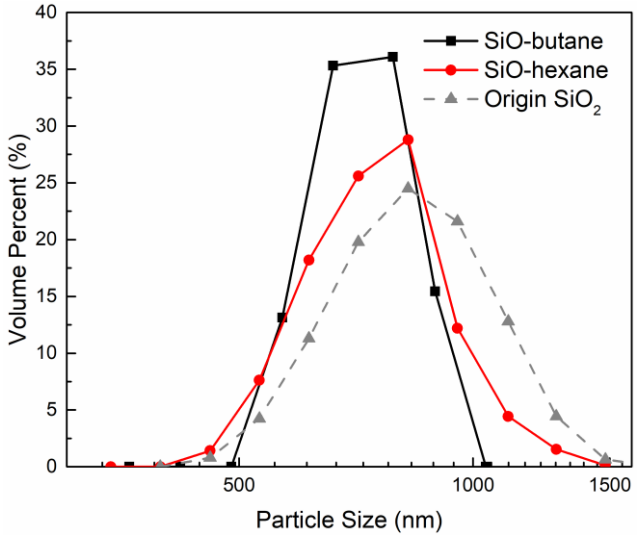

Figure 3-7 Size distributions of 800 nm SiO-butane and SiO-hexane and Original SiO_2.

To investigate the stability of the particles further, the zeta potential of the esterified particles is measured at a pH of ~9-10 (corresponding to a highly negatively stable environment, and the pH chosen for experiments). This is also completed in solutions of 4-Methyl-2-pentanol (MIBC) of varying concentrations, to mimic experimental conditions relating to adsorption studies (see Chapter 6 for further information). The absolute zeta potential values are seen to slightly reduce with particle hydrophobicity, which would be expected from a partial reaction of negative hydroxyl groups. However, the zeta potential ranges from -70 to -60 mV is still in the very stable range for all species. There is no discernible effect of MIBC, inferring a lack of interaction at the particle surface.

Table 3-1. pH and zeta potential values of esterified particles in MIBC solutions.

MIBC	Origin SiO_2	SiO-butane	SiO-hexane

concentration	pH	Zeta (mV)	pH	Zeta (mV)	pH	Zeta (mV)
0	9.84	-72.02 ± 0.2	9.10	-64.65 ± 0.6	8.43	-60.11 ± 0.1
0.01 M	9.81	-73.96 ± 0.5	9.08	-64.87 ± 0.5	8.40	-60.02 ± 0.8
0.03 M	9.85	-72.6 ± 0.8	9.16	-63.89 ± 0.4	8.71	-59.67 ± 0.6
0.05 M	8.60	-71.63 ± 0.4	8.88	-63.56 ± 0.4	8.66	– 59.87 ± 0.2

3.3 Summary

Silica particle sizes are checked with SEM and the results are close to the value provided by the manufacturer. Silica particles with the base solution in the suspensions are stable and not very likely to aggregate if they are well dispersed, so in the calculation and simulation, we ignore the aggregation of particles. Generally, the mean particle sizes before and after the esterification are not changed and the small distribution variation can be ignored. Thus, we assume that the particle size is not changed by the esterification reaction and uses the same size as the original particles. Since the contact angle of the single particle is difficult to measure, the author uses the contact angle of the silica wafer to replace the real single particle's contact angle.

4. Characterisation of Bidisperse Particle Sedimentation Behaviour: Influence of Concentration and Size Ratio

4.1 Introduction

The sedimentation of colloidal suspensions has been intensively studied for many years (Siano 1979, Bloesch and Burns 1980, Concha and Bürger 2002). Its importance is found in many practical applications, such as solid-fluid separations (Marton et al. 2013, Hunter et al. 2020, Lockwood et al. 2021), food (Dulova and Trapido 2011), as well as cosmetics and paints (Bartlett et al. 2012), where sedimentation theory is used to predict the efficiency of industrial processes or product shelf-life, for example. Therefore, a number of studies have been reported over the years on characterising complex colloidal settling (e.g., (Vesaratchanon et al. 2007, Padding and Louis 2008)) and the prediction of settling rates (e.g., (Cao et al. 2015, Antonopoulou et al. 2018)).

Therefore, the aim of this work is to investigate the sedimentation of bidisperse colloidal particles of the same material with an analytical centrifuge. Specifically, two-size particle ratios of colloidal silica are used (500:800 nm and 100:500 nm sizes) in various mixing ratios and total volume fractions. Sedimentation profiles from dilute systems are converted to size distributions and compared to dynamic light scattering and scanning electron microscopy (SEM) for comparison. Then, the fractional interfacial sedimentation rates are measured for various systems, where instrumental limitations due to reduced light transmission are examined. Extracted settling rates of both the larger and smaller particle fractions are then compared to bidisperse modified Richardson-Zaki and Batchelor models, which are used to highlight the influence of mixture ratios on particle drag in reducing the settling velocity or wake effects that may increase the following object's velocity from local hydrodynamic effects.

4.2 Experiment Materials

The non-hydrophobized spherical silica particles in three sizes (100, 500 and 800 nm) are used in the experiment, the size distributions of particles are measured in Chapter 3 and used the size provided by the manufacturer. The particle size distributions measured in Chapter 3 are in the lowest concentration while sedimentation studies are made with higher concentrations.

LUMiSizer® analytical centrifuge is used to measure the sedimentation of particles, the sedimentation fronts are analysed through a pulsed optical source (near infrared, 880 nm) scanned every 10 mins automatically. The technique of LUMiSizer® has been illustrated in Chapter 3 which used the STEP® technology to analyse the data.

In this study, the acceleration value ranges from 975 m/s^2 to 1195 m/s^2 (estimated from the change in x between the start and end of each experiment). Initially, the sedimentation of monodisperse nanoparticle suspensions (nominal 100, 500 and 800 nm as detailed) is measured for volume fractions ϕ = 0.001-0.03. Then, bidisperse nanoparticle suspensions of 100 and 500 nm particles (labelled 100:500), as well as 500 and 800 nm particles (500:800) are prepared in various mixing ratios (on a volume basis) 1:2, 1:1, and 2:1.

To verify the sedimentation under earth gravity, a Turbiscan® (Formulation, France) earth gravity optical analyser is used. 500:800 nm particle dispersions are placed in 20 ml sedimentation cells. The Turbiscan® utilises detectors at 180^o (transmission) and 45^o (backscatter) allowing analysis of opaque dispersions. The whole measuring time is more than 48 h due to the slow settling time of the colloidal particles under earth gravity.

4.3 Experiments Results and Analysis

To further investigate the comparison of analytical centrifuge and DLS, bidisperse particle size distributions of the 100:500 and 500:800 ratio systems (both at a relative volume mixing

ratio of 1:1) using LUMiSizre and Zetasizer are shown in Fig. 4-1. The monodisperse size distribution is shown in Appendix (Fig. A3).

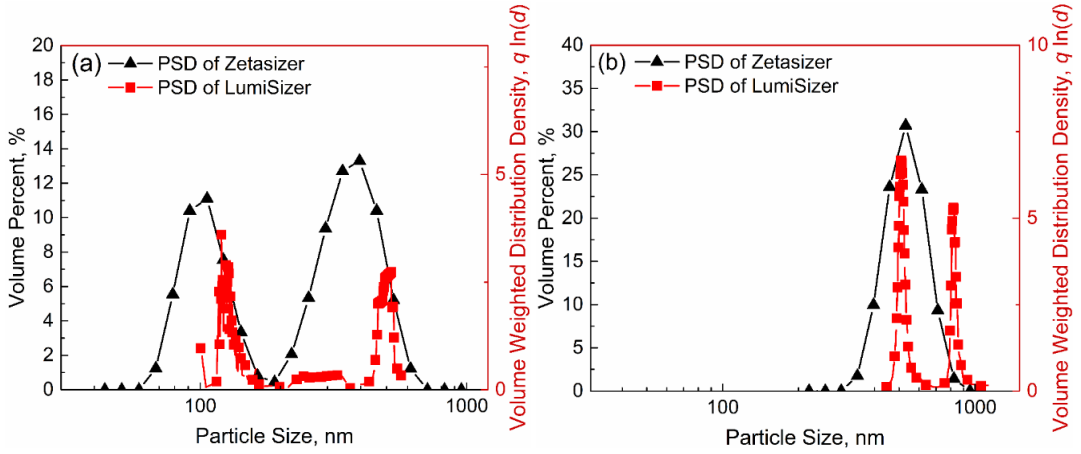

Figure 4-1 Particle size distributions for bidisperse silica systems, as measured by the Zetasizer® as a volume distribution (black, left-hand axis), and the LUMiSizer®, as a volumetric differential distribution (red, right-hand axis). Shown are 1:1 volume ratio dispersions for the cases of (a) 100 and 500 nm particles, and (b) 500 and 800 nm particles.

It is clear, again, that the DLS size data has a greater level of polydispersity that the centrifuge measurements. For the 500:800 mixture, the increase in the measured size range is to a level where only a broad monodisperse peak is actually measured, rather than the two discrete sizes, which are, however, clearly analysed with the centrifuge. From the LUMiSizer® distributions also, the intensities of the two peaks are relatively close in both systems, indicating that the mixing ratio of 1:1 is recovered by the weighted distribution correctly. In general, the bidisperse suspensions accentuate the trends observed in the single particle systems where the DLS technique leads to greater spread in the size measurements (Chiu et al. 2011), which is not consistent with the level of monodispersity evident with the analytical centrifuge or SEM.

4.3.1 Sedimentation of 500 and 800 nm Particle Mixtures

An example LUMiSizer® light transmission sedimentation profile of a 500:800 nm particle mixture is presented in Fig. 4-2 to illustrate a typical change with time in transmission

percentage over the sample height. Each profile signifies the transmission situation at a particular time, with green colours representing transmission at the end of the measurement, and a red colour designating profiles at the beginning. When there are two kinds of particles at different velocities, as in the example provided, the profile will present an inflexion point that represents a border between particle factions, which can be tracked by the instrument. The transmission profiles in Fig. 4-2 clearly highlight two species present at higher and lower transmission levels (Ullmann et al. 2017) that settle with time, with each curve representing a time period of 10 seconds. The higher percentage transmission represents the upper interface (smaller 500 nm silica in this case) while the lower one represents the larger 800 nm silica particles. The mean interface positions are defined and tracked using the average transmission in each fraction. As sedimentation occurs, the profiles move from the meniscus to the bed. The mean sedimentation velocities of the two-particle fractions can be determined from the change in the average interface positions (shown by the horizontal bars in Fig. 4-2) over time. It is clear, in the case presented in Fig. 4-2, that the lower interface sediments faster (and thus is associated with the larger particle species) from the greater separation between each transmission profile.

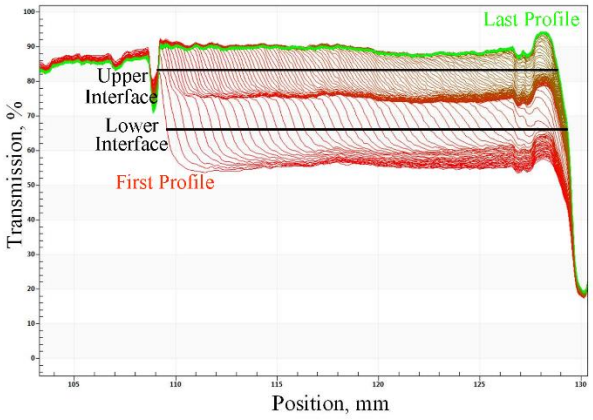

Figure 4-2 LUMiSizer® transmission profiles of bidisperse silica suspensions (500 and 800 nm particles) at a volume ratio of 1:1 and total volume fraction of 0.001, under a 1000 rpm centrifuge speed. Solid horizontal lines indicate mean transmission values for each separate interface.

What is an important consideration in the analysis is how the total particle volume fraction of the two species affects the total transmission, and thus the ability to designate each separate interface. It is also noted that the measured transmission is not strictly equal to the transmission within the suspension sample. Instead, it can be considered as a normalised total transmittance, which also depends on light reflection at the four walls. To better understand these limitations, given in Fig. 4-3 are the average mean transmission positions and ranges for the upper and lower interfaces at various total volume fractions of 500:800 nm mixtures, for relative volume ratios of 1:2, 1:1 and 2:1. It is clear that the transmission of the lower interface ‘disappears’ with an increase in the total volume fraction of the particles, a phenomenon that is slightly more pronounced with a higher ratio of smaller species. Essentially, the lower interface can only be detected if there is a measurable transmission difference between the 500 and 800 nm particle fractions. If the upper dispersion fraction has zero transmission (e.g., the initial concentration of the smaller particles is great enough to fully extinguish the light through the cell) then it is not possible to distinguish the lower interface, and it is masked. Therefore, there is an upper limit to the particle volume fractions that can be measured in bidisperse systems with this device. Although the lower interface of the 1:2 is recognised at 0.03, it is very hard to obtain any statistical data. From the results presented in Fig.4-3, the highest concentration that two interfaces could still be clearly detected is a volume fraction of 0.02 (in the case of the 1:2 and 1:1 ratio systems) and 0.015 (for the 2:1 system).

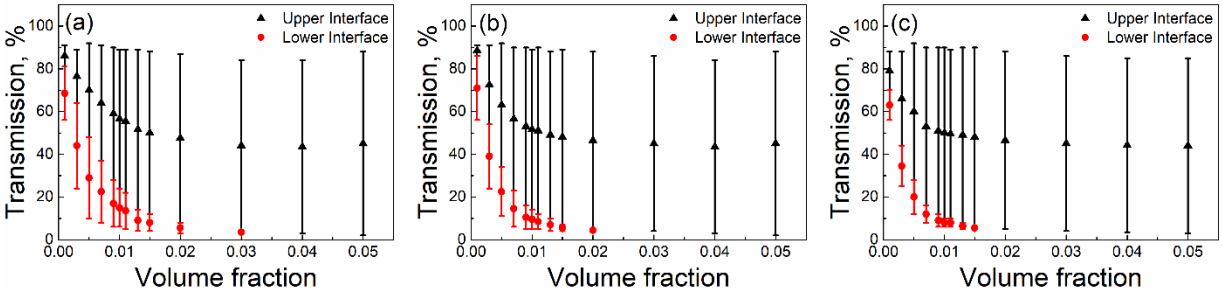

Figure 4-3 Time-averaged LUMiSizer® light transmission profiles for the case of 500: 800 nm particle mixtures under 1000 rpm at various total volume fractions, with different volume ratios of (a) 1:2, (b) 1:1, and (c) 2:1. Data points represent mean time-averaged value of the interface transmission, while scale bar represent averaged transmission range of each interface.

Some samples were also characterised with the Turbiscan® gravity settling system, to confirm the reasons for the extinguishment of the lower interface in the LUMiSizer®. While the Turbiscan® does not utilise centrifugal force to accelerate phase separation, it has a backscatter detector that can be used to measure interfaces in concentrated systems that exhibit zero transmission. These results are shown within the Appendix (Fig. A4) for a 1:1 ratio system of 500:800 nm particles, at total volume fractions of 0.02 and 0.04. Each interface could be tracked clearly in both cases, highlighting that size fractional separation occurs at higher concentrations, and the lack of a second visual interface with LUMiSizer® data (beyond a volume fraction of 0.02) is simply from instrument limitations. The result means that total volume fractions are still below a point where hindered settling becomes significant enough to impede size fraction separation, which would cause sedimentation to occur alternatively through a collective zonal front (Cao et al. 2015).

While there are limitations to the analysis by the LUMiSizer®, for total volume fractions ϕ = 0.02 and below, the front tracking model is clearly able to differentiate the average settling velocity of each separate interface for suspensions below this concentration. An example of the front tracking data is given in Fig. 4-4, showing the normalised height versus time (for the case of total volume fractions of 0.01 and 0.015 and a 1:1 volume ratio of 500:800 nm

particles at 1000 rpm). Other example datasets for the 500:800 particle systems are given in the Appendix (Fig. A5).

The average settling rate for each interface can be determined from the linear gradient change (indicated by dashed lines in the figure). Clear delineation between the interfaces is observed and assumed to correlate to the separated size fractions. Additionally, it is noted that the actual experimental change in height versus time is not quite linear, with the change increasing slightly towards the end of the running time, with the interfaces near the base of the sample tube (which is more noticeable for the slower, upper, interface). This phenomenon is to be expected, and due to the enhancement in centrifugal force as the interface moves outwards as sedimentation continues, causing particle depletion (Antonopoulou et al. 2018). Nonetheless, given the relatively small nature of this deviation, the average linear change in height versus time is used to estimate the mean settling rate for each particle species as the concentration is varied (for tests at both 1000 and 2000 rpm). To further confirm the accuracy of the front averaging, velocity distributions for example 500:800 mixtures are extracted using the constant position mode, where the peak means are compared to estimates from front tracking (see Appendix, Fig. A6 & and Table A1). Both methods give values within 5%, although the front tracking method is used in the results presented due to its simplicity.

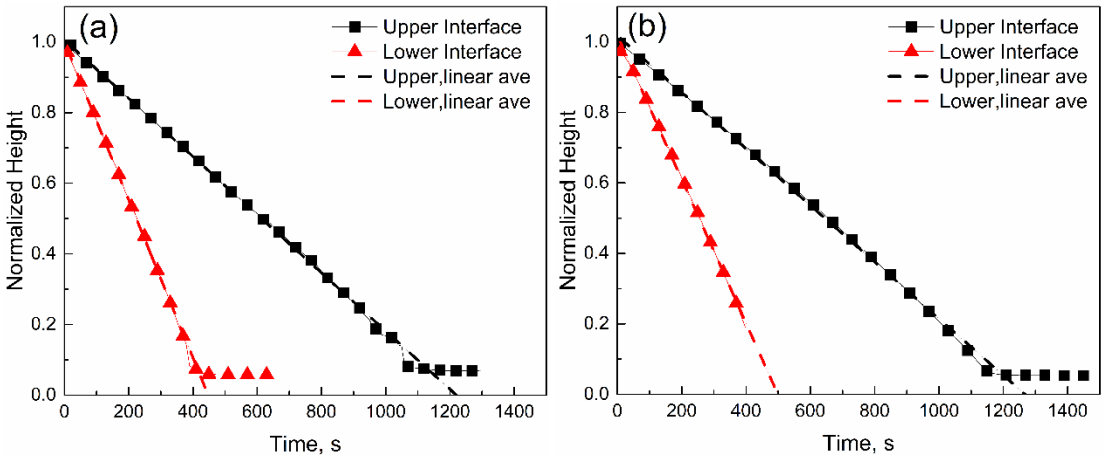

Figure 4-4 Normalised sedimentation front versus time data for 500 and 800 nm particle dispersions (at a 1:1 concentration ratio) under a centrifuge speed of 1000 rpm, and total volume fractions of (a) 0.001, and (b) 0.015. Dashed lines represent the average interpolated linear settling rate for each species.

For the various sedimentation rate data collected, results are compared firstly to the Richardson-Zaki ('R-Z') model (RICHARDSON 1954) to understand the influence of concentration on interface settling rates. The R-Z model for bidisperse systems can be described as follows in Eq. (4.1) and Eq. (4.2):

$$v_i = u_i^0 f_i \tag{4.1}$$

$$f_i = (1-\phi)^n \tag{4.2}$$

Here, v_i is the velocity (m/s) of species i and u_i^0 is the free-settling ('Stokes') velocity of an isolated particle of species i. Critically also, f_i is the hindered settling function of the R-Z model for monodisperse systems that is directly applied to polydisperse systems. It dictates the changes in sedimentation velocity with total particle volume fraction, $\phi = \Sigma\, \phi_i$, where n is an empirical value that is often quoted to be in the range of 4.65-6 (Johnson et al. 2016), depending on conditions such as Reynolds number. In this study, the value of n is taken as 5.1, as determined for spherical particles at low Reynolds numbers by Garside and Al-Dibouni (Garside and Al-Dibouni 1977), although, given the small total volume fractions, a variance of n within this range would only modify predicted settling rates in an order of 1%.

In addition to the Richardson-Zaki model, data is compared with the Al-Naafa and Selim (Al‐Naafa and Selim 1992) modified Bachelor settling model (Batchelor 1982) in a wider volume fraction range. Bachelor's theory is based on pairwise particle interactions and has been shown to match well with experimental data in relatively dilute suspensions (Davis and Birdsell 1988, Al‐Naafa and Selim 1992). Linear hindrance coefficients are used to describe the hindering effect. The hindered settling velocity, v_i, of a particle of species (*i)* in a polydisperse suspension of, *N*, discrete particles is given by Eq. (4.3):

$$v_i = u_i^0 (1 + \sum_{j=1}^{N} S_{ij} \phi_j) \tag{4.3}$$

Here, again, u_i^0 is the Stokes velocity of species *i*, while ϕ_j is the volume fraction of species *j* in the mixture, and S_{ij} are dimensionless sedimentation coefficients from the study of Batchelor and Wen (Batchelor and Wen 1982) which are related to the radius ratio $\chi = d_j/d_i$ and the relative density ratio $\gamma = (\rho_j-\rho_f)/(\rho_i-\rho_f) = 1$ of the bidisperse system. To calculate the small and large particle velocities, the large to small and small to large ratios are both useful, $\lambda = 5$ or 0.2 (for the 100:500 nm case) and 1.6 or 0.625 (for the 500:800 nm case). With the known parameters, the values of S_{ij} for each species can be extrapolated from Batchelor's model S_{ij} tables. Thus, the hindered settling velocities of upper and lower interfaces can be obtained. The S_{ij} values used in this study are recorded within the Appendix (Eq. S1-4) following the values set by Batchelor and Wen for the given size ratios (Batchelor and Wen 1982).

The Stokes terminal velocity can be independently calculated for spherical particles under centrifugal acceleration by Eq. (4.4):

$$u_i^0 = \frac{d^2(\rho_d - \rho_c)a}{18\mu_c} \tag{4.4}$$

where d is the disperse phase diameter (m), ρ_d is the dispersed phase density (kg/m^3), and a is the acceleration experienced (m/s^2). Additionally, ρ_c (kg/m^3) and μ_c (Pa.s) are the density and viscosity of the continuous phase, respectively.

When particles of two sizes are settling together, the upflow of displaced fluid is caused by the combined effect of the sedimentation of the larger and smaller particles. In Al-Naafa and Selim's paper (Al‐Naafa and Selim 1992), the upper zone and lower zone are separated and the sedimentation coefficients are related to each specific species' concentration. For the lower zone, two expressions for sedimentation velocities in the combined settling zone were proposed by them, as given in Eq. (4.5) and Eq. (4.6), where v is the settling velocity, l and s are the large and small particles, respectively, and the subscript '2' refers to the subscripts '1'and '2' refer to the upper and lower zone.

$$v_{l,2} = (1-\phi_l-\phi_s)^{5.55}[u_l^0(1-\phi_l) - u_s^0\phi_s] \tag{4.5}$$

$$v_{s,2} = (1-\phi_l-\phi_s)^{5.55}[u_s^0(1-\phi_s) - u_l^0\phi_l] \tag{4.6}$$

For the upper zone, the lower zone settling velocities $v_{l,2}$ and $v_{s,2}$ are used to calculate the volume fraction $\phi_{s,1}$ which can be expressed as given in Eq. (4.7), where $\phi_{s,2}$ is the initial concentration of the smaller particle species.

$$\phi_{s,1} = \frac{v_{l,2}-v_{s,2}}{v_{l,2}-v_{s,1}}\phi_{s,2} \tag{4.7}$$

Since the upper zone contains only the slower-settling smaller particles, the settling velocity of the upper zone is given more simply as Eq. (4.8) (Al‐Naafa and Selim 1992).

$$v_{s,1} = u_s^0(1-\phi_{s,1})^{6.55} \tag{4.8}$$

The work of Al-Naafa & Selim (Al‐Naafa and Selim 1992), who also studied dilute suspensions of nanoparticles (ϕ < 0.03), confirmed the theoretical exponent prediction of 6.55

given by Batchelor (Batchelor 1972) and thus is also used in the current model. As the volume concentration in this study is less than 0.05, the velocity of the upper zone (Brady and Durlofsky 1988) in dilute suspension can be given as per Eq. (4.9). Eq. (4.7) and (4.9) can then be solved simultaneously for $\phi_{s,1}$ and $v_{s,1}$.

$$v_{s,1} = u_s^0(1 - 6.55\phi_{s,1}) \tag{4.9}$$

Fig. 4-5 presents both the upper and lower interface settling rate data for 500:800 particle mixtures with ratios of 1:2, 1:1 and 2:1 (data generated at both 1000 and 2000 rpm are shown). Settling rates are compared to both the Richardson & Zaki power-law model and the Al-Naafa & Selim ('N-S') modified Batchelor model, where the upper interface is predicted using a 500 nm particle size to calculate the initial settling rate (u_1^0), and the lower interface using an 800 nm size (u_2^0). It is noted also that while the lower (faster) settling interface could only be detected for total volume fractions < 0.02, the upper (slower) settling interface is measured for total volume fractions up to 0.05.

In particular for mixing ratios of 1:2 and 1:1, the upper (slower) settling interface is better predicted by the R-Z model, whereas the N-S model slightly overpredicts sedimentation. The lower (faster) interface settles at rates slightly below those of either theoretical models, (inferring enhanced hindered settling) although it is better predicted by the N-S model, up to the instrument limit of detection (consistent with previous work which used the Batchelor model (Abbas et al. 2006)). For the 2:1 ratio case, both models give a similar prediction for the larger particles, while in this case, the smaller particles have a reduced settling rate in comparison to either model (inferring enhanced hindered effects for the upper zone). Both models give overall best predictions for the 1:1 case. Therefore, it is clear then that the relative particle ratios affect sedimentation, for the same total concentration, implying mixture fractions influence the hindered settling behaviour. In addition, the effect of

centrifugal force on the accuracy of model predictions is minimal, as there is little difference in correlation between the 1000 and 2000 rpm cases (although the actual settling rates are considerably different) implying that the accelerated fractionation is not considerably affecting results.

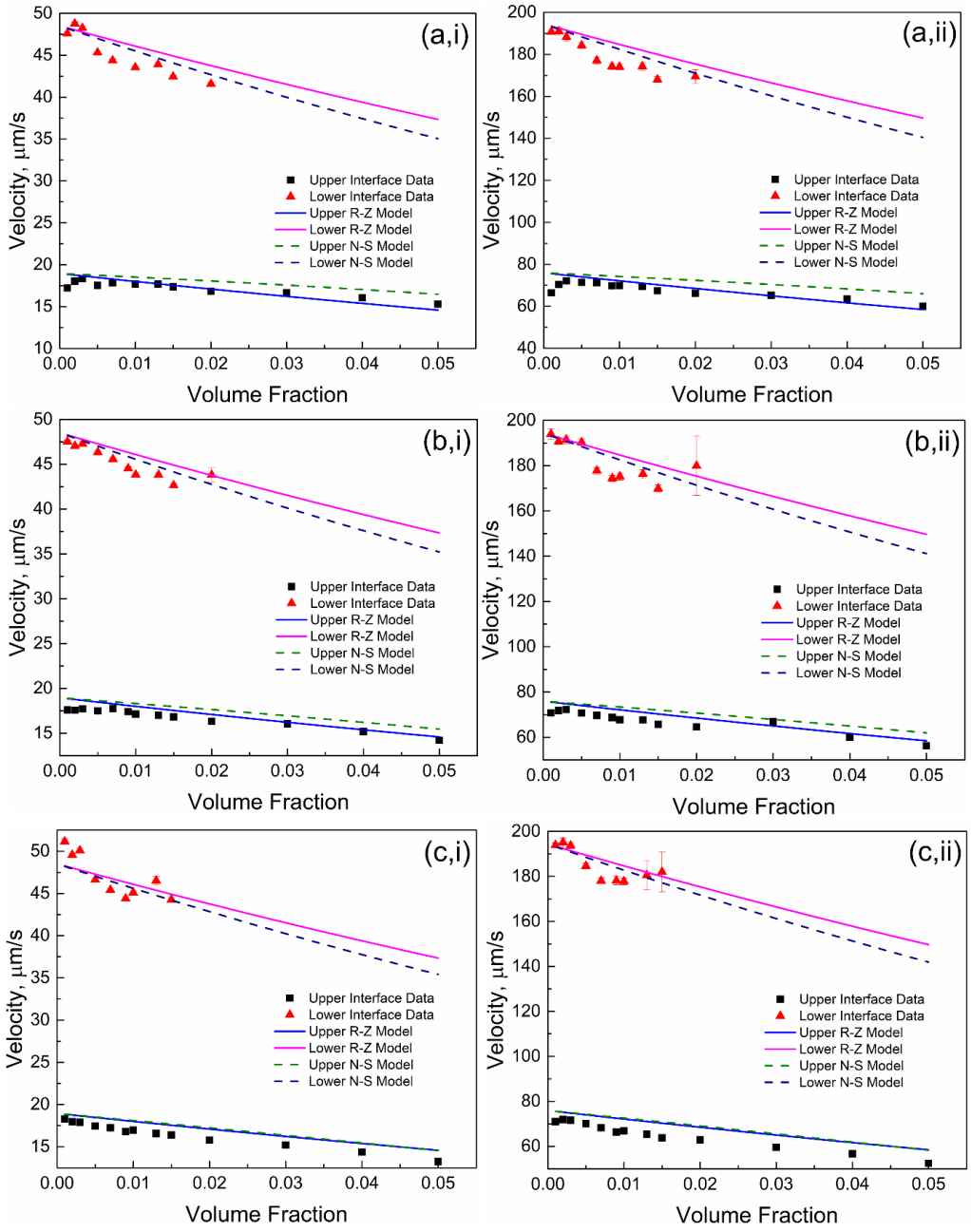

Figure 4-5 Comparison of averaged linear settling velocities for 500 and 800 nm mixed particle dispersions at various total volume fractions, to calculated estimations using the Richardson & Zaki ('R-Z') [13] and Al-Naafa & Selim ('N-S') [16] models. Shown is data for relative 500:800 nm particle ratios of (a) 1:2 (b) 1:1, and (c) 2:1, all under centrifuge speed of (i) 1000 rpm and (ii) 2000 rpm.

Interestingly, both theories work better for lower zone for 1:2 mixture but better for upper zone for 2:1 mixture. It caused by the consideration that both theories ignored the interparticle interactions and N-S model assumes the diluted suspensions. For lower zone, 1:2 ratio means less 500 nm particles in suspension and less 500 nm settle at the same time as 800 nm which lead to closer situation as the theories assumption. The case is the same for upper zone for 2:1 mixture. It is another evidence that interparticle interactions are important.

Additional hydrodynamic or dispersion interactions between particle fractions may also contribute to a modified hindering effect, which is not considered by the model functions. For example, particle wake effects can cause additional drag and what is known as drafting-kissing-tumbling events, but these are generally found for systems with Reynolds number >1 (e.g., Zaidi *et al.* (Zaidi et al. 2015)) where Reynolds numbers estimated from terminal velocities in the current study are in the order of 10^{-4} to 10^{-3}.-Simulations by Yin & Koch (Yin and Koch 2007) explained reduced settling rates in terms of structural anisotropy that occurs in the dispersions, although again, effects are most evident for larger Reynolds numbers than in the studies case. However, we believe they may be more pronounced in bidisperse systems, where the larger particles settle through the smaller fraction. For example, previous simulations of bidisperse colloidal suspensions at low Reynolds number by Abbas *et al.* (Abbas et al. 2006) indicated that particle diffusion and transverse velocities can be significantly modified for each phase, depending on the mixture ratio, leading to variance in settling velocities. Additionally, bidisperse simulations by Koo (Koo 2008) again for relevant low Reynolds numbers, showed consistently that settling velocities were lower than empirical predictions at low total volume fractions, and varied depending on size ratio.

4.3.2 Sedimentation of 100 and 500 nm Particle Mixtures

One potential difference between the 100:500 nm particle mixtures and the 500:800 nm systems is the increased influence of Brownian motion on the smaller 100 nm species. To

illustrate the effect of Brownian motion, the Peclet number (Cui et al. 2015), which is the ratio of the advective transport and diffusive transport rates, can be calculated using the terminal velocity of particles. For *l*, the characteristic length (m) of particle, taken as the diameter, *v* the relative flow velocity, taken as the terminal settling velocity (m/s), and *D* (m^2/s) the mass diffusion coefficient of the particles in the fluid, the Peclet number can be calculated from the Stokes-Einstein Eq.(4.10) (Dill et al. 2010):

$$Pe = \frac{vl}{D} \tag{4.10}$$

Peclet number calculations are given in Table 4-1 for both 100 and 500 nm particles at various centrifuge speeds from 1000 to 4000 rpm. In general, Peclet numbers < 0.1 infer diffusion-dominated behaviour (Solari et al. 2011). Using this threshold, it is clear that in the lower rpm region (below 3000 rpm) the behaviour of 100 nm silica particles is mainly controlled by Brownian motion (Chung and Hogg 1985), which may lead to a reduction in the clarity of the upper interface fraction observed through transmission.

Table. 4-1. Peclet numbers for 100 nm and 500 nm silica particles under different centrifugal rotation speeds, using their terminal velocities.

Particle size	1000 rpm	2000 rpm	3000 rpm	4000 rpm
100 nm	0.01	0.04	0.09	0.16
500 nm	0.64	25.68	57.71	102.61

The interface transmission profiles for the 100:500 nm particle mixtures are shown within the Appendix (Fig. A7) for an overall volume fraction of 0.01 and a 1:1 particle ratio. Indeed, it is evident that for lower rpm (1000 & 2000 rpm) the upper interface is not easily discernible at all. However, for 3000 and 4000 rpm, both particle fractions can be detected with separate interfaces. We believe Brownian diffusion of the 100 nm particles at the lower rpm is

significant enough to continue mixing with the larger particle fraction, reducing the separation. Therefore, for the main experiments presented, only data at 4000 rpm is analysed for the 100:500 nm particle systems. A further example of the raw transmission profiles is given in Fig. 4-6 (for the case of a 1:1 particle ratio and total volume fraction of 0.02).

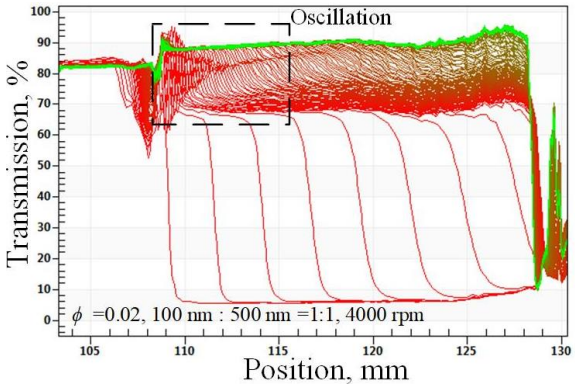

Figure 4-6 LUMiSizer® transmission profiles of bidisperse silica suspensions (100 and 500 nm particles) at a volume ratio of 1:1 and total volume fraction of 0.02, under a 4000 rpm centrifuge speed.

From the transmission profiles in Fig.4-6, there is some other interesting behaviour observed for the upper (100 nm) particle fraction. In particular, there is some evidence of an oscillation phenomenon towards the beginning of the sedimentation in the upper transmission area near the meniscus (see the annotated box in the figure). We believe that, despite the high 4000 rpm centrifuge, this observed oscillation may be due to the Brownian motion of the 100 nm particles still having some effect. In general, there will be some time lag before the smaller 100 nm particles attain their terminal velocity in the high gravity field due to the competing Brownian motion, which makes the initial profiles relatively noisy. In addition, it may indicate some nanoparticle adsorption either to the liquid meniscus itself or to the tube walls. While these are uncoated silica nanoparticles, they may still have a large enough particle contact angle to adsorb to air-water interfaces, although detachment energies should still be low (Hunter et al. 2007). It also may be a direct optical effect of the meniscus or upper discontinuity in the tube. It is noted that due to the much larger size ratio for the 100:500 nm

particle case, the relative transmission of the 100 nm particles is much greater than for the 500 nm particles, making any distinction of the upper particle zone difficult at low total concentrations.

Despite these additional variations, average settling rates from each particle fraction are still successfully measured for a range of particle mixture ratios and total volume fractions. Fig. 4-7 presents two examples of the particle fraction interface versus time data for the 100:500 nm particle mixtures at different total volume fractions (and a 1:1 relative particle ratio). Within the Appendix (Fig. A8) gives further examples of settling data from other total volume fractions analysed with the same particle ratio. In general, average linear settling rates for both particle fractions are clearly estimated from these figures (shown by the dashed lines) although the interfacial data is noisier for the 100 nm fraction at low total particle levels (likely due to the competing influence of Browning motion, as discussed).

Using these calculated averages, the settling velocities of the 100:500 nm particle mixtures in different volume fractions are shown in Fig.4-7 (i, a-c), again in comparison to estimations from the R-Z power-law model and the N-S modified Batchelor model. Evaluations are similarly made at three different particle mixture ratios (1:2, 1:1 and 2:1 relative ratios). From the results, both models predict the settling rates of both particle species to greater accuracy than the 500:800 nm systems, likely because of the larger degree of separation in particle settling rates from the wider size ratio and centrifuge speed. The modified Batchelor model does also give some improvement in prediction for the larger (faster settling) particle fraction, especially in the case where there is a greater degree of larger particles in the mixtures, likely due to the separation of the individual particle fractions within the model.

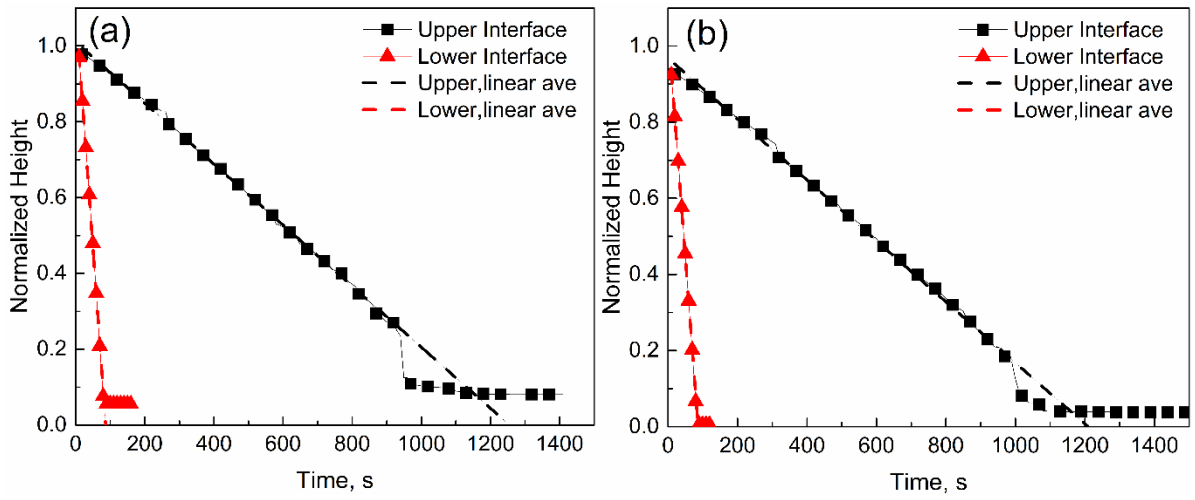

Figure 4-7 Normalised sedimentation front versus time data for 100: 500 nm particle dispersions (at a 1:1 concentration ratio) under a centrifuge speed of 4000 rpm, and total volume fractions of (a) 0.015, and (b) 0.03. Dashed lines represent average interpolated linear settling rates for each species.

Fig. 4-8 (ii, a-c) displays further analysis of the interaction between particle species. In particular, the measured settling velocity of smaller particles is estimated in different sections; being those before complete sedimentation of the larger 500 nm fraction (black circles) and those afterwards (inverted red triangles) in comparison to the calculated terminal velocity.

It is observed that in all cases, the initial settling rate of the 100 nm particles is slower than the rate post 500 nm particle deposition, meaning that the 500 nm particles further hindered the sedimentation of the 100 nm fraction. This effect also appears more significant in mixtures with a greater ratio of 100 nm particles, highlighting the impact of the relative concentration of the smaller species again, in which the larger particles sediment through (consistent with the 500:800 case).

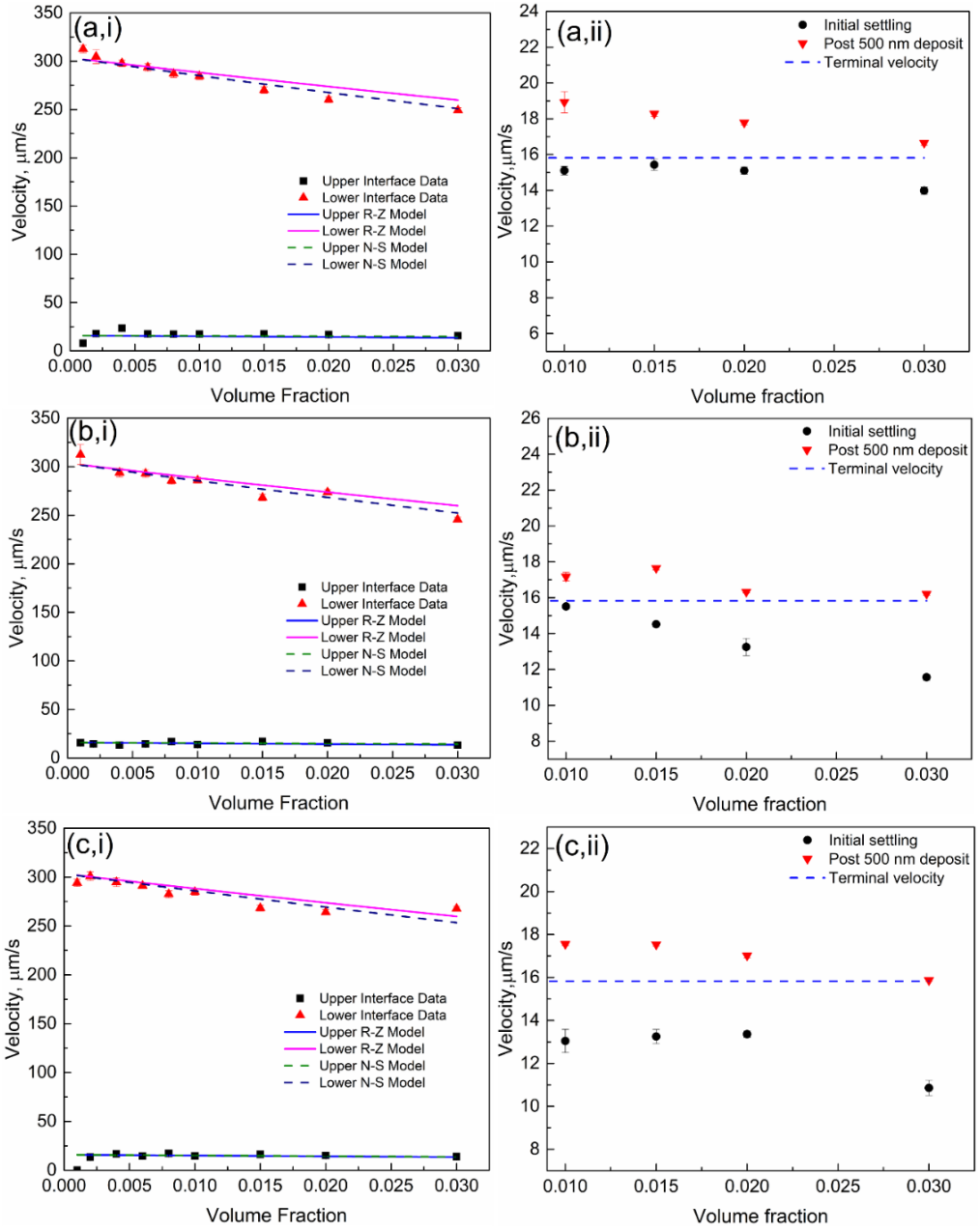

Figure 4-8 (i) Comparison of averaged linear settling velocities for 100 and 500 mixed particle dispersions at various total volume fractions, against calculated estimations, using the Richardson & Zaki ('R-Z') [13] and Al-Naafa & Selim ('N-S') [16] models. (ii) The analysis of 100 nm particle velocities before and after 500 nm particle fraction has settled. Data is given for particle ratios of (a) 1:2, (b) 1:1, and (c)2:1.

The increase in the settling rate post-deposition of the 500 nm species may be explained by the reduced overall hindered settling effects from the lower total volume fraction once the 500 nm particles have sedimented (and this relative effect is more significant for cases of higher 500 nm ratios). However, again there is evidence of greater hindering effects for the

sedimentation of the smaller species in the initial times when the two fractions are in contact. Again, we believe there is enhanced dispersion anisotropy from the larger particles settling through the smaller fraction, while due to the greater size ratio, backflow effects may be heightened, which have experimentally been determined to influence sedimentation of spheres in Stokes flow regimes where Re << 1 (Reed and Anderson 1980, Ambari et al. 1998). As an extension Howard et al. (Howard et al. 2018) highlighted the effects of upflow and zonal banding in simulations of heavy particles in mutually buoyant suspensions subjected to variable shear, all be it for systems at higher concentrations. There is also potential for the 100 nm aggregates to affect sedimentation by increasing the local effective volume fraction of the dispersion in the initial region before they settle out. Lastly, a comment is made regarding the influence of these dispersion effects on non-spherical systems, which may be of more interest industrially. Given that drag is enhanced in non-spherical particle systems (Yaghoobi and Torabi 2012, Paul et al. 2017), any hydrodynamic influence of particle phases settling through one another will be heightened, potentially reducing phase separation more than for spherical systems.

4.4 Conclusion

In this study, centrifugal sedimentation experiments are conducted with bidisperse colloidal silica dispersions in two different size ratios, using an analytical photo centrifuge (LUMiSizer®). Specifically, particle mixtures of 500:800 nm dispersions (mean size ratio of 1.6) and 100:500 nm dispersions (mean size ratio of 5) are investigated at three different volume mixture ratios (1:2, 1:1 and 2:1) to understand the importance of fluid-particle effects from the larger size fraction on the settling of the smaller particles. Results are compared to modified empirical models to predict the influence of total volume fraction on settling rate. For truly dilute suspensions (where the influence of volume fraction is ignored) the LUMiSizer® is able to gain very reproducible size distributions for both monodisperse and

bidisperse systems, by integration of the velocity distribution (and using Stokes law to convert to size). Distributions compared very well to estimates from SEM and manufacturer expectations, and in fact, are a lot closer than measurements using dynamic light scattering (DLS) with a Zetasizer®. In particular, results showed that DLS is not very suitable to measure the size distribution of colloidal bidisperse suspensions, where size peaks may overlap.

For sedimentation studies at various total volume fractions, the LUMiSizer® is shown to have an upper concentration limitation where only one interface could be detected by the instrument. For the 500:800 nm mixtures, this volume fraction is ~0.015 for most mixtures. However, below this limitation, both particle fractions separated clearly, and average settling rates of each size fraction are able to be analysed. Settling data is compared to the Richardson-Zaki (Richardson and Zaki 1954) model and the modified Batchelor model of Al-Naafa & Selim (Al‐Naafa and Selim 1992). The 500:800 nm particle mixture data, in general, compared well to both models, although the Batchelor model proved more accurate at predicting the lower faster interface rate (of the larger particles) while both models slightly over predicted the upper slower interface (smaller particle fraction). The correlation is also dependent on the mixture ratio, with predictions poorest for systems with higher fractions of smaller particles. It appears that the smaller particle fraction experiences a greater degree of a hindrance than model, which may be due to dispersion anisotropy or backflow causing enhanced drag from the larger particle fraction, as it settles through the smaller particle zone.

For the case of the 100:500 nm particle mixtures, it is evident that Brownian motion is contributing significantly to the overall movement of the 100 nm particles, which is confirmed with the estimation of the Peclet number. Therefore, higher centrifugal rotation rates (of 3000 and 4000 rpm) have to be used to clearly separate the particle fractions. Again, interfacial settling data is compared to the empirical models, where the modified Batchelor

model provided better estimates again for the lower interface (larger particles). In this case, the influence of the larger particle fraction is highlighted by analysing the velocity of the upper (smaller) particle fraction before and after sedimentation of the larger particles. Again, evidence of enhanced drag is evident in the separation of the smaller 100 nm particles, where their initial settling velocity is below their predicted terminal velocity within the initial time window before complete sedimentation of the larger particles. Once more, these effects are more prevalent for systems with a greater volume fraction of smaller species. Overall, the results highlight the practical advantages and limitations of using analytical photo centrifuges for the characterisation of bidisperse sedimentation. It also suggests a more complete model is required to take into account the additional hindrance factors evidenced, and in particular, the influence of particle mixture ratio.

5. 1D Simulation of Bidisperse Particle Sedimentation Under Earth Gravity and Centrifuge

5.1 Introduction

The suspension viscosity model (Zhang and Acrivos 1994) is one of the most popular models to predict the settling velocity of particles with the advantage of reducing the velocity to zero at the maximum volume fraction. Particles in suspension do not sediment alone but move and are hindered by surrounding particles, where the effect of hindrance increases as the particle volume fraction increase. Usually, sedimentation literature neglect particle interactions (Lockett and Al-Habbooby 1974, Ackerson et al. 1999, Genovese 2012) for convenience and based on the hard-sphere assumption which means there is no restriction on the minimum separation distance between two colloidal particles. However, the assumption may not be suitable (Antonopoulou et al. 2018) for highly charged colloidal particles. Effective volume fraction and effective diameter have been used to describe interparticle interactions and depletion interactions, respectively. Particles in suspension do not sediment alone but are also hindered by surrounding particles. An effective volume fraction is defined based on the effective particle size and an exclusion volume around the particle. To describe colloidal suspensions, Metin (Metin 2012) has demonstrated the use of effective particle size and taking into account the interparticle interactions using an effective maximum volume fraction. This method can be applied in the monodisperse sedimentation model and can be extended to bidisperse models.

In this chapter, a continuum-based approach has been used. Solid concentrations are tracked to predict the velocities of interfaces. A mathematical suspension viscosity model for the sedimentation of bidisperse colloidal particles has been developed. Hindered settling effects are considered in a one-dimensional model (Davis and Russel 1989) rather than the

Richardson-Zaki like hindrance function relationship. Furthermore, the effective maximum volume fraction (Metin 2012) method which has been validated for describing the shear rheology of colloidal suspension has been used in the model, and interparticle interactions are also taken into consideration. The numerical implementation of this model using an adaptive finite difference solver is described.

5.2 Simulation Methodology

5.2.1 Bidisperse Sedimentation Model

This work considers bidisperse suspensions of origin spherical colloidal silica particles without particle aggregation. To simulate bidisperse sedimentation, a model for bidisperse, colloidal suspensions is proposed, based on the model of Davis and Russel (Davis and Russel 1989), and as described herein. The particle volume fraction of *i* component, at a height *x* and time *t* (ϕ_i) is described by the advection-diffusion equation for a bidisperse system as Eq. (5.1):

$$\frac{\partial \phi_i}{\partial t} + \frac{\partial}{\partial x}[\phi_i u_{si}(\phi_i)] = \frac{\partial}{\partial x}[D_i(\phi_i)\frac{\partial \phi_i}{\partial x}], \tag{5.1}$$

Where $u_{si}(\phi_i)$ is the hindered settling velocity (m/s) of the *i* component particles in suspension (upward direction is chosen as positive) and $D_i(\phi_i)$ is the diffusion coefficient of *i* component. The continuous phase is assumed to be stagnant, except for the displacement caused by sedimentation. The assumption allows the application of the zero-flux boundary conditions as Eq. (5.2):

$$\phi_i u_i(\phi_i) - D_i(\phi_i)\frac{\partial \phi_i}{\partial x} = 0, x \in \{0, x_{\max}\}, t \geq 0, \tag{5.2}$$

Where $x = 0$ at the base of the sample and $x = x_{\max}$ at the meniscus. The suspension is assumed to be well-dispersed after mixing and the initial condition can be Eq. (5.3):

$$\phi_i(x) = \phi_{0i}, x \in (0, x_{\max}), t = 0, \tag{5.3}$$

Where ϕ_{0i} is constant and the initial concentration of suspension component *i*. Then, the diffusion coefficient can be incorporated from the Stokes-Einstein equation Eq. (5.4):

$$D_i(\phi_i) = \frac{k_B T}{3\pi\mu d_i}, \tag{5.4}$$

Where k_B is the Boltzmann's constant ($J \cdot K^{-1}$) and the T is the absolute temperature (K), μ is the kinematic viscosity ($m^2 s^{-1}$) and d_i is the diameter (m) of *i* component.

In the advection part, the hindered settling velocity is given by Eq. (5.5):

$$u_{si}(\phi_i) = u_{\mathrm{Ti}} f_{\mathrm{hi}}(\phi_i), \tag{5.5}$$

Where $f_{\mathrm{hi}}(\phi_i)$ is a function to describe the hindrance effect and u_{Ti} means the particle terminal velocity of *i* component. The terminal velocity in Stokes' law is calculated by Eq. (5.6):

$$u_{\mathrm{Ti}} = \frac{d_i^{\,2}(\rho_{di} - \rho_c)\mathrm{g}}{18\mu_c}, \tag{5.6}$$

Where d_i is the diameter of the dispersed phase, ρ_{di} is the dispersed phase density (kg/m^3), g is the acceleration (m/s^2), ρ_c and μ_c are the density and viscosity of the continuous phase, respectively. For ultrapure water, ρ_c = 997.1 kg/m^{-3} and μ_c =8.9×10^{-4} Pa·s.

The most popular hindered settling function is the simple formula of Richardson and Zaki (Richardson and Zaki 1997), which has been applied to many systems from monodisperse to polydisperse. The formula is shown as Eq. (5.7):

$$f_{hi} = (1-\phi_i)^n, \tag{5.7}$$

Where *i* means different species, ϕ means volume fraction of particle and *n* is suggested to be 5.1 for colloidal particles at low Reynolds numbers by Garside and Al-Dibouni (Garside and

Al-Dibouni 1977) with higher accuracy in the monodisperse system. In the polydisperse system of Richardson and Zaki, ϕ is replaced by the total volume fraction of particles. However, this formula does not take particle sizes and mixing ratios into consideration. It is also an entirely empirical approximation and has no realistic upper bounding in relation to particle volume fraction.

In this study, as an alternative, the hindrance function is described as being related to the mixture viscosity (Rao et al. 2002) as presented in Eq. (5.8). It has been previously utilised to simulate 1D sedimentation profiles of monodisperse colloidal particles (Antonopoulou et al. 2018) and here is significantly extended for using in bidisperse sedimentation.

$$f_{\mathrm{hi}}(\phi_i) = \frac{\mu_c(1-\phi_{0i})}{\mu}, \tag{5.8}$$

Here, μ is the mixture viscosity of the bidisperse suspension that has been used in the model, while μ_c again is the continuous phase viscosity (of ultrapure water at 25 ^{o}C, as described).

The mixture viscosity can be estimated using a number of relative viscosity models, which are normally bound by the maximum volume fraction of the dispersion, often, the random close packing volume fraction, ϕ_{rcp}, is used. In this study, for initial monodisperse simulations, a modified effective maximum volume fraction, $\phi_{max}^{\mathrm{eff}}$, is defined, based on the effective diameter of the particles in monodisperse systems (Antonopoulou et al. 2018). Then, the viscosity of silica monodisperse suspensions which is called the Quemada model with the effective volume fraction (Genovese 2012) can be calculated using Eq. (5.9) and (5.10):

$$\mu = \mu_c \mu_r, \tag{5.9}$$

$$\mu_r = \left(1-\frac{\phi}{\phi_{\max}^{\mathrm{eff}}}\right)^{-2} \tag{5.10}$$

Where the μ_r is the relative viscosity. For bidisperse systems, the effective maximum volume fraction is $\phi_{max,b}$, and is modified according to the work of Qi and Tanner (Qi and Tanner 2011, Qi and Tanner 2011), where it is given by Eq. (5.11):

$$\phi_{\max,b} = \phi_{rcp} + \xi_k \xi_\lambda \phi_{rcp}(1-\phi_{rcp}), \tag{5.11}$$

Here, k is the fraction of small particles, and λ is the particle size ratio of large particles to small particles. When it is used in the monodisperse, the model will back to simple ϕ_{rcp} in the viscosity model. Under the assumption of hard spheres, for monodisperse systems ϕ_{rcp} = 0.639. The two coefficients ξ_k and ξ_λ are expressed as Eq. (5.12) and (5.13):

$$\xi_\lambda = 1 - e^{-\frac{(\lambda-1)^{\frac{1}{3}}}{6}}, \tag{5.12}$$

$$\xi_k = \begin{cases} 1 - \frac{1}{0.0729}(k-0.27)^2, & k \le 0.27 \\ 1 - \frac{1}{0.284}(k-0.27)^4, & k > 0.27 \end{cases}, \tag{5.13}$$

The relative viscosity of bidisperse suspension μ_r (Qi and Tanner 2011) that is used in this study can be defined as Eq. (5.14)-(5.16) and the new μ_r in Eq. (5.14) should be used to replace the monodisperse μ_r with a bidisperse μ_r in Eq.(5.10) when calculating the bidisperse fluid viscosity. The bidisperse viscosity will back monodisperse one when there is only one component in the same position of suspension.

$$\mu_r = [(1-\frac{\phi_L}{1-c_L\phi_L})(1-\frac{\phi_S}{1-c_S\phi_S})]^{-\frac{5}{2}}, \tag{5.14}$$

$$c_L = \frac{1-\phi_{rcp}}{\phi_{rcp}}, \tag{5.15}$$

$$c_S = \frac{1-(\phi_{\max,b}^{eff} - \phi_L)}{\phi_{\max,b}^{eff} - \phi_L}, \tag{5.16}$$

The maximum obtainable volume fraction, $\phi_{max,b}$, is further modified, to account for the minimum separation distance obtainable between stabilised colloidal particles, thus giving an overall effective maximum bidisperse volume fraction ($\phi^{eff}_{max,b}$) following on from similar estimations used in simulations of monodisperse sedimentation (Antonopoulou et al. 2018). The bidisperse effective volume fraction can be calculated as Eq. (5.17) (Metin 2012):

$$\phi^{\text{eff}}_{\text{max,b}} = \phi_{\text{max},b}\left(\frac{d_{ave} + \bar{s}}{d_{ave}}\right)^{-3}, \tag{5.17}$$

The Sauter mean diameter (A. et al. 1998) of a bidisperse distribution of spherical particles can be calculated as Eq. (5.18):

$$d_{ave} = \frac{d_L d_S(\phi_L + \phi_S)}{d_L\phi_S + d_S\phi_L}, \tag{5.18}$$

Where d means the diameter and ϕ means volume concentration. The subscribe S and L mean small and large particles, respectively.

The d_{ave} is the average diameter calculated by Eq. (5.18), $\bar{s}$ is the minimum separation distance between the surfaces of two particles. The modified kinematic viscosity allows the hindered settling velocity to become zero at the effective maximum volume fraction and it takes interparticle interactions into account.

For the particle diameter larger than 800 nm, the minimum separation distance $\bar{s}$ can be calculated (Antonopoulou et al. 2018) by DLVO theory. However, the DLVO theory in the bidisperse system is different from the mono system as shown follow.

The total interaction potential, U is given by (Rhodes 2008) as Eq. (5.19):

$$U(s) = U_{VDW} + U_{EDL}, \tag{5.19}$$

Where U_{VDW} is the attractive component and U_{EDL} is the repulsive component of the interaction potential.

For van der Waals (VDW) attraction part, the effective Hamaker constants A_H of silica particles in water are the same (Leong and Ong 2003) using 2.5×10^{-20} J for the silica-water-silica system. Then, the attraction can be described as Eq. (5.20):

$$U_{VDW} = -\frac{A_H}{6}\left[\frac{2R_1R_2}{s^2+2R_1s+2R_2s} + \frac{2R_1R_2}{s^2+2R_1s+2R_2s+4R_1R_2} + \ln\left(\frac{s^2+2R_1s+2R_2s}{s^2+2R_1s+2R_2s+4R_1R_2}\right)\right], \quad (5.20)$$

Where R is the radius of particles and s is the distance of closest approach between the particle surfaces, the subscript number 1 and 2 mean component numbers.

For electric double layer (EDL) Interaction, a new formula can be calculated as Eq. (5.21):

$$U_{EDL} = \frac{128\pi \frac{R_1R_2}{R_1+R_2} k_B T N_A I \gamma_1 \gamma_2}{\kappa^2} \exp(-\kappa s), \quad (5.21)$$

Where N_A is the Avagadro constant, I is the ionic strength of the electrolyte (mol m^{-3}), γ is the reduced surface potential (V), and κ is the inverse Debye length (m^{-1}).

For monovalent electrolytes (like KCl), the inverse Debye length is given by (Tadmor et al. 2002) Eq. (5.22):

$$\kappa = \sqrt{\frac{2N_A I e^2}{\varepsilon_0 \varepsilon_r k_B T}} \quad (5.22)$$

Where ε_0 =8.85×10^{-12} F m^{-1} is the permittivity of free space (Rhodes 2008) and ε_r is the relative permittivity of the medium. In the case of ultrapure water at 298.15 K, ε_r=78.304 (Dunn and Stokes 1969). Fig.5-1. shows the corresponding interaction potential for 500:800 silica dispersed in 10^{-4} M KCl and in 10^{-2} M KCl,

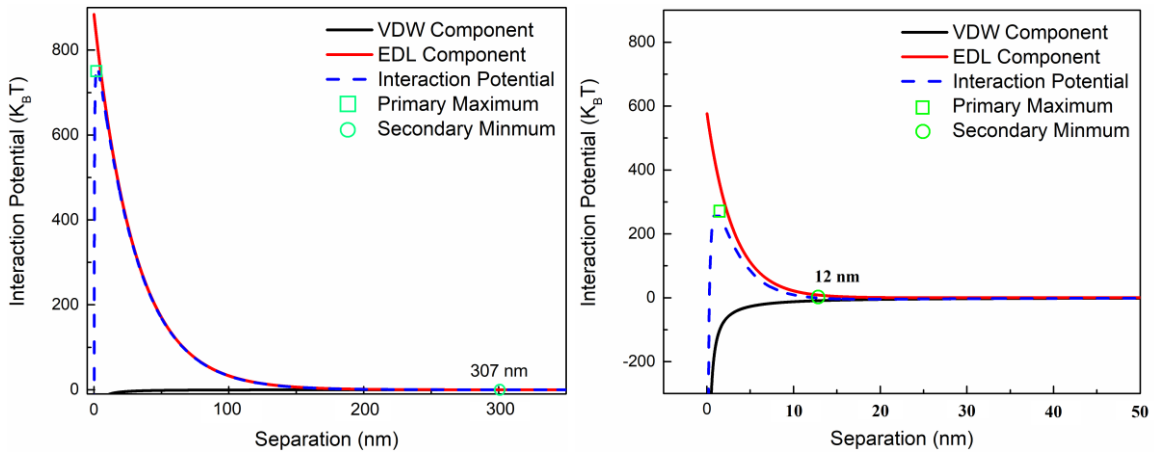

Figure 5-1 DLVO-computed interaction potential normalised by thermal energy for silica in 10^{-4} M KCl suspension(left) and 10^{-2} M KCl (right), using a Hamaker constant of 2.5×10^{-20} J for the 500 :800 nm silica-water-silica system.

When the position that suspension back to monodisperse such as heavier particles all settled and only lighter particles left, the viscosity model will back to the monodisperse one. The secondary minimum can be calculated to be the minimum separation distance of the bidisperse system. However, the DLVO theory is not very suitable for particles that are smaller than 800 nm in diameter. For particles small as 100 nm, the calculation of separation distance is several times larger than the diameter of particles in a very diluted salt solution (such as 10^{-4} M KCl). When small particles in a very dilute solution, the standard DLVO secondary separation distance might be several times larger than the particle size which is not physical for particle sediment bed. The minima separation distance both influences the viscosity model in the fluid and the sedimentation bed. With a very dilute salt concentration the separation distance is relatively large comparing with the particle size. The calculation is more physical when particles are in the bulk fluid and slightly changes the 'apparent' viscosity during settling. However, the sedimentation bed should be compressed, and particles are closer to each other than the minima separation distance situation especially with centrifugal forces. It is worth to notice that the simulation mainly focuses on the prediction and volume fraction change of the bulk fluid. In this study, the author used the calculated

secondary minima separation distance of 500:800 in the simulation, but for 100:500 cases we used double times of Debye length to replace the minima distance calculated from DLVO theory.

5.2.2 Centrifugal Force

The sedimentation model can be adapted for centrifugal force conditions. To do this, the gravity acceleration, *g*, in Eq. (5.6), is replaced by the centrifugal acceleration, The base of the sample is determined to be at a radial distance of 129.3 mm from the centre of rotation. The centrifugal acceleration, *a*, is given by Eq. (5.23):

$$a = (2\pi n)^2 r, \tag{5.23}$$

where *n* is the number of centrifuge revolutions per second and *r* is the radial position in the centrifuge (with $r = 0$ at the centre of rotation). To mimic the LUMiSizer® experiments, the distance, *r*, is varied according to the sediment front in the sample cell, as given by Eq. (5.24):

$$r = r_{\max} - x, \tag{5.24}$$

Here, r_{max} is the radial position (m) at the base of the sample (129.3 mm exactly) and *x* is the relative position of the settling interface, between 20 mm (at time zero) towards 1-2 mm (at time infinity) being the height of the consolidated sediment bed. As the particle sediment towards the end of the tube, the acceleration does slightly increase with the settling interface. It has been reported (Antonopoulou et al. 2018) that the centrifugal acceleration varies by about 19 % across the sample cell in LUMiSizer®. For this study, it ranged from 975 m/s^2 to 1195 m/s^2 (estimated from the change in *x* between the start and end of each experiment).

5.2.3 Numerical Implementation

The numerical model is implemented in MATLAB (version 2016a). A very fine spatial mesh is required near the front and in the sediment to accurately capture the solution behaviour and

prevent numerical instabilities (Thackham et al. 2009). The NAG Library has been chosen which includes a collection of general-propose subroutines in MATLAB (mark 25). The d03pp subroutine, a finite difference-based solver, is used that integrates a system of advection-diffusion equations with scope to use an adaptive spatial mesh, which is chosen to solve the initial boundary value problem. Time integration is then carried out using a backward differentiation formula, with a variable time step, determined automatically using a user-specified local error tolerance (Berzins and Furzeland 1992).

The subroutine generates a new spatial mesh every 10 time steps, based on the current solution profile $m(x,t)$ which can be calculated as Eq. (5.25). In the routine, the total volume fraction is chosen as the monitor. The monitor function must be large in the sedimentation and near the front. The monitor function $m(x,t)$ (Antonopoulou et al. 2018) is used to check when the adaptive mesh should be used.

$$m(x,t)=\begin{cases} K(x,t)^{0.9}, if\ \phi<1.01\phi_0 \\ \phi' \quad , \ otherwise \end{cases}, \tag{5.25}$$

Where $K(x, t)$ is the smooth function curvature estimator given by Eq. (5.26):

$$K(x,t)=\frac{|\phi''|}{(1+\phi'^2)^{\frac{3}{2}}}, \tag{5.26}$$

given and discretised by Sfakianakis (Sfakianakis 2009), where ϕ' denotes the first spatial derivative of ϕ. This monitor function used the first spatial derivative of ϕ in the sediment and the curvature numerical stability. A maximum adjacent cell ratio of 1.1 is set, allowing this monitor function to be used. Based on the maximum resolution of LUMiSizer® and considering the efficiency of simulation, 2000 spatial mesh points are considered sufficient for simulations in centrifugal forces conditions. The local tolerance is varied with a fixed spatial mesh to understand its effect on the solution. In this study, when it is between 1×10^{-3}

and $1 \times 10^{-6,}$ the results changed the solution by less than 0.1 %, suggesting that a choice of 1×10^{-4} would give an appropriate resolution for the model.

5.3 Materials

The colloidal silica particles used are Angstrom Sphere® silica powder, with nominal quoted mean sizes of 100, 500 and 800 nm (Fiber Optic Center Inc., USA). The particles were checked with SEM and LUMiSizer® previously to confirm the mean size is close to the manufacturer estimations and they are used in the modelling. The particle densities(ρ_p) are measured as 2.2 g/cm^3 for 100 nm silica particles and 1.92 g/cm^3 for 500 nm and 800 nm particles, using a Pycnomatic ATC gas pycnometer (Thermo Electron, USA). The density results are close to expectations for silica particles (Hyde et al. 2016). Suspensions were prepared by adding silica powder to a 1×10^{-4} M potassium chloride (KCl) background electrolyte solution, using KCl crystalline powder (Fluka Chemie GmbH, Germany) and ultrapure Milli-Q™ water, with the resistivity of 18.2MΩ cm at 298 K (Milli-Q, Millipore, USA). The suspensions were placed in an ultrasonic bath (XUBA3, Grant) for 15 mins prior to characterisation without heating. Then, samples were further dispersed using an ultrasonic probe, Sonic Dismembrator (Fisher Scientific), at 80% amplitude for 5 mins. The purpose of the ultrasonic bath and probe is to fully homogenise the suspensions before any measurements were taken. Bidisperse nanoparticle suspensions of 100 and 500 nm particles (labelled 100:500), as well as 500 and 800 nm particles (500:800) are prepared in various mixing ratios (on a volume basis) as shown in Table 5-1.

Table 5-1. Experimental conditions and sample components for bidisperse sedimentation experiments.

Components (nm: nm)	100:500	500:800
Mixing ratios	1:1	1:2, 1:1, 2:1

Rotation rate (rpm)	4000	1000
Total volume fraction range (Φ_0)	0.01 – 0.03	0.01 – 0.03

5.4 Earth Gravity Volume Fraction Profile

The sedimentation of bidisperse mixtures of 500 and 800 nm particles (500:800) with a total initial volume fraction, $\phi_0 = 0.02$, is simulated under earth gravity conditions for a 1:1 particle ratio. No earth gravity simulations of 100:500 nm systems are attempted due to the longer timescales involved. The volume fraction profile is displayed in Fig.5-2 after a time of 11 h, at which point the difference in interfacial position between the two species makes them both clearly visible.

It is noted that the individual species concentration is shown, rather than the total concentration. The volume fractions for both species are high in the sediment area (near $X/X_{max} = 0$), where they approached the effective maximum volume fractions. In the supernatant zone above the upper sediment interfaces, both volume fractions of components rapidly fall towards zero. In the suspension zones, the situation is more complicated than for monodisperse systems. The suspension consists of two zones: Suspension 1 (containing only 500 nm particles) and Suspension 2 (containing a mixture of 500:800 nm particles). In Suspension 1, the simulation actually used the monodisperse viscosity model, while in Suspension 2, the particle size interaction effect is considered by using the bidisperse mixture viscosity model, which led to a small effective viscosity change (noting also the total volume fraction in Suspension 2 is double Suspension 1, and so hindered settling effects are greater). Therefore, in fact, the volume fractions in the two suspension areas are slightly different due to the hindrance function changes from bidisperse to monodisperse, which also affected the settling rate. However, the volume fractions remained constant in each zone, as would be expected without high levels of polydispersity (Abeynaike et al. 2012, Bux et al. 2015). It

means when the concentrations are stable at each settling zones and only varied when one kind of particle left that zone. There is a clear zone interface between only small particles and the two mixtures.

The two mean interface positions (between Suspension 2 and 1, and between Suspension 1 and the supernatant) are also marked in Fig. 5-2 and are used to validate the model to experimental sedimentation fronts. The volume fraction values used to define the interfaces are half of the initial volume fractions of each species (ϕ_i = 0.005). The volume fraction profiles around the interfaces showed an S-shape curve under earth gravity, which is due to the diffusive effect of the particles' Brownian motion. This effect is most clear in Suspension 1, containing only the 500 nm particles, as would be expected from their smaller size.

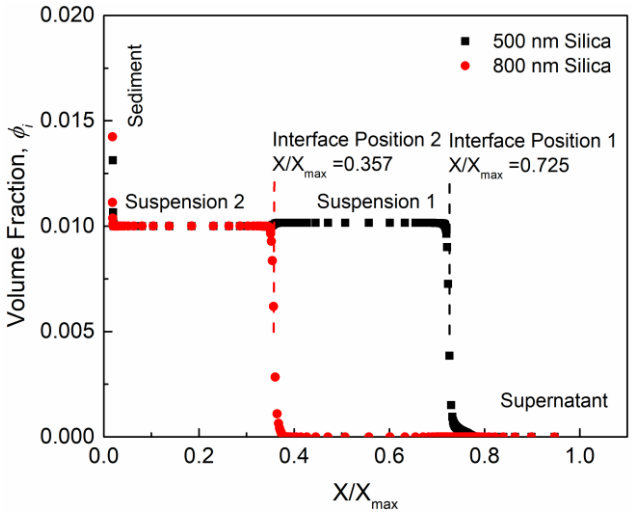

Figure 5-2 Simulation concentration profile for a 500 and 800 nm suspension mixture in 1:1 mixing ratio with ϕ_0 =0.02 under earth gravity conditions after 11h. The data are plotted at the spatial points where the solution is calculated according to the meshes.

5.5 Simulations under Centrifugal Conditions for Both Particle Size Ratios

Examples of the simulated volume fraction profiles of 500:800 nm centrifugal bidisperse sedimentation using the modified viscosity model are shown in Fig. 5-3. Three total volume fractions are displayed (ϕ_0 = 0.01, ϕ_0 = 0.02 and ϕ_0 = 0.03) with suspensions subject to a centrifugal force consistent with a rotation rate of 1000 rpm (allowing direct validation of the

front settling rates to experimental data from the LUMiSizer®) with a spatially varying range of centrifugal acceleration from 121.8 g at the upper meniscus to 145.3 g at the base. A mixing ratio of 1:2 (500:800) is chosen for the example, as the distinction between the size fractions is clear. Results for other size ratios (2:1 and 1:1) are shown within Appendix for the same total volume fractions. The reason that ϕ_0 = 0.03 is chosen as the highest total volume fraction simulated, is due to the experimental limitations of the LUMiSizer® in measuring bidisperse systems at greater concentration, as discussed in a previous experiment study. In terms of the model, it would be able to simulate any concentration below the effective maximum packing fraction.

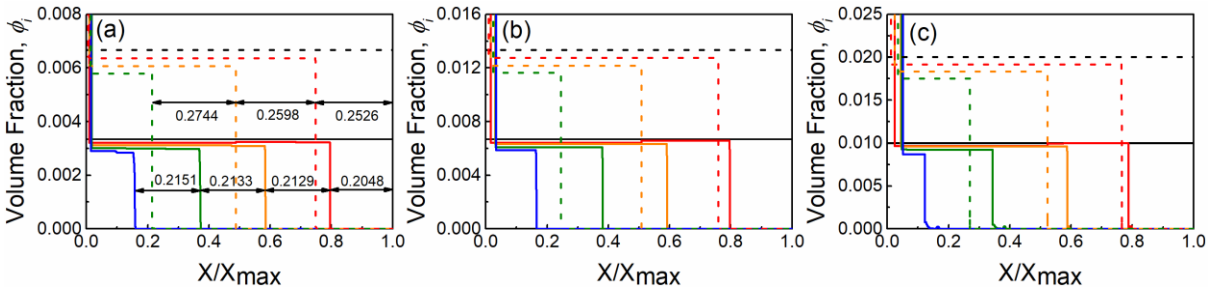

Figure 5-3 Simulated concentration profiles of 500 nm and 800 nm particles under 1000 rpm over time, at a mixing ratio 1:2, and total initial volume fractions of (a) ϕ_0 = 0.01, (b) ϕ_0 = 0.02, (c) ϕ_0 = 0.03. Profile shown are for the 500 nm fraction at times of 0 s (black dashed line), 120 s (red dashed line), 240 s (gold dashed line) and 360 s (green dashed line) for all concentrations.

It is first observed that, unlike under earth gravity conditions, there is a distinct concentration decreased with time for both particle species (which is most notable for the larger 800 nm particles). In Fig. 5-3 (a), for large particles, the concentration decreased ~13.2 % (from 0.00667 to 0.00579 in 360 s) while for smaller 500 nm species particles, the decrease is ~12.9 % (from 0.00333 to 0.0029 in 960 s). These decreases are similar to previous simulations of centrifugal sedimentation of 500 nm monodisperse particles (Antonopoulou et al. 2018). Due to the radially varying acceleration in the set-up, particles in suspension closer to the sediment bed have a higher sedimentation velocity than those above. As a result, particles are evacuated into the sediment bed faster rate than they are replaced from above,

which results in a decreasing volume fraction across the suspension. As the height of the sediment bed increases in time, the centrifugal acceleration at the top of the bed less efficiently as time goes on, so the rate of decrease of the volume fraction of the suspension slightly decreases in time.

The relative increase in gravitational acceleration over time also results in an acceleration of the separation velocity, which can be seen from Fig. 5-3 (a) by the spatial distance between each profile front increasing in time (again considered at a relative concentration of each component of $0.5 \times \phi_{0,i}$). The arrows in Fig. 5-3 (a) illustrate the distances between profiles, which are seen to increase over time under centrifugal acceleration. It is also noted that the centrifugal acceleration minimises secondary particle movement due to Brownian diffusion, resulting in an almost completely vertical concentration change at the suspension interfaces (no characteristic S-type curve, as evidenced under earth gravity conditions).

Mixtures of 100 and 500 nm particles (100:500) are also investigated, as shown in Fig. 5-4, are concentration profiles for a particle volume ratio of 2:1, and total volume fraction ϕ_0 = 0.03, under centrifugation of 4000 rpm. Similar data for mixing rations of 1:1 is presented within the Appendix (Fig. A7). Previous experimental studies of the same systems indicated at high centrifugal speeds of >3000 rpm are required to represent data with low noise levels, due to the additional Brownian motion of the smaller 100 nm particles. One of the resulting limitations of such high centrifuge speeds is the large disparity in the time scale of the two species, due to the larger size ratio. Indeed, here the larger 500 nm particles in suspension settled within just 77 s, with the smaller 100 nm particles settling in a similar time to the smaller particles in the 500:800 simulations (<1000 s).

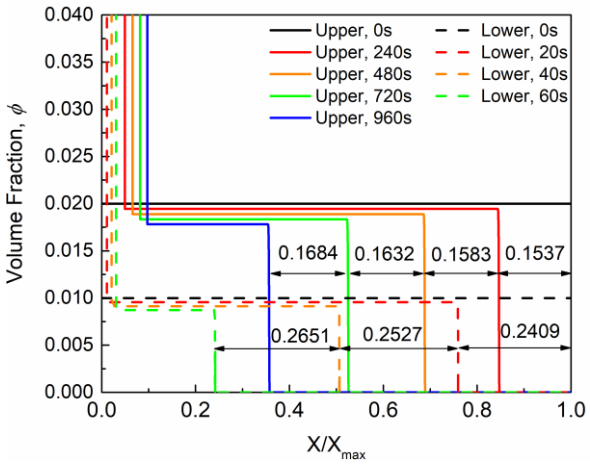

Figure 5-4 Simulated concentration profiles of 100 nm (small) and 500 nm (large) particles under 4000 rpm, at a mixing ratio of 2:1 (100:500) and total initial volume fraction, ϕ_0 = 0.03.

Concentration decreases of both species over time are also observed in Fig. 5-4, which is a similar trend to the 500:800 nm case. In Fig. 5-4, for the small (100 nm) particles, the concentration decreased by ~10.9% (in 960 s) while the larger (500 nm) particle concentration decreased ~12.7% (in 60 s). Again, the reduced concentrations also correlated to an increase in the sedimentation rate over time (with distance differences for each timestep again shown within the arrow). Also, as with the 500:800 nm case under centrifuge, the influence of particle Brownian motion on diffusion at zonal interfaces is minimal. It is noted that the calculated Peclet number for the 100 nm under 4000 rpm is 0.164, which means the Brownian motion dominate the simulation, but the centrifugal force also have important effect.

5.6 Front Height versus Time Validation

In Fig.5-5, experimental and model interface height profiles under earth gravity are compared for a suspension of initial total volume fraction ϕ_0 = 0.02 and a mixing ratio = 1:1. The experimental data is collected from Turbiscan®, using the backscatter sensor. The model data is obtained in the appropriate conditions under the same earth gravity. Here, the 'Lower' interface represents the distinction between the lower zone containing a mixture of 500 and

800 nm particles, and the upper zone containing only 500 nm particles. The 'Upper' interface is the distinction between the 500 nm suspension and the particle-free supernatant. While each particle type can be tracked independently in the simulation, it is assumed experimentally that the lower observable interface also tracks the sedimentation rate of the larger 800 nm particles.

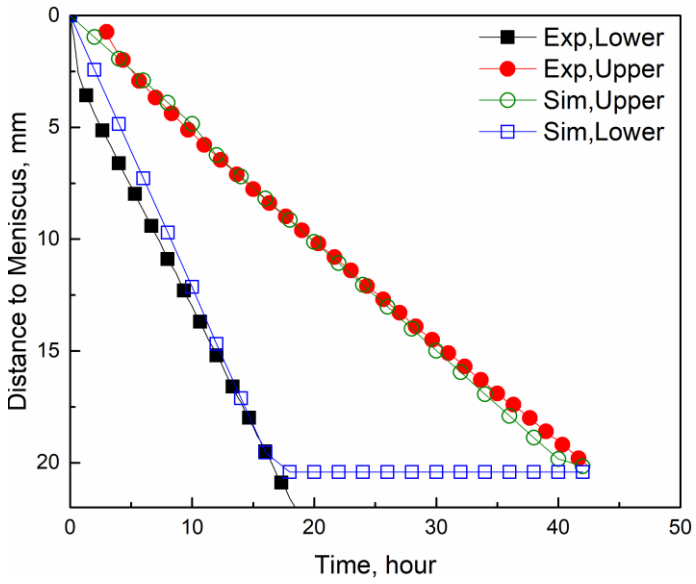

Figure 5-5 Comparison between simulated and experimental interface front height versus time profiles of 500:800 nm mixtures under earth gravity, at a mixing ratio of 1:1 and a total volume fraction, ϕ_0 = 0.02. Shown is both the 'Upper' interface (representing the 800 nm fraction).

Comparisons between the experimental and simulation data sets are very close, inferring, experimentally, the technique is able to track both particle species accurately, and, most importantly, the underlying physics are correctly captured in the model. However, there are some small deviations on the height vs. time profiles. The settling velocity deviation percentage between experiment and the model was 4.4% for the smaller (500 nm) species, and 12.4% for larger (800 nm) species, with an overprediction in the separation rate by the model in both cases. The fact that the simulation overpredicts the settling rates is interesting, as it indicates that the mixture viscosity model may be underrepresenting hindered settling effects, to some degree.

Nonetheless, some of the deviations found with the larger species may be due to experimental uncertainty and limitation. In particular, at the early time periods, it is found that the experimental data does not extrapolate linearly from a zero-bed height for the 800 nm front (which can be observed in Fig. 5-5). This small deviation infers either some error in the experimental measured (due to a lack of clear distinction of interface fronts from the backscatter signal at early time periods) or other effects, such as sample mixing, may have affected separation at early time periods. The small deviation may have also been caused by setup differences in the simulation. The height of the cell in the simulation is actually smaller than the experimental, due to the computational cost (with a 2 cm total height being used for the simulation, against the experimental sample cell of 4 cm). Despite these differences, the correlation is close enough to give good confidence in the model, where front height validation is then extended to the centrifugal cases.

Fig.5-6 presents the comparison of experimental and simulated front height versus time data for the 500:800 bidisperse suspensions, at a mixing ratio of 1:2, under a 1000 rpm centrifuge speed at three total volume fractions (ϕ_0 = 0.01-0.03). Comparison data for mixing ratios of 1:1 and 2:1, for the same three volume fractions, are given in the Appendix (Figs. A12, A13). There is a slight difference in the suspension height between the experiments and simulations, due to different initialisations required to reduce the computational time (where, experimentally total effective heights are about 21 mm, while they are 20 mm for calculation convenience in the simulations). Here, the normalised height is displayed, as calculated from the ratio of interface position and to the total cell height. Thus, simulation results can be converted to the same cell size as the experimental one.

Generally, the simulation results matched well with experiments, but there are again deviations, with the model over predicting both interfaces (and so consistent with the gravitational results for the same system). Interestingly in this case, unlike in the gravitational

system, the differences between the simulation and experimental data are similar for both larger and smaller particle interfaces, averaging at ~8-12% overprediction in all cases for the simulations, with no defined function of concentration evident on the error. It is noted that the experimental data for the lower (800 nm) interface is difficult to resolve at the highest volume fraction case, with a high degree of uncertainty, due to the difficulty of resolving the lower and upper zone in cases of low transmission. This problem also led to difficulties resolving the lower interface near the base of the same in the other cases. Indeed, for the 1:1 and 2:1 particle mixture, with a larger proportion of smaller particles in the upper zone, it is not possible to extract lower interface data at all for the higher concentrations (Appendix, Fig. A12-13).

Despite these experimental limitations, the centrifugal data does suggest a similar level of accuracy for the monodisperse and bidisperse mixture viscosity models, and additional error evident in the gravitation case for the larger particle interface may be therefore due more to experimental uncertainty. Also, if one considers the relative error of the upper interface, it appears the effect of centrifugation may be to accentuate any limitations in the model accurately describing the underlying physics (with error increasing from ~4% to ~10% on average). Essentially, it appears the experimental data displays a slightly higher level of hindrance in settling than the mixture viscosity models predict. The reason for the discrepancy may be from a number of sources. It may be, simply, that the minimum interparticle distance due to the electric double layer is in fact greater than the calculated value (leading to a lower maximum effective volume fraction and increased relative hindrance effects). Alternatively, it may be from more dynamic effects that are not currently incorporated into the model. In particular, previous studies on bidisperse colloidal sedimentation have observed effects, such as dispersion anisotropy caused by particle wakes, or backflows, that enhance drag from the larger particle fraction, as it settles through the

smaller particle zone (Ambari et al. 1998, Yaghoobi and Torabi 2012, Howard et al. 2018). It does also seem that the mixture fraction influences the degree of error as well, where the differences between the experimental and simulated upper interface increase with the increasing proportion of smaller particles in particular (when one observes Fig. 5-6 in comparison to Figs. A12-13).

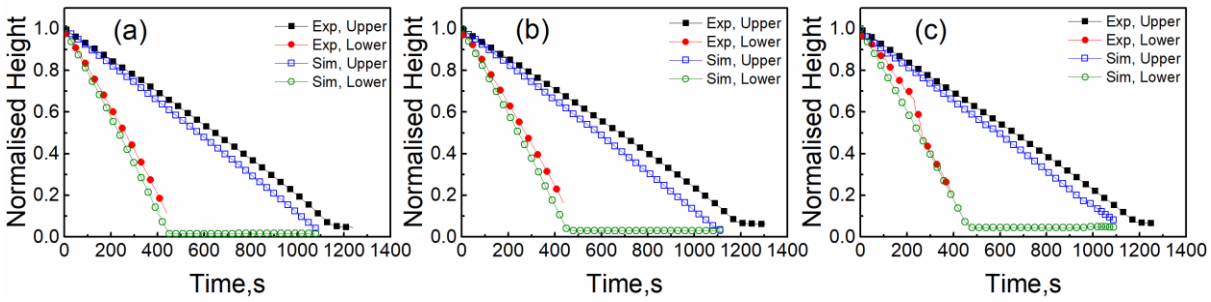

Figure 5-6 Comparison between simulated and experimental interface front height versus time profiles of 500:800 nm mixtures under 1000 rpm and a mixing ratio of 1:2. (a) ϕ_0 = 0.01, (b) ϕ_0 = 0.02, (c) ϕ_0 = 0.03. Again, the 'Upper' interface and 'Lower' interfaces represent the 500 and 800 nm fractions, respectively.

An example comparison of experimental data and simulation results for the 100:500 nm dispersion is shown in Fig. 5-7, for a mixing ratio of 2:1 and a total volume fraction, ϕ_0 = 0.03. Data for mixture ratios of 1:1 at total volume fractions of 0.01-0.03 are presented in the Appendix (Fig. A14). It is obvious that the 500 nm particles settle much faster than in the 500:800 case, due to the larger centrifugal speed of 4000 rpm, which is required for the 100 nm particles to settle completely. This higher centrifugation, as well as the greater size ratio, meant that there is quite a restricted time where both particle fractions are in the suspension together, unlike the 500:800 systems, which is thought to potentially reduce the bidisperse interactions. Additionally, there is a lack of resolution in the upper 100 nm interface for some systems, where due to their smaller size, there is evidence of adhesion to the meniscus (where it is known attraction forces can pull particles together (Wi et al. 2011) as well as the cell walls. Collectively this led to some small jumps in the interface data for the upper 100 nm

interface (e.g., Fig. A14 (a)). However, for most systems, meaningful interface velocities could still be extracted.

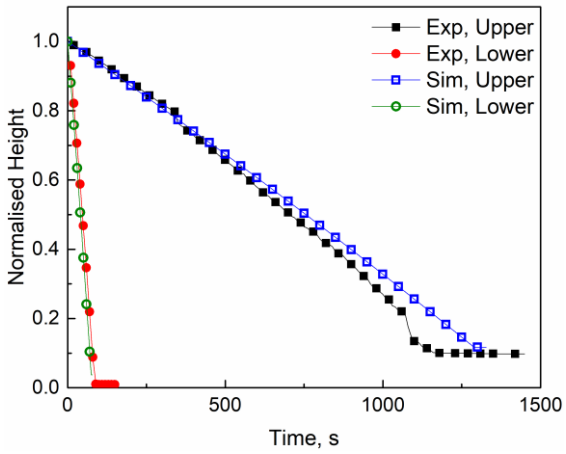

Figure 5-7 Comparison between simulated and experimental interface front height versus time profiles of 100:500 nm mixtures under 4000 rpm and a mixing ratio of 2:1 and total volume fraction, ϕ_0 = 0.03. Here, the 'Lower' and 'Upper' interfaces represent the 500 nm and 100 nm fractions, respectively.

There are two stages of sedimentation for 100:500 cases. First, both species existed on the suspension, then second, 500 nm settled quickly and only 100 nm are left on the suspension and continue its sedimentation. For 100 nm particles, it means there are two sedimentation velocities before and after 500 nm particles settled. The settling velocity of the first stage is labelled with subscript 1 and the second stage is labelled as 2 in Table 5-2.

Table 5-2. Simulation settling velocities of two species in mixing ratio = 2:1, under 4000 rpm, ϕ_0 = 0.03. Subscript '1' refers to case where both species present, and '2' refers to where there are only 100 nm within the dispersions.

Species	$u_{1,\,exp}$ (μm/s)	$u_{1,\,sim}$ (μm/s)	$u_{2,\,exp}$ (μm/s)	$u_{2,\,sim}$ (μm/s)
100 nm	10.681	13.329	15.869	14.194
500 nm	267.654	268.637	N/A	N/A

In comparison between the simulation and experiments, the deviation from the averaged linear settling rate for the larger 500 nm particles is only 0.37%, while for the small 100 nm particles settling together with the 500 nm fraction the deviation is a larger 24.9% reducing to 10.5% for the section where the 100 nm species settles alone. However, it must be noted that

experimentally this equated to only the first few data points, and so there is a relatively large degree of error associated with the experimental data for the initial mixed period. Interestingly, the simulated velocity of 100 nm increased after 500 nm the settled, which is the same as experimental data but in a lower level. In the simulation, the velocity change is caused by the effective viscosity decreasing due the lack of the 500 nm component, as well as the increase in the centrifugal force as the settling front progresses. It may be that the deviations between velocities for the 100 nm particles are because the double layer may be under-represented for these small particles, and so the effective volume fraction may be slightly larger than simulated. Interestingly also, the simulation does not over predict the settling rate of the smaller species, as in the case of the 500:800. This result may further indicate that additional hydrodynamic interactions between the species in the 500:800 mixtures may be the reason for enhanced hindered settling, as the greater size ratio for the 100:500 systems means that the species only interact together for a very small period of time.

5.7 Simulation Results Comparison

5.7.1 Mixture of 500: 800

The bidisperse settling velocities of the 500:800 case have been plotted in Fig.5-8. Three initial volume fractions ranging from 0.01 to 0.03 are shown. Part of the experimental data of large species is not shown due to the limitation of LUMiSizer®, but small species are all well performed. From the comparison between experiment, simulation, and R-Z prediction (Richardson and Zaki 1954), we can see that the simulation data generally match well with experiments. There are deviations between the 3 results, especially for large particles. For large particles, in 3 mixing ratios among all volume fractions, the largest deviation between experimental results and simulation results is 6.61 % overpredicted shown in Fig.5-8 (a), ϕ_0 = 0.02, and the smallest one is 1.24 % underpredicted shown in Fig.5-8 (b), ϕ_0 = 0.02. In the case of small particles, deviations are much smaller than large particles and very close to the

R-Z results. The largest deviation between experimental results and simulation results is 10.00 % overpredicted which shows in Fig.5-8 (c), ϕ_0 = 0.03, and the smallest one is 1.8 % overpredicted which shows in Fig.5-8 (a), ϕ_0 = 0.03. Although large particle results showed larger absolute errors, the relative errors are very close to the small ones.

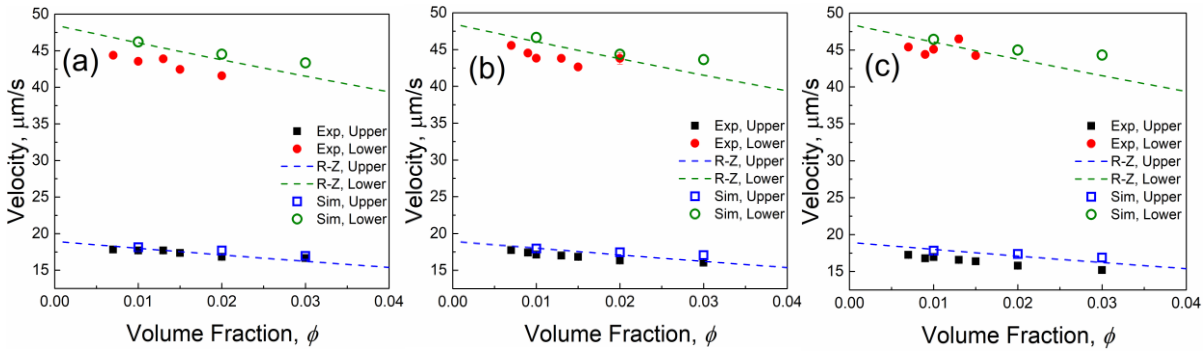

Figure 5-8 Bidisperse separation velocities for different initial volume fraction, 500 nm (small) and 800 nm (large) particles under 1000 rpm. Experimental data and Richardson-Zaki [3] results are provided and compared at different volume fractions using 1-D bidisperse model. (a) Mixing ratio =1:2, (b) Mixing ratio =1:1, (c) Mixing ratio = 2:1.

The small overprediction may case by the slight difference in real meniscus height which lead to centrifugal force differences or the wide size distribution which means the particles are not truly monodisperse exactly at the same size but with a distribution. The centrifugal force is more sensitive for large particles and causes a larger absolute error, but the relative errors are almost the same level for both species.

5.7.2 Mixture of 100:500

The bidisperse settling velocities of 100:500 cases are plotted in Fig.5-9. Mixing ratio = 1:1 is used as an example to compare with experimental data and the classical empirical model (R-Z). It is shown that velocities of both species are close to the experiment data and around the R-Z model predictions.

The biggest deviation for large particles is shown at ϕ_0 = 0.03 with 7.85 % overprediction and for the small particles that is 12.83% overprediction shown at ϕ_0 = 0.01. The deviation may

cause by the hydrodynamic effect which is not considered in the simulation and the 'meniscus effect' close to the interface. The experiment data of 100 nm at low concentration also experienced an oscillation for the whole transmission profile which led to the settling interface becoming hard to track and affecting the observed settling velocities.

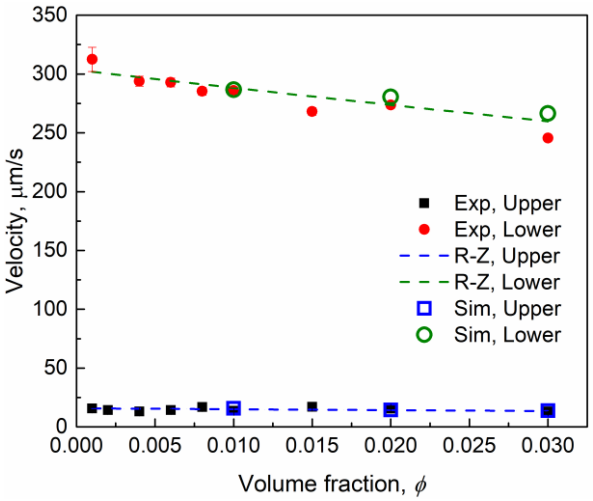

Figure 5-9 Bidisperse separation velocities for different initial volume fractions, 100 nm (small) and 500 nm (large) particles. Experimental data and Richardson-Zaki [3] results are provided and compared at different volume fractions using the 1-D bidisperse model. Mixing ratio=1:1.

5.8 Conclusions

In this study, a 1-D sedimentation model for bidisperse, colloidal suspensions is proposed, which uses a bidisperse mixture viscosity model to consider the effect of hindered settling and particle interactions. The model also modifies the hard sphere assumption by using an effective maximum volume fraction on bidisperse suspension, which is computed based on DLVO theory.

The proposed model compared to experimental data, and the empirical Richardson-Zaki model, using two different size ratios (of 500:800 nm and 100:500 nm particles) at different mixing ratios and total concentrations. Results highlightes that interparticle interaction is an important aspect in determining the sedimentation velocities of colloidal suspensions, especially for bidisperse systems. The inclusion of a minimum interparticle distance is a

significant addition to sedimentation models and will be especially applicable at high volume fractions. The use of an adaptive spatial mesh in a finite difference solver is also shown to be an efficient way to numerically implement the sedimentation model and reduce computation cost, allowing the simulation to be numerically stable.

The proposed model is validated under both earth gravity and various centrifugal force conditions. It is found that the predicted volume fraction of both species' components reduced in time under centrifuge (due to the increase in force at the bottom of the simulated dispersion cell) whereas they remains almost constant at earth gravity, as concentrations are not great enough to force physical interaction between the size classes. The bidisperse simulation model is also used to track the suspension interfaces of each size fraction, and therefore gain an average estimated settling rate. For the 500:800 nm mixture cases, deviations in average settling rates between simulations and experimental data was <10% in all cases. However, there is a clear trend of the simulation slightly over predicting settling rates of the particle phase with the lowest mixture fraction.

These results suggest that hindrance effects in bidisperse systems is higher than the mixture viscosity model prediction, and maybe due to secondary hydrodynamic factors that are not explicitly accounted for. Settling rate validation for the 100:500 nm is generally closer than in 500:800 cases, which may be due to the centrifugal force being larger and the interaction time between the species was smaller, meaning the sedimentation better described by the viscosity model. The proposed model is shown to fit the bidisperse experimental data well and showed good agreement compared with the classical theory (R-Z). However, it provides more detail and uses more physical methodologies to analyse and simulate the results which also tracks the concentration changes. The model could also be extended to a true polydisperse system, with appropriate modification the viscosity mode, and therefore used to predict the

concentration changes and settling rates of many systems undergoing centrifugal sedimentation and separation.

6. Characterising Colloidal Adsorption Rate & Network Structure at Air-Water Interfaces

6.1 Introduction

Interfacial tension is a phenomenon that, at the molecular level, results from the difference in energy between molecules at a fluid interface when compared to their bulk counterparts(Berry et al. 2015). All of the molecules of a liquid attract each other. These interactions of molecules in the bulk of a liquid are balanced so that equal forces attract them in all directions. The excess energy presents at the surface is called surface free energy and can be quantified as a measurement of energy/area (Jones 1974). Behave like surfactant, small solid particles can also absorb at liquid interfaces and change the apparent surface tension (Manga et al. 2016). The adsorption process is regarded as an irreversible process and is influenced by the particle radius and wettability (Binks and Lumsdon 2000, Binks 2002). It is reported that nanoparticle adsorption at liquid interfaces is thermodynamically favoured, but the process can be kinematically limited, a situation arises when a significant energy barrier to adsorption (Xu et al. 2009). Particle adsorption networking is important when the adsorption interface is crowded, the collapse behaviour of nanoparticles with different wettability can be investigated using the Langmuir-Blodgett trough.

The Langmuir and Langmuir-Blodgett (LB) (Schwartz 1997) devices are efficient and effective in investigating floating monolayers, precise deposition of multilayers onto solid substrates or simply as platforms for use in observing surface chemistry effects such as the breakdown of an enzyme or the crystalline structure of a surfactant (Oliveira Jr et al. 2022). An extension of the Langmuir trough has been to spread a variety of particles at the air/water interface and to investigate the surface pressure (Π) – area (A) relationships as the particles are compressed (Chen 2001, Tsai et al. 2006, Kohoutek et al. 2020). Particles are insoluble in

water and can be easily spread on a water surface to form monolayers at the air/water interface. Monolayers formed at the plate liquid interface are also called Langmuir-Blodgett films (Schwartz 1997), which represent the extreme case when considering adsorption to interfaces because all molecules are concentrated in a one-molecule thick layer at the interface.

To measure the particle adsorption rate and the adsorption kinetic of colloidal particles, dynamic surface tension can be used to probe quantitatively the dynamics of nanoparticle adsorption, provided that a suitable model exists to connect dynamic surface tension to transient coverage of the interface by nanoparticles (Bizmark et al. 2014). For many surface tension measurement methods, the pendant drop tensimeter is very suitable for long time measurement (Oliveira Jr et al. 2022). Pendant drop tensiometer is arguably the simplest, most robust, and most versatile of the surface tension measurement method (Tabor et al. 2015), where the measurement consists simply of a fluid droplet suspended from a needle. The ability to determine the interfacial tension from the shape of a pendant liquid drop deformed by gravity was first proposed over a century ago by Worthington. Using an appropriate scaling and axisymmetric Young-Laplace equation, and drop character parameters, the relationship between the shape of the drop and interfacial tension can be formed (Bashforth and Adams 1883). The asymptotic results (Fainerman et al. 1994) can be employed to interpret data from the early (short-time, $t \to 0$) and late (long-time, $t \to \infty$) stages of nanoparticle adsorption as follows:

$$t \to 0: \quad \gamma = \gamma_0 - 2RTC_0\sqrt{\frac{Dt}{\pi}} \tag{6.1}$$

$$t \to \infty: \quad \gamma = \gamma_\infty + \frac{RT\Gamma_\infty^2}{C_0}\sqrt{\frac{\pi}{4Dt}} \tag{6.2}$$

Where R is the gas constant, T is the temperature, C_0 is the molar bulk concentration, Γ_∞ is the molar surface concentration at the steady state, and D is the nanoparticle diffusion coefficient.

In this thesis, to investigate the particle adsorption networking and the particle adsorption process influenced by the particle wettability, Langmuir- Blodgett trough and pendant drop tensiometer are used to record the particle adsorption data and then analysed with suitable models.

6.2 Methodology

6.2.1 Materials

Silica particles are a very common material in the industry and have a stable chemical property. 800 nm silica is a relatively large particle size for colloidal particles but still can be well suspended and easier to simulate in the later Chapter 7. 800 nm silica particles are relatively large colloidal particles which is easy to be influenced by the gravity and more likely to generate surface deformation at the liquid interfaces. Also, it costs less computation resource in the simulation. In this chapter, the esterified 800 nm spherical silica particles prepared as described in Chapter 3 are used. The particle characters were measured in Chapter 3 and marked as SiO-butane and SiO-hexane with static contact angles 46.6º and 68.5º, respectively.

Different concentrations of MIBC (pure water and 0.01M to 0.05M) are used as subphase in the Langmuir-Blodgett trough and the pendant drop tensiometer measurements. MIBC is often added in forth floatation systems, where it is not thought to physically absorb on most particle systems. Furthermore, it can reduce the surface tension slightly and can be used to investigate what occurs with the mixed particle-MIBC systems on the overall surface tension, as a potential route to directly measuring particle adsorption.

6.2.2 Langmuir Trough

In the study, A KSV NIMA Langmuir trough (Biolin Scientific, Germany) and software are used to measure the surface pressure changes upon rearrangement of adsorbed nanoparticles. The trough contained a centrally mounted spring microbalance, connected with a small filter paper pressure sensor (or 'Whilhelmy plate'(Barnes and Gentle 2005)) positioned to touch the subphase interface. After leaving the plate to become saturated with the water, the resultant relative pressure (Π) as measured via a controller connected to a personal computer is zeroed. The surface pressure, Π, and the surface pressure is measured by the Whilhelmy plate method (Barnes and Gentle 2005). The schematic of the principle is shown in Fig.6-1. With Langmuir troughs, the surface pressure and the mean molecular area are continuously monitored during the compression (expansion). The means molecular area can be determined by monitoring the distance the barriers have moved and with the known dimensions of the trough. In this method, a measurement is made by determining the force due to surface tension on a plate suspended so that it is partially immersed in the subphase. The force is then converted into surface tension (mN/m) with the help of the dimensions of the plate.

The trough contains two baffles on either side of the pressure sensor, originally positioned to give an internal area of 1000 cm^2, but in the experiment, the maximum area is set at about 500 cm^2. The baffles are moved towards each other at the same time with cm^2/min moving velocity (to give a minimum separation area of 100 cm^2) and increase in surface pressure.

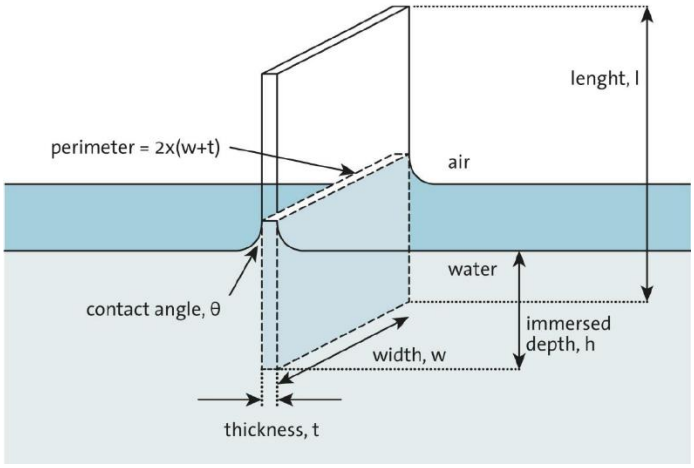

Figure 6-1 A Wilhelmy plate partially immersed in a water surface inspired by (Karim and Kavehpour 2018).

The plate is often very thin and made of platinum, but even plates made of glass, quartz, mica and filter paper can be used. In this study, the author uses filter paper. The forces acting on the plate consist of the gravity and surface tension downward, and buoyancy due to displaced water upward. For a rectangular plate of dimensions l_p, w_p and t_p, of material density ρ_p, immersed to a depth h_l in a liquid of density ρ_l, the net downward force is given by the following Eq. (6.3):

$$F = \rho_p g l_p w_p t_p + 2\gamma t_p w_p \cos\theta - \rho_l g t_l w_l h_l \tag{6.3}$$

Where γ is the liquid surface tension, θ is the contact angle of the liquid on the solid plate and g is the gravitational constant. The surface pressure is then determined by measuring the change in F for a stationary plate between a clean surface and the same surface with a monolayer present. If the plate is completely wetted by the fluid the surface pressure, then the surface pressure obtained from the following Eq. (6.4):

$$\Pi = -\Delta\gamma = -[\Delta F / 2(t_p + w_p)] = -\Delta F / 2w_p, if \quad w_p \gg t_p \tag{6.4}$$

Pendant drop surface measurement is a traditional and robust surface tension measurement. A pendant drop at equilibrium obeys the Young-Laplace equation, shown in Eq. (6.5), which

relates the Laplace pressure across an interface with the curvature of the interface and the interfacial tension γ:

$$\gamma(\frac{1}{R_1}+\frac{1}{R_2}) = \Delta P \equiv \Delta P_0 - \Delta\rho g z \tag{6.5}$$

Where R_1 and R_2 are the principal radii of curvature; $\Delta P \equiv P_{in} - P_{out}$ is the Laplace pressure across the interface; $\Delta\rho = \rho_d - \rho$ is the density difference; and ρ_d and ρ are the drop phase density and continuous phase density respectively. When particles are compressed and touched with each other, theoretically, there is a hexagonal close packed (HCP) area for specific volume V_s of suspension with a known particle volume concentration x_v and can be calculated is well described in John and Spencer's work (Clint and Taylor 1992).

Before every measurement, the 150 mL KSV NIMA Langmuir-Blodgett trough was tested with deionized water from a MilliQ® system (Millipore Ltd., 18.2MΩ cm) as a standard with no more than 2 mN/m oscillation. Then it is filled with different concentrations of MIBC subphases (pure water and 0.01M to 0.05M). Calibration and pure water tests are measured before any surface pressure measurement to make sure the setups are correct and there is no contamination in the trough. The schematic of the Langmuir trough is shown in Fig.6-2.

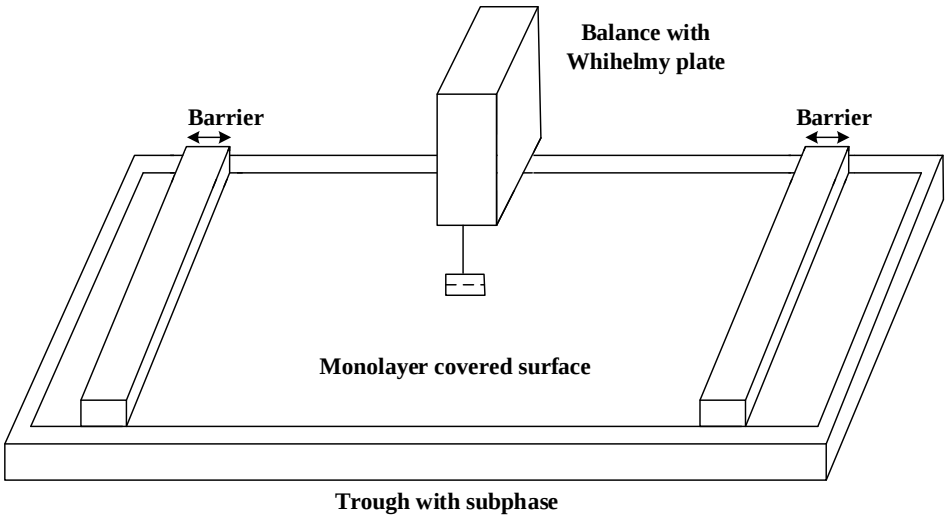

Figure 6-2 Schematic of Langmuir trough.

The trough is filled with the aqueous phase of volume 70 mL (thickness 5 mm). Several drops of nano-particle suspensions are placed on the water surface between the barriers of the trough. The surface area between the barriers varies from 600 to 400 cm^2 and vice versa in a cycle of monolayer compression (or expansion), which takes 600 s at a constant surface rate of 5 cm^2/min. Between the compression and expansion, the author waited for 60 s to allow relaxation of the monolayer. After that, the particle suspension should diffuse on the interface and form a monolayer of particles and a stable constant value of Π is established.

To deposit particle monolayers onto the water surface, the dried particles are first dispersed in an acetone solvent (99%). 10 wt.% particle dispersions are made in solvent using the horn sonicator for dispersion (on a moderate settling for 10 min, waiting for cooling and keeping weight, then, using bath sonicator for 5 min when using).

The way that acetone is used in this study as the initial solvent experiment to transport an amphiphile to the surface using a micro syringe (Hamilton 100 μL) to deposit it onto the surface. Dispersions are added in a drop-wise fashion, by gently touching droplets formed at the end of the syringe needle onto the surface. Nanoparticles are well dispersed in acetone first and dropped on the subphase interface with a constant distance of each drop. The method

is shown in Fig.6-3. Drops can be easily spread on the surface to form an insoluble monolayer. After 3 mins the dispersion solvent had evaporated, a good monolayer is formed, and the surface measurement would be started.

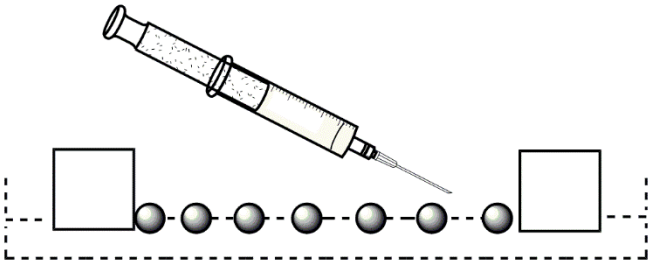

Figure 6-3 Schematic of particles deposited onto a Langmuir-Blodgett trough.

To further investigate the difference between HCP and experiment results, an Hitachi TM3030 Plus SEM (Hitachi High-Tech, USA) is used to observe the monolayer captured from Langmuir trough under low and high surface pressures. Particles are taken from the Langmuir trough interface under different surface pressure using the same suspension sample for comparison. Then, the samples are placed in the drying oven for 10 mins and finally put into the SEM.

6.2.3 Pendant Drop Tensimeter

A KSV Tensiometer CAM 200 (KSV INSTRUMENTS LTD. Finland) is used to measure the surface tension of the droplet. The surface tension vs time data is measured with the curve of the droplet profile and the recorded time. The close cuvette fills with 10 mL solvent at the bottom and 3 mL solvent in a big syringe. A drop is prepared and suspended on the needle of a big syringe, then, waited for 20 mins to make sure the environment is saturated and the drop on the needle does not change. The pendant droplet then injected with a minimum volume mostly around 8.5 to 9 μL, but for some relative low surface tension suspensions (high MIBC concentrations), the volume of the droplet can be smaller because the needle cannot hold the drop. Particles with different hydrophilicity (Origin SiO_2, SiO-butane, and SiO-hexane) are

used to make suspensions with 0.03M MIBC and loaded into the syringes as materials. The surface tension of 0.03M MIBC is measured as 48.5 mN/m with a good agreement with other researchers' work (Peng et al. 2021) which is close to 50 mN/m.

The pendant drop tensiometer without a cuvette is not very suitable for long time measurement in the air or open environment (Javadi et al. 2010, Winkelmann et al. 2012) because of evaporation. A number of interfacial studies have been previously performed by various authors, which discussed different effects of evaporation, such as the investigation by Fainerman et al.(Fainerman et al. 2007). Unexpected changes in surface tension are observed when measured with the drop profile method, which is explained by the evaporation effect of the surfactant from the surface of the aqueous solution drops. There is an improvement in the method to eliminate the effect of evaporation with a close cuvette and moisture environment (Winkelmann et al. 2012) which has been proved.

Fig.6-4. shows surface tension of a pure water droplet against the air in a close cuvette (not completely sealed) with 10 mL total volume in which 1 mL water is injected with a bigger syringe to provide an evaporation environment. At the start of the experiment, a test drop of water or MIBC solution (marked as drop 2) is prepared and suspended on the big needle. It needs a few minutes for establishing a saturated atmosphere. The experiment should be started after the test droplet stable state with no obvious change in the volume. Then, the measuring drop (marked as drop 1) is injected which started the formal measurement.

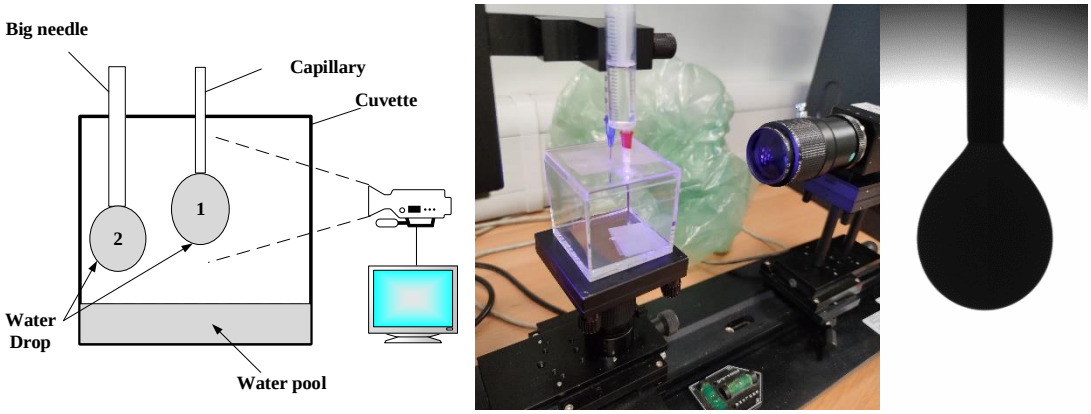

Figure 6-4 Schematic of pendant drop surface tension measurement with cuvette (left), real device and a drop profile (right).

6.3 Results and Analysis

6.3.1 Langmuir Trough

An example of a typical Π-A isotherm generated from compression of the SiO-butane monolayer is given in Fig.6-5. Measurements were repeated no less than 3 times for each coating. The SiO-butane particles are a good example to show the pressure-area isotherms because it clearly shows the layer formation point and collapse point and their relation to particle network formation shown in Fig.6-5. The original 800 nm SiO_2 does not form a monolayer on the subphase in this study (used 5 times larger volume than SiO-butane but still no visible monolayer and no surface pressure change in the device), thus, they are not shown in the results. It maybe the contact angle of original particles is quite small and when the particle spreads and, in the process, forms a monolayer, most particles are immersed under the liquid interface and cannot hold themselves with a narrow contact line.

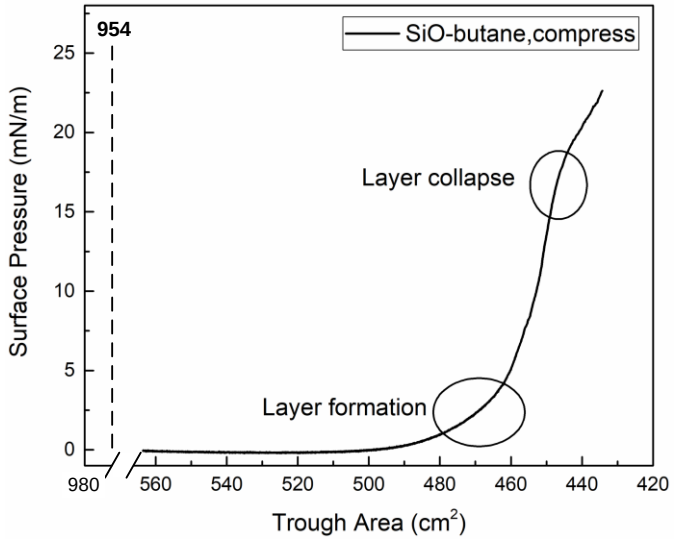

Figure 6-5 Pressure-Area isotherm of the SiO-butane silica particle monolayer with water. Highlighted in circles are the points of layer formation and collapse. The dotted line denotes the theoretical hexagonal close packing (HCP) area (954 cm^2).

The particle layer displays the expected trend for SiO-butane particles. At a high trough area, the silica floats on the surface as single particles or small non-connected aggregate island clusters, which do not affect the interface pressure. As the area is reduced to a critical point, the rafts join into a single inter-connected layer, producing a lateral force (Pugnaloni et al. 2005) resulting in a sharp increase in surface pressure (Monteux et al. 2007). If the area is further reduced under compression, a second critical point occurs, where the layer collapses and particles are either expelled into the bulk medium or the layer folded onto itself (Hórvölgyi et al. 1996, Bordács et al. 2006, Horozov et al. 2006).

The relative abruptness of the monolayer formation and collapse can be used as a guide to understanding the relative homogeneity or aggregated nature of particle networks(Bordács et al. 2006). There is a ‘monolayer region’ between the highlighted points of layer formation and collapse. However, it is not truly monolayer for those hydrophilic particles. Silica is nominally hydrophilic in nature and the inter-particle interactions will be dominated by symmetric bulk fluid electrostatics (such as DLVO (Hiemenz and Rajagopalan 1997)). The sudden, steep increase in surface pressure per area reduced, indicates the initial particle rafts

quite suddenly re-conform into a single network with little lateral resistance, to minimise the free energy state. There is a predicted theoretical hexagonal close-packed (HCP) area position in Fig.6-5.

The comparison of HCP and experimental data are shown in the Appendix (Table. A2). The dotted vertical line crossing the isotherm represents a theoretical hexagonal close-packed area for particles. It is clear that the theoretical HCP position is far away from the close packing position in the experiment results, likely because of either aggregation and overlap of particles or that particles are being dispersed into the subphase. It may suggest some of the particles are not quite aligned in a perfect monolayer and possibly are pushed on top of one another and aggregated during the compression progress.

The surface pressure changes during compression, expression and recompression of treated silica particles with pure water subphase are shown in this study. The comparison of SiO-butane and SiO-hexane particles is shown in Fig.6-6. Other surface tension vs area profiles with different MIBC concentrations results are shown in the Appendix (Fig. A15-A16).

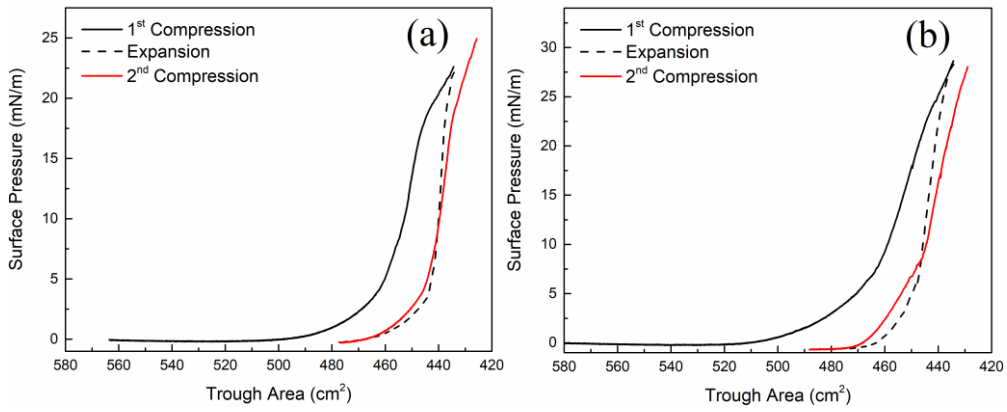

Figure 6-6 Repeated compression of (a)SiO-butane particle and (b) SiO-hexane layers with water subphase.

Changes in the pressure isotherm from the monolayers that are initially compressed, expanded, and recompressed are measured to gauge network hysteresis in particle layers.

Fig.6-6. also shows the initial compression and secondary compression (after trough expansion). The repeated compression behaviour of SiO-butane particles is similar. After trough expansion, the secondary compression leads to monolayer formation at a reduced area, suggesting significant layer hysteresis. It is evident from the results that secondary monolayer formation occurs close to the minimum trough area from the first compression cycle. It is probable under intimal compression, particles are gradually being expelled into the subphase, or aggregated as the trough baffles compress the monolayer, progressively destroying the network structure. These aggregates are far away from a monolayer (maybe multiple layers) and are e completely inelastic on formation.

The normalised HCP and Langmuir trough experiment results are compared in Fig.6-7. The details are summarised in the Appendix (Table. A2). Different volumes of particle suspensions are used for SiO-butane and SiO-hexane particles in the experiment due to the Langmuir trough area limitation. For SiO-butane particles, the theoretical HCP is 954 cm^2 while it is 621 cm^2 for SiO-hexane particles. To better compare the two particles, normalised packing areas are used (which is the ratio between the packing area and the hexagon close packing area). It is obvious that the HCP theoretical results are different to the experimental packing areas, and overpredicted the results – although, much less so with SiO-hexane particles. There is also a possibility that some of the particle immersed and settled in the subphase and the number of particles immersed decreasing with the hydrophobicity.

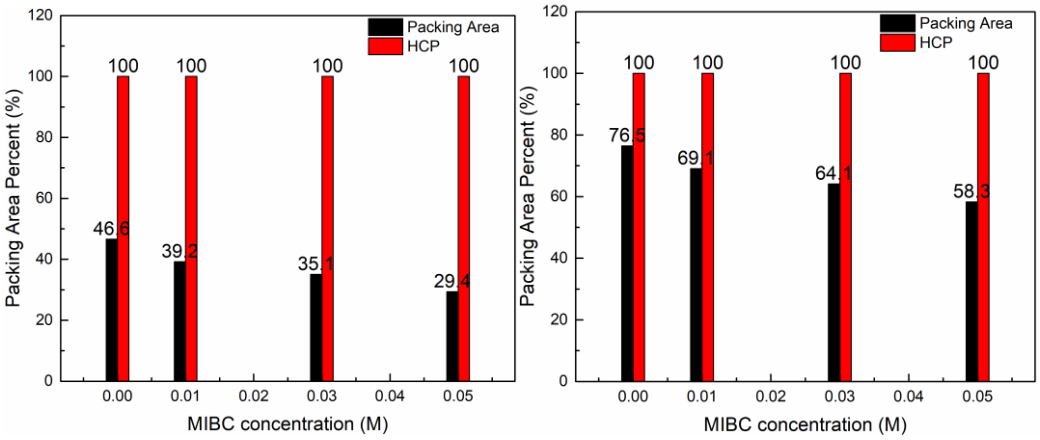

Figure 6-7 Normalised HCP and experiment comparison with different MIBC concentrations. (a) SiO-butane, (b) SiO-hexane.

The results of SiO-butane and SiO-hexane on water subphase under low and high surface pressures are shown in Fig.6-8 to 6-19.

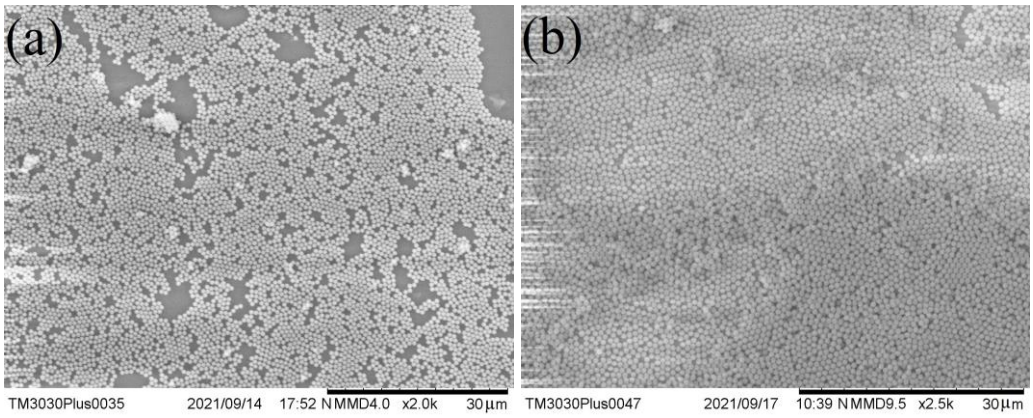

Figure 6-8 SEM results of SiO-butane on water subphase under different surface pressure (a) low surface pressure 1.5 mN/m, (b) high surface pressure 20 mN/m.

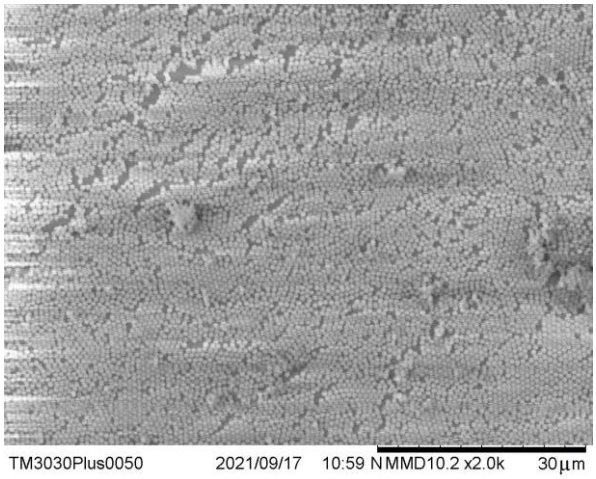

Figure 6-9 SEM result of SiO-hexane on water subphase under close packing condition with a surface pressure of 12 mN/m.

It is clear that for SiO-butane particles, when the surface pressure is low, particles have shown a degree of aggregation and the degree is increased at high surface pressure. It can explain why the experiment data is far away from the theoretical HCP result. The SiO-hexane particles present less extensive aggregation during the compression, correlating to their packing being close to the theoretical HCP area. For SiO-butane particles, the contact angle is larger and more hydrophobic than the origin SiO_2 particles. When using origin SiO_2 particles, monolayers cannot be formed or observed, and all are settled or immersed in the subphase. From the SEM pictures of low- and high-pressure situations, we can find that some SiO-butane particles show monolayer on low surface pressure but folded to double or even multilayers with the compression of barriers.

The comparison of MIBC concentration surface pressure results (including water subphase) is shown in Fig.6-10. To further investigate systems directly correlated with the surface tension investigations, a comparison of SiO-butane and SiO-hexane monolayers with 0.05 M MIBC concentrations is shown in Fig.6-11 and 6-12, with the expansion and recompressions shown within the appendix (Fig.A15 and A16).

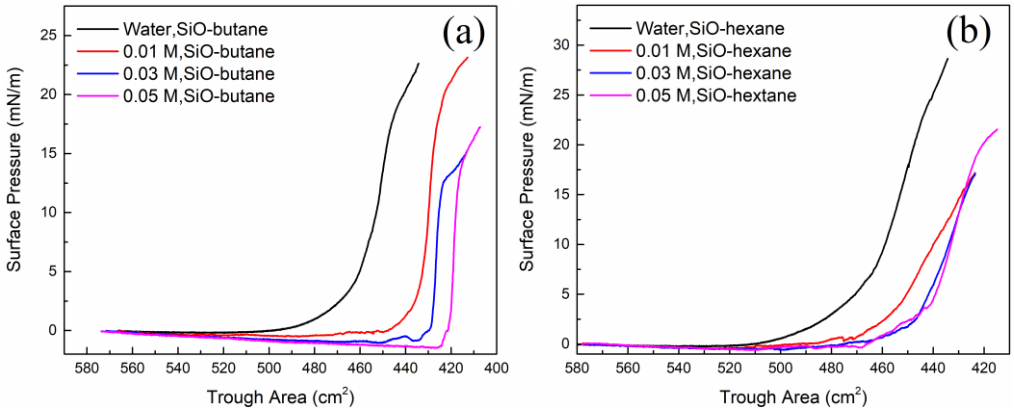

Figure 6-10 Surface tension vs trough area Comparison of (a) SiO-butane and (b) SiO-hexane with different concentrations of MIBC.

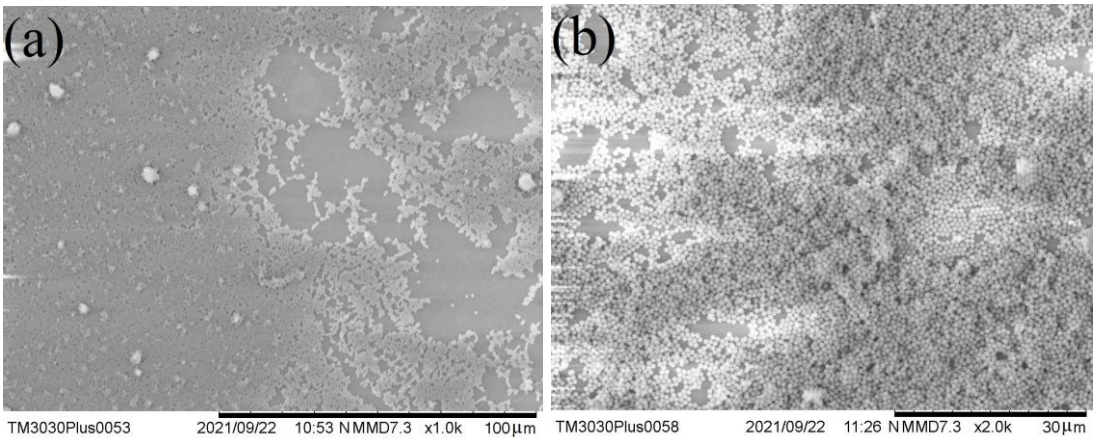

Figure 6-11 SEM results of SiO-butane on 0.05M MIBC subphase under different surface pressure (a) low surface pressure -0.3 mN/m, (b) high surface pressure 15 mN/m.

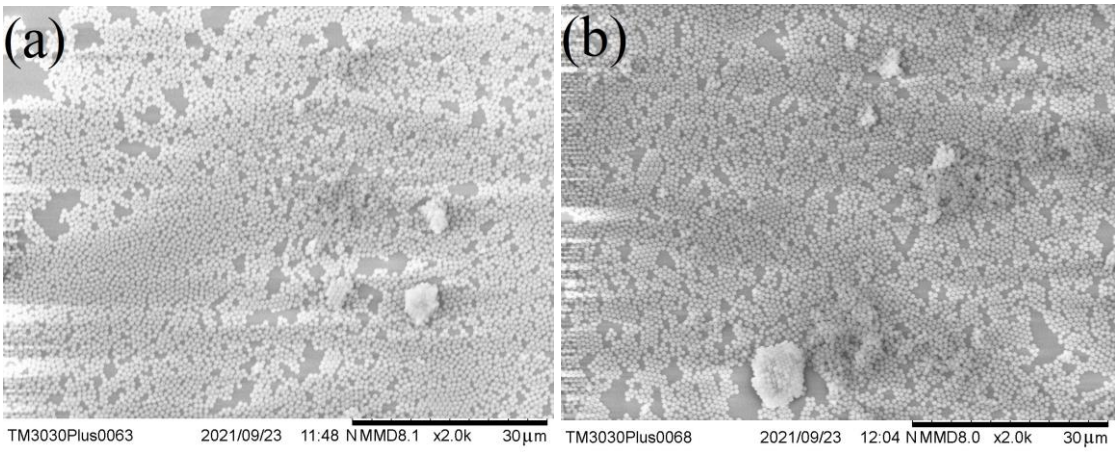

Figure 6-12 SEM results of SiO-hexane on 0.05M MIBC subphase under different surface pressure (a) low surface pressure 0.3 mN/m, (b) High surface pressure 5 mN/m.

The maximum surface pressure during compressing decreases with MIBC concentrations so does the packing position. The curves of SiO-butane and SiO-hexane are different. Generally, the curve of SiO-hexane shows more straight without a very obvious inflexion point (layer formation and layer collapse points) as SiO-butane and the surface pressure increase faster and higher than the butane one. It indicates that longer range aggregates and less clear multilayers.

It is clear that the aggregation and overlap occur during the compression process, and the aggregation is more significant with higher concentrations of MIBC. The slight aggregation of particles is also visible before and after compression and become more considerable with MIBC concentrations. For SiO-hexane particles, the contact angle is the largest among the three particles and the most hydrophobic. Before and after compression, the particles always show good monolayer behaviour, with most particles in a hexagonal arrangement, but with some bigger aggregation clusters. That is why SiO-hexane shows closer but still has deviation with HCP prediction.

6.3.2 Pendant Drop

The results of pendant drop surface tension measurement are shown in Fig.6-13 before and after using a cuvette to keep the moisture environment. It is clear that the volume of drop changed a lot without the use of the cuvette, but only < 5% with the cuvette and liquid pool. Thus, in this study, the author uses a plastic cuvette and pool to ensure the moisture environment and reduce the evaporation effect. When not using the cuvette and measuring the surface tension of the droplet, there is also evidence of oscillations of the droplet, which is more obvious with the hydrophobic particles – as shown within the Appendix (Fig. A17) with a big ‘apparent’ surface tension oscillation. The drop volume also decreased. It is assumed to be caused by the fast evaporation, which leads to rapid surface area decreases, where the number of particles per surface area changes at the interface. With the volume decreasing, the

total surface area of the droplet also decreases, whereupon the particles move closer and may reach close packing. As the volume keeps decreasing, there is no space for particles to become closer anymore, so they push against one another and finally, the oscillation occurs. These results are similar to the work of Joshi and Sun (Joshi and Ying 2010) who simulated a droplet with particle adsorbed, with the volume of the droplet decreasing, the particles collide and even show multiplayer out of the droplet. With a cuvette, the volume changes in a very small range and thus can be ignored, then, the surface tension which we will call the 'apparent' surface tension of the drop can be analysed. It is named as 'apparent' because the 800 nm silica particles shouldn't alter the real surface tension, but they may cause a deformation of the drop shape (Manga et al. 2016) and the pendant drop shows this as a surface tension variation. For convenience, the author still uses surface tension to describe the 'apparent' surface tension in this study. The pH of the particle suspensions that the author used is all around pH = 8.6 ± 0.5 and the zetapotential were around -48 ± 0.4 mV. It means the suspension is stable and not likely to aggregate.

The sedimentation length l_g (Cherepanov and Smorodin 2017) of the colloids is calculated, which is rearranged from the Laplace-Perring distribution law and can be calculated as Eq.(6.6),

$$l_g = \frac{k_B T}{(\rho_s - \rho_f) V g} \tag{6.6}$$

Where the subscript *s* and *f* means the solid and fluid, respectively. *V* is the volume of particle and *g* is the gravity. If the sedimentation length is much greater than the diameter of colloidal particle, the particle can diffuse a distance greater than this diameter, otherwise, when the sedimentation length is less than the diameter, the particle can only diffuse by much shorter length. In this study, the sedimentation length is 1598 nm only about twice of the diameter which means the particle can diffused but the range is restricted.

Pendant drop surface tension vs time data of original and esterified particles under 0.03M MIBC concentrations are shown in Fig.6-14. The raw data that includes the volume change of the droplet is shown in Appendix (Fig. A18).

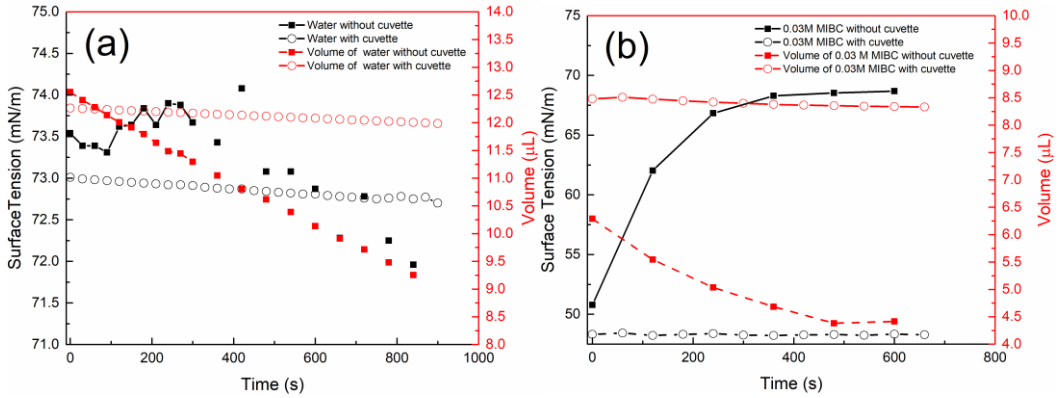

Figure 6-13 Pendant drop surface tension and volume results of (a) water and (b) 0.03M MIBC without particles before and after using cuvette.

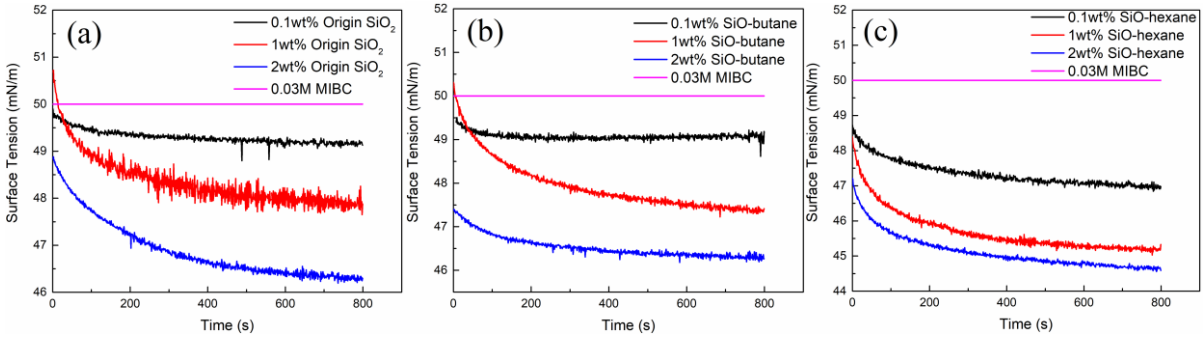

Figure 6-14 The surface tension results of particles under different particle concentrations with 0.03 M MIBC. (a) Origin SiO2. (b) SiO-butane. (c) SiO-hexane.

The initial 0.03 M MIBC surface tension without particles is around 50 mN/m, which is shown as a pink straight line in Fig.6-14. When particles are added, the initial surface tension (t = 0) is slightly altered in different ranges, although not significant, it may be caused by slight differences in the MIBC concentration due to minor evaporation. However, the critical trends are clear, which show the equilibrium surface tension of all three species particles decreased with time. In the first about 50 s, the surface tension decreased fast and then the gradient become slower and slower until reached a plateau. What is also apparent is that both particle type and concentration affect the final apparent surface tensions. In terms of particle

type, at the low 0.1 wt% concentration, the equilibrium change in surface tension is the largest for the SiO-hexane particles than the other species. This may infer more complete monolayer adsorption of the more hydrophobic particles, which is consistent with the Langmuir trough studies on the monolayer coverage. The surface tension changes are more significant for all particle species at the higher mass concentrations. This difference may infer greater overall particle coverage in all cases (hence, more interfacial distortion) or potentially the presence of some multilayers. However, given that all the particle species are stable in the dispersion, there would be a little drive for multilayer adsorption from particles in the bulk, and any such changes may be more from interfacial reorganisation as the interfacial pressure increases (and formation of particle rafts, again, as evidenced in the Langmuir trough data).

From the study of Rana et al (Rana et al. 2012) the adsorption mechanism of colloidal particles cannot be only described as a diffusion-only mechanism (Eastoe and Dalton 2000) but as a mixed kinetic diffusion mechanism(Eastoe and Dalton 2000). However, at the initial stage where only small numbers of particles are adsorbed on the liquid-gas interface, we still can use some diffusion-like models to analyse the results. Therefore, to calculate the adsorption rate. There is a need to find a property fitting model to explain the surface tension vs time data. Dynamic surface tension can be used to probe quantitatively the dynamics of nanoparticle adsorption, provided that a suitable model exists to connect dynamic surface tension to transient coverage of the interface by nanoparticles. Bizmark et al (Bizmark et al. 2014) studied the kinetics of the adsorption of small ethyl cellulose nanoparticles at the water-air interface. In particular, for $t \rightarrow 0$ which is usually called the early stage of adsorption, the initial decay of surface tension is given by a modified short-time approximation as Eq.(6.7) (Dugyala et al. 2016):

$$\gamma = \gamma_0 - 2N_A C_0 \Delta E \sqrt{\frac{Dt}{\pi}} \tag{6.7}$$

In this equation, γ is the interfacial tension at any given time t, γ_0 is the pure solution interfacial tension, N_A is the Avogadro number, C_0 is the initial bulk concentration of particles (mol/L) and ΔE is the detachment energy of the particle. The above equation assumes that the adsorption of particles to the interface is instantaneous. Bizmark et al (Bizmark et al. 2014) also used Eq. (6.7) to fit the initial γ vs $\sqrt{t}$ data with ΔE as the fitting parameter for several initial concentrations of particles C_0.

In this study, the author uses the model of Bizmarks et al (Bizmark et al. 2014) to analyse the first stage of adsorption which is mainly assumed to be dominated by the particle diffusion effect.

At an initial time, the adsorption is limited by the diffusion process as the interface is free of particles. Once the nanoparticle adsorbs to the interface it is very unlikely that it detaches from the interface due to high detachment energy. Therefore, the author uses a modified diffusion-controlled theory to model the early time adsorption process. To include the energy barrier effects on the adsorption process, we replace the particle diffusivity D with the effective diffusion coefficient D_{eff} in Eq. (6.7). We, therefore, calculate the effective diffusivity of the particles by modelling the early time dynamic surface tension data using the adsorption kinetic model as Eq. (6.8) (Dugyala et al. 2016):

$$\gamma = \gamma_0 - 2N_A C_0 \Delta E \sqrt{\frac{D_{eff} t}{\pi}} \tag{6.8}$$

Where D_{eff} is the effective diffusion constant. The particle detachment energy from the interface is calculated from Eq. (2.7). Since the actual position of nanoparticles with respect to the interface is difficult to measure, the contact angle of the sized silica nanoparticles is assumed to be that of the contact angle of the treated silica wafers (see Chapter 3) and the equation can be expressed as a linear Eq. (6.9):

$$\gamma = P_1 - P_2\sqrt{t} \tag{6.9}$$

Where P_1 is the pure solution interfacial tension (γ_0) and P_2 is $2N_AC_0\Delta E\sqrt{(D_{eff})}/\sqrt{\pi}$. By using the fitting parameters, the effective diffusivity of the particles (D_{eff}) is calculated to be compared with the Stokes-Einstein equation for free diffusion ($D_0 = k_BT/6\pi\mu r$), which for 800 nm silica particles is 5.40259 e^{-13}).

The effective diffusion D_{eff} due to the presence of an energy barrier U is related to the bare diffusion coefficient D_0 (without any adsorption barrier) by Eq. (6.10):

$$D_{eff} = D_0 \exp(-\frac{U}{k_BT}) \tag{6.10}$$

The bare diffusivity of the particle D_0 is calculated by using the Stokes-Einstein equation. k_B is the Boltzmann constant (1.380649×10^{-23} J/K). This energy barrier is used to compare with thermal energy. From the linear fitting results in Table.6-2, we can see that the effective diffusivity D_{eff} of the particles is several orders of magnitude lower than the bare diffusivity D_0. By using this equation, the energy barrier U is calculated from the effective diffusivity values. Since the particles used are electrostatically stabilized, the energy barrier is likely to be of electrostatic origin and therefore we calculate the DLVO interactions near the interface. With the modified short-time approximation model, provided that the bulk concentration is not significantly changed by the attachment of nanoparticles at the interface, we can fit the short-time data (less than 50 s) and obtain the effective diffusion coefficient and the energy barrier. The detailed results of the linear fitting are shown in Fig. 6-15. The effective diffusion and resultant energy barriers are shown for all systems in Table.6-2.

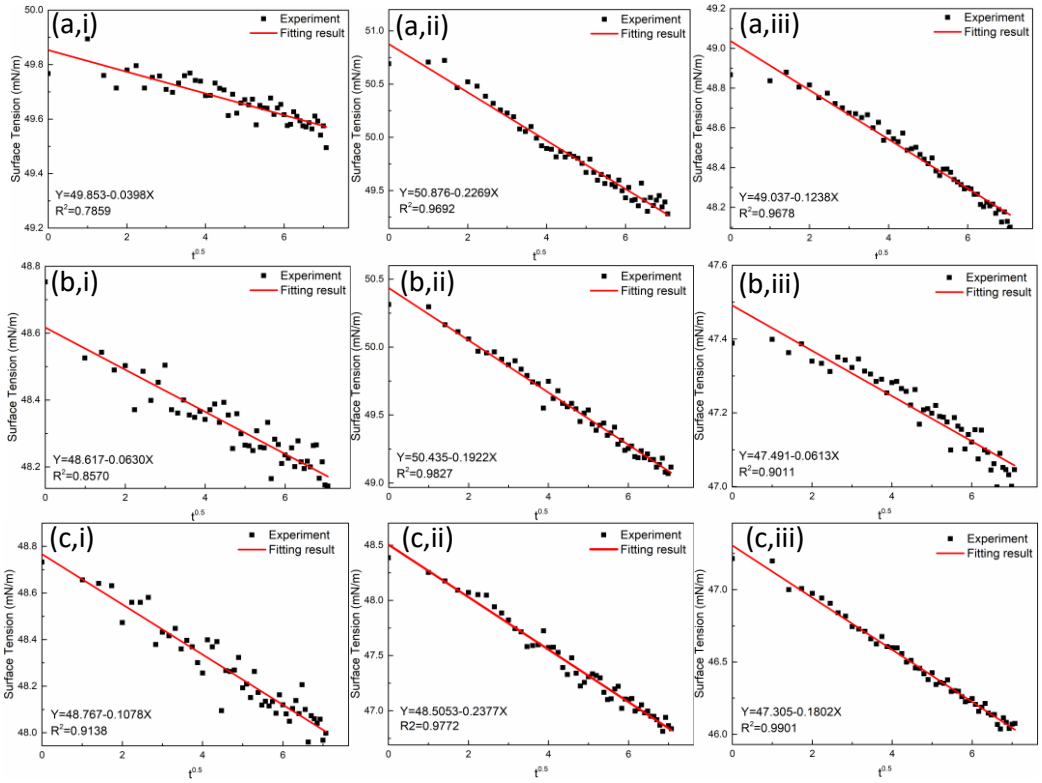

Figure 6-15 Modified short time approximation linear fitting results of surface tension vs $t^{0.5}$. (a) Origin SiO2, (b) SiO-butane, (c) SiO-hexane. (i) 0.1wt%, (ii)1wt%, (iii)2wt%.

Table.6-2. Modified short time approximation linear fitting results of surface tension vs $t^{0.5}$.

0.1 wt%	Intercept, mN/m	Deviation, mN/m	Gradient, mN m $s^{-0.5}$	Deviation, mN m $s^{-0.5}$	R^2	$D_{eff}\times10^{-30}$, m^2/s	U/k_BT
Origin SiO_2	49.853	0.0146	-0.0398	0.0029	0.7859	230.62	35.39
SiO-butane	48.617	0.0183	-0.0630	0.0036	0.8570	5.11	39.20
SiO-hexane	48.767	0.0234	-0.1078	0.0047	0.9138	0.89	40.95

1 wt%	Intercept, mN/m	Deviation, mN/m	Gradient, mN m $s^{-0.5}$	Deviation, mN m $s^{-0.5}$	R^2	$D_{eff}\times10^{-30}$, m^2/s	U/k_BT
Origin SiO_2	50.876	0.0286	-0.2269	0.0057	0.9692	75.03	36.51
SiO-butane	50.435	0.0181	-0.1922	0.0036	0.9827	0.48	41.57
SiO-hexane	48.505	0.0257	-0.2377	0.0051	0.9772	0.043	43.97

2 wt%	Intercept, mN/m	Deviation, mN/m	Gradient, mN m $s^{-0.5}$	Deviation, mN m $s^{-0.5}$	R^2	$D_{eff} \times 10^{-30}$, m^2/s	U/k_BT
Origin SiO_2	49.037	0.0160	-0.1238	0.0032	0.9678	5.58	39.11
SiO-butane	47.491	0.0144	-0.0613	0.0029	0.9011	0.012	45.25
SiO-hexane	47.305	0.0128	-0.1802	0.0026	0.9901	0.006218	45.91

The intercepts are the initial pure solution concentrations, and they are all close to 50 mN/m which is the 0.03M MIBC initial surface tension. The energy barrier (U/ k_BT) is calculated from the effective diffusion (D_{eff}). We can see from Table 6-2 and Fig. 6-16 that the adsorption energy barrier increases with particle hydrophobicity and also increase with particle concentrations.

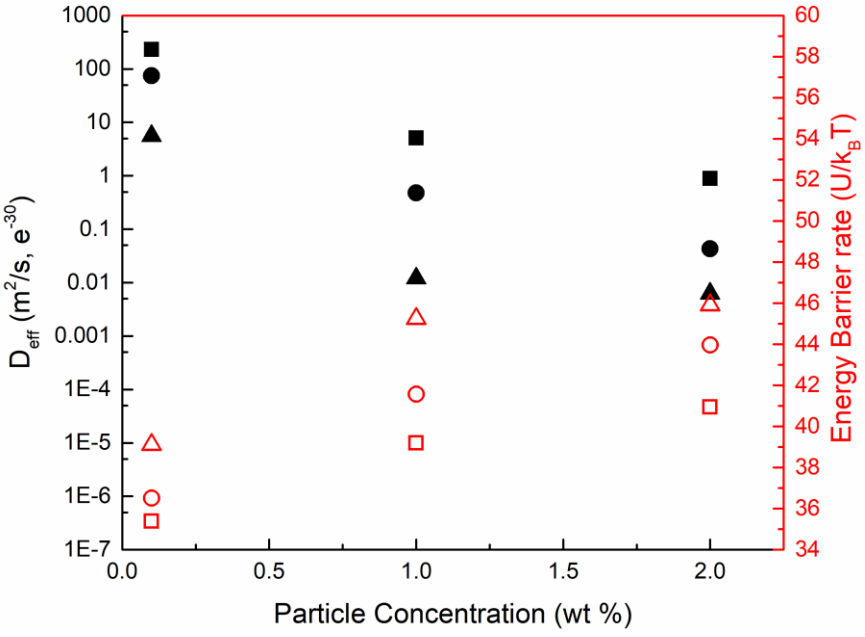

Figure 6-16 Effective diffusion coefficient and energy barrier results of modified short time approximation model. The square is Origin SiO_2, the circle is SiO-butane, and the triangle is SiO-hexane. Black solids are the effective diffusion coefficient (D_{eff}) and red hollows are the energy barrier rate.

It shows for higher concentration and higher hydrophobicity, the thermal energy of the particles is not enough to overcome the energy barrier (Dugyala et al. 2016). It highlights out that only diffusion mechanism is not enough to drive the particle adsorption. Basically, given the similar gradient values, the diffusion is heavily weighted to ΔE (the change in interfacial contact energy) which is obviously higher for hydrophobic particles. Normally, this energy is

considered the free energy for detachment, but it also provides a great energy barrier to initial adsorption. Once particles initially form a three-phase contact line with the droplet, at a contact angle far away from the minimum energy state, they will be at larger energy than particles with a smaller contact angle. This ends up resulting in an increase in the energy barrier, U. However, the value of U is much smaller than the ΔE value (several orders of magnitude) so the increase in energy barrier with contact angle is relatively minor. Although the adsorption energy barrier is larger, particle adsorption amount can still be increased (Ferdous et al. 2012) which has been reflected in the equilibrium dynamic surface tension γ_∞. With more particles adsorbed, the equilibrium dynamic surface tension γ_∞ has lower values.

The analysis of the energy barrier is based on Eq. (6.8) which assumes the particles are dominated by the diffusion effect. We could analyse this equation, for the same data, if the wettability changed to more hydrophobic, ΔE is higher for hydrophobic particle, then the D_{eff} should be smaller if the curve has the same gradient. For very small particles that are truly controlled by diffusion, the curve should have square times magnitude of slope to get a larger D_{eff} with the change of wettability. But actually, it doesn't, which shows the particle is not mainly controlled by the diffusion but by a more complicated mechanism (such as the mixed diffusion-kinetic (Eastoe and Dalton 2000) at the first stage of the adsorption for large colloidal particles as 800 nm silica.

For 800 nm silica particles, the diffusion of the particle is small when compared with other researchers (Bizmark et al. 2014, Dugyala et al. 2016) who studied only less than 100 nm particles or even smaller. In those scales, particle diffusion is dominated, but it is not so significant for large particles as the 800 nm tested. Indeed, 800 nm particles are still controlled by gravity & buoyancy (which is what is causing the deformation of the surface) as well as, potentially, dynamic effects from the injection of a droplet. For large colloidal particles, the inertia effect provided by the injection and formation of a droplet (Matsunaga et

al. 2022) may also help the adsorption because they are hardly balanced. The results show, broadly, a very large energy barrier that cannot be overcome by diffusion alone. The short-time effective diffusion coefficient also highlights that a diffusion-only mechanism cannot explain all colloidal particle adsorption, especially for large colloids.

To investigate the rate changes further, long-time data are analysed with a different model (for data later than 50 s, which is the late stage). In some references, those data cannot be explained with only diffusion-like mechanism but a more complex one named mixed diffusion-kinetic controlled mechanism (Rana et al. 2012). However, the author still can use a modified long-time approximation to fit the data and obtain the adsorption rate.

The original long-time (Eastoe and Dalton 2000) is described as Eq. (6.11):

$$t \to \infty: \quad \gamma = \gamma_{\infty} + \frac{RT\Gamma_{\infty}^{2}}{C_0}\sqrt{\frac{\pi}{4Dt}} \tag{6.11}$$

Where R is the gas constant, T is the temperature, C_0 is the molar bulk concentration, Γ_∞ is the molar surface concentration at a steady state, and D is the nanoparticle diffusion coefficient. The γ_∞ is the intercept and $t^{-0.5}$ is the x coordinate.

During the later stages of adsorption, as the interface approaches maximum coverage, the presence of already adsorbed particle hinders particle attachment, and the adsorption flux is smaller than the predicted by Fick's law. In addition to the energy of specific physicochemical interactions between an adsorbing particle and the pristine interface, which are operative during all stages of the adsorption process, there is now an energy ϕ_s associated with the interaction between an adsorbing particle and already adsorbed ones (Bizmark et al. 2014). A quantitative account of this interaction, which is essentially steric in nature, is possible in the context of generalized RSA theory, which relates the respective interaction energy to the so-called generalized blocking function. This function quantifies the effect of

already adsorbed particles on the particle-interaction potential and, consequently, on the driving force for adsorption.

There is a modified long-time approximation model (Bizmark et al. 2014). Θ is the surface coverage (the fraction of the area of the interface occupied by nanoparticles) and Θ_{max} is the maximum coverage of the interface (0.91 in this study). The dimensionless adsorption rate k_a which follows:

$$\overline{k_a} \equiv k_a \frac{L}{D_0} \tag{6.12}$$

$$L \equiv \frac{1}{N_A C_0 S} \tag{6.13}$$

Where $S = \pi r^2$, and the relation between dimensionless k_a and non-dimensionless k_a is established. In the early stage of adsorption ($t \rightarrow 0$) when only a few particles are present at the interface. Using this approximation, we can get Eq. (6.14):

$$\Theta = \Theta_{max} - \frac{K_1}{\sqrt{\tau}} \tag{6.14}$$

Where

$$K_1 = \Theta_{max} (\Theta_{max} / 4.64 \overline{k_a})^{0.5} \tag{6.15}$$

The τ is the dimensionless time and k_a is the adsorption constant.

The detachment energy is replaced (Bizmark et al. 2014) by

$$|\Delta E| = \frac{\gamma_0 - \gamma_\infty}{\Theta_{max}} \pi r^2 \tag{6.16}$$

In the novel result of long-time approximation, the relation of surface tension (γ) and time (t) can be Eq. (6.17):

$$\gamma = \gamma_{\infty} + \frac{K_1 |\Delta E|}{(\pi r^2)^2 N_A C_0} \sqrt{\frac{1}{D_{eff} t}} \tag{6.17}$$

We can see $\gamma \propto (1/\sqrt{t})$ and the slope is Eq. (6.18):

$$Grad = \frac{K_1 |\Delta E|}{(\pi r^2)^2 N_A C_0 \sqrt{D_{eff}}} \tag{6.18}$$

The K_1 can be calculated with the linear fitting results of late-stage surface tension data and given knowledge of the adsorption energy, particle radius, and bulk concentration(Bizmark et al. 2014). The dimensionless k_a can be obtained from the relationship between K_1 and dimensionless k_a as Eq (6.14). Finally, with the dimensionless rule, the non-dimensional k_a can be obtained.

The adsorption constant, k_a can be calculated to analyse the overall rate of particle adsorption. The maximum value of the interaction energy ϕ attributed to specific particle-interface interaction, ϕ_b, may be approximately inferred from k_a as Eq. (6.19):

$$k_a \cong \frac{D}{r} \sqrt{\frac{\phi_b}{\pi k_B T}} \exp(-\frac{\phi_b}{k_B T}) \tag{6.19}$$

To estimate k_a from the rate data, the long-time approximation surface tension data is fitted vs $t^{-0.5}$, from 50 s to the equilibrium state (different with samples) using original SiO_2, SiO-butane, and SiO-hexane, and are shown in Fig.6-17. The detailed results are shown in Table.6-3.

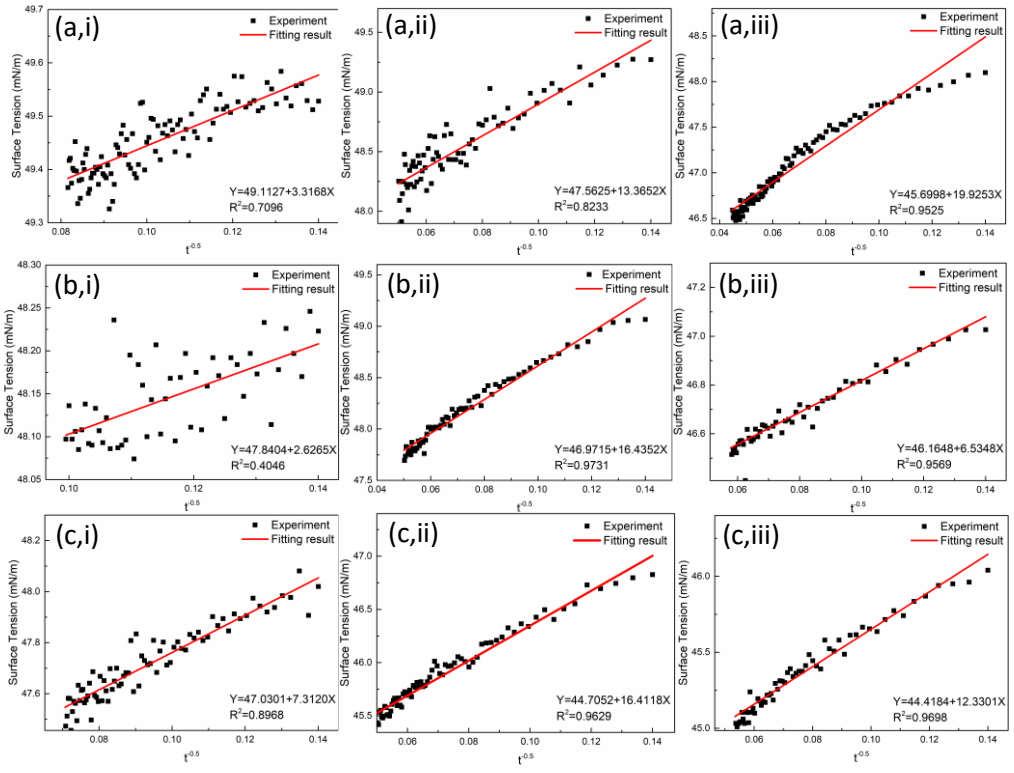

Figure 6-17 Modified long-time approximation linear fitting result of surface tension vs $t^{-0.5}$. (50 s to equilibrium). (a) Origin SiO_2, (b) SiO-butane, (c) SiO-hexane. (i) 0.1wt%, (ii)1wt%, (iii)2wt%.

Table 6-3. Modified long-time approximation linear fitting results of surface tension vs $t^{-0.5}$.

0.1 wt %	Intercept, mN/m	Deviation, mN/m	Gradient, mN m^{-1} $s^{0.5}$	Deviation, mN m^{-1} $s^{0.5}$	R^2	$K_1 \times 10^{-5}$, -	$k_a \times 10^6$, m/s
Origin SiO_2	49.1127	0.02224	3.3168	0.21282	0.7096	34.51	3.715
SiO-butane	47.8404	0.05196	2.6265	0.44409	0.4046	3.734	317.3
SiO-hexane	47.0301	0.01947	7.3120	0.20309	0.8968	2.568	671.0

1 wt %	Intercept, mN/m	Deviation, mN/m	Gradient, mN m^{-1} $s^{0.5}$	Deviation, mN m^{-1} $s^{0.5}$	R^2	$K_1 \times 10^{-5}$, -	$k_a \times 10^6$, m/s
Origin SiO_2	47.5625	0.02548	13.3653	0.33129	0.8233	207.6	1.027
SiO-butane	46.9715	0.01125	16.4352	0.14623	0.9731	19.63	114.8
SiO-hexane	44.7052	0.01326	16.4118	0.1724	0.9629	5.081	1714

2 wt %	Intercept, mN/m	Deviation, mN/m	Gradient, mN m^{-1} $s^{0.5}$	Deviation, mN m^{-1} $s^{0.5}$	R^2	$K_1 \times 10^{-5}$, -	$k_a \times 10^6$, m/s
Origin SiO_2	45.6998	0.01499	19.9253	0.20995	0.9525	156.2	3.627
SiO-butane	46.1648	0.00742	6.5348	0.0879	0.9569	6.112	2370
SiO-hexane	44.4184	0.01014	12.3301	0.12609	0.9698	4.074	5331

The intercept is the calculated equilibrium surface tension γ^{eq}, when particles dominate the liquid-gas interface at an equilibrium state. The value of γ^{eq} decreases with particle concentrations and hydrophobicity. It is interesting that the R^2 also increases with particle concentrations and hydrophobicity, which means the data is closer to the long-time approximation model. It maybe 0.1 wt% does not generate a full HCP layer, and does not fully fill the drop interface, so the data does not reach the equilibrium state. Generally, the gradient of fitting increases with concentration but shows a couple of anomalous points when it comes to SiO-butane. It is very clear, from the tabled data, that the adsorption constant k_a generally increases with particle concentration and also increases with hydrophobicity dramatically. The k_a constants are plotted for all systems versus concentration in Fig. 6-18, for ease of observation.

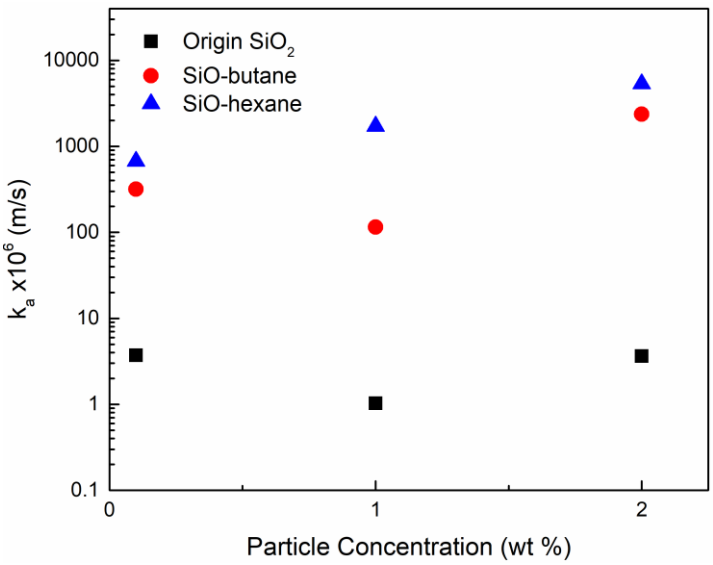

Figure 6-18 Adsorption rate results of long-time approximation model.

The adsorption rates increase several orders of magnitude with the increase of hydrophobicity and slightly increase with concentrations. It means with the increase of particle hydrophobicity, the particle adsorbs several orders of magnitude faster than untreated original silica particles. With the increase of hydrophobicity, the detachment energy decreases with contact angles and particles are easier to adsorbed on the interface.

For concentration influence, the k_a ratios between 0.1 wt% SiO-hexane and 2 wt% SiO-hexane become 7.9 times, with 20 times concentration increase. However, for Origin SiO_2 the adsorption rate is even slightly down with concentration in the range of 0.1 wt% to 2 wt%. The increase rate of adsorption ratio is lower than the concentration increases which is similar as Bizmark's work (Bizmark et al. 2014) that they increased 10 times of concentration and increased 3 times the adsorption rate. That indicates the increase of the concentration can help the adsorption rate become larger but may not be the most significant method. The long-time approximation model is able to quantitatively show the impact of hydrophobicity, in particular, on particle adsorption, due to it describing the adsorption when the surface becomes crowded. For 0.1 wt% drops, the k_a of SiO-hexane is 181 times larger than the original SiO_2 and the ratio increases to 1470 at 2 wt%. The hydrophobicity dramatically

influenced the adsorption rate. The increase ratio also shows the adsorption rate changes significantly more with hydrophobicity than with concentration.

However, the adsorption rate does not always increase with concentrations in results, there are inflexion points at 1 wt% for Origin and SiO-butane which reaches the minimum adsorption rate for both species. For Origin particles, the adsorption rate is even not fully back to the level of 0.1 wt% after it reaches 2 wt% concentration. Similar phenomena show in Bizmarks' study (Bizmark et al. 2014) but inversely, they found a maximum inflexion point for small EC nanoparticles in their particles with the increase in mass concentrations. It may be from competition between particles for the adsorption site as described in the mixed diffusion-kinetic theory (Eastoe and Dalton 2000) when the concentration is significantly increased. This competition is balanced out with the increase in the number of particles when concentration increases from 1 to 2 wt%. Also, multilayers cannot be completely ruled out as the Langmuir trough results show in previous work. The multilayers will distort the interface more and then influence the apparent surface tension which is analysed with the shape of the droplet. It cannot be denied that the inflexion points may simply be from poor data at the 0.1 wt% for uncoated/butane particles (the butane data is particularly scattered for 0.1 wt%).

6.4 Conclusion

To analyse the hydrophobicity effect of particles on adsorption, for untreated particles, Brownian motion is too small and not very possible to drive particles away from the interface. However, other dynamic effects may let the particles to become detached or move away from the interface, due to the low energy barrier. For hydrophobic particles, the detachment energy is larger and the contact area also greater, so therefore, it is hard to leave the interface. The adsorbed particles may freely move on the interface to increase space for unabsorbed particles and increase the possibility of adsorption (Eastoe and Dalton 2000). However, the hydrophilic particles are more likely to leave the interface and back to the bulk fluid or be

immersed more in a fluid phase, which may ‘hinder’ other particles and decrease the adsorption possibility because actually, when they are immersed in the bulk phase, but they actually adsorbed, the interface shape may not obviously change due to the adsorption, thus, the apparent surface distorts cannot be observed by devices. The interface distorts will be simulated in the next chapter to see the wettability difference between particles. The details on the liquid interface may be the reason that the more hydrophobic, the adsorption shows more stable, and the adsorption number steady climbed then shows larger k_a.

7. Simulation of Colloidal Adsorption using an LBM-DEM Methodology

7.1 Introduction

The Lattice Boltzmann method has been proved to be an efficient alternative simulation method for N-S equations and has shown good results in multiphase fluid flow problems (Wang et al. 2014). Furthermore, wettability and complex boundary geometry are easily applied in LBM with less computational cost (Li et al. 2014). It is a very attractive method to study multiphase problems such as adsorption at the liquid-liquid and liquid-gas interfaces.

Although, the BGK approximation scheme is simple and widely used in the LBM models, the MRT models also have physical advantages in that they are flexible enough to incorporate additional physics that cannot be naturally represented by the models based on the BGK approximation (Premnath and Abraham 2007). The advantages of MRT are mentioned in Chapter 2. In the MRT scheme, by choosing different and carefully separated time scales to represent changes in the various physical processes due to collisions, the stability of the LBM can be significantly improved (Lallemand and Luo 2000). Thus, in practice, the MRT scheme shows better performance both on stability and accuracy than the BGK model which only has one relaxation time.

LBM shows good performance at the fluid flow problems, especially at the mesoscopic scales (Yang et al. 2018). However, LBM is mainly focused on the fluid flow not the movement of the particles or solid walls. DEM has the advantage of not only simulating the movement of solid objects and can take object parameters and other solid forces into consideration but the particle collisions. The combination of two methods should be an attractive method to study the particle adsorption process. Immersed moving boundary (Noble and Torczynski 1998, Owen et al. 2011) method has been proved to be a good efficient coupling method which

only needs the additional solid fraction information of nodes input in the LBM. Forces such as the drag force caused by the fluid flow and particle adhesion force caused by the multiphase calculated in the LBM and translated to the DEM and provided fluid-caused forces. However, other forces such as electromagnetic forces are not considered.

In this chapter, a 3D MRT-pseudopotential single-component multiphase LBM-DEM coupling model is used to simulate the particle adsorption at the liquid interface. In this model, in order to better couple the LBM and DEM, and solve the density accumulation problem caused by the normal contact angle adjustment (Martys and Chen 1996, Sbragaglia et al. 2006, Li et al. 2014), a novel fluid-solid force scheme is proposed and a new adhesion force exchange from LBM to DEM is proposed and discussed. This study can be a pioneer work in the coupling of single-component multiphase LBM and DEM models and the application of the coupling model to particle adsorption problems. It is worth to notice that also only one particle is included in the simulation of this chapter, the movement of the particle is still governing with DEM and ready for multi-particles.

7.2 Evolution Equations and Boundary Conditions of LBM and DEM

7.2.1 Governing Equations of LBM

In this section, we will introduce the Lattice Boltzmann method that is used in this study including basic equations and some novel schemes in three-dimension implementation. Since Multi-relaxation time schemes (d'Humières 2002) have been widely used for years, a single relaxation scheme (SRT) or so-called BGK scheme is not used in the study. The evolution equations of LBM which is also called the governing equations can replace the function of N-S equations when calculating the fluid flow and can deduce the N-S equations with multi-scale Chapman-Enskog expansion (Li 2015). The Lattice Boltzmann equations (LBE) with a discrete extra force term in the SRT scheme can be written as Eq. (7.1) and the MRT version is shown as Eq. (7.2) in the following:

$$f_\alpha(x+e_\alpha\delta t,t+\delta t)=f_\alpha(x,t)-\frac{1}{\tau}[f_\alpha(x,t)-f_\alpha^{eq}(x,t)]+\delta t\mathbf{F}_\alpha \tag{7.1}$$

$$f_\alpha(x+e_\alpha\delta t,t+\delta t)=f_\alpha(x,t)-\mathbf{M}^{-1}\mathbf{\Lambda}[\mathrm{m}(x,t)-\mathrm{m}^{eq}(x,t)]+\mathbf{M}^{-1}(\mathbf{I}-\frac{\mathbf{\Lambda}}{2})\bar{\mathbf{S}}(x,t) \tag{7.2}$$

The $f_\alpha(x,t)$ and $f_\alpha^{eq}(x,t)$ are the density distribution function and its corresponding equilibrium part along the discrete lattice direction α. t is the time and e_α are the discrete lattice velocities which are selected such that their directions match with a standard D3Q19, three-dimensionless lattice model (d'Humières 2002). τ is a non-dimensional relaxation parameter in the BGK approximation and it is included in the MRT relative term $\mathbf{\Lambda}$ which is a diagonal matrix. m(x,t) and m^{eq}(x,t) are moment space version of density distribution and they obey the transform rule: m = $\mathbf{M}f$, so as the equilibrium m^{eq}(x,t). $\mathbf{M}^{-1}$ is the inverse of matrix $\mathbf{M}$. Where the $\mathbf{I}$ is the identity matrix. $\bar{\mathbf{S}}$ is the extra force term in moment space. The first term in the right hand is the distribution function of this time step, the second term is the collision operator term, and the third term is the extra force term. Since the SRT scheme is not used in the study, we will focus on the MRT governing equations.

The distribution discrete direction weight factor $\boldsymbol{\omega}_\alpha$ used in the D3Q19 model is given as

$$\omega_\alpha=\begin{cases}1/3, & \alpha=0\\ 1/18, & \alpha=1,...,6\\ 1/36, & \alpha=7,...,18\end{cases} \tag{7.3}$$

Then, the discrete lattice velocities e_α is expressed by:

$$e_\alpha=\begin{bmatrix}0&1&-1&0&0&0&0&1&1&-1&-1&1&-1&1&-1&0&0&0&0\\0&0&0&1&-1&0&0&1&-1&1&-1&0&0&0&0&1&1&-1&-1\\0&0&0&0&0&1&-1&0&0&0&0&1&1&-1&-1&1&-1&1&-1\end{bmatrix} \tag{7.4}$$

To convert the distribution function to moment space m(*x*,*t*), a transform matrix **M** is needed and can be calculated with the discrete lattice velocities (d'Humières 2002) which is given by Eq. (7.5):

$$\mathbf{M}=\begin{bmatrix}
1 & 1 & 1 & 1 & 1 & 1 & 1 & 1 & 1 & 1 & 1 & 1 & 1 & 1 & 1 & 1 & 1 & 1 & 1\\
-30 & -11 & -11 & -11 & -11 & -11 & -11 & 8 & 8 & 8 & 8 & 8 & 8 & 8 & 8 & 8 & 8 & 8 & 8\\
12 & -4 & -4 & -4 & -4 & -4 & -4 & 1 & 1 & 1 & 1 & 1 & 1 & 1 & 1 & 1 & 1 & 1 & 1\\
0 & 1 & -1 & 0 & 0 & 0 & 0 & 1 & 1 & -1 & -1 & 1 & -1 & 1 & -1 & 0 & 0 & 0 & 0\\
0 & -4 & 4 & 0 & 0 & 0 & 0 & 1 & 1 & -1 & -1 & 1 & -1 & 1 & -1 & 0 & 0 & 0 & 0\\
0 & 0 & 0 & 1 & -1 & 0 & 0 & 1 & -1 & 1 & -1 & 0 & 0 & 0 & 0 & 1 & 1 & -1 & -1\\
0 & 0 & 0 & -4 & 4 & 0 & 0 & 1 & -1 & 1 & -1 & 0 & 0 & 0 & 0 & 1 & 1 & -1 & -1\\
0 & 0 & 0 & 0 & 0 & 1 & -1 & 0 & 0 & 0 & 0 & 1 & 1 & -1 & -1 & 1 & -1 & 1 & -1\\
0 & 0 & 0 & 0 & 0 & -4 & 4 & 0 & 0 & 0 & 0 & 1 & 1 & -1 & -1 & 1 & -1 & 1 & -1\\
0 & 2 & 2 & -1 & -1 & -1 & -1 & 1 & 1 & 1 & 1 & 1 & 1 & 1 & 1 & -2 & -2 & -2 & -2\\
0 & -4 & -4 & 2 & 2 & 2 & 2 & 1 & 1 & 1 & 1 & 1 & 1 & 1 & 1 & -2 & -2 & -2 & -2\\
0 & 0 & 0 & 1 & 1 & -1 & -1 & 1 & 1 & 1 & 1 & -1 & -1 & -1 & -1 & 0 & 0 & 0 & 0\\
0 & 0 & 0 & -2 & -2 & 2 & 2 & 1 & 1 & 1 & 1 & -1 & -1 & -1 & -1 & 0 & 0 & 0 & 0\\
0 & 0 & 0 & 0 & 0 & 0 & 0 & 1 & -1 & -1 & 1 & 0 & 0 & 0 & 0 & 0 & 0 & 0 & 0\\
0 & 0 & 0 & 0 & 0 & 0 & 0 & 0 & 0 & 0 & 0 & 0 & 0 & 0 & 0 & 1 & -1 & -1 & 1\\
0 & 0 & 0 & 0 & 0 & 0 & 0 & 0 & 0 & 0 & 0 & 1 & -1 & -1 & 1 & 0 & 0 & 0 & 0\\
0 & 0 & 0 & 0 & 0 & 0 & 0 & 1 & 1 & -1 & -1 & -1 & 1 & -1 & 1 & 0 & 0 & 0 & 0\\
0 & 0 & 0 & 0 & 0 & 0 & 0 & -1 & 1 & -1 & 1 & 0 & 0 & 0 & 0 & 1 & 1 & -1 & -1\\
0 & 0 & 0 & 0 & 0 & 0 & 0 & 0 & 0 & 0 & 0 & 1 & 1 & -1 & -1 & -1 & 1 & -1 & 1
\end{bmatrix} \tag{7.5}$$

Relaxation times are all included in the diagonal matrix (Premnath and Abraham 2007) **Λ**, their values represent different meanings in the MRT scheme:

$$\mathbf{\Lambda} = diag(s_\rho, s_e, s_\varepsilon, s_j, s_q, s_j, s_q, s_j, s_q, s_\upsilon, s_\pi, s_\upsilon, s_\pi, s_\upsilon, s_\upsilon, s_\upsilon, s_m, s_m, s_m) \tag{7.6}$$

Then, in this thesis their values (Sajjadi et al. 2018) can be:

$$\mathbf{\Lambda} = diag(0, 1.19, 1.4, 0, 1.2, 0, 1.2, 0, 1.2, \frac{1}{\tau}, 1.4, \frac{1}{\tau}, 1.4, \frac{1}{\tau}, \frac{1}{\tau}, \frac{1}{\tau}, 1.98, 1.98, 1.98) \tag{7.7}$$

The value s_e related to bulk viscosity in Eq. (7.8) and s_υ related to the kinetic viscosity in Eq. (7.9):

$$\xi = \frac{2}{9}(\frac{1}{s_e} - 0.5) \tag{7.8}$$

$$\upsilon = \frac{1}{3}(\frac{1}{s_\upsilon} - 0.5) \tag{7.9}$$

In the SRT scheme, $\mathbf{F}_\alpha$ is the total force which includes, such as interparticle interaction force $\mathbf{F}_{\text{int}}$, body force $\mathbf{F}_b$, and fluid-solid interaction force $\mathbf{F}_s$. The Guo forcing term (Li et al. 2016) can be used to imply the extra force in LBM and the term $\delta t\mathbf{F}_\alpha$ can be expressed as Eq.(7.10):

$$\delta t\mathbf{F}_\alpha = \delta_t(1-\frac{1}{2\tau})\omega_\alpha[\frac{\mathbf{e}_\alpha-\mathbf{u}}{c_s^2}+\frac{(\mathbf{e}_\alpha\cdot\mathbf{u})}{c_s^4}\mathbf{e}_\alpha]\cdot\mathbf{F}_{total} \tag{7.10}$$

MRT scheme changes the collision operator into a moment space, the simple collision operator in SRT has been changed, and the new equilibrium distribution function in moment space m^{eq} (d'Humières 2002) can be Eq. (7.11):

$$m^{eq}=\mathbf{M}f^{eq}=\begin{bmatrix}
\rho \\
-11\rho+19\frac{j_x^2+j_y^2+j_z^2}{\rho} \\
3\rho-\frac{11}{2}\frac{j_x^2+j_y^2+j_z^2}{\rho} \\
j_x \\
-\frac{2}{3}j_x \\
j_y \\
-\frac{2}{3}j_y \\
j_z \\
-\frac{2}{3}j_z \\
\frac{2j_x^2-(j_y^2+j_z^2)}{\rho} \\
-\frac{1}{2}\frac{2j_x^2-(j_y^2+j_z^2)}{\rho} \\
\frac{j_y^2-j_z^2}{\rho} \\
-\frac{1}{2}\frac{j_y^2-j_z^2}{\rho} \\
\frac{j_xj_y}{\rho} \\
\frac{j_yj_z}{\rho} \\
\frac{j_xj_z}{\rho} \\
0 \\
0 \\
0
\end{bmatrix} \tag{7.11}$$

The macroscopic density ρ and velocity $\boldsymbol{u}$ can be calculated as Eq. (7.12) and (7.13):

$$\rho=\sum_\alpha f_\alpha \tag{7.12}$$

$$\boldsymbol{u}^{\mathrm{eq}} = \boldsymbol{u} = \frac{\sum_{\alpha} f_{\alpha}\boldsymbol{e}_{\alpha} + \frac{dt}{2}\boldsymbol{F}_{\mathrm{total}}}{\rho} \tag{7.13}$$

The $\mathbf{F}_{\mathrm{total}}$ is the extra forces that acted on the node, such as body force $\mathbf{F}_{\mathrm{b}}$, fluid-fluid interaction force $\mathbf{F}_{\mathrm{int}}$, and other forces.

For the single component multiphase pseudopotential (Shan-Chen) model (Shan and Chen 1993), the author used non-idea fluid (Yuan and Schaefer 2006) to mimic the real fluid, then, the pressure (Li et al. 2016) of the fluid node can be calculated as Eq. (7.14):

$$p = c_s^2\rho + \frac{Gc^2}{2}[\psi(\rho)]^2 \tag{7.14}$$

The pressure p can also be calculated from the equation of state (EOS) of non-ideal fluid, c_s^2 =1/3, ρ is the node density, G is a sign function, c = dx/dt = 1 in most cases, and ψ is the effective density of the fluid. For the non-ideal fluid, EOS is a thermodynamic equation that describes the relationship between pressure, temperature, and density of a non-ideal fluid. According to the results in the study by Yuan (Yuan and Schaefer 2006), for Peng-Robinson (P-R) EOS when acentric factor ω is set as 0.344, the simulation result is more similar to the experiment result of water. Thus, P-R EOS is used in this thesis. To describe the result more clearly, the author uses the concept of reduced variables and express the density, pressure, and temperature as $\rho_{\mathrm{R}}=\rho/\rho_{\mathrm{c}}$, $p_{\mathrm{R}}=p/p_{\mathrm{c}}$, and $T_{\mathrm{R}}=T/T_{\mathrm{c}}$, respectively.

P-R EOS can be expressed as Eqs. (7.15 – 7.18):

$$p = p_{EOS} = \frac{\rho RT}{1-b\rho} + \frac{a\alpha(T)\rho^2}{1+2b\rho-b^2\rho^2} \tag{7.15}$$

$$\alpha(T) = [1+(0.37464+1.54226\omega-0.26992\omega^2)\times(1-\sqrt{T/T_c})]^2 \tag{7.16}$$

$$a = 0.45724(RT_c)^2/p_c \tag{7.17}$$

$$b = 0.1873RT_c / p_c \tag{7.18}$$

To simulate water a =3/49, b=2/21, R=1, and ω=0.344. The critical density can be calculated as ρ_c= 0.25342/b. In Hu et al (Hu et al. 2013) study, there is an improvement that can improve the stability of the model and achieve a higher density ratio with a simple coefficient with the EOS. The parameter in Hu's study can also adjust the interface thickness of the multiphase.

From Eq. (7.14) the effective density of the fluid is given by Eq. (7.19):

$$\psi(x) = \sqrt{\frac{2(p_{EOS} - \rho c_s^2)}{Gc^2}} \tag{7.19}$$

The value of G is not important, and its function is to make sure the equation is above 0. With the effective density of each node, we can calculate the fluid-fluid interaction force $\mathbf{F}_{\text{int}}$ for multiphase (Shan and Chen 1993) as Eq. (7.20) and Eq. (7.21):

$$\boldsymbol{F}_{\text{int}}(x) = -G\psi(x,t)c^2 \sum_{1}^{18} w_\alpha \psi(x + \boldsymbol{e}_\alpha \delta t, t)\boldsymbol{e}_\alpha \tag{7.20}$$

$$w_\alpha = \begin{cases} 1/6 & \alpha = 1-6 \\ 1/12 & \alpha = 7-18 \end{cases} \tag{7.21}$$

The body force $\mathbf{F}_b$ can be calculated in different schemes (Chen et al. 2014) Eq. (7.22) and Eq. (7.23):

$$\mathbf{F}_b = \rho(x)\mathbf{g} \tag{7.22}$$

$$\mathbf{F}_b = \rho(x)\mathbf{g}\left(1 - \frac{\langle\rho\rangle}{\rho(x)}\right) \tag{7.23}$$

Where $\langle\rho\rangle$ is the average density of the fluid domain. The Eq. (7.23) is more suitable for periodic boundary cases without walls.

When the multiphase droplet or bubble contact solid hydrophobic or hydrophilic walls, the fluid-solid interaction (Li et al. 2014) and wetting conditions can be implemented. The fluid-solid force can be calculated as Eq. (7.24):

$$\mathbf{F}_s = -G_w \psi(x) \sum_{0}^{18} \omega_\alpha \psi(x) B_n(x + e_\alpha) e_\alpha \tag{7.24}$$

B_n is a function related to the solid fraction of the fluid neighbour site, pure solid is 1 and pure fluid is 0.

It is worth noting that the method above Eq. (7.24) will change the density of fluid close to the solid wall and the value increases or decreases with the absolute value of G_w. It is neglectable when the solid wall is not moving or the fluid flow is stable, but these phenomena will generate problems such as density oscillation when it is not a fixed solid wall and coupling with other methods. It is necessary to find a fluid-solid force scheme that does not obvious change the density around walls and can achieve different contact angles.

Here, the author proposes a new version of the solid-fluid force that only act on the interface of the multiphase and avoid the density collective effect on the solid interface and will not cause problems when coupling with other methods such as DEM in multiphase problems. The new scheme of solid-fluid force is given by Eq. (7.25):

$$\mathbf{F}_s = -G_w \psi(x) \sum_{0}^{18} \omega_\alpha \left| \psi(x) - \psi(x + e_{\alpha'}) \right| B_n(x + e_\alpha) e_\alpha \tag{7.25}$$

Where α' is the opposite direction of α and the $\psi(x+e_{\alpha'})$ is the effective density of $x+ e_{\alpha'}$ node. The contact angle results of the new fluid-solid force are shown in the next section.

The total force at the fluid node thus can be Eq. (7.26):

$$\mathbf{F} = \mathbf{F}_{\text{int}} + \mathbf{F}_b + \mathbf{F}_s \tag{7.26}$$

For the multiphase model using non-ideal fluid EOS, there is always a problem with thermo-consistence (Li et al. 2013). To solve it, Li et al (Li et al. 2013) proposed a new scheme with a coefficient σ to adjust and achieve the thermos-consistence. The improved $\bar{\mathbf{S}}$ (Mu et al. 2017) with Shan-Chen multiphase model in MRT extra force term can be expressed as Eq. (7.27):

$$\bar{\mathbf{S}} = \begin{bmatrix} 0 \\ 38(u_x F_x + u_y F_y + u_z F_z) + \dfrac{114\sigma \mathbf{F}^2}{\psi^2(\dfrac{1}{s_e} - 0.5)} \\ -11(u_x F_x + u_y F_y + u_z F_z) \\ F_x \\ -\dfrac{2}{3}F_x \\ F_y \\ -\dfrac{2}{3}F_y \\ F_z \\ -\dfrac{2}{3}F_z \\ 2(2u_x F_x - u_y F_y - u_z F_z) \\ -2u_x F_x + u_y F_y + u_z F_z \\ 2(u_x F_y - u_z F_z) \\ -u_y F_y + u_z F_z \\ u_y F_x + u_x F_y \\ u_z F_y + u_y F_z \\ u_z F_x + u_x F_z \\ 0 \\ 0 \\ 0 \end{bmatrix} \tag{7.27}$$

Where $\mathbf{F}$ is the total fluid-fluid interaction force F_{int}, F_{x}, F_{y}, and F_{z} are the total force F_{total} in three directions. σ is the parameter to achieve thermodynamic consistency.

In the original Shan-Chen model, there is no way to adjust the surface tension of multiphase, then the author adds another term to adjust the surface tension and this term is a scheme like pressure tension. In this study, the author used Li and Luo's (Li and Luo 2013) surface

tension adjustment method in three dimensions which has also been applied by Ammar et al (Ammar et al. 2017) as Eq. (7.28):

$$C=\begin{bmatrix} 0 \\ \frac{2}{5}s_e(Q_{xx}+Q_{yy}+Q_{zz}) \\ 0 \\ 0 \\ 0 \\ 0 \\ 0 \\ 0 \\ 0 \\ -s_\upsilon(2Q_{xx}-Q_{yy}-Q_{zz}) \\ 0 \\ -s_\upsilon(Q_{yy}-Q_{zz}) \\ 0 \\ -s_\upsilon Q_{xy} \\ -s_\upsilon Q_{yz} \\ -s_\upsilon Q_{xz} \\ 0 \\ 0 \\ 0 \end{bmatrix} \tag{7.28}$$

The terms of Q are calculated from the following equation:

$$Q=\kappa\frac{G}{2}\psi(x)\sum_{i=1}^{18}w(|\boldsymbol{e}_\alpha|^2)[\psi(x+\boldsymbol{e}_\alpha)-\psi(x)]\boldsymbol{e}_\alpha\boldsymbol{e}_\alpha \tag{7.29}$$

The calculation of $\boldsymbol{e}_\alpha\boldsymbol{e}_\alpha$ can be $Q_{xx} = \boldsymbol{e}_x\boldsymbol{e}_x$, $Q_{xy} = \boldsymbol{e}_x\boldsymbol{e}_y$.

With the modifications in LBM the pressure calculation can be:

$$\mathbf{P}_{original}=(\rho c_s^2+\frac{Gc^2\psi^2}{2})\mathrm{I}+\frac{G\psi}{2}\sum_\alpha w_\alpha[\psi(x+e_\alpha\delta_t)-\psi(x)]e_\alpha e_\alpha \tag{7.30}$$

$$\mathbf{P}_{new}=\mathbf{P}_{original}+2G^2c^4\sigma|\nabla\psi|^2\mathbf{I}+(1+2\kappa)\frac{Gc^4}{12}\psi\nabla^2\psi\mathbf{I}+(1-\kappa)\frac{Gc^4}{6}\psi\nabla\nabla\psi \tag{7.31}$$

Where

$$\nabla^2\psi = 2\sum_{\alpha\neq 0} w(|e_\alpha|^2)(\psi(x+e_\alpha)-\psi(x)) \tag{7.32}$$

$$\nabla\psi = \sum_{\alpha} w(|e_\alpha|^2)\psi(x+e_\alpha)e_\alpha \tag{7.33}$$

With the Eq. (7.30-7.33), it is easy to calculate the surface tension at each LBM fluid node.

Since the density of multiphase is initialised artificially, it is needed to do a smoothing on initialisation. For density initialization, for the stability of the bubble and to reduce the calculation time, the initialisation of vapour-liquid bubble (Jain 2010) can be ：

$$\rho(x,y,z,t=0) = \rho_{ave} + \frac{\rho_l-\rho_v}{2}\tanh(\frac{2}{D_{thick}}\sqrt{(x-x_c)^2+(y-y_c)^2+(z-z_c)^2}-r) \tag{7.34}$$

Where *D* is the thickness of the interface, larger means more stable. *c* represents the centre of the bubble or droplet, *r* is the radius of the bubble.

After the calculation of macroscopic parameters such as velocity and density, it is needed to update the viscosity of each fluid node to ensure their density-viscosity relationship when calculating the macroscopic results and update for the next step. The viscosity at the multiphase interface can be smoothed as (Fang et al. 2017):

$$\nu = \nu_l\frac{\rho-\rho_v}{\rho_l-\rho_v} + \nu_v\frac{\rho_l-\rho}{\rho_l-\rho_v} \tag{7.35}$$

ρ is the local density and *v*, *l* mean the vapour and liquid phases.

The classical simple static boundary conditions (such as periodic boundary and bounce-back boundary) are well described in the work of Nie and Lin (Nie and Lin) and simply used in this thesis.

7.2.2 DEM Equations

The solid particles' movement is controlled with DEM. The translational and rotational velocities of a single particle within a suspension based on Newton's equation in a finite difference scheme (Peng et al. 2010) are reported as:

Translational

$$m_p \frac{dv_p}{dt} = \mathbf{F} \tag{7.36}$$

And rotational

$$I_p \frac{dw_p}{dt} = \mathbf{M}_C \tag{7.37}$$

Where m_p and v_p are the mass and translational velocity of the particle, respectively. **F** is the total force experienced by the particle such as contact force, surface force, drag force and Brownian random force. I_p and w_p are the rotational inertia and rotational velocity, respectively. $\boldsymbol{M}_C$ is the total torque exerted on the particle. In colloidal suspensions, particle *i* often collides with multiple neighbouring particles simultaneously.

In this study, **F** in DEM includes:

$$\mathbf{F} = f_C + f_B + f_{LBM} + f_{Buo} + f_G \tag{7.38}$$

Where $\boldsymbol{f}_C$ is the real-contact force, $\boldsymbol{f}_B$ is the Brownian random force, $\boldsymbol{f}_{LBM}$ is the force from LBM when it is a momentum exchange method and only single-phase flow, it becomes drag force and $\boldsymbol{f}_G$ is the gravity force.

For Brownian force, it becomes the dominant transport mechanism for particles less than 500 nm. The Brownian random force (Peng et al. 2010) is modelled as a Gaussian white noise process can be Eq.(7.39):

$$F_B = \xi \sqrt{\frac{6\pi d_p \mu_f k_B T}{\Delta t_s}} \tag{7.39}$$

Where k_B =1.38×10-16 erg/K is the Boltzmann constant, T is the Kelvin temperature, and t_s is the particle time step. The parameter ξ is a Gaussian random number with zero mean and unit variance. It is of great importance to generate a random number, which is able to represent the range of [0,1] and most importantly has good statistical properties. The Polar method described by Ross (Ross and SheldonM) is employed to generate the white Gaussian noise:

$$\xi = \psi \sqrt{-2\log(S)/S} \tag{7.40}$$

Where $S = \psi_1^2 + \psi_2^2$, and ψ, ψ_1, ψ_2 is the random number between [-1,1].

7.2.3 Two-way LBM-DEM Coupling

To couple the LBM and DEM, an immersed moving boundary method was proposed by Noble and Torczyniski (Noble and Torczynski 1998) and then developed by many researchers (Owen et al. 2011, Chen et al. 2013, Yang et al. 2018, Wang et al. 2019). In this method, the LBE is modified to include a term which is dependent on the proportion of the nodal cell that is covered by solid. In the immersed moving boundary method, for convenience, we use the SRT scheme as an example to illustrate the coupling method which is also easy to be expanded to MRT schemes. The schematic of immersed moving boundary method with force calculation explanation is shown in Fig.7-1. The LBE is modified to include an additional collision term, Ω_α^s, and can be written to include an extra force term as Eq. (7.41):

$$f_\alpha(x + c_\alpha \delta t, t + \delta t) - f_\alpha(x,t) = -(1 - B_n)[\frac{1}{\tau}[f_\alpha(x,t) - f_\alpha^{eq}(x,t)]] + \sum_s B_s \Omega_\alpha^s + (1 - B_n)\delta t \mathbf{F}_{total} \tag{7.41}$$

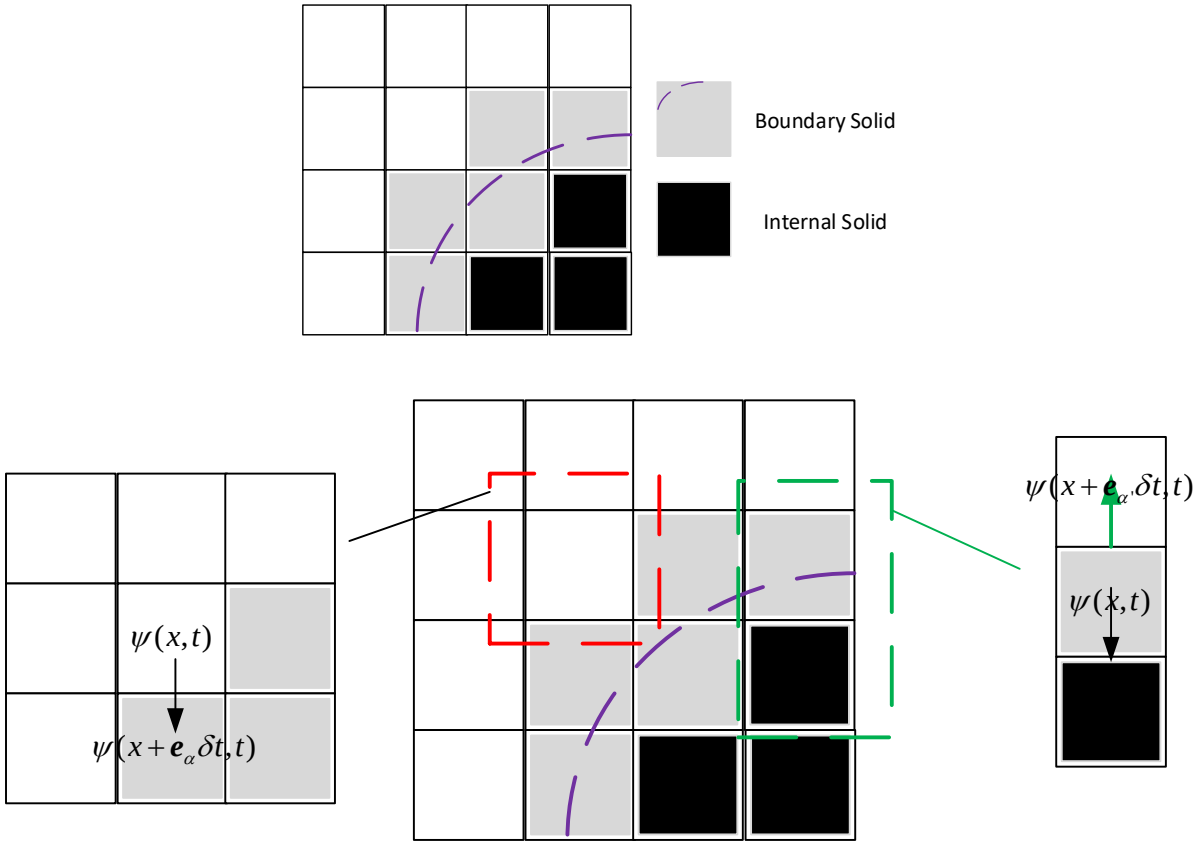

Figure 7-1 Schematic of partially solid nodes and boundary effective density.

Extra forces should also be calculated on partially solid nodes and the summary is the $\mathbf{F}_{totoal}$. When the node is a fluid node, then the force calculation is normal and when it points to an internal solid node, then the neighbour node at $x+\boldsymbol{e}_\alpha$ direction becomes the neighbour node at $x+\boldsymbol{e}_{\alpha'}$ (opposite direction) node. In Fig.7-1, when the local node is a fluid node and it points to a boundary solid node (grey node), then the calculation is normal (black arrow direction) as it points to a fluid node. However, when the local node is a boundary solid node and it points to an internal solid node (pure black), then, it should use the opposite direction node (green arrow direction) as an alternative and calculate the force. The additional collision operator, Ω_α^s, is based on the concept of the bounce-back rule of the non-equilibrium part of the particle distribution function and can be calculated as Eq. (7.42):

$$\Omega_\alpha^s = [f_{\alpha'}(x,t) - f_{\alpha'}^{eq}(\rho, v_p)] - [f_\alpha(x,t) - f_\alpha^{eq}(\rho, v_p)] \tag{7.42}$$

v_p is the body velocity of the particle, α' means the opposite direction. Bn is the weighting function of the coverage of solid which is 1 for pure solid and 0 for pure fluid nodes. When the boundary node is a pure solid node, it will back to the simple bounce-back condition.

The drag force from the LBM is still calculated with the momentum exchange method (Mei et al. 2002) which has been developed for years (Caiazzo and Junk 2008, Chen et al. 2013, Wen et al. 2014). The Galilean invariant momentum exchange scheme (Wen et al. 2014) is expressed as Eq. (7.43):

$$F_{drag}(x_s) = (e_\alpha - v) f_\alpha(x_f, t) - (e_{\alpha'} - v) f_{\alpha'}(x_b, t) \tag{7.43}$$

Where $\tilde{f}$ is the distribution function after the collision and before streaming. This method actually calculated the exchange of distribution functions related to the solid wall during the whole process. The schematic of momentum exchange is shown in Fig.7-2.

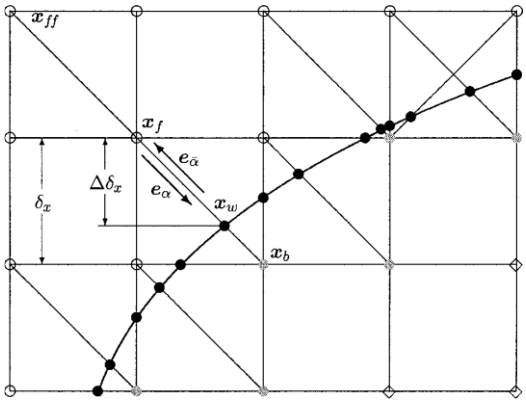

Figure 7-2 The schematic of momentum exchange method (Mei et al. 2002).

At each boundary node point, when droplet or bubble contact with the solid way, droplet or bubble would attach and adsorb on the solid way due to the mini free energy. Since there is a force that attracts the droplet adsorbed at the interface, there should be a counter force to the solid object. There are only several papers of study (Joshi and Sun 2009, Fabian et al. 2011, B et al. 2013, Chen et al. 2015) focused on the multiphase force acting on the solid object. In

this study, the author combines some of the former researcher's work and used a novel scheme to calculate the $\mathbf{F}_{adh}$ adhesion force caused by the multiphase model at the solid boundary.

There are mainly two parts that contribute to the adhesion force from the neighbour fluid nodes. One comes from the fluid-fluid interaction, and another comes from the fluid-solid interaction. The adhesion force should follow the main two principles (Chen et al. 2015):

1). When a particle is completely submerged in one of the fluid phases, particle trajectory and total force from LBM should be close to the one obtained by the single phase, as long as the particle is far away from the fluid interface.

2). When a particle is suspended on the interface of the two-phase fluid, the final static contact angle determined by the stable position of the particle, under the condition of zero gravity, should be consistent with the contact angle formed by a flat solid surface in contact with the two fluid components.

It is easy to analyse that if the adhesion force is the simple counter force of the boundary solid node when the particle is immersed in the middle position of the interface, the forces from the liquid phase and from the gas phase are not balanced and the object will move towards the liquid phase due to large effective density in liquid nodes. The object will be attracted to the liquid phase and finally totally immersed. Thus, it is needed to propose a novel scheme that can follow the main two principles and realise the adsorption process.

Based on the main rules, a novel fluid-fluid part adhesion counter force from the fluid is proposed. The 1st part $\boldsymbol{F}_{\text{int,adh}}$ can be Eq. (7.44):

$$\boldsymbol{F}_{\text{int},adh}(x) = -G\psi(x,t)c^2\sum_{1}^{18} w_\alpha \,|\psi(x+\boldsymbol{e}_\alpha\delta t,t)-\psi(\rho_{ave})|\,\boldsymbol{e}_\alpha \tag{7.44}$$

Where α directions are directions pointed from the solid to the fluid nodes. The equation in the absolute sign means the deviation between the density to the average density ρ_{ave}. This adhesion force scheme is calculated near the interface where the density difference between average density should be large and used the gradient of the effective density.

The 2nd part $\mathbf{F}_{s,adh}$ is the force caused by the fluid-solid addition force (Joshi and Sun 2009) however, that scheme is too large for the new $\mathbf{F}_{adh}$, thus a modified version of $\mathbf{F}_{s,adh}$ for spherical particles in this study can be calculated as Eq. (7.45):

$$\mathbf{F}_{s,adh} = -(G_w / 3)\psi_c(x)\sum_{0}^{18}\omega_\alpha\psi(x)B_n(x+e_\alpha)e_\alpha \tag{7.45}$$

The ψ_c is the critical effective density which can be calculated with the definition of EOS. The force should be calculated at all solid nodes. In this equation, one effective density is replaced by the critical effective density to represent the middle interface effective density of the multiphase.

The new scheme does not obey the mainly two rules and when the object is close to the interface, the force will attract the object to the interface and reach 0 on the stable interface. Then, stop the object and leave the interface. When fluid is all covered by the same phase of fluid, the net force can be close to 0.

The total adhesion force caused by the multiphase model can be summed as Eq. (7.46):

$$F_{adh} = F_{\text{int},adh} + F_{s,adh} \tag{7.46}$$

The force calculation should also consider the solid fraction of the solid node which has been considered in the equation of the additional operator but not in the adhesion force calculation. The adhesion force curve in LBM units of D =16 diameter fixed single spherical particle

along the covering diameter of the particle with G_w= 0 is shown in Fig. 7-3. The initial liquid interface is adjusted to realise different immersed diameter cases.

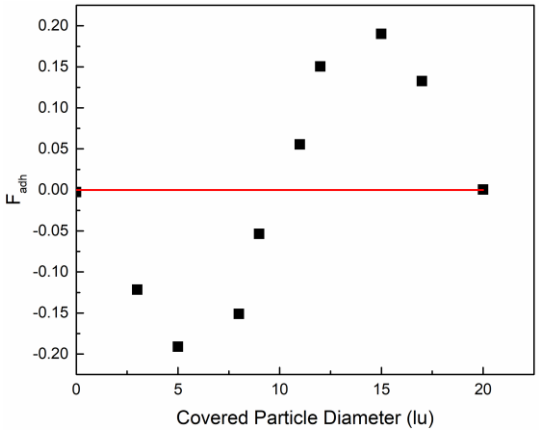

Figure 7-3 F_{adh} vs covering diameter with G_w = 0.

When simulating particles near the interface, it is hard to eliminate the pseudo current effect near the multiphase interface (Joshi and Sun 2009, Chen et al. 2015) which will generate a large drag force and affect the particle movement. In fact, when the particle is close to the interface, the particle should be dominated by the multiphase interface, not the drag force.

7.2.4 Force Conversion between LBM and DEM

Since DEM normally uses physical units and only converts the size into Lattice units, it is necessary to convert the macroscopic information such as density, velocity, and forces. The conversion between the LBM, DEM and the physical units is shown as follows based on the principle of non-dimensionless number consist (Krüger et al. 2016).

In this study, we mark the macroscopic parameters in lattice with a subscript L, for density, velocity, length and time are ρ_L, u_L, l_L, and t_L. Then we set the density, velocity, length and time in real units as ρ (kg/m^3), u (m^2/s), l (m), and t (s). The ratio between real units and lattice units are calculated as $C_l = l / l_L$, $C_t = t / t_L$, $C_\rho = \rho / \rho_L$. Based on the definition of velocity, $u = l / t$. The ratio of velocity can be calculated as $C_u = C_l / C_t$. Reynolds number (Re)

is used as the dimensionless number in most cases and used in the study, and the definition of Re is shown as Eq. (7.47):

$$\mathrm{Re} = \frac{ul}{\upsilon} = \frac{u_L l_L}{\upsilon_L} = \mathrm{Re}_L \tag{7.47}$$

Where the u is the velocity, l is the character length and υ is the kinematic viscosity of the bulk fluid (m^2/s). The lattice Re_L number should be equal to the real Re number. According to the Re number, the kinematic viscosity ratio can be $C_\upsilon = C_l\ C_u = C_l^2 / C_t$. Then the ratios of pressure (p) surface tensor (σ) and forces (F) can be easily defined based on their definitions in Eq. (7.48 – 7.50):

$$C_p = \frac{C_\rho C_l^2}{C_t^2} = C_\rho C_u^2 \tag{7.48}$$

$$C_\sigma = C_p \tag{7.49}$$

$$C_F = \frac{C_\rho C_l^4}{C_t^2} \tag{7.50}$$

It is worth noticing that it is not the absolute value of the pressure, but the pressure difference has a physical meaning. Based on the equations above it is easy to convert lattice units to physical units and DEM units which used mostly physical units but only have a length ratio.

The time steps are using the same logic as Owen et al (Owen et al. 2011) study and keep the DEM steps several integral times of LBM steps to ensure the fluid flow can be well developed.

7.3 Verifications of the LBM-DEM Model

7.3.1 Grid Independence Verification.

To choose a suitable particle size for simulation, a grid-independent test is conducted as follows. Flow around the sphere is a classical simulation test case to check the drag force coefficient (C_d) of particle and the accuracy of the simulation. The drag force of a single spherical particle can be calculated as Eq. (7.51):

$$C_d = \frac{2F_d}{U^2 A} \tag{7.51}$$

Where the F_d is the drag force and can be calculated from the momentum exchange method in LBM calculation, U is the flow relative velocity and A is the cross-sectional area of the spherical particle.

In this test, the diameter of spherical particles D = 12, 16, 20, and 24 were tested and the deviation percentages between simulation and the empirical model result are shown in Fig.7-4. The computation domain is 80×80×150, the particle is placed at the middle position of the domain with a constant inlet velocity v = 0.0001 and relaxation time τ = 1. It is clear that the deviation changes little with the increase of diameter. For a good shape of spherical particles and considering the computational cost, D =16 is chosen as the diameter of spherical particles in this study.

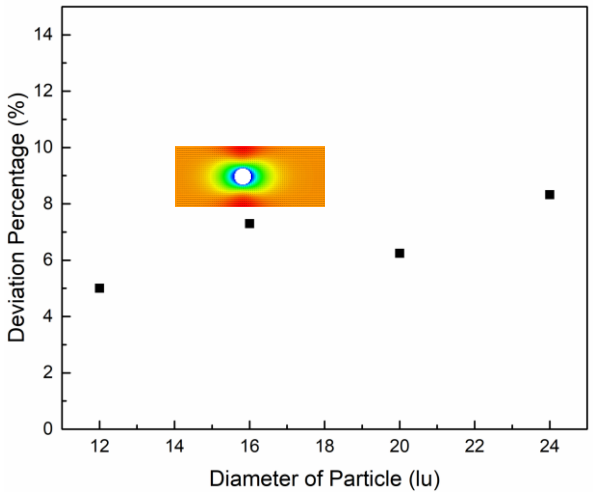

Figure 7-4 C_d deviation of a spherical particle between simulation results and empirical model results (Turton 1986) using D = 12, 16, 20 ,24.

7.3.2 LBM Model Verifications

Pipe flow is another common verification test for CFD simulation. In this study, pipe flow is simulated and compared with the analytical solution of Poiseuille flow (Bao and Meskas 2014, Portinari and Portinari 2015) which is a laminar flow driven by pressure difference or body force in a pipe. The simulation diameter of the pipe is D = 40, and length L =100, with body force g = 0.00001 at y direction and relaxation time τ = 0.6. With periodic boundary conditions in all directions. The comparison between the simulation result and analytical solution is shown in Fig.7-5. The pipe flow velocity on y direction agrees well with the analytical results with less than 5% deviation which is acceptable and less than single relaxation time LBM (Shi et al. 2006).

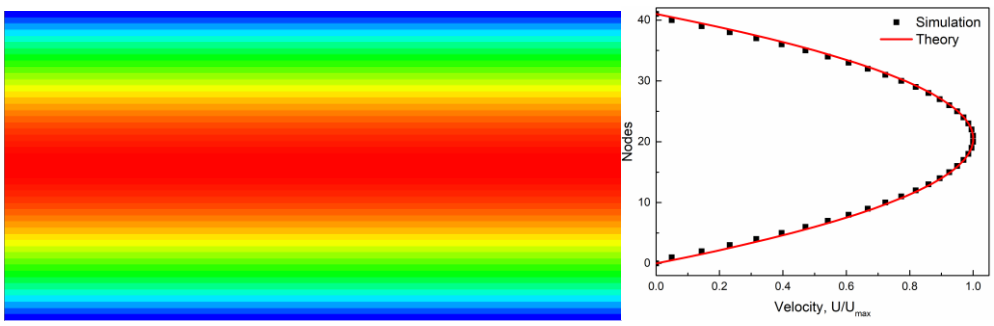

Figure 7-5 Simulation fluid flow and comparison of simulation results and analytical solution.

The flow around a spherical particle (D =16) in different Re numbers is also tested and compared in Fig.7-6. This test is usually used to check the drag force calculation. The calculation domain is 80×80×250, the particle is placed at (40, 40, 120), and the relaxation time τ =0.6. The inlet is a velocity boundary condition, and the outlet is an extrapolation boundary condition, other boundary conditions are periodic boundary conditions. Inlet velocities can be changed to achieve different Re numbers. The computation setups are the same in the grid verification test but with different velocities and viscosity to achieve different Re numbers. The simulation drag coefficient results are compared with empirical model results (Turton 1986). The deviation between simulation and empirical results is less than 8 % in all cases with Re between 0.001 and 200. Considering the pixel differences and the slight setup differences, we assume the drag force is accurate enough.

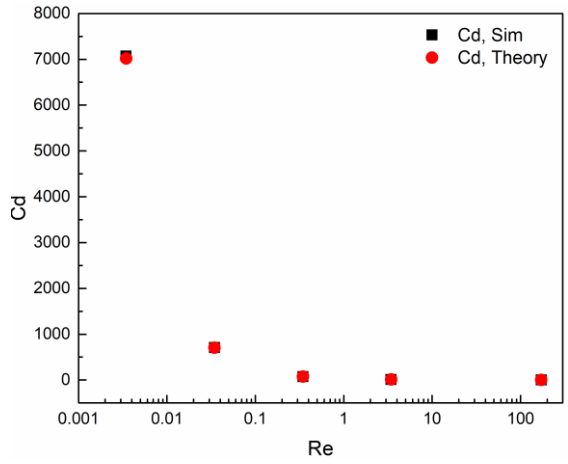

Figure 7-6 Flow around sphere Cd vs Re.

The contact angle test of a droplet on the plate is also conducted to verify the wettability change of the solid wall. The calculation is 120×120×87 with a 3-thickness solid wall at the bottom of the domain. All other directions are periodic boundary conditions. The spherical droplet was symmetrically initialized as D = 40 on the top of the plate with 1 node overlapping with the solid wall. The initial fluid density ρ_l = 8.76, gas density ρ_g = 0.02, with fluid and gas viscosity υ_l = 1, υ_g = 0.05, respectively. The thermos consistency coefficient T_c

= 0.13. The system is a gravity-free field with a solid wall bottom, and periodic boundary conditions are applied in other directions. The initial version contact angle results achieved by Eq. (7.24) are shown in Fig.7-7 which means the contact angle can be linearly change with the coefficient. This scheme will accumulate or repulse density around the solid interface when the solid wall is hydrophilic or hydrophobic. Because the forces act on all fluid nodes that contact with solid wall it will give them additional attractive force or repulsive force to achieve contact angles. This scheme is good at a wide contact angle range and can adjust wettability easily and linearly. However, it causes a stability problem and extra forces when solid objects were moving, thus, it is not considered very suitable to couple with moving boundaries.

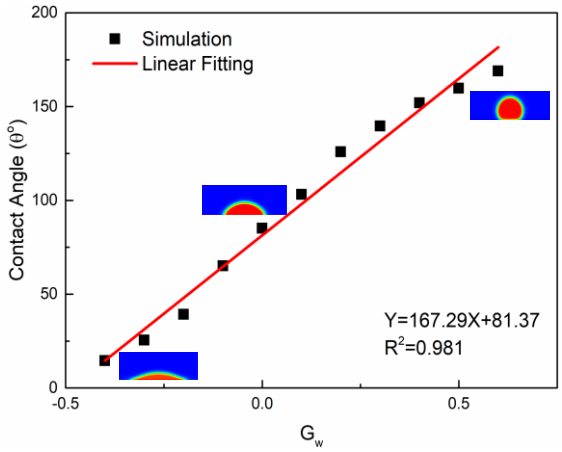

Figure 7-7 Initial version Contact angle vs G_w using Eq. (7.24).

With a new solid-fluid force scheme that mimics the wetting effect of the solid wall using Eq. (7.25), the new contact angle results are shown in. Fig.7-8.

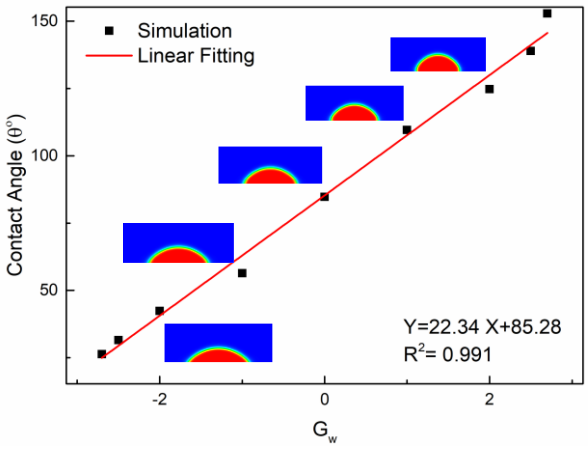

Figure 7-8 New version Contact angle vs G_w using Eq. (7.25).

The later fluid-solid force scheme has a narrow range of contact angle adjustment (about 25^o to 150^o), but it doesn't change the density of the solid interface and mainly effect the multiphase interface. Thus, it is better to combine with other methods and will not generate density oscillation problems during solid moving and no extra force when an object is immersed in a single phase. In this study, the author used this scheme as a novel fluid-solid force to treat the adjustment of the contact angle problems.

7.4 Single Particle Adsorption Simulation

7.4.1 Single Particle Adsorption Process

From the literature review, it is known that it is very hard to experimentally observe a single colloidal particle adsorbed at the liquid-gas interface. In this chapter, the author simulated a process of that single colloidal particle silica particle with different wettability settling and adsorbed at the interface. The computation domain of a single particle adsorption process is 80×80×120 with particle diameter D = 16 initially placed at (40, 40, 40) without initial velocities. The schematic of the simulation domain and boundary conditions are shown in Fig.7-9.

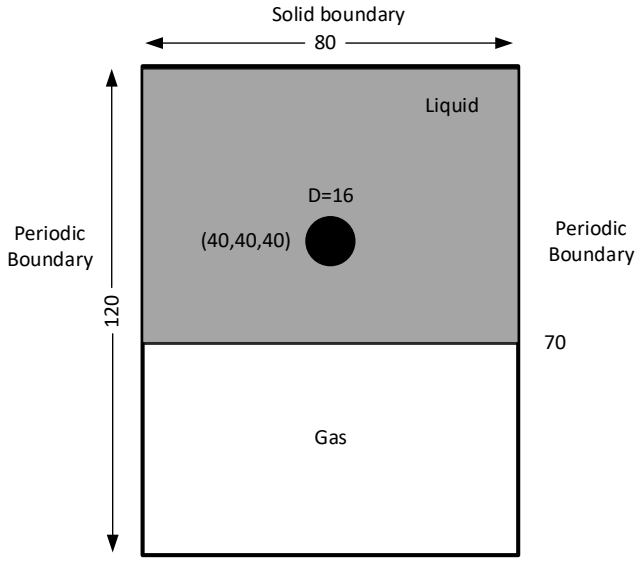

Figure 7-9 Schematic of single particle adsorption.

In order to keep the simulation stable and remain the large density ratio between liquid and gas phases. The initial fluid density ρ_l = 8.76, gas density ρ_g = 0.02, the thermos consistency coefficient σ = 0.13, the liquid-gas interface position is Z = 65. To mimic the large viscosity ratio between liquid and gas phases and maintain the stability of the simulation, the author uses fluid kinetic viscosity υ_l=1, gas kinetic viscosity υ_g=0.05, and the viscosity ratio is 20. LBM simulation can be unstable when the fluid velocity is too large, where compressive effects will show. To keep the numerical simulation stable, the maximum velocity of the particle is capped at 0.1 m/s to avoid a large velocity change when the particle is close to the interface where the adhesive force is huge. There are simulation results with three different wettability according to the contact angles of Original SiO_2, SiO-butane, and SiO-hexane, which measured experimentally with silica wafers and shown in Chapter 3 Fig.3-6. With the linear fitting results of contact angle and the solid-fluid interaction factor, we can set the wetting factor in the simulation as -2.7, -1.8 and -0.9 for Original SiO_2 (25.3º), SiO-butane (46.6º), and SiO-hexane (68.5º), respectively. It is worth to note that also only experimentally studied silica contact angle up to SiO-hexane, to further study the hydrophobic effect of particles, an additional 90º contact angle case (not hydrophilic and not hydrophobic) which is

marked as SiO-90^{o} is also conducted. Earth gravity simulation cost a long time on a small scale. To accelerate the simulation, in this study, instead of earth gravity the author used an acceleration of 1085 m^2/s which is the average acceleration of 1000 rpm in LUMiSizer. Here, In order to convenient compare particle adsorptions in different gravity force conditions, a dimensionless time can be used to check the results which are suitable for different gravity cases (Tilehboni et al. 2015) with $T^*=t/(d/g)^{0.5}$ to compare them in a unit time.

The Bond number is a dimensionless number that can be used to describe the effect ratio of gravity force and surface tension force. The Bond number of adsorption particles is defined as:

$$Bo = \frac{\Delta\rho g R^2}{\gamma} \tag{7.52}$$

Where $\Delta\rho$ particle is the density difference between particles and the bulk fluid, g is the gravity or acceleration the particle experienced R is the radius of the particle and γ is the surface tension of the interface. In order to prove that the gravity change to the adsorption process can be ignored, a test with different gravity is conducted which generated different Bo numbers in a small magnitude range.

The stable state of Original SiO_2 particle adsorption results with different gravity forces on particles are shown in Appendix (Fig. A20). It shows that although the gravity force on the particles changes several magnitudes from 1 to 1000 m/s^2, and the Bond number increases the same magnitude from ($1.53e^{-10}$) to ($1.53e^{-7}$), the effect of gravity is still very small and not large enough to influence the adsorption process visibly. Thus, in the later study of particle adsorption, to accelerate the calculation and obtain the result faster, the acceleration of 1085 m/s^2 is used.

The terminal velocity of a single particle in a multiphase fluid phase is checked with the terminal velocity of single particle settling. The theoretical terminal velocity of 800 nm silica particle under 1085 m^2/s acceleration is 4×10^{-5} m/s and the average settling velocity in the settling process of simulation is 3.633×10^{-5} m/s. Thus, the settling velocity of particles is verified. The adhesive force caused by the multiphase region when particles away from the multiphase interface are small and the magnitude is about 1% of drag force, thus, can be also ignored in single phase situation.

The particle adsorption behaviour process showed that the model can simulate the process with different contact angles. The adsorption results of single particles with different wettability are shown in Fig.7-10 to 7-12. The additional SiO-90^o results are shown in Appendix (Fig.A19). The initial time, when the particle is close to the interface, is marked as $T^* = 0$, given when the adhesion force F_{adh} starts to dominate the adsorption process. The longer time settling of the single particle is omitted in the Figures. There are mainly 4 steps of particle adsorption: settling, contact, oscillation, and stable adsorption. In the settling step, the particle is dominated by the body force and moves close to the multiphase interface. In this stage, the adhesive force generated by the multiphase model can be ignored. The balance between body force, buoyancy force and drag force allow the particle reaches a terminal velocity. Then, when the particle is close to the multiphase interface, the adhesion force caused from the multiphase effect generally dominated the movement of the particle and attracts it to the multiphase interface to reach the minimum free energy position. After contact with the interface, a short time oscillation shows in the simulation (when the particle starts the adsorption and oscillates around the liquid-gas interface). The immersed interface area therefore changes and allows the particle to reach its stable position. Finally, after the short time oscillation, the particle reaches a balance position and is stably adsorbed at the interface. Only when the extra forces are larger than the maximum adhesive force of the

particle which is more than thousands of normal gravity forces, the detachment will occur, which does not eventuate in these simulations. These simulations allow us to detail the adsorption process, and how it changes with particle wettability, where also oscillation period increases with the hydrophilicity.

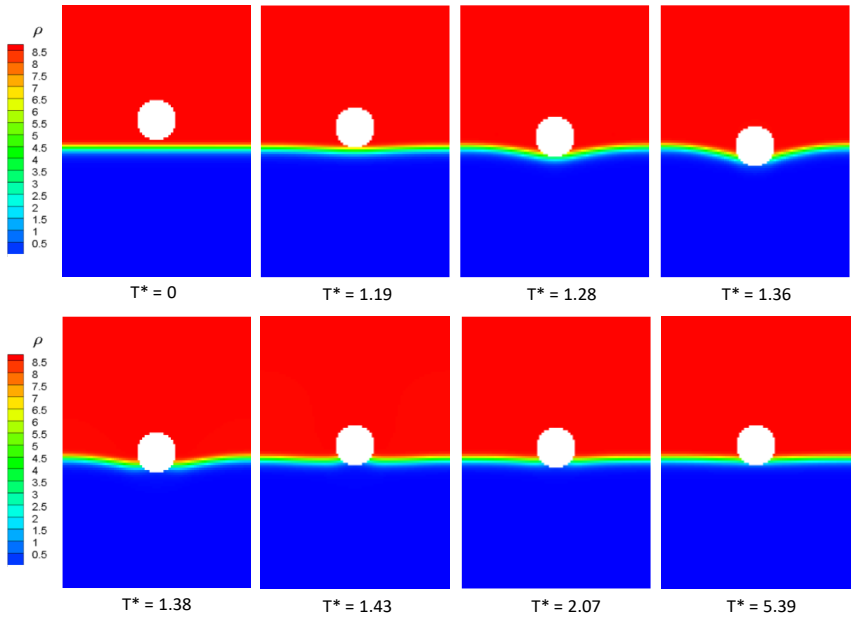

Figure 7-10 Single particle adsorption simulation process using Origin SiO_2 ($T^*=t/(d/g)^{0.5}$).

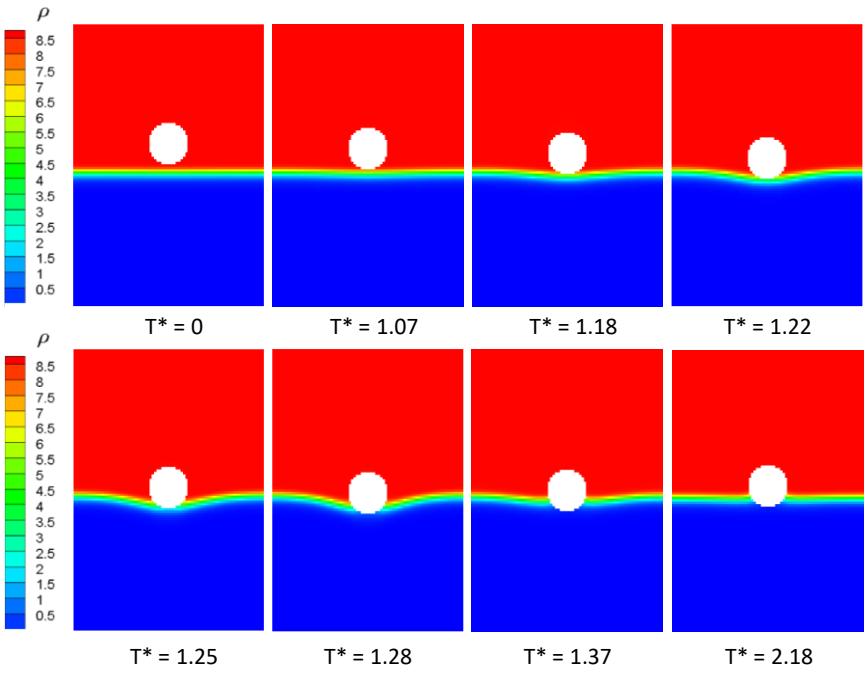

Figure 7-11 Single particle adsorption simulation process using SiO- butane ($T^*=t/(d/g)^{0.5}$).

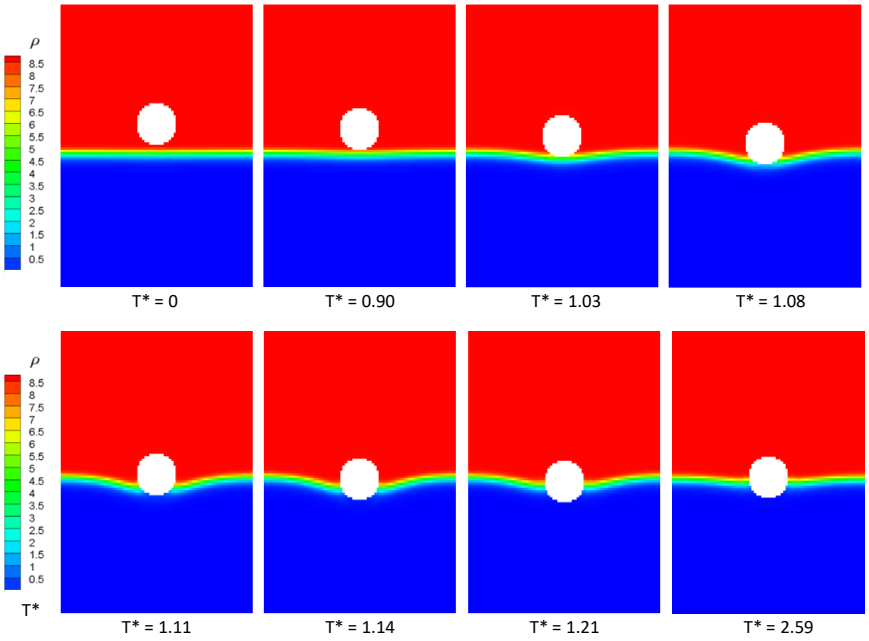

Figure 7-12 Single particle adsorption simulation process using SiO- hexane ($T^*=t/(d/g)^{0.5}$).

7.4.2 Particle Adsorption Analysis

The adsorption detail of single colloidal particle is hard to obtain, and the force experienced during the adsorption process is nearly impossible to track. However, the knowledge of single particle adsorption and the force the attracting the particle is significant in the adsorption process and the stable state. In order to study the stable process of particle adsorption, the adhesion force F_{adh} and particle position are tracked and compared with wettability as shown in Fig.7-13. The adhesion force is recorded when the force is 10 times larger than the calculated drag force. The oscillation time means the time that a particle needed to be stably adsorbed at the liquid-gas interface from the time that attracted by the liquid interface. The adsorption time (in real units and dimensionless units) from contact to stability is recorded in Table.7-1.

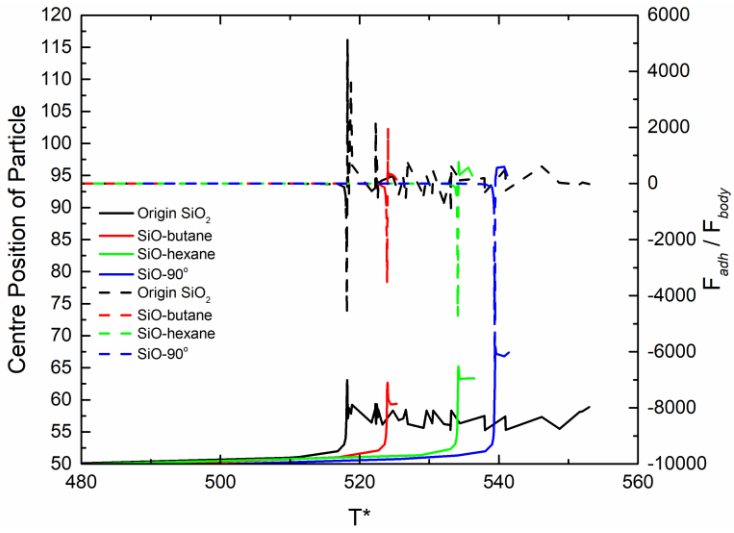

Figure 7-13 Comparison of adsorption force F_{adh} (dash line) and the centre position of particle (solid line) for the single particle with different wettability when close to the multiphase interface.

It is clear from the T^* simulation results of silica particle with different wettability, the time that the particle touches the liquid interface slightly changed and generally increases with particle hydrophobicity. This caused by the F_{adh} form the multiphase model which slightly attached the particle to the interface. The force is very small when the particle away from the interface but will generally increase when particles close to the interface. The Original SiO_2 has a larger hydrophilicity, and this effect shows more obvious than more hydrophobic particle such as SiO-hexane and that effect increased particle settling when it close to liquid interface and finally caused shorter T^* when Original SiO_2 touch the interface. When check the time cost on adsorption where the F_{adh} starts to dominate the movement, it is obvious to see that there is an oscillation time that starts from the point of particle adsorption and ends when the particle is stable. The stable state is defined as the point where the centre of the particle only oscillates in a 1-pixel width length. That oscillation time can reflect the stability of adsorption in some degree, where particles that are attached to the liquid interface, but not stably captured by the interface, oscillate up and down at the interface to a larger extent. The hydrophilic particle such as Original SiO_2 shows early adsorption start time but also observed larger oscillation time and the F_{adh} force has a larger oscillation magnitude. The whole

adsorption time insists the particle attachment time and the oscillation time. For Original SiO_2 the particle attachment time is relatively short because the immersed length of the particle is quite small, and the attachment almost finished immediately after the touching with the interface but cost more on oscillation. However, for hydrophobic particles such as SiO-hexane, the immersed length is larger and need more time to get particle immersed but be stable quickly. Experimentally, more particle adsorbed at the interface may be back into the bulk interface by the extra influence of this oscillation and thus generating additional deviations. However, the attachment time is usually very short for colloids and the increase is not much obvious, thus, particles that more hydrophobic such as SiO-hexane show a significant less time cost than that of Original SiO_2. The occupied cross-section surface area of SiO-hexane is 1.95 times large than Original SiO_2, and it is easy to say that the SiO-hexane particles are much more stable and will be less influenced by flow dynamic effect or contact forces from other particles in multi-particle cases. Although there is no experimental data of SiO-90^o, it continues the trend with deeper immersed length and shorter oscillation time which shows more stable. The Oscillation time can be used to calculate a single particle adsorption rate in the later analysation.

Table 7-1 Oscillation time cost in real units and in dimensionless time cost for single particle adsorption process.

	Original SiO_2	SiO-butane	SiO-hexane	SiO-90^o
Oscillation time (real), s	9.66×10^{-4}	2.345×10^{-5}	1.028×10^{-5}	8.40×10^{-6}
Oscillation time (dimensionless), T^*	34.74	0.8636	0.3784	0.30935
Stable centre position	(40,40,58.13)	(40,40,59.32)	(40,40,63.36)	(40,40,66.78)

It is obvious that the Original SiO_2 takes a longer time to be stable and hydrophobic particles are easier to reach stable and stop the oscillation. The stable state of particles with different

wettability is shown in Fig.7-14. The simulated stable particle contact angle is slightly different from the wafer contact angle with the same energies, where the deviation is about 10%. The immersed volume of the particle increases with particle hydrophilicity so does the deformation of the interface and the cross-section area of the particle. For the hydrophilic particles, the adhesion force added on the particles is relative larger than close neutral particles (SiO-hexane and SiO-90^{o}) and the force is helpful to stable the particle. The interfaces of Fig.7-14 (c) and (d) are not shown flat interface because one node variation of interface generate a very small adhesion force due to the small hydrophilicity. However, the increased pseudo drag force caused by the pseudo current of the multiphase model at the interface enlarged the drag force effect and have an additional pull-out force to the particle and push it out of the fluid interface. The pseudo drag force is relatively small for hydrophilic particles in the simulation comparing with the large adhesion force but obvious when particle is close-neutral. The unphysical phenomena are caused by the multiphase pseudo current and can be eliminated if the pseudo current is none.

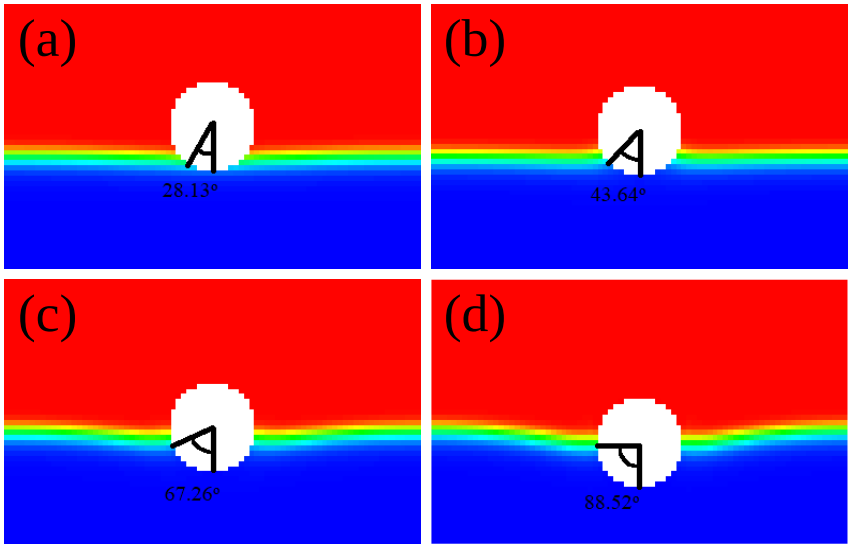

Figure 7-14 Contact angle and contact lines of single particles with different wettability at stable state, (a) Origin SiO_2, (b) SiO-butane, (c) SiO-hexane, (d) SiO-90^{o}.

From the results of the simulation, it is clear that with the contact angle increasing, the fluid covering area at the surface of the particles decreases. The particles stable position also

increases with hydrophobicity which is shown in Table 7-1 meaning there is less immersed part in the liquid phase. Physically, the detachment energy of the particle at the interface increases with hydrophobicity. It is evident that the simulation can not only realise single-phase fluid flow but also mimic the process of particle adsorption at the liquid-gas interface and achieve different wettability. The force ratio between the gravity and adsorption force also shows that normally adsorption is irreversible, with more hydrophobic the particle is, the more irreversible the cases will show due to the increase of cross-section area. For more hydrophilic particles as Original SiO_2, it is easier to immerse and back to the liquid phase by extra forces. It can explain why the R^2 in Chapter 6, Fig.6-17, for hydrophilic particles are smaller and means the results are not perfectly stable because of the long oscillation time. It may also explain why the Original SiO_2 is likely immersed in the Langmuir trough experiment (and therefore no surface pressure experiments were possible). The adsorption area of Original SiO_2 is quite small, and the minimum adsorption force is only several magnitudes of body force and could be overcome by the injection effect in the experiment (where the spread of particles may push particles into the bulk).

Unstable adsorption and oscillation may also influence the adsorption rate and disturb other particle adsorptions. A smaller adsorption cross-section area means less stability for adsorption and the particle may move back to the bulk phase when influenced by dynamic effects or other particle influences. However, particles with a more hydrophobic interface (close to 90^o contact angle) have a larger cross-sectional area and can hold themselves stable at the interface and reach the equilibrium state faster. Here, the 0.1wt% experiment data is used to compare with simulation results, the lowest concentration, since it is not possible to track single particle adsorption in the experiment process.

The adsorption rate in the simulation is calculated using the occupied contact line at the liquid interface and the total adsorption time cost on a single particle. Mark the occupied

contact line of single particle as l_a and the adsorption time cost (listed in Table 1) to form the contact line as t_a, then the adsorption rate is simply calculated as $k_a = l_a/t_a$. The adsorption rate in the simulation is then converted to real units and compared with the experiment results. The comparison of single particle adsorption rate with experiment data is shown in Table.7-2 and illustrated in Fig.7-15.

Table 7-2 Comparison of adsorption rate between 0.1 wt% experiment data and simulation results.

	Origin SiO_2	SiO-butane	SiO-hexane	SiO-90°
Experiment $k_a \times 10^6$, m/s	3.716	317.3	671.0	--
Ratio to Origin SiO_2	1	85.4	180.6	--
Simulation k_a, m/s	0.000781	0.0471	0.144	0.190
Ratio to Origin SiO_2	1	60.3	183.8	243.0

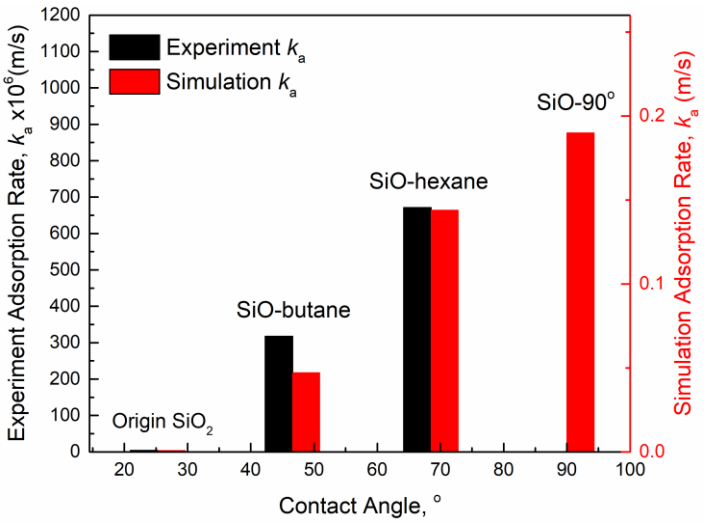

Figure 7-15 Adsorption rate results from pedant drop surface tension experiment results and LBM-DEM simulation

There are several orders of magnitude deviations between the experiment data and the simulations. However, the trends between particle types are similar from the Original SiO_2 to SiO-hexane and of exactly the same order. In the simulations, the adsorption rate increases 60.3 times from the Original SiO_2 to SiO-butane and 183.8 times from Original SiO_2 to SiO-

hexane with 29% and 0.16% percentage deviation, respectively to the experimental data. The increased percentages of experiment and simulation compared with Original SiO_2 are therefore of the same magnitude and show especially good agreement for the change to the SiO-hexane. It is noted, importantly, that the experimental data is based on linear fitting results, but the simulations are from single test cases at each condition. The percentage deviation may be caused by the capped effect (capped particle velocity to 0.1 m/s to keep stable) which limited the adsorption velocity of particles or the simple relatively poor data of 0.1 wt% which has been illustrated in Chapter 6. It is emphasised, that in terms of the absolute order of magnitude differences, single particle adsorption is also different from that of mass of particles and ignores particle-particle effects, and the important effect of particle concentration. There may be hundreds of thousands of particles experimentally adsorbed at the same time, but it is not possible to simulate that large number of particles due to huge computation cost and study time. The simulation used PBC as boundary to realise the mass of particles adsorption at the same time which means the results can multiply several orders of magnitude to compare with the experiment result. However, it is not real and not good comparison because it cannot mimic the multiparticle collision and aggregation as shown in the experiment results in Chapter 6. The SiO-butane particle shows larger aggregation and multilayer, but SiO-hexane shows better monolayer structure. It can explain why the result of SiO-hexane is closer to the experiment data. Although the simulation can only qualitatively compare with the experiment data, the simulation results successfully achieve the influence effect caused by particle wettability. The unexpected slow relaxation that mentioned by the Kaz et al (Kaz et al. 2012) can also been a possibility that cannot be included in the simulation.

In order to check the surface tension influence on the adsorption process. Particle adsorption using SiO-hexane particles with different surface tension is conducted. The surface tension

coefficient is changed from -0.05 to 0.05 representing -33% and 36% surface tension change for the interface. However, with the surface tension change, the adsorption process and the stable state does not have a visible change which has shown in Appendix, (Fig. A21). The Bond number is very small for this simulation which means the gravity force can even be ignored and particle movement is mainly dominated by the hydrodynamic effect and the multiphase attraction force. The particle adsorption profiles are almost the same just with some deviation caused by the pseudo current. It is worth noticing that the increase of surface tension will also increase the pseudo current in the flow and means larger drag force errors which have been mentioned by Joshi and Sun (Joshi and Sun 2009). The adsorption process results with moderate surface tension change show that the surface tension change in a moderate range does not change the absorption results and the changes in the process are very hard to observe. However, the surface tension change leads to a larger pseudo current around the interface which may influence the start stage of particle adsorption, larger surface tension means a larger pseudo-current. It means it is necessary to find out a method to decrease the pseudo current in large density cases in the future work.

7.5 Summary

The single particle adsorption process is achieved in this chapter, and the adsorption process and results are analysed. The particle adsorption process from the bulk phase to the liquid-gas interface has been well tracked in detail. In the simulation results, four steps of adsorption are observed: settling, contact, oscillation, and stable adsorption. The particle hydrophilicity significantly influences the later three processes and decreases the oscillation time and increased the stability. It has been shown that the coupling LBM-DEM multiphase model can simulate the particle adsorption process and correctly (albeit only qualitatively) predict the trend caused by different particle surface wettability. The adsorption simulation shows a cross-section change of particles at the liquid-gas interface and the deformation caused by the

particle adsorption, thus, we can see the single particle adsorption process in detail and analyse the change and compare it with experiment data. The deviations between 0.1 wt % experiment data and simulation results are several orders of magnitude but agree well with the trend, especially for SiO-hexane. In this study, moderate surface tension changes in simulation does not significantly influence the adsorption process due to the huge gap between the effect of gravity force and surface tension effect.

Although the trend of adsorption has been achieved, there is several magnitudes of deviation between the experiment and simulation, there are deviation reasons as follows:

1) The simulation is single particle adsorption without other influences, although the periodic boundary conditions are used, the real situation is more complex than a single one.

2) The adsorption force at the interface can only qualitatively represent the phenomena and need more quantitively verification with experiment data and an improved force scheme which can represent the process more physically.

3) The drag force effect caused by the pseudopotential multiphase model is not neglectable. In this multiphase model, the pseudo current cannot be eliminated and definitely influenced the simulation, especially at the multiphase interface. Normally, the adsorption force is much larger than the drag force effect, the drag force can be larger when particles are moving fast and close to the liquid interface.

8. Conclusions and Recommendations

8.1 Conclusions

In conclusion, this thesis has detailed investigation into the dynamics of bidisperse colloidal particle sedimentation and colloidal particle adsorption at the liquid-gas interfaces, as well as numerical studies on the settling process and colloidal particle air-water surface adsorption. Firstly, work conducted in Chapter 4 studied bidisperse colloidal systems with an analytical centrifuge in different particle size mixing ratios, which leads to detailed observations on the influence factors of bidisperse settling and size distribution comparison between light scanning and DLS method, highlighting bidisperse colloidal particle behaviour under acceleration conditions. Then, a 1D simulation study is performed in Chapter 5, which modified the Davis-Russel model with a bidisperse scheme and viscosity modifications. The simulation results show good agreement with the experimental data with less than 10% deviation. To investigate the particle adsorption and the networking of particle structure, particle adsorption experiments at the liquid-gas interface were conducted with a Langmuir trough and pendant drop tensiometer in Chapter 6. Results highlight the influence of particle contact angle and addition of surfactant frother (MIBC) on adsorption, where particles showed different surface pressure changes, surface tension changes, and adsorption rates. Critically, short and long-time adsorption data were fitted to kinetic models, quantifying the effect of contact angle and concentration on the diffusion absorption rate. Finally, a complex 3D LBM-DEM simulation model is proposed in Chapter 7 that combines the advantages of both methods to create an accurate numerical model to track the detail of the colloidal particle adsorption process and the wettability influences.

In terms of producing hydrophobic particles for adsorption studies, it is found that the esterification technique (detailed in Chapter 3) is successful, but the contact angle can only be

checked with the same material silica wafer. Then, 3 different hydrophobic particles are obtained. Particle size and stability in the bulk phase are also checked in a wide range of pH to ensure there are no significant aggregation in the experimental study.

The settling behaviour of bidisperse colloidal silica suspensions in two different size ratios (100:500 nm and 500:800 nm) with various mixture ratios and volume fractions, using an analytical centrifuge is conducted in Chapter 4 and further numerical studied with models in Chapter 5, highlighting a number of important results in bidisperse systems that may be extended to polydisperse systems. Specifically, particle mixtures of 500:800 nm dispersions (mean size ratio of 1.6) and 100:500 nm dispersions (mean size ratio of 5) are investigated at three different volume mixture ratios (1:2, 1:1 and 2:1) to understand the importance of fluid-particle effects from the larger size fraction on the settling of the smaller particles. Distributions compared very well to estimates from SEM and manufacturer expectations, and in fact, are a lot closer than measurements using dynamic light scattering (DLS) with a Zetasizer®. In particular, results showed that DLS is not very suitable to measure the size distribution of colloidal bidisperse suspensions, where size peaks may overlap. The first major conclusion is that for sedimentation studies at various total volume fractions, the LUMiSizer® is shown to have an upper concentration limitation where only one interface could be detected by the instrument. For 500:800 mixtures, results are compared with Richardson-Zaki (RICHARDSON 1954) and modified Batchelor model (Batchelor 1982) predictions. The Batchelor model proves more accurate at predicting the lower interface rate, while both models over-predicted the upper interface, likely due to increased drag that is most evident with higher fractions of smaller particles. For 100:500 cases, higher centrifugal rotation speeds are required to settle the 100 nm particles, and the influence of Brownian motion is evident. It is also found that the smaller particles obtained a lower initial settling

rate than their terminal velocity, due to induce anisotropic effects from the 500 nm fraction, which is again more evident with a greater proportion of smaller particles.

To further study the bidisperse sedimentation, a modified 1D model based on a monodisperse system (Antonopoulou et al. 2018) is proposed in Chapter 5 to track the settling process of the bidisperse system in detail using an effective maximum volume fraction with a bidisperse viscosity scheme. A numerical implementation of the model using an adaptive finite difference solver is described which can be used for the concentration profile prediction of both species. The model is shown to be a good fit with 100:500 spherical silica mixture and 500:800 spherical silica mixture on 3 mixing ratios with slightly over prediction that is mostly less than 10 %. This work suggests that the effective maximum volume fraction accurately captures interparticle interactions and provides insights into the effect of bidisperse suspension on different size ratios and mixing ratios. However, it may be that other fluid drag effects may need to be captured to fully equate simulated predictions to the experimental results.

In some progresses such as flotation, sedimentation is the first step and followed with particle adsorption with liquid-gas interface and particle wettability is an important factor. Hydrophobic silica particles are prepared in Chapter 3 and used as materials in Chapter 6. The correlation between the network interactions observed on the Langmuir-Blodgett rough and the adsorption surface tension change is recorded with a pendant surface tension meter. The results show how the surface pressure changes with particle wettability. The particle pressure curve shows smoother, and the inflexion point of close packing becomes harder to observe. Interestingly, the Original SiO_2 particles cannot form a particle network layer at the air-water interface, and thus, are not recorded. The SEM images of particle hexagonal packing structure are checked. Slightly aggregations are found more considerable with higher concentration of MIBC and the less hydrophobic particles. The pendant drop surface tension

meter recorded the surface changes when particle adsorption occurs, thus, the absorption rate can be calculated. As particle hydrophobicity increases, the adsorption rate also increases dramatically and generally increases with particle concentrations. The match between adsorption data to diffusion models was significant, allowing quantification of the role of hydrophobicity on the rate of colloidal adsorption to a level never previously investigation.

Since it is hard to track single particle adsorption, the author proposed an LBM-DEM coupling method to simulate the particle adsorption process in Chapter 7. Furthermore, a novel scheme of fluid-solid force and adhesion force schemes were proposed which show better results and are more suitable for moving solid object cases. Four steps of adsorption are summarised and the adsorption rate in the simulation is compared with the experimental data which qualitatively proves the model. The single particle adsorption process is recorded and analysed. Particle adsorptions at different contact angles are achieved and the adsorption process is tracked in detail successfully. The simulation results are compared with the 0.1 wt % experimental data and agree very well with the trend (in terms of hydrophobicity) but still have deviations in the magnitude. Chapter 7 provides new insight into the study of particle adsorption and shows the potential of the LBM-DEM coupling method in the multiphase study.

In summary, the bidisperse colloidal particle sedimentation and particle adsorption at liquid-gas interfaces are studied experimentally and numerically. From the experimental study of sedimentation, limitations of measuring devices are found and analysed, and the bidisperse mixture ratios effects and particle velocities in species are analysed in detail and compared with the classical theories. The 1D model shows great (quantitative) agreement with the experiment data and can be extended to the polydisperse system and used to track the concentration changes of each species. The particle adsorption experiment reveals the adsorption particle network structure and the surface pressure performance with compression

of the interface. The adsorption rate of particles is calculated in different concentrations and particle wettability which shows the influence of particle hydrophobicity not only affects the adsorption stability but also the rate. Finally, a tentative 3D LBM-DEM simulation model is proposed which can be a pioneer work to study the numerical adsorption process with those two coupling methods.

8.2 Recommendations and Further Study

In this study, only single particle adsorption work is conducted due to the time limitation and covid influence. However, there are some future works that can be done:

1) Experimental validation of predicted concentration profiles in bidisperse mixtures (using instruments like the X-ray sediment analyser).

2) Experimental investigation into the absorption of the smaller 500 and 100 nm particles at air-water interfaces, to see how well the diffusion kinetic models can fit (noting that with the smaller particles, the droplet may not deform to the same extend, owing to lower mass).

3) DLVO theory can be added in the DEM model to achieve a better particle-particle interaction and consider more physical particle suspension in reality which is better for sedimentation of mass of particles. For spherical colloidal particles, the DLVO theories can simply use the centre coordinate and get the forces of spherical particles then used in the DEM model to simulate the DLVO effects. The salt concentration on adsorption experiment can also be considered.

4) Mass of particle adsorption is recommended to consider more complex collision and dynamic influence which can be closer to the real cases that mass of particles adsorbed at liquid-gas interface and particles need to find a place to adsorb. Particles should be placed randomly on the fluid phase of the suspension, and then experience gravity force or an initial velocity. Maybe extend the LBM-DEM model to look at multiple particles settling in 2 phase

systems, so as to consider more explicit fluid-particle dynamics in bidisperse systems. The simulation may need several months and better run on an advanced computer with larger GPU memory.

5) The improvement of a single component multiphase model should be considered to decrease the pseudo current at the liquid interface which influenced the movement of particles which is larger at higher surface tension and density ratio cases. Although Hu's adjustment can decrease the pseudo current, it also increases the thickness of the multiphase interface which generated a blur fluid interface and is not what we want.

Appendix

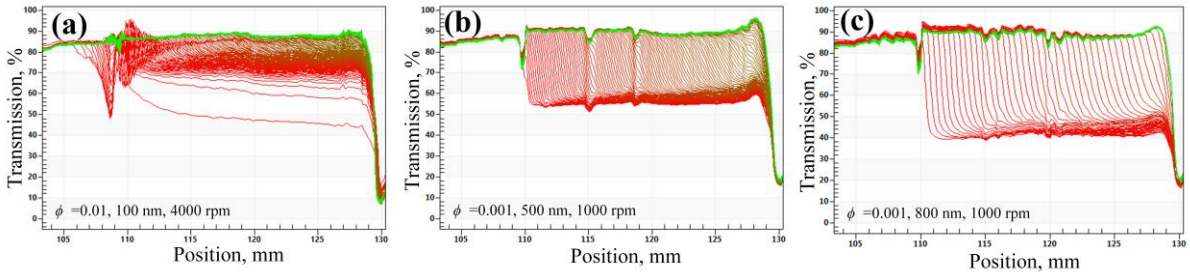

Fig. A1: LUMiSizer® light transmission profiles of silica nanoparticle dispersions under centrifugal sedimentation. (a) 100 nm particles under 4000 rpm; (b) 500 nm particles under 1000 rpm; (c) 800 nm particles under 1000 rpm.

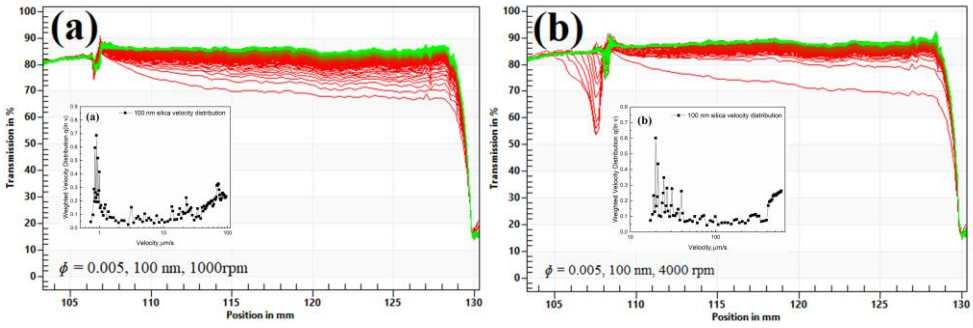

Fig.A2: Transmission profiles of 0.5 vol% 100 nm silica nanoparticle sedimentation and particle velocity distributions under (a) 1000 rpm (b) 4000 rpm.

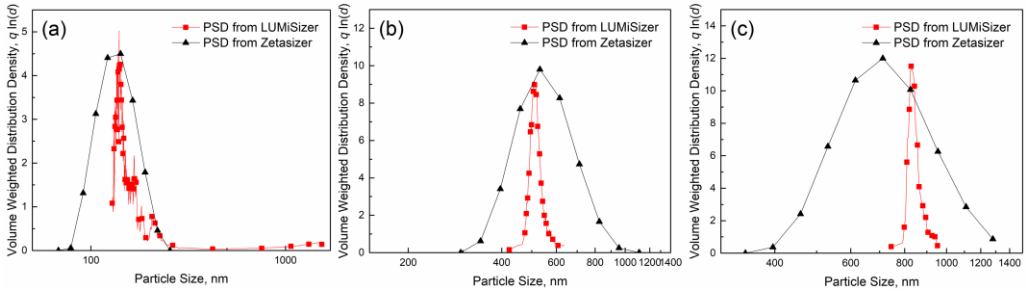

Fig.A3: Volume-weighted particle size distribution of three nanoparticles measured by Zetaszier and LUMiSizer®. (a) 100 nm, (b) 500 nm, and (c) 800 nm.

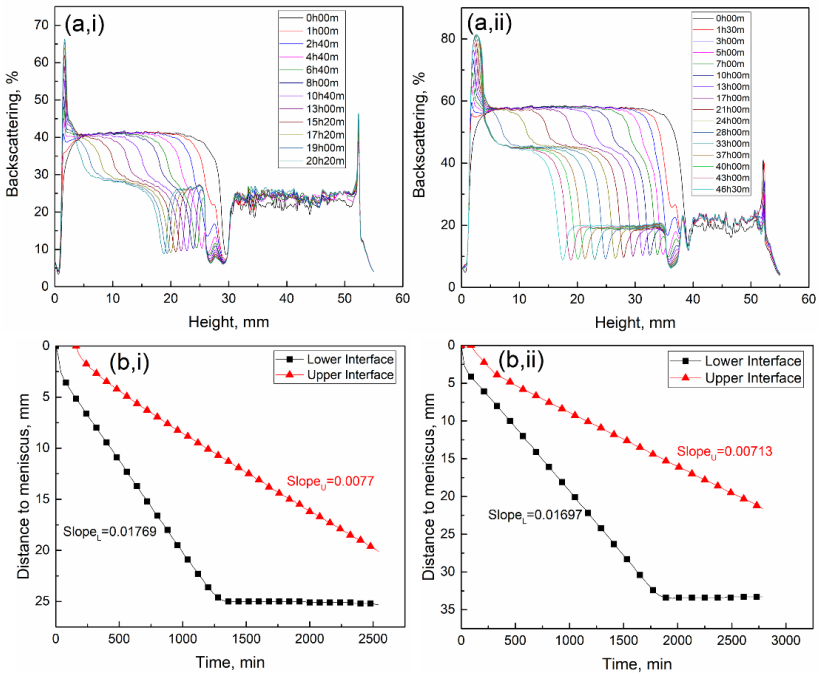

Fig. A4: Turbiscan® gravitational sedimentation data; (a) backscatter profiles versus time, and (b) extracted height versus time profiles for bidisperse silica suspensions at total volume fractions of (i) 0.02 and (ii) 0.04. Data for 500 and 800 nm particle mixtures at a 1:1 concentration ratio.

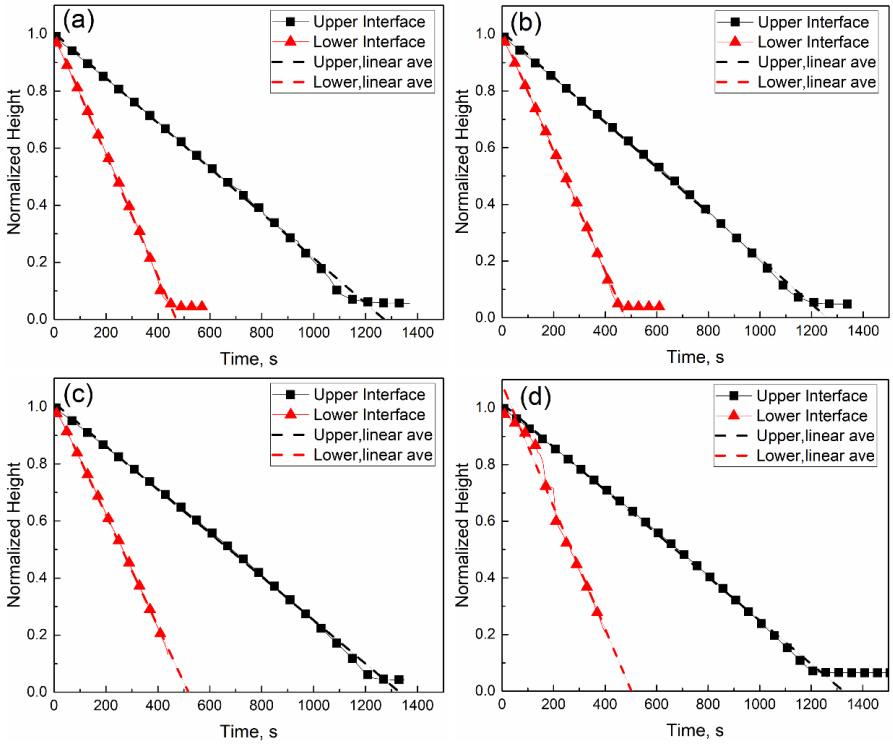

Fig. A5: Normalised sedimentation front versus time data for 500: 800 nm mixed particle dispersions (at a 1:1 concentration ratio) under a centrifuge speed of 1000 rpm, and total volume fractions of (a) 0.002, (b) 0.005, (c) 0.01 and (d) 0.015. Dashed lines represent average linear settling rates of each species.

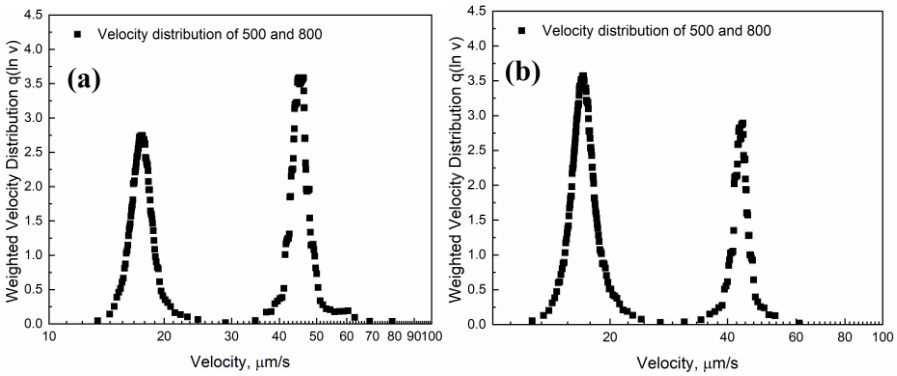

Fig.A6: Velocity distributions of 500:800 = 1:1 mixture under 1000 rpm for a total volume fraction of (a) 0.005, (b) 0.01.

Table A1: Velocity results from LUMiSizer® 'Constant Position' mode velocity distribution and front tracking at upper and lower interfaces.

Volume fraction of 500: 800	Peak distribution Velocity (upper) µm/s	Front tacking results(upper) µm/s	Peak distribution Velocity (lower) µm/s	Front tacking results (lower) µm/s
0.5 vol%	17.67	17.49	45.87	46.34
1 vol%	17.16	17.13	43.83	43.83

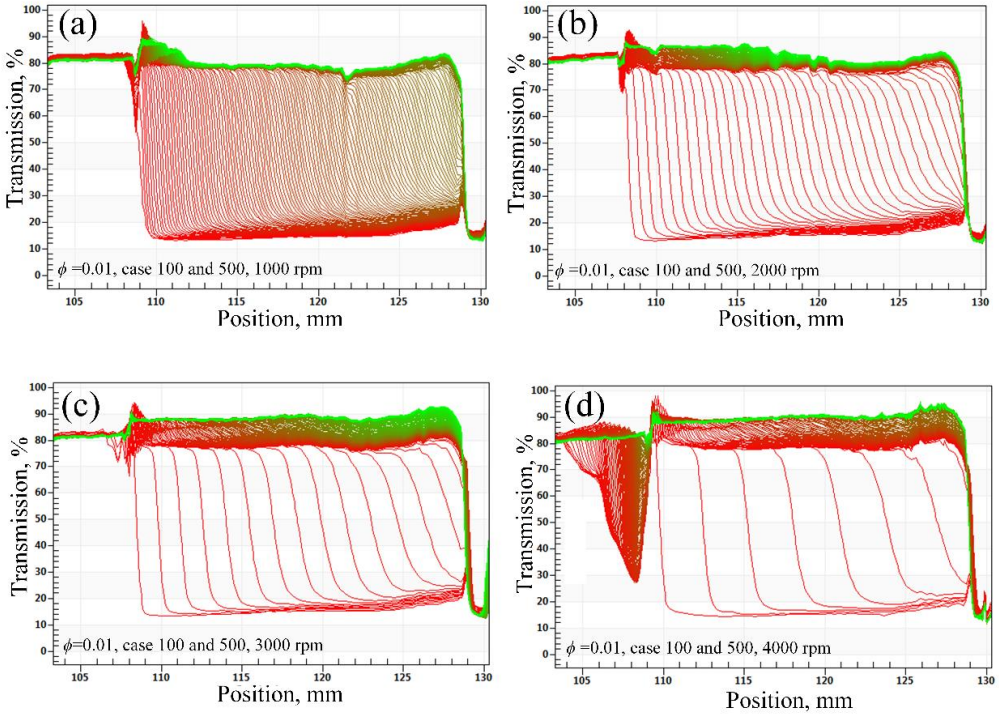

Fig. A7: LUMiSizer® light transmission profiles for bidisperse 100:500 nm mixed silica suspensions with a total volume fraction of 0.01 and a 1:1 concentration ratio, under varying centrifuge speeds of (a) 1000 rpm, (b) 2000 rpm, (c) 3000 rpm, and (d) 4000 rpm.

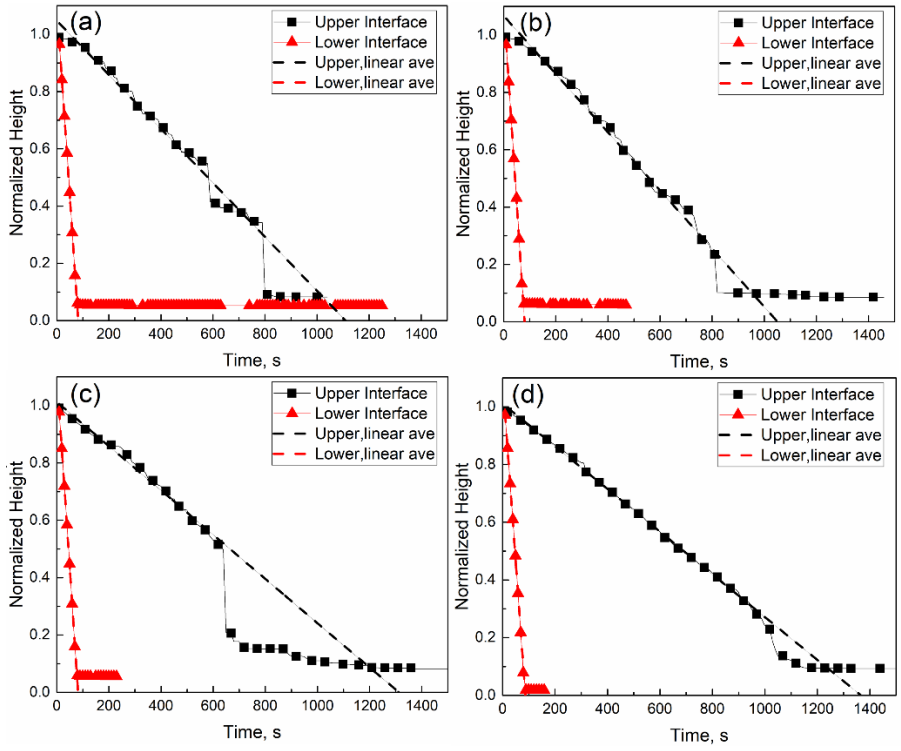

Fig. A8: Normalised sedimentation front versus time data for 100: 500 nm mixed particle dispersions (at a 1:1 concentration ratio) under a centrifuge speed of 4000 rpm, and total volume fractions of (a) 0.004, (b) 0.006, (c) 0.01 and (d) 0.02. Dashed lines represent average linear settling rates of each species.

The S_{ij} and equations of Batchelor's model

The equations that are used to calculate the Batchelor's model in the paper come from Batchelor's paper (see paper ref [14]). The coefficients are from the paper of Batchelor and Wen (see paper ref [15]). In Batchelor's equation, λ is the diameter ratio of bidsiperse particles and γ is the particle density ratios after minus the fluid density. In the present case, we have two size ratios for S_{sl} and S_{ls} to obtain small and large particle velocity. λ= 5 or 0.2 (for the 100:500 nm case) and 1.6 or 0.625(for the 500:800 nm case) while γ =1. When λ =1, γ =1, S_{ij} = -6.55 is used for a monodisperse system in Batchelor's model and then we can calculate other unknown S_{ij} values for 100:500 and 500:800 systems. With the known

parameters, we can extrapolate and obtain the S_{ij} values in Batchelor's model from Table 3 of Batchelor's paper [15].

For 100 and 500 nm

$$v_s = u_s^0(1-6.55\phi_s-0.745\phi_l) \quad \text{(Eq. S1)}$$

$$v_l = u_l^0(1-2.114\phi_s-6.55\phi_l) \quad \text{(Eq. S2)}$$

For 500 and 800 case

$$v_s = u_s^0(1-6.55\phi_s-1.26\phi_l) \quad \text{(Eq. S3)}$$

$$v_l = u_l^0(1-1.84\phi_s-6.55\phi_l) \quad \text{(Eq. S4)}$$

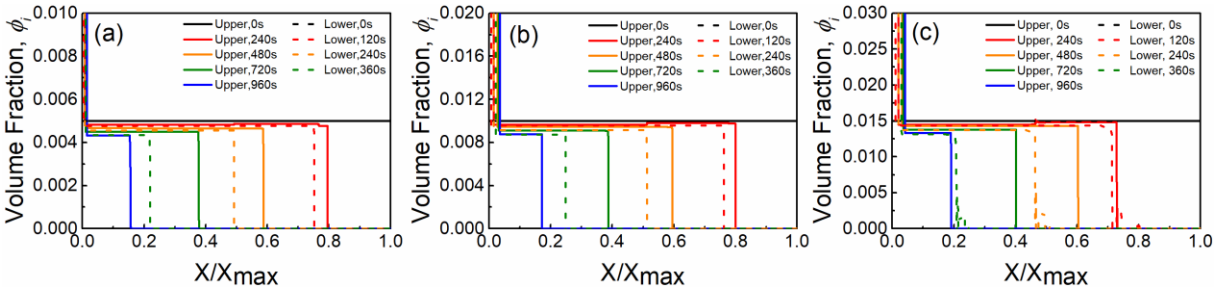

Fig. A9: Simulation concentration profiles of 500 nm (Upper) and 800 nm (Lower) particles under 1000 rpm, at mixing ratio = 1:1, using 1-D bidisperse model. (a) ϕ_0 = 0.01, (b) ϕ_0 = 0.02, (c) ϕ_0 = 0.03.

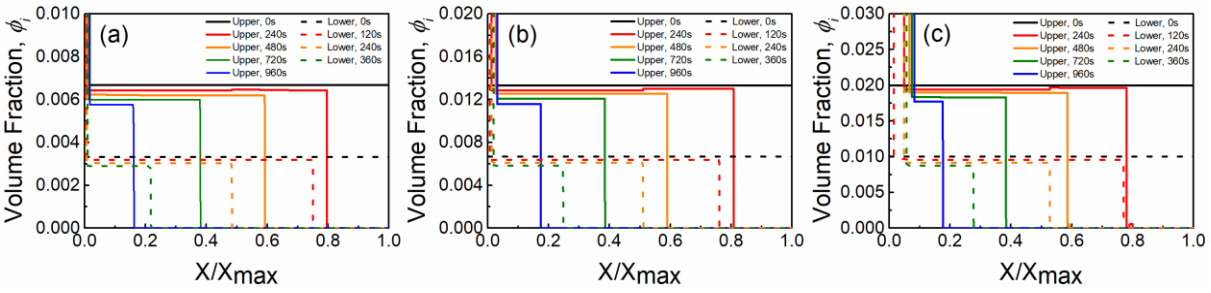

Fig. A10: Simulation concentration profiles of 500 nm (Upper) and 800 nm (Lower) particles under 1000 rpm, at mixing ratio = 2:1, using 1-D bidisperse model. (a) ϕ_0 = 0.01, (b) ϕ_0 = 0.02, (c) ϕ_0 = 0.03.

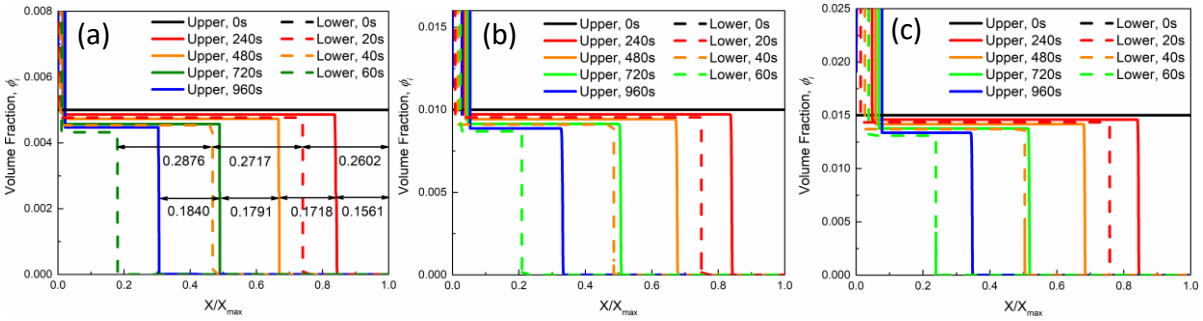

Fig. A11: Simulation concentration profiles of 100 nm (Upper) and 500 nm (Lower) particles under 4000 rpm, at mixing ratio = 1:1, using 1-D bidisperse model. (a) ϕ_0 = 0.01, (b) ϕ_0 = 0.02, (c) ϕ_0 = 0.03.

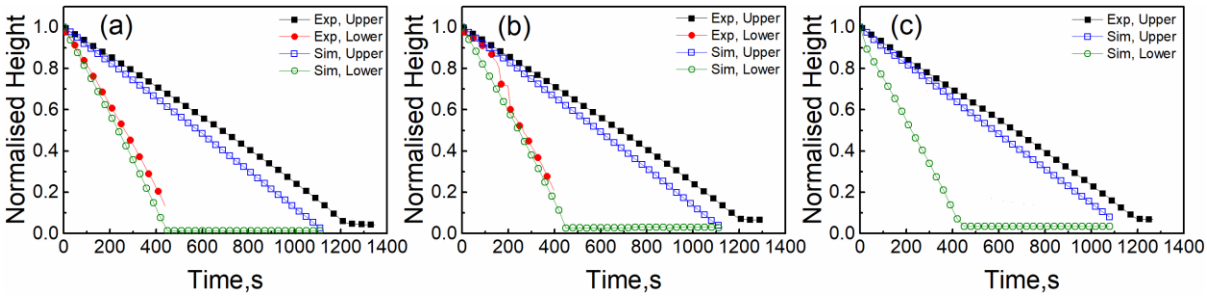

Fig. A12: Height vs Time profiles of 500 nm (Upper) and 800 nm (Lower) particles under 1000 rpm, at mixing ratio = 1:1, using 1-D bidisperse model. (a) ϕ_0 = 0.01, (b) ϕ_0 = 0.02, (c) ϕ_0 = 0.03.

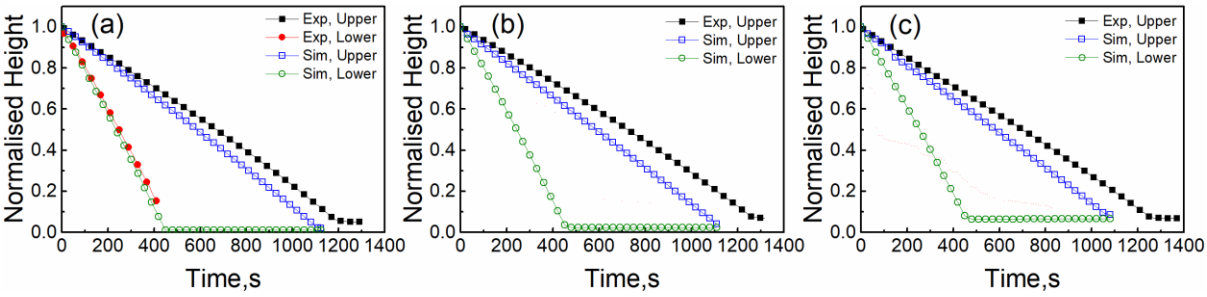

Fig. A13: Height vs Time profiles of 500 nm (Upper) and 800 nm (Lower) particles under 1000 rpm, at mixing ratio = 2:1, using 1-D bidisperse model. (a) ϕ0 = 0.01, (b) ϕ0 = 0.02, (c) ϕ0 = 0.03.

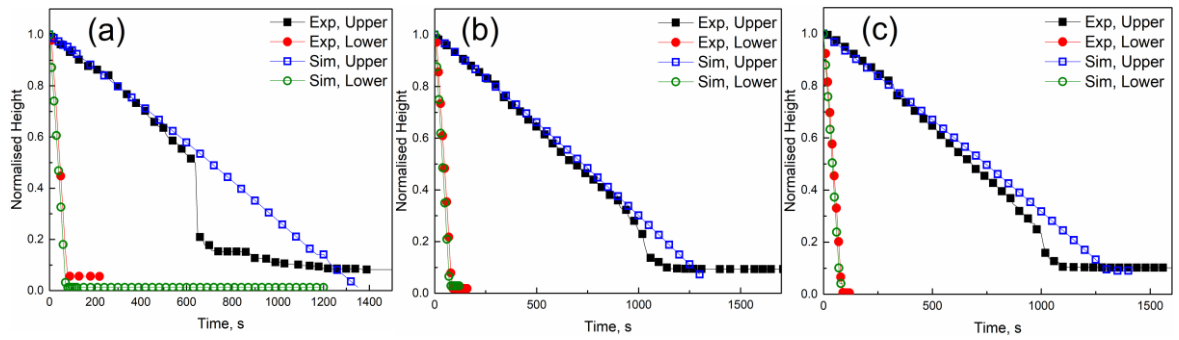

Fig. A14: Height vs Time profiles of 100 nm (Upper) and 500 nm (Lower) particles under 4000 rpm, at mixing ratio = 1:1, using 1-D bidisperse model. (a) ϕ_0 = 0.01, (b) ϕ_0 = 0.02, (c) ϕ_0 = 0.03.

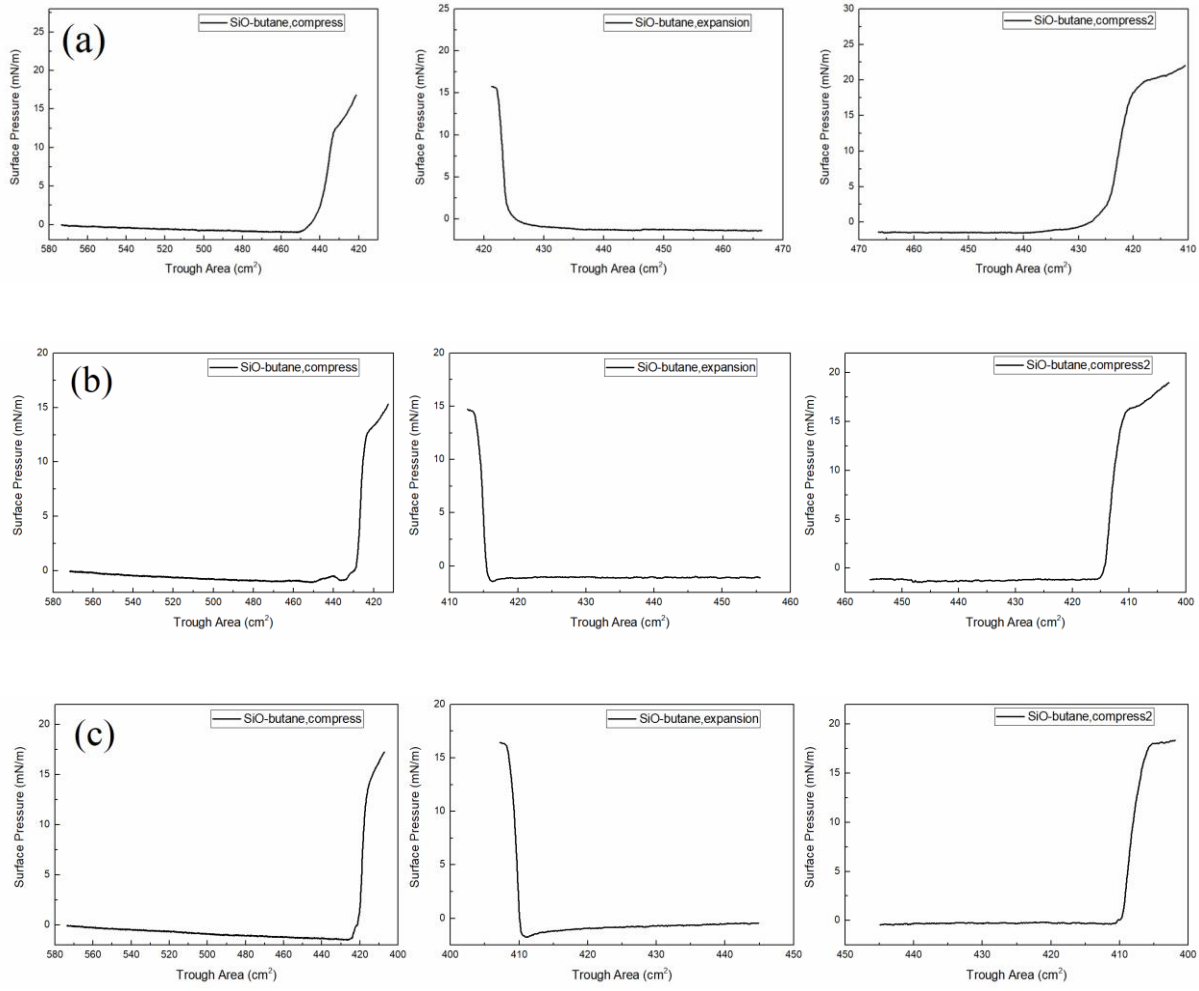

Fig. A15, Surface vs Trough area of SiO-butane on (a) 0.01M MIBC (b) 0.03 M MIBC, (c) 0.05M MIBC subphase.

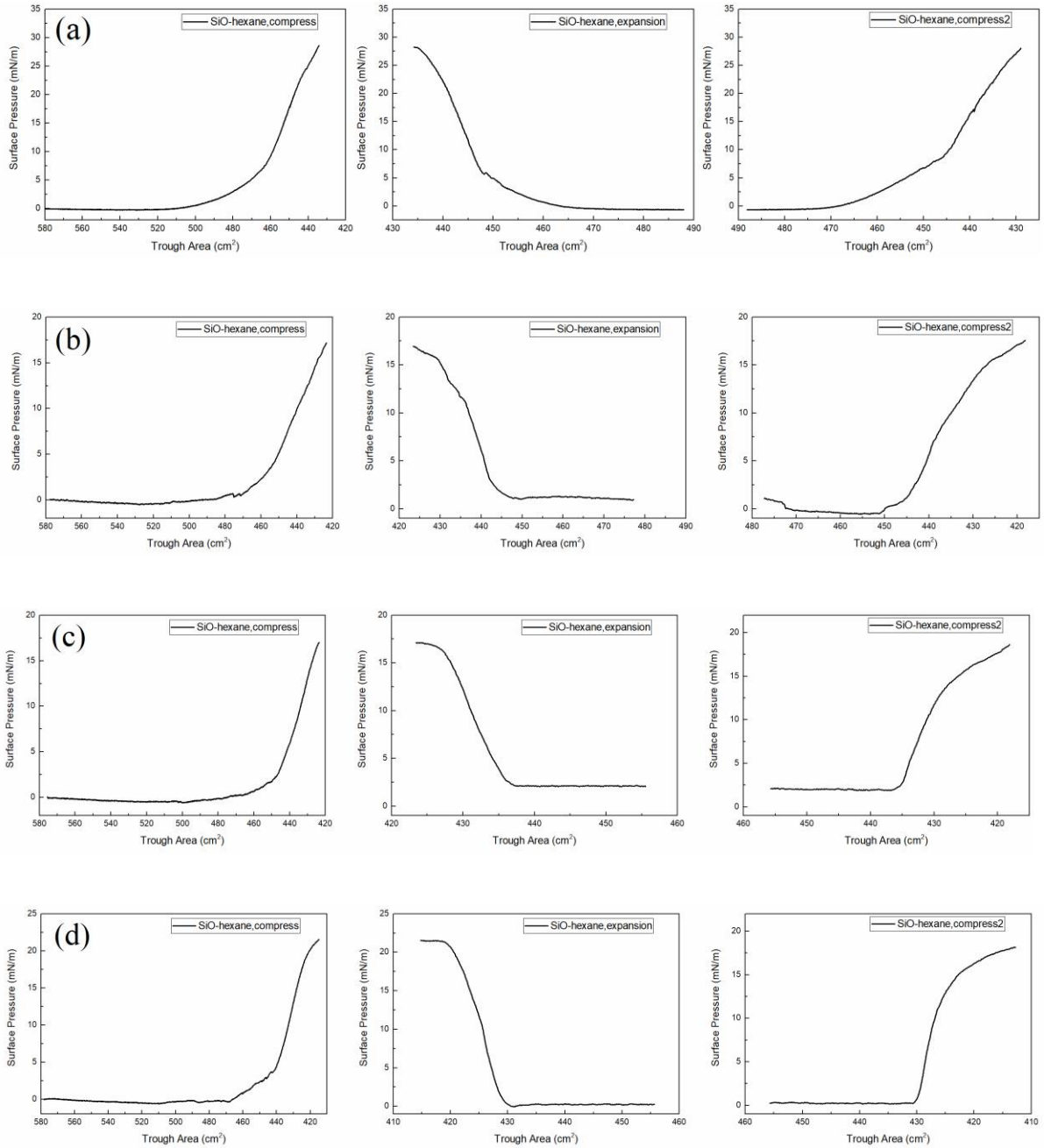

Fig.A16. Surface Tension vs Trough area of SiO-hexane on (a) water (b), 0.01M MIBC (c),0.03M MIBC (d),0.05M MIBC subphase.

Table.A2 HCP packing area and experimental packing area comparison.

SiO-butane

Subphase concentration	Exp packing area, cm^2	HCP packing area, cm^2	Packing Area Ratio
Water	445	954	0.466
0.01 M	374	954	0.391
0.03 M	335	954	0.351
0.05 M	280	954	0.294

SiO-hexane

Subphase concentration	Exp packing area, cm^2	HCP packing area, cm^2	Packing Area Ratio
Water	475	621	0.765
0.01 M	429	621	0.691
0.03 M	398	621	0.641
0.05 M	362	621	0.584

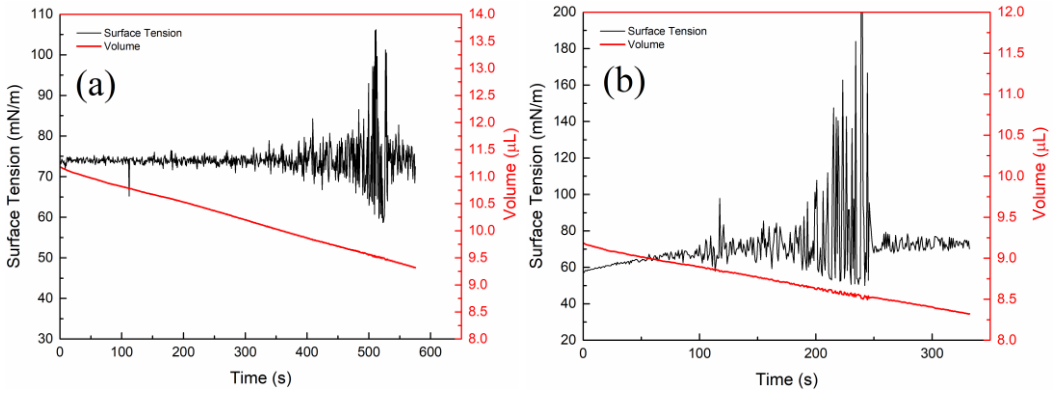

Fig.A17. Oscillation pictures of SiO-hexane particles in (a) water subphase and 0.03M MIBC subphase without cuvette.

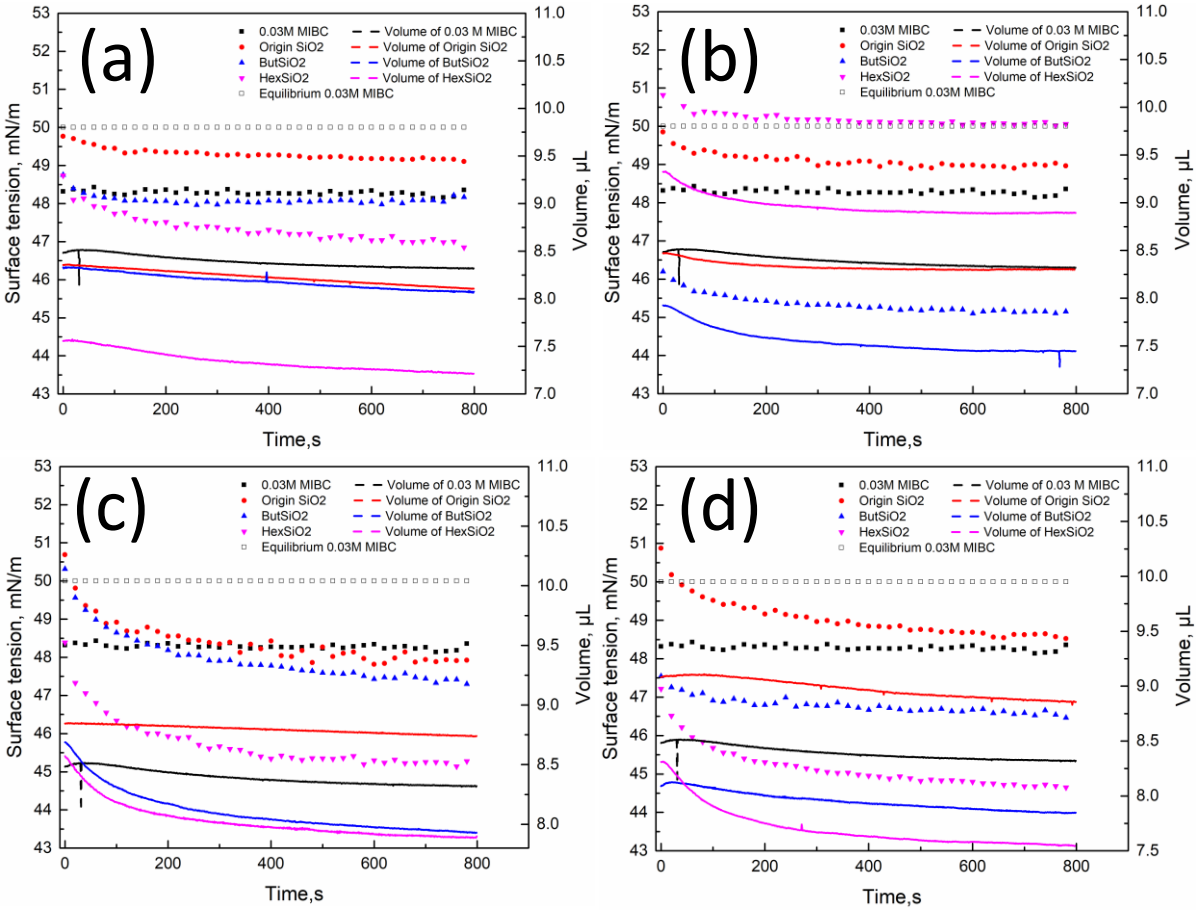

Fig. A18. Pendant drop with cuvette surface tension vs time with different particles under different weight percent. (a) 0.1wt%, (b)0.5wt%,(c)1wt%,(d)2wt%

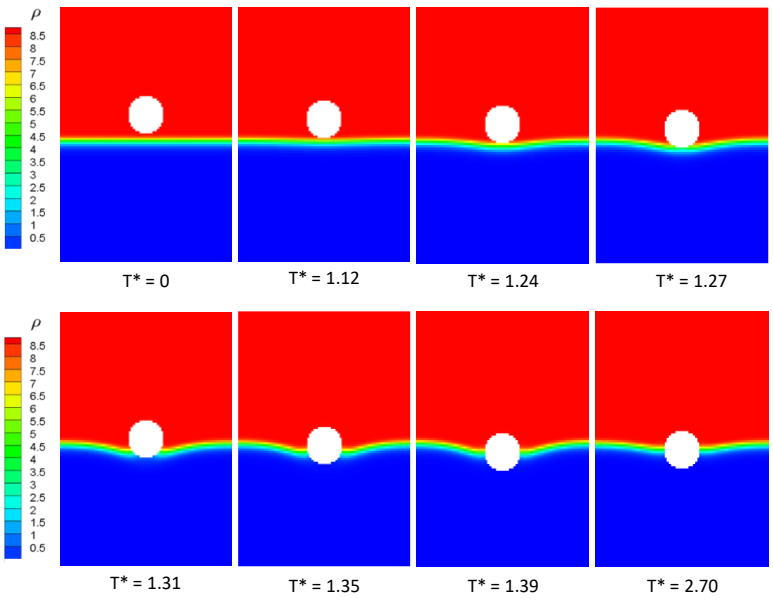

Fig. A19. Single particle adsorption simulation process using SiO- 90º ($T^*=t/(d/g)^{0.5}$).

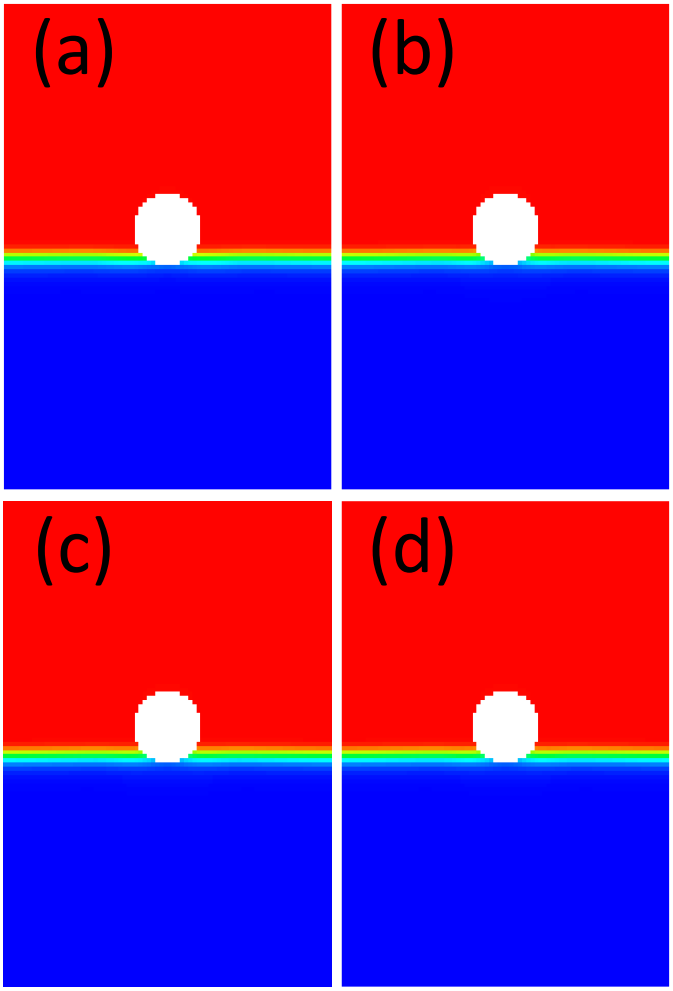

Fig.A20. Stable states of Original SiO_2 particle adsorption with different gravity force. (a) 1 m/s^2, (b) 10 m/s^2 (c) 100 m/s^2 (d) 1000 m/s^2.

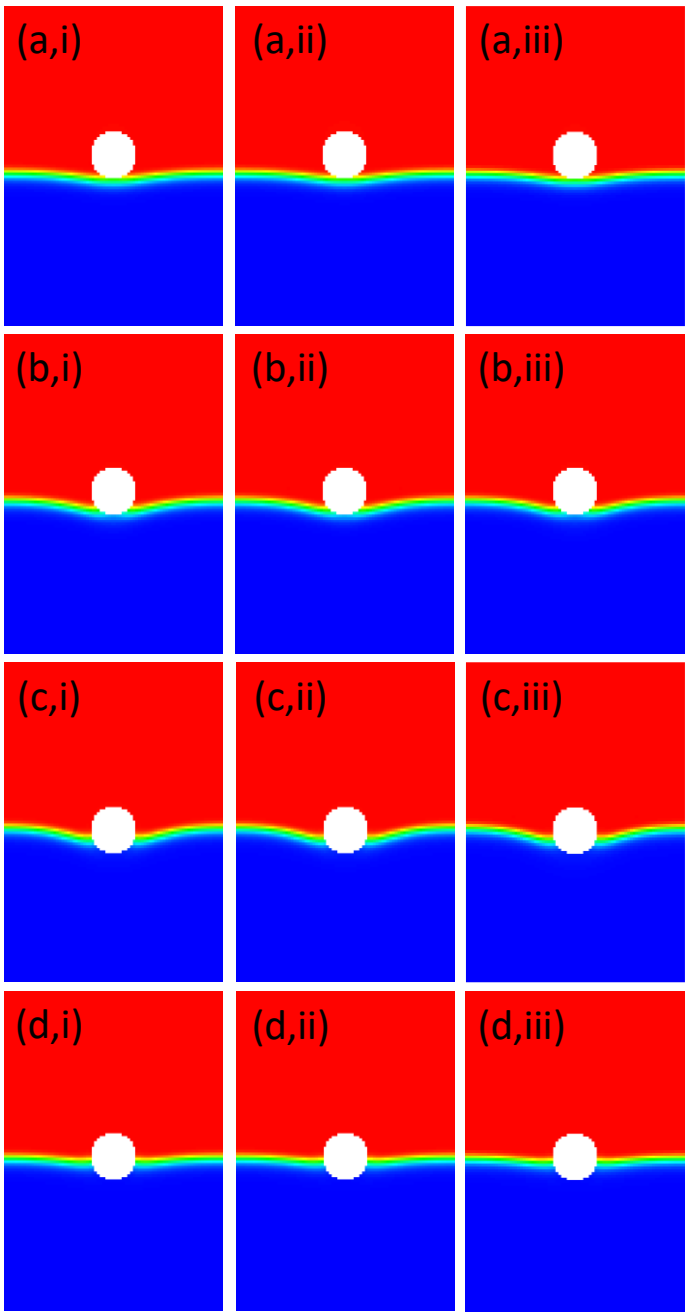

Fig. A21. ***SiO-hexane particle adsorption with different surface tension. (a) z = 57, (b) z = 60 (c) z = 64 (d) stable. (i)-0.05, (ii)0, (iii)0.05.***

Bibliography

A., W., *et al.* (1998). "On the Sauter mean diameter and size distributions in turbulent liquid/liquid dispersions in a stirred vessel." Chemical Engineering Science.

Abbas, M., *et al.* (2006). "Dynamics of bidisperse suspensions under Stokes flows: Linear shear flow and sedimentation." Physics of Fluids **18**(12): 121504.

Abeynaike, A., *et al.* (2012). "The experimental measurement and modelling of sedimentation and creaming for glycerol/biodiesel droplet dispersions." Chemical engineering science **79**: 125-137.

Ackerson, B. J., *et al.* (1999). "Crystallization by settling in suspensions of hard spheres." Physical Review E **59**(6): 6903.

Afra, B., *et al.* (2019). "Direct numerical simulation of freely falling particles by hybrid immersed boundary – Lattice Boltzmann – discrete element method." Particulate Science And Technology: 1-13.

Aidun, C. K. and J. R. Clausen (2009). "Lattice-Boltzmann Method for Complex Flows." Annual Review of Fluid Mechanics **42**(1): 439-472.

Al‐Naafa, M. and M. S. Selim (1992). "Sedimentation of monodisperse and bidisperse hard‐sphere colloidal suspensions." AIChE Journal **38**(10): 1618-1630.

Ambari, A., *et al.* (1998). "Backflow effect in model sedimentation experiments." Physics of Fluids A Fluid Dynamics **5**(8): 2061-2063.

Ammar, S., *et al.* (2017). "A multiphase three-dimensional multi-relaxation time (MRT) lattice Boltzmann model with surface tension adjustment." Journal of Computational Physics **343**: 73-91.

Anderson, W., *et al.* (2013). "A comparative study of submicron particle sizing platforms: Accuracy, precision and resolution analysis of polydisperse particle size distributions." J Colloid Interface **405**(Complete): 322-330.

Anjali, T. G. and M. G. Basavaraj (2016). "Contact angle and detachment energy of shape anisotropic particles at fluid-fluid interfaces." J Colloid Interface Sci **478**: 63-71.

Antonopoulou, E., *et al.* (2018). "Numerical and experimental analysis of the sedimentation of spherical colloidal suspensions under centrifugal force." Physics of Fluids **30**(3): 030702.

Aveyard, R., *et al.* (1994). "Aspects of aqueous foam stability in the presence of hydrocarbon oils and solid particles." Advances in colloid and interface science **48**: 93-120.

Aveyard, R. and J. H. Clint (1995). "Liquid droplets and solid particles at surfactant solution interfaces." Journal of the Chemical Society Faraday Transactions **91**(17): 2681-2697.

B, G. L. A., *et al.* (2013). "Simulation of self-assemblies of colloidal particles on the substrate using a lattice Boltzmann pseudo-solid model." Journal of Computational Physics **248**(1): 323-338.

Ballard, N., *et al.* (2018). "Colloidal particles at fluid interfaces: Behaviour of isolated particles." Soft Matter **15**(6).

Bao, J. and L. Schaefer (2013). "Lattice Boltzmann equation model for multi-component multi-phase flow with high density ratios." Applied Mathematical Modelling **37**(4): 1860-1871.

Bao, Y. B. and J. Meskas (2014). "Lattice Boltzmann Method for Fluid Simulations."

Bargie, M. and E. M. Tory (2010). "A comparison of the results of two methods for computing the sedimentation behavior of bidisperse suspensions." International Journal of Mineral Processing **95**(1-4): 53-61.

Barnes, G. T. and I. R. Gentle (2005). "Interfacial Science: An Introduction."

Bartlett, P., *et al.* (2012). "Sudden collapse of a colloidal gel." Physical Review E **85**(2): 021404.

Bashforth, F. and J. C. Adams (1883). An attempt to test the theories of capillary action by comparing the theoretical and measured forms of drops of fluid, University Press.

Batchelor, G. (1972). "Sedimentation in a dilute dispersion of spheres." Journal of fluid mechanics **52**(2): 245-268.

Batchelor, G. (1982). "Sedimentation in a dilute polydisperse system of interacting spheres. Part 1. General theory." Journal of Fluid Mechanics **119**: 379-408.

Batchelor, G. and C.-S. Wen (1982). "Sedimentation in a dilute polydisperse system of interacting spheres. Part 2. Numerical results." Journal of Fluid Mechanics **124**: 495-528.

Behra, J. S., *et al.* (2019). "Characterization of Sodium Carboxymethyl Cellulose (Na CMC) aqueous solutions to support complex product formulation – a rheology and light scattering study." Acs Applied Polymer Materials.

Berres, S. and R. Bürger (2003). "On gravity and centrifugal settling of polydisperse suspensions forming compressible sediments." International Journal of Solids and Structures **40**(19): 4965-4987.

Berry, J. D., *et al.* (2015). "Measurement of surface and interfacial tension using pendant drop tensiometry." Journal of colloid and interface science **454**: 226-237.

Berzins, M. and R. Furzeland (1992). "An adaptive theta method for the solution of stiff and nonstiff differential equations." Applied numerical mathematics **9**(1): 1-19.

Bhatnagar, P. L., *et al.* (1954). "A Model for Collision Processes in Gases. I. Small Amplitude Processes in Charged and Neutral One-Component Systems." Physical Review **94**(3): 511-525.
Binks, B. P. (2002). "Particles as surfactants-similarities and differences." Current Opinion in Colloid & Interface Science **7**(1-2): 21-41.
Binks, B. P. (2017). "Colloidal particles at a range of fluid–fluid interfaces." Langmuir **33**(28): 6947-6963.
Binks, B. P. and S. O. Lumsdon (2000). "Influence of Particle Wettability on the Type and Stability of Surfactant-Free Emulsions." Langmuir **16**(23): 8622-8631.
Bizmark, N., *et al.* (2014). "Irreversible adsorption-driven assembly of nanoparticles at fluid interfaces revealed by a dynamic surface tension probe." Langmuir **30**(3): 710-717.
Bloesch, J. and N. Burns (1980). "A critical review of sedimentation trap technique." Schweizerische Zeitschrift für Hydrologie **42**(1): 15-55.
Bordács, S., *et al.* (2006). "Compression of Langmuir films composed of fine particles: collapse mechanism and wettability." Langmuir **22**(16): 6944-6950.
Boscarino, S., *et al.* (2016). "On linearly implicit IMEX Runge-Kutta methods for degenerate convection-diffusion problems modeling polydisperse sedimentation." Bulletin of the Brazilian Mathematical Society, New Series **47**(1): 171-185.
Bournival, G., *et al.* (2015). "The roles of particles in multiphase processes: Particles on bubble surfaces." Adv Colloid Interface Sci **225**: 114-133.
Bournival, G., *et al.* (2015). "The roles of particles in multiphase processes: Particles on bubble surfaces." Advances in Colloid and Interface Science **225**: 114-133.
Bouzidi, *et al.* (2001). "Momentum transfer of a Boltzmann-lattice fluid with boundaries." Physics of Fluids.
Brady, J. F. and L. J. Durlofsky (1988). "The sedimentation rate of disordered suspensions." The Physics of fluids **31**(4): 717-727.
Braun, A., *et al.* (2011). "Validation of dynamic light scattering and centrifugal liquid sedimentation methods for nanoparticle characterisation." Advanced Powder Technology **22**(6): 766-770.
Bresme, F. and M. Oettel (2007). "Nanoparticles at fluid interfaces." Journal of Physics Condensed Matter An Institute of Physics Journal **19**(41): 413101.
Bürger, R., *et al.* (2002). "Model equations and instability regions for the sedimentation of polydisperse suspensions of spheres." ZAMM ‐ Journal of Applied Mathematics and Mechanics/Zeitschrift für Angewandte Mathematik und Mechanik: Applied Mathematics and Mechanics **82**(10): 699-722.
Bux, J., *et al.* (2015). "In situ characterisation of a concentrated colloidal titanium dioxide settling suspension and associated bed development: Application of an acoustic backscatter system." Powder Technology **284**: 530-540.
Caiazzo, A. and M. Junk (2008). "Boundary forces in lattice Boltzmann: Analysis of Momentum Exchange algorithm." Computers & Mathematics with Applications **55**(7): 1415-1423.
Cao, D.-Q., *et al.* (2015). "Solid–Liquid Separation Properties in Centrifugal Sedimentation of Bidisperse Colloidal Suspension." Journal of Chemical Engineering of Japan **48**(7): 556-563.
Chen, H., *et al.* (1992). "Recovery of the Navier-Stokes equations using a lattice-gas Boltzmann method." Physical Review A **45**(8): R5339.
Chen, L., *et al.* (2014). "A critical review of the pseudopotential multiphase lattice Boltzmann model: Methods and applications." International Journal of Heat and Mass Transfer **76**: 210-236.
Chen, L., *et al.* (2013). "Sharp-interface immersed boundary lattice Boltzmann method with reduced spurious-pressure oscillations for moving boundaries." Physical Review E Statistical Nonlinear & Soft Matter Physics **87**(5): 053306.
Chen, S. (2001). "Langmuir− Blodgett fabrication of two-dimensional robust cross-linked nanoparticle assemblies." Langmuir **17**(9): 2878-2884.
Chen, Y., *et al.* (2013). "Momentum-exchange method in lattice Boltzmann simulations of particle-fluid interactions." Physical Review E Statistical Nonlinear & Soft Matter Physics **88**(1): 013303.
Chen, Y., *et al.* (2015). "Lattice Boltzmann simulation of particle motion in binary immiscible fluids." Communications in Computational Physics **18**(3): 757-786.
Cheng, Z., *et al.* (2019). "The effect of pore structure on non-Darcy flow in porous media using the lattice Boltzmann method." Journal of Petroleum Science and Engineering **172**: 391-400.
Cherepanov, I. N. and B. L. Smorodin (2017). "Influence of Sedimentation Length on the Convective Stability of a Colloidal Suspension." Journal of experimental and theoretical physics **125**(6): 1199-1207.
Cheung, M. K., *et al.* (1996). "Sedimentation of noncolloidal bidisperse suspensions." AIChE journal **42**(1): 271-276.
Chiavassa, G., *et al.* (2016). "Hybrid WENO schemes for polydisperse sedimentation models." International Journal of Computer Mathematics **93**(11): 1801-1817.
Chiu, H.-T., *et al.* (2011). "Using analytical centrifugation to characterize the dispersibility and particle size distributions of organic/inorganic composite coatings." Journal of Polymer Research **18**(6): 1587-1596.

Chong, J., *et al.* (1971). "Rheology of concentrated suspensions." Journal of applied polymer science **15**(8): 2007-2021.
Chorin, A. J. (1968). "Numerical solution of the Navier-Stokes equations." Mathematics of computation **22**(104): 745-762.
Chu, C. and D. Lee (2001). "Experimental analysis of centrifugal dewatering process of polyelectrolyte flocculated waste activated sludge." Water Research **35**(10): 2377-2384.
Chun, B. and A. Ladd (2007). "Interpolated boundary condition for lattice Boltzmann simulations of flows in narrow gaps." Physical Review E Statistical Nonlinear & Soft Matter Physics **75**(6): 066705.
Chung, H. and R. Hogg (1985). "The effect of Brownian motion on particle size analysis by sedimentation." Powder technology **41**(3): 211-216.
Churaev, N. (1995). "The relation between colloid stability and wetting." Journal of colloid and interface science **172**(2): 479-484.
Churaev, N. and B. Derjaguin (1985). "Inclusion of structural forces in the theory of stability of colloids and films." Journal of colloid and interface science **103**(2): 542-553.
Clint, J. H. and S. E. Taylor (1992). "Particle size and interparticle forces of overbased detergents: A Langmuir trough study." Colloids & Surfaces **65**(1): 61-67.
CODATA, V. (2019). "Vacuum electric permittivity." The NIST Reference on Constants, Units, and Uncertainty; NIST: Gaithersburg, MD, USA **20**.
Concha, F. and R. Bürger (2002). "A century of research in sedimentation and thickening." KONA powder and particle Journal **20**: 38-70.
Cui, W., *et al.* (2015). "Rotation and migration of nanoparticles for heat transfer augmentation in nanofluids by molecular dynamics simulation." Case Studies in Thermal Engineering **6**: 182-193.
Cundall, P. A. and O. Strack (1979). "A discrete numerical model for granual assemblies." Geotechnique **29**(1): 47-65.
Cundall, P. A. and O. D. L. Strack (1979). "A discrete numerical model for granual assemblies." Geotechnique **29**(1): 47-65.
d'Humières, D. (2002). "Multiple–relaxation–time lattice Boltzmann models in three dimensions." Philosophical Transactions of the Royal Society of London. Series A: Mathematical, Physical and Engineering Sciences **360**(1792): 437-451.
Dai, Z., *et al.* (2000). "Particle–bubble collision models — a review." Advances in Colloid and Interface Science **85**(2): 231-256.
Dash, S. and T. Lee (2015). "Two spheres sedimentation dynamics in a viscous liquid column." Computers & Fluids **123**: 218-234.
Davies, G. B., *et al.* (2014). "Detachment energies of spheroidal particles from fluid-fluid interfaces." The Journal of Chemical Physics **141**(15): 154902.
Davis, K. and W. B. Russel (1989). "An asymptotic description of transient settling and ultrafiltration of colloidal dispersions." Physics of Fluids A: Fluid Dynamics **1**(1): 82-100.
Davis, R. and K. Birdsell (1988). "Hindered settling of semidilute monodisperse and polydisperse suspensions." AIChE Journal **34**(1): 123-129.
Davis, R. H. and A. Acrivos (1985). "Sedimentation of Noncolloidal Particles at Low Reynolds Numbers." Annual Review of Fluid Mechanics.
Davis, R. H. and H. Gecol (1994). "Hindered settling function with no empirical parameters for polydisperse suspensions." AIChE journal **40**(3): 570-575.
Derjaguin, B. and S. Dukhin (1993). "Theory of flotation of small and medium-size particles." Progress in Surface Science **43**(1-4): 241-266.
Derjaguin, B. v. and L. Landau (1993). "Theory of the stability of strongly charged lyophobic sols and of the adhesion of strongly charged particles in solutions of electrolytes." Progress in Surface Science **43**(1-4): 30-59.
Detloff, T., *et al.* (2006). "Particle Size Distribution by Space or Time Dependent Extinction Profiles obtained by Analytical Centrifugation." Particle & Particle Systems Characterization.
Dickinson, E. (2013). "Stabilising emulsion ‐ based colloidal structures with mixed food ingredients." Journal of the Science of Food and Agriculture **93**(4): 710-721.
Dill, K. A., *et al.* (2010). Molecular driving forces: statistical thermodynamics in biology, chemistry, physics, and nanoscience, Garland Science.
Ding, W. T. and W. J. Xu (2018). "Study on the multiphase fluid-solid interaction in granular materials based on an LBM-DEM coupled method." Powder Technology: S0032591018303590.
Dong, X., *et al.* (2017). "Morphology-Controlled Coating of Colloidal Particles with Silica: Influence of Particle Surface Functionalization." Langmuir the Acs Journal of Surfaces & Colloids **33**(9): 2235-2247.
Dorrell, R. and A. J. Hogg (2010). "Sedimentation of bidisperse suspensions." International Journal of Multiphase Flow **36**(6): 481-490.

Du, R., *et al.* (2006). "Multi-relaxation-time lattice Boltzmann model for incompressible flow." Physics Letters A **359**(6): 564-572.
Dugyala, V. R., *et al.* (2016). "Role of electrostatic interactions in the adsorption kinetics of nanoparticles at fluid-fluid interfaces." Physical chemistry chemical physics : PCCP **18**(7): 5499-5508.
Dulova, N. and M. Trapido (2011). "Application of Fenton's reaction for food-processing wastewater treatment." Journal of Advanced Oxidation Technologies **14**(1): 9-16.
Dunn, L. and R. Stokes (1969). "Pressure and temperature dependence of the electrical permittivities of formamide and water." Transactions of the Faraday Society **65**: 2906-2912.
Dutta, B. K. and S. Bhattacharyya (2009). "An effective voidage model for sedimentation of bidisperse solid suspension." Chemical Engineering and Processing: Process Intensification **48**(8): 1382-1389.
E., M., *et al.* (2004). "Simulation of sedimentation of bidisperse suspensions." International Journal of Mineral Processing.
Eastoe, J. and J. Dalton (2000). "Dynamic surface tension and adsorption mechanisms of surfactants at the air–water interface." Advances in colloid and interface science **85**(2-3): 103-144.
Elliott, *et al.* (2018). "Salt enhanced solvent relaxation and particle surface area determination via rapid spin-lattice NMR." Powder Technology An International Journal on the Science & Technology of Wet & Dry Particulate Systems.
Fabian, *et al.* (2011). "From bijels to Pickering emulsions: A lattice Boltzmann study." Physical Review E **83**(4): 46707-46707.
Fainerman, V., *et al.* (2007). "Studies of the rate of water evaporation through adsorption layers using drop shape analysis tensiometry." Journal of colloid and interface science **308**(1): 249-253.
Fainerman, V. B., *et al.* (1994). "The analysis of dynamic surface tension of sodium alkyl sulphate solutions, based on asymptotic equations of adsorption kinetic theory." Colloids & Surfaces A Physicochemical & Engineering Aspects **87**(1): 61-75.
Fang, W.-Z., *et al.* (2017). "Lattice Boltzmann modeling of pool boiling with large liquid-gas density ratio." International Journal of Thermal Sciences **114**: 172-183.
Fei, J., *et al.* (2022). "A coupled LBM-DEM method for simulating the multiphase fluid-solid interaction problem."
Feng, Y. T., *et al.* (2007). "Coupled lattice Boltzmann method and discrete element modelling of particle transport in turbulent fluid flows: Computational issues." International Journal for Numerical Methods in Engineering **72**(9).
Ferdous, S., *et al.* (2012). "Effects of temperature, pH, and ionic strength on the adsorption of nanoparticles at liquid–liquid interfaces." Journal of Nanoparticle Research **14**(5): 1-12.
Franks, G. V., *et al.* (2000). "Effect of Suspending Medium Properties on the Rheological Behaviour of Attractive Particle Networks." Institution of Engineers, Australia.
Frisch, U., *et al.* (1986). "Lattice-gas automata for the Navier-Stokes equation." Physical review letters **56**(14): 1505.
Garside, J. and M. R. Al-Dibouni (1977). "Velocity-voidage relationships for fluidization and sedimentation in solid-liquid systems." Industrial & engineering chemistry process design and development **16**(2): 206-214.
Ge, L., *et al.* (2020). "CFD-DEM investigation of the interaction between a particle swarm and a stationary bubble: Particle-bubble collision efficiency." Powder Technology.
Genovese, D. B. (2012). "Shear rheology of hard-sphere, dispersed, and aggregated suspensions, and filler-matrix composites." Advances in colloid and interface science **171**: 1-16.
Gunstensen, A. K., *et al.* (1991). "LATTICE BOLTZMANN MODEL OF IMMISCIBLE FLUIDS." PHYSICAL REVIEW A **43**(8): 4320-4327.
Guo, J., *et al.* (2003). "Interfacial interaction between the bubbles and particles in the flotation process." Acta Scientiae Circumstantiae.
Habte, M. A. and C. Wu (2017). "Particle sedimentation using hybrid Lattice Boltzmann-immersed boundary method scheme." Powder Technology **315**: 486-498.
Hac, A. E., *et al.* (2005). "Diffusion in Two-Component Lipid Membranes—A Fluorescence Correlation Spectroscopy and Monte Carlo Simulation Study." Biophysical Journal **88**(1): 317-333.
Hansen, P. H., *et al.* (2001). "Structural characterization of dense colloidal films using a modified pair distribution function and Delaunay triangulation." Langmuir **17**(16): 4867-4875.
He, X., *et al.* (1998). "Discrete Boltzmann equation model for nonideal gases." Physical review. E, Statistical physics, plasmas, fluids, and related interdisciplinary topics **57**(1): R13-R16.
Hernando, L., *et al.* (2015). "Experimental investigation of batch sedimentation of concentrated bidisperse suspensions." Powder Technology **275**: 273-279.
Heurtault, B. (2003). "Physico-chemical stability of colloidal lipid particles." Biomaterials **24**(23): 4283-4300.
Hiemenz, P. and R. Rajagopalan (1997). "Electrostatic and polymer-induced colloid stability." Principles of colloid and surface chemistry. 3rd ed. New York: Marcel Dekker: 604-610.

Hirt, C. W. and B. D. Nichols (1981). "Volume of fluid (VOF) method for the dynamics of free boundaries." Journal of Computational Physics **39**(1): 201-225.
Horozov, T. S., *et al.* (2006). "Effect of particle hydrophobicity on the formation and collapse of fumed silica particle monolayers at the oil–water interface." Colloids and Surfaces A: Physicochemical and Engineering Aspects **282**: 377-386.
Horozov, T. S., *et al.* (2008). "Novel film-calliper method of measuring the contact angle of colloidal particles at liquid interfaces." Langmuir the Acs Journal of Surfaces & Colloids **24**(5): 1678-1681.
Hórvölgyi, Z., *et al.* (1996). "Monoparticulate layers of silanized glass spheres at the water− air interface: particle− particle and particle− subphase interactions." Langmuir **12**(4): 997-1004.
Howard, A. A., *et al.* (2018). "Settling of heavy particles in concentrated suspensions of neutrally buoyant particles under uniform shear." Fluid Dynamics Research **50**(4): 041401-.
Hu, A., *et al.* (2013). "On equations of state in pseudo-potential multiphase lattice Boltzmann model with large density ratio." International Journal of Heat and Mass Transfer **67**: 159-163.
Hu, J. and Z. Guo (2019). "Effect of interaction between a particle cluster and a single particle on particle motion and distribution during sedimentation: A numerical study." Physics of Fluids **31**(3): 033301.
Hunter, T. N., *et al.* (2007). "Determination of contact angles of nanosized silica particles by multi-angle single-wavelength ellipsometry." Australian Journal of Chemistry **60**(9): 651-655.
Hunter, T. N., *et al.* (2020). "Concentration profiling of a horizontal sedimentation tank utilising a bespoke acoustic backscatter array and CFD simulations." Chemical Engineering Science **218**: 115560.
Hussain, S.-A. and D. Bhattacharjee (2009). "Langmuir–Blodgett films and molecular electronics." Modern Physics Letters B **23**(29): 3437-3451.
Hussain, S. A. (2009). "Langmuir-Blodgett Films a unique tool for molecular electronics." arXiv preprint arXiv:0908.1814.
Hyde, E. D., *et al.* (2016). "Colloidal silica particle synthesis and future industrial manufacturing pathways: a review." Industrial & Engineering Chemistry Research **55**(33): 8891-8913.
Iijima, M. and H. Kamiya (2009). "Surface modification for improving the stability of nanoparticles in liquid media." KONA Powder and Particle Journal **27**: 119-129.
Isa, L., *et al.* (2011). "Measuring single-nanoparticle wetting properties by freeze-fracture shadow-casting cryo-scanning electron microscopy." Nature Communications **2**(1): 438.
Isa, L., *et al.* (2014). "Adsorption of sub-micron amphiphilic dumbbells to fluid interfaces." Langmuir the Acs Journal of Surfaces & Colloids **30**(18): 5057-5063.
Jain, P. K. (2010). Simulation of two-phase dynamics using lattice boltzmann method (LBM), University of Illinois at Urbana-Champaign.
Javadi, A., *et al.* (2010). "Adsorption of alkanes from the vapour phase on water drops measured by drop profile analysis tensiometry." Soft Matter **6**(19): 4710-4714.
Jodin, M.-C., *et al.* (2004). "Repercussions of size heterogeneity on the measurement of specific surface areas of colloidal minerals: Combination of macroscopic and microscopic analyses." American Mineralogist **89**(10): 1456-1463.
Johnson, M., *et al.* (2016). "Characterization of multiple hindered settling regimes in aggregated mineral suspensions." Industrial & Engineering Chemistry Research **55**(37): 9983-9993.
Jones, D. (1974). "The free energies of solid-liquid interfaces." Journal of Materials Science **9**(1): 1-17.
Joshi, A. S. and Y. Sun (2009). "Multiphase lattice Boltzmann method for particle suspensions." Physical Review E Statistical Nonlinear & Soft Matter Physics **79**(6): 066703.
Joshi, A. S. and S. Ying (2010). "Numerical Simulation of Colloidal Drop Deposition Dynamics on Patterned Substrates for Printable Electronics Fabrication." Journal of Display Technology **6**(11): 579-585.
Karim, A. M. and H. P. Kavehpour (2018). "Effect of viscous force on dynamic contact angle measurement using Wilhelmy plate method." Colloids and Surfaces A: Physicochemical and Engineering Aspects **548**: 54-60.
Kaz, D. M., *et al.* (2012). "Physical ageing of the contact line on colloidal particles at liquid interfaces." Nature materials **11**(2): 138-142.
Kes, M., *et al.* (2009). "Determination of the particle interactions, rheology and the surface roughness relationship for dental restorative ceramics." Journal of the European Ceramic Society **29**(14): 2959-2967.
Kharrat, *et al.* (2014). "Influences of hydrophilic and hydrophobic silica nanoparticles on anionic surfactant properties: Interfacial and adsorption behaviors." Journal of Petroleum Science & Engineering.
Kohoutek, T., *et al.* (2020). "Controlled self-assembly of Langmuir-Blodgett colloidal crystal films of monodispersed silica particles on non-planar substrates." Colloids and Surfaces A: Physicochemical and Engineering Aspects **593**: 124625.
Koo, S. (2008). "Sedimentation velocity of bidisperse suspensions." Journal of Industrial and Engineering Chemistry **14**(5): 679-686.
Koo, S. (2009). "Estimation of hindered settling velocity of suspensions." Journal of Industrial and Engineering Chemistry **15**(1): 45-49.

Koo, S. (2011). "Numerical simulation of bidisperse hard spheres settling in a fluid." Korean Journal of Chemical Engineering **28**(2): 364-369.
Krishnamoorthy, P. (2010). "Sedimentation model and analysis for differential settling of two-particle-size suspensions in the Stokes region." International journal of sediment Research **25**(2): 119-133.
Krishnamoorthy, P., *et al.* (2007). "An Experimental Study and Correlation for Differential Settling of Bidisperse Suspensions." Chemical & Biochemical Engineering Quarterly **21**(3): 241-250.
Krüger, T., *et al.* (2016). "The Lattice Boltzmann Method - Principles and Practice."
Kumar, A., *et al.* (2013). "Amphiphilic Janus particles at fluid interfaces." Soft Matter **9**(29): 6604-6617.
Kupershtokh, A. L., *et al.* (2009). "On equations of state in a lattice Boltzmann method." Computers & Mathematics with Applications **58**(5): 965-974.
Kynch and J. G. (1952). "A theory of sedimentation." **48**: 166-160.
Kynch, G. J. (1952). "A theory of sedimentation." Transactions of the Faraday society **48**: 166-176.
Ladd, *et al.* (1994). "Numerical simulations of particulate suspensions via a discretized Boltzmann equation. Part 1. Theoretical foundation." J Fluid Mech.
Ladd, A. (1994). "Numerical simulations of particulate suspensions via a discretized Boltzmann equation. Part 2. Numerical results." J. Fluid Mech.
Ladd, A. J. C. (1994). "Numerical simulations of particulate suspensions via a discretized Boltzmann equation. Part 1. Theoretical foundation." Journal of Fluid Mechanics **271**: 285-309.
Ladd, A. J. C. (2006). "Numerical simulations of particulate suspensions via a discretized Boltzmann equation. Part 2. Numerical results." Journal of Fluid Mechanics **271**: 311-339.
Lallemand, P. and L. S. Luo (2000). "Theory of the lattice boltzmann method: dispersion, dissipation, isotropy, galilean invariance, and stability." Physical review. E, Statistical physics, plasmas, fluids, and related interdisciplinary topics **61**(6 Pt A): 6546-6562.
Langevin, P. (1908). "Sur la théorie du mouvement brownien." Compt. Rendus **146**: 530-533.
Lee, Y.-L., *et al.* (2006). "Monolayer behavior of silica particles at air/water interface: a comparison between chemical and physical modifications of surface." Journal of colloid and interface science **296**(1): 233-241.
Leong, Y.-K. and B. Ong (2003). "Critical zeta potential and the Hamaker constant of oxides in water." Powder Technology **134**(3): 249-254.
Lerche, D. (2019). "Comprehensive characterization of nano-and microparticles by in-situ visualization of particle movement using advanced sedimentation techniques." KONA Powder and Particle Journal **36**: 156-186.
Levine, S., *et al.* (1989). "Stabilization of emulsions by fine particles I. Partitioning of particles between continuous phase and oil/water interface." Colloids and surfaces **38**(2): 325-343.
Li, J. (2015). "Chapman-Enskog Expansion in the Lattice Boltzmann Method." arXiv preprint arXiv:1512.02599.
Li, Q. and K. Luo (2013). "Achieving tunable surface tension in the pseudopotential lattice Boltzmann modeling of multiphase flows." Physical Review E **88**(5): 053307.
Li, Q., *et al.* (2014). "Contact angles in the pseudopotential lattice Boltzmann modeling of wetting." Physical Review E **90**(5): 053301.
Li, Q., *et al.* (2013). "Lattice Boltzmann modeling of multiphase flows at large density ratio with an improved pseudopotential model." Physical Review E **87**(5): 053301.
Li, Q. and K. H. Luo (2014). "Thermodynamic consistency of the pseudopotential lattice Boltzmann model for simulating liquid-vapor flows." Applied thermal engineering: Design, processes, equipment, economics.
Li, Q., *et al.* (2016). "Lattice Boltzmann methods for multiphase flow and phase-change heat transfer." Progress in Energy and Combustion Science **52**: 62-105.
Li, Q., *et al.* (2012). "Forcing scheme in pseudopotential lattice Boltzmann model for multiphase flows." Physical Review E **86**(1): 016709.
Li, X. L., *et al.* (2001). "High efficient method for incompressible N-S equations and analysis of two-dimensional turbulent channel flow." Acta Mechanica Sinica **33**(5): 577-587.
Liang, G., *et al.* (2013). "Simulation of self-assemblies of colloidal particles on the substrate using a lattice Boltzmann pseudo-solid model." Journal of Computational Physics **248**: 323-338.
Liang, Y., *et al.* (2007). "Interaction forces between colloidal particles in liquid: theory and experiment." Adv Colloid Interface Sci **134-135**: 151-166.
Liascukiene, I., *et al.* (2018). "Capture of colloidal particles by a moving microfluidic bubble." Soft Matter **14**(6): 992-1000.
Lin, *et al.* (2003). "Nanoparticle Assembly and Transport at Liquid-Liquid Interfaces." Science.
Lin, Y., *et al.* (2005). "Nanoparticle Assembly at Fluid Interfaces: Structure and Dynamics." Langmuir.
Liu, W. and C. Y. Wu (2019). "A hybrid LBM-DEM framework with an improved immersed moving boundary method for modelling complex particle-liquid flows involving adhesive particles."
Lockett, M. and H. Al-Habbooby (1974). "Relative particle velocities in two-species settling." Powder technology **10**(1-2): 67-71.

Lockett, M. J. and K. Bassoon (1979). "Sedimentation of binary particle mixtures." Powder Technology **24**(1): 1-7.
Lockwood, A. P., *et al.* (2021). "Structure and sedimentation characterisation of sheared Mg (OH) 2 suspensions flocculated with anionic polymers." Chemical Engineering Science **231**: 116274.
Manga, M. S., *et al.* (2016). "Measurements of sub-micron particle adsorption and particle film elasticity at oil-water interfaces." Langmuir: acs.langmuir.5b04586.
Mao, R., *et al.* (2001). "Water holding capacity and microstructure of gellan gels." Carbohydrate polymers **46**(4): 365-371.
Marton, K., *et al.* (2013). "Elimination of dust particle sedimentation in industry environment." Journal of Electrostatics **71**(3): 208-213.
Martys, N. S. and H. Chen (1996). "Simulation of multicomponent fluids in complex three-dimensional geometries by the lattice Boltzmann method." Physical review E **53**(1): 743.
Masliyah, J. H. (1979). "Hindered settling in a multi-species particle system." Chemical Engineering Science **34**(9): 1166-1168.
Matsunaga, T., *et al.* (2022). "Axisymmetric free-surface flow simulation using the moving surface mesh particle method and application to drop formation." Journal of Computational Physics: 111298.
Maxwell, R., *et al.* (2012). "Computer simulations of particle–bubble interactions and particle sliding using Discrete Element Method." Journal of colloid and interface science **381**(1): 1-10.
Mei, R., *et al.* (2002). "Force evaluation in the lattice Boltzmann method involving curved geometry." Physical Review E **65**(4 Pt 1): 041203.
Meng, X., *et al.* (2017). "Conditional siphon priming for multi-step assays on centrifugal microfluidic platforms." Sensors and Actuators B: Chemical **242**: 710-717.
Metin, C. (2012). "Characterization of nanoparticle transport in flow through permeable media."
Mirza, S. and J. Richardson (1979). "Sedimentation of suspensions of particles of two or more sizes." Chemical Engineering Science **34**(4): 447-454.
Monteux, C., *et al.* (2007). "Determining the mechanical response of particle-laden fluid interfaces using surface pressure isotherms and bulk pressure measurements of droplets." Physical chemistry chemical physics **9**(48): 6344-6350.
Morgan, S., *et al.* (2021). "Adsorption trajectories of nonspherical particles at liquid interfaces." Physical Review E **103**(4): 042604.
Moser, R. D., *et al.* (1999). "Direct numerical simulation of turbulent channel flow up to Re τ= 590." Physics of fluids **11**(4): 943-945.
Mu, Y.-T., *et al.* (2017). "Nucleate boiling performance evaluation of cavities at mesoscale level." International Journal of Heat and Mass Transfer **106**: 708-719.
Mynam, M., *et al.* (2011). "Efficient lattice Boltzmann algorithm for Brownian suspensions." Philos Trans A Math Phys Eng Sci **369**(1944): 2237-2245.
Newell, D. B. and E. Tiesinga (2019). "The international system of units (SI)." NIST Special Publication **330**: 1-138.
Nie, D. and J. Lin (2009). "A fluctuating lattice-Boltzmann model for direct numerical simulation of particle Brownian motion." Particuology **7**(6): 501-506.
Nie, D. M. and J. Z. Lin "Boundary Conditions in Lattice Boltzmann Method." Chinese Journal of Computation Physics.
Noble, D. R. and J. R. Torczynski (1998). "A Lattice-Boltzmann Method for Partially Saturated Computational Cells." International Journal of Modern Physics C.
Noskov, B. A. (1996). "Fast adsorption at the liquid-gas interface." Advances in Colloid and Interface Science **69**: 63-129.
Oliveira Jr, O. N., *et al.* (2022). "The past and the future of Langmuir and Langmuir–Blodgett films." Chemical Reviews **122**(6): 6459-6513.
Ossenkamp, G. C., *et al.* (2002). "Toward Functionalized Surfaces through Surface Esterification of Silica." Langmuir **18**(15): 5749-5754.
Othman, S. A. and S. Radiman (2016). "Formation of polyaniline emeraldine base (PANI-EB) nanoparticles using Langmuir- Blodgett technique."
Owen, D. R. J., *et al.* (2011). "An efficient framework for fluid–structure interaction using the lattice Boltzmann method and immersed moving boundaries." International Journal for Numerical Methods in Engineering **87**(1-5): 66-95.
Padding, J. and A. Louis (2008). "Interplay between hydrodynamic and Brownian fluctuations in sedimenting colloidal suspensions." Physical Review E **77**(1): 011402.
Padding, J. T. and A. A. Louis (2018). "interplay between hydrodynamic and brownian fluctuations in sedimenting colloidal suspensions interplay between hydrodynamic and brownian fluctuations in sedimenting colloidal suspensions."

Park, S.-J. and M.-K. Seo (2011). Interface science and composites, Academic Press.
Paul, N., *et al.* (2017). "Influence of shape and surface charge on the sedimentation of spheroidal, cubic and rectangular cuboid particles." Powder Technology **322**: 75-83.
Paunov, V. N., *et al.* (2002). "Adsorption of charged colloid particles to charged liquid surfaces." LANGMUIR **18**(18): 6946-6955.
Peng, M., *et al.* (2021). "From Surface Tension to Molecular Distribution: Modeling Surfactant Adsorption at the Air–Water Interface." Langmuir **37**(7): 2237-2255.
Peng, Z., *et al.* (2010). "DEM simulation of aggregation of suspended nanoparticles." Powder Technology **204**(1): 91-102.
Peskin, C. S. (1972). "Flow patterns around heart valves: A numerical method." Journal of Computational Physics **10**(2): 252-271.
Portinari, M. and M. Portinari (2015). "2D and 3D Verification an Validation of the Lattice Boltzmann Method."
Poslinski and J. A. (1988). "Rheological Behavior of Filled Polymeric Systems I. Yield Stress and Shear-Thinning Effects." Journal of Rheology **32**(7): 703-735.
Premnath, K. N. and J. Abraham (2007). "Three-dimensional multi-relaxation time (MRT) lattice-Boltzmann models for multiphase flow." Journal of Computational Physics **224**(2): 539-559.
Preuss, M. and H.-J. Butt (1998). "Measuring the Contact Angle of Individual Colloidal Particles." Journal of Colloid & Interface Science **208**(2): 468-477.
Pugnaloni, L. A., *et al.* (2005). "Brownian dynamics simulation of adsorbed layers of interacting particles subjected to large extensional deformation." Journal of colloid and interface science **287**(2): 401-414.
Qi, F. and R. I. Tanner (2011). "Random close packing and relative viscosity of multimodal suspensions." Rheologica Acta **51**(4): 289-302.
Qi, F. and R. I. Tanner (2011). "Relative viscosity of bimodal suspensions." Korea-Australia rheology journal **23**(2): 105-111.
Rana, S., *et al.* (2012). "Control of surface tension at liquid-liquid interfaces using nanoparticles and nanoparticle-protein complexes." Langmuir the Acs Journal of Surfaces & Colloids **28**(4): 2023.
Rao, R., *et al.* (2002). "A numerical and experimental study of batch sedimentation and viscous resuspension." International journal for numerical methods in fluids **39**(6): 465-483.
Reed, C. C. and J. L. Anderson (1980). "Hindered settling of a suspension at low Reynolds number." AIChE Journal **26**(5).
Reguera, J., *et al.* (2015). "Contact angle and adsorption energies of nanoparticles at the air–liquid interface determined by neutron reflectivity and molecular dynamics." Nanoscale **7**(13): 5665-5673.
Rey, M., *et al.* (2018). "Amphiphile-induced anisotropic colloidal self-assembly." Langmuir **34**(34): 9990-10000.
Rhodes, M. J. (2008). Introduction to particle technology, John Wiley & Sons.
Richardson, J. and W. Zaki (1954). "'The Fall Velocities of Spheres in Viscous Fluids." Trans. Inst. Chem. Eng **32**: 35-41.
Richardson, J. and W. Zaki (1954). "The sedimentation of a suspension of uniform spheres under conditions of viscous flow." Chemical Engineering Science **3**(2): 65-73.
Richardson, J. and W. Zaki (1997). "Sedimentation and fluidisation: Part I." Chemical Engineering Research and Design **75**: S82-S100.
RICHARDSON, J. t. (1954). "Sedimentation and fluidisation: Part I." Transactions of the Institution of Chemical Engineers **32**: 35-53.
Ross and SheldonM A first course in probability /-6th ed, A first course in probability /-6th ed.
Ruiz Barlett, V., *et al.* (2009). "Differences between fixed time step and kinetic Monte Carlo methods for biased diffusion." Journal of Computational Physics **228**(16): 5740-5748.
Sajjadi, H., *et al.* (2018). "Double MRT Lattice Boltzmann simulation of 3-D MHD natural convection in a cubic cavity with sinusoidal temperature distribution utilizing nanofluid." International Journal of Heat and Mass Transfer **126**: 489-503.
San Chan, Y. and M. M. Don (2013). "Biosynthesis and structural characterization of Ag nanoparticles from white rot fungi." Materials Science and Engineering: C **33**(1): 282-288.
Satoh, A. (2012). "On the method of activating Brownian motion for application of the lattice Boltzmann method to magnetic particle dispersions." Molecular Physics **110**(1): 1-15.
Sbragaglia, M., *et al.* (2006). "Surface roughness-hydrophobicity coupling in microchannel and nanochannel flows." Physical Review Letters **97**(20): 204503.
Schumacher, G. A. and T. G. van de Ven (1987). "Brownian motion of charged colloidal particles surrounded by electric double layers." Faraday Discussions of the Chemical Society **83**: 75-85.
Schwartz, D. K. (1997). "Langmuir-Blodgett film structure." Surface Science Reports **27**(7-8): 245-334.

Sfakianakis, N. (2009). "Finite difference schemes on non-uniform meshes for hyperbolic conservation laws." University of Crete, Heraklion.
Shan, X. and H. Chen (1993). "Lattice Boltzmann model for simulating flows with multiple phases and components." Phys Rev E Stat Phys Plasmas Fluids Relat Interdiscip Topics **47**(3): 1815-1819.
Shao, J. Y., *et al.* (2013). "A stencil adaptive phase-field lattice Boltzmann method for two dimensional incompressible multiphase flows: ADAPTIVE PHASE-FIELD LBM FOR MULTIPHASE FLOWS." International Journal for Numerical Methods in Fluids **72**(6): 671-696.
Shi, Y., *et al.* (2006). "Lattice Boltzmann method for incompressible flows with large pressure gradients." Phys.rev.e **73**(2): 026704.
Shiels, J., *et al.* (2018). "Synthesis and physical property characterisation of spheroidal and cuboidal nuclear waste simulant dispersions." Materials **11**(7): 1235.
Siano, D. B. (1979). "Layered sedimentation in suspensions of monodisperse spherical colloidal particles." Journal of Colloid and Interface Science **68**(1): 111-127.
Sl, A., *et al.* (2021). "Numerical investigation on the mixing mechanism in a cross-torus paddle mixer using the DEM-CFD method."
Sobisch, T. and D. Lerche (2018). "Separation behaviour of particles in biopolymer solutions in dependence on centrifugal acceleration: Investigation of slow structuring processes in formulations." Colloids and Surfaces A: Physicochemical and Engineering Aspects **536**: 74-81.
Solari, C. A., *et al.* (2011). "Flagellar phenotypic plasticity in volvocalean algae correlates with Péclet number." Journal of the Royal Society Interface **8**(63): 1409-1417.
Spruijt, E. and P. Biesheuvel (2014). "Sedimentation dynamics and equilibrium profiles in multicomponent mixtures of colloidal particles." Journal of Physics: Condensed Matter **26**(7): 075101.
Struis, R. P., *et al.* (2013). "Inertisation of heavy metals in municipal solid waste incineration fly ash by means of colloidal silica–a synchrotron X-ray diffraction and absorption study." Rsc Advances **3**(34): 14339-14351.
Style, R. W., *et al.* (2015). "Adsorption of soft particles at fluid interfaces." SOFT MATTER **11**(37): 7412-7419.
Su, Y., *et al.* (2006). "Linear adsorption of nonionic organic compounds from water onto hydrophilic minerals: silica and alumina." Environmental Science & Technology **40**(22): 6949-6954.
Sussman, M., *et al.* (1998). "An improved level set method for incompressible two-phase flows." Computers & Fluids **27**(5-6): 663-680.
Suzuki, K. and T. Inamuro (2011). "Effect of internal mass in the simulation of a moving body by the immersed boundary method." Computers & Fluids **49**(1): 173-187.
Sviatskii, V., *et al.* (2016). "Regeneration of a fibrous sorbent based on a centrifugal process for environmental geology of oil and groundwater degradation." Acta Montanistica Slovaca.
Swift, M. R., *et al.* (1995). "Lattice Boltzmann Simulation of Non-Ideal Fluids." Physical Review Letters **75**(5): 830-833.
Swift, M. R., *et al.* (1995). "LATTICE BOLTZMANN SIMULATION OF NONIDEAL FLUIDS." PHYSICAL REVIEW LETTERS **75**(5): 830-833.
Tabor, *et al.* (2015). "Measurement of surface and interfacial tension using pendant drop tensiometry." Journal of Colloid and Interface Science **454**: 226-237.
Tadmor, R., *et al.* (2002). "Debye Length and Double-Layer Forces in Polyelectrolyte Solutions." Macromolecules **35**(6): 2380-2388.
Tao, S. and Z. Guo (2015). "Boundary condition for lattice Boltzmann modeling of microscale gas flows with curved walls in the slip regime." Physical Review E Statistical Nonlinear & Soft Matter Physics **91**(4): 043305.
Thackham, J. A., *et al.* (2009). "Computational approaches to solving equations arising from wound healing." Bulletin of mathematical Biology **71**(1): 211-246.
Thareja, P., *et al.* (2008). "Polymer foams stabilized by particles adsorbed at the air/polymer interface." Macromolecular rapid communications **29**(15): 1329-1334.
Tilehboni, S., *et al.* (2015). "Numerical simulation of droplet detachment from solid walls under gravity force using lattice Boltzmann method." Journal of Molecular Liquids **212**: 544-556.
Timothy, *et al.* (2009). "Effect of esterically bonded agents on the monolayer structure and foamability of nano-silica." Colloids & Surfaces A Physicochemical & Engineering Aspects.
Tory, E. M. and R. A. Ford (2004). "Simulation of sedimentation of bidisperse suspensions." International Journal of Mineral Processing **73**(2-4): 119-130.
Toschi, F. and S. Succi (2005). "Lattice Boltzmann method at finite Knudsen numbers." EPL (Europhysics Letters) **69**(4): 549.
Trau, M., *et al.* (1992). "An ellipsometric study of thin films on silica plates formed by alkylchlorosilylation reagents." Journal of colloid and interface science **148**(1): 182-189.
Trefalt, G., *et al.* (2016). "Charge regulation in the electrical double layer: ion adsorption and surface interactions." Langmuir **32**(2): 380-400.

Tsai, P.-S., *et al.* (2006). "Fabrication of hydrophobic surfaces by coupling of langmuir− blodgett deposition and a self-assembled monolayer." Langmuir **22**(13): 5660-5665.
Turton, R. (1986). "A short note on the drag correlation for spheres." Powder Technol **47**(1): 83-86.
Ueno, K., *et al.* (2008). "Colloidal stability of bare and polymer-grafted silica nanoparticles in ionic liquids." Langmuir **24**(10): 5253-5259.
Ullmann, C., *et al.* (2017). "Performance of analytical centrifugation for the particle size analysis of real-world materials." Powder technology **319**: 261-270.
Usher, S. P., *et al.* (2013). "Characterisation of dewaterability from equilibrium and transient centrifugation test data." Chemical Engineering Science **93**: 277-291.
van Deventer, B. B., *et al.* (2011). "Aggregate densification and batch settling." Chemical Engineering Journal **171**(1): 141-151.
Verway, J. and J. T. G. Overbeek (1948). "gTheory of the Stability of Lyophobic Colloids• h Elsevier Publ." Co., Amsterdam: 66.
Vesaratchanon, S., *et al.* (2007). "Sedimentation in nano-colloidal dispersions: effects of collective interactions and particle charge." Advances in colloid and interface science **134**: 268-278.
Vesaratchanon, S., *et al.* (2007). "Sedimentation in nano-colloidal dispersions: Effects of collective interactions and particle charge." Adv Colloid Interface **134**(none): 268-278.
Wang, A., *et al.* (2017). "Effects of contact-line pinning on the adsorption of nonspherical colloids at liquid interfaces." Physical review letters **119**(10): 108004.
Wang, H., *et al.* (2012). "Numerical simulation of particle capture process of fibrous filters using Lattice Boltzmann two-phase flow model." Powder Technology **227**: 111-122.
Wang, M., *et al.* (2019). "A novel algorithm of immersed moving boundary scheme for fluid-particle interactions in DEM-LBM." Computer Methods in Applied Mechanics and Engineering **346**(APR.1): 109-125.
Wang, X., *et al.* (2014). "An efficient boundary condition-implemented immersed boundary-lattice Boltzmann method for simulation of 3D incompressible viscous flows." Computers & Fluids **100**: 165-175.
Watson, A. D., *et al.* (2005). "Sedimentation in bidisperse and polydisperse colloids." Journal of Colloid & Interface Science **286**(1): 176-186.
Wen, B., *et al.* (2014). "Galilean invariant fluid-solid interfacial dynamics in lattice Boltzmann simulations." Journal of Computational Physics **266**: 161-170.
Wi, H. S., *et al.* (2011). "Nanoparticle Adsorption at Liquid-Vapor Surfaces: Influence of Nanoparticle Thermodynamics, Wettability, and Line Tension." Langmuir the Acs Journal of Surfaces & Colloids **27**(16): 9979.
Winkelmann, M., *et al.* (2012). "Characterisation of alkyl amines at the water/air surface with the drop and bubble profile analysis tensiometry." J Colloid Interface **372**(1): 202-206.
Xing, Y., *et al.* (2017). "Recent experimental advances for understanding bubble-particle attachment in flotation." Adv Colloid Interface Sci **246**: 105-132.
Xu, *et al.* (2009). "Hydrophobic coating- and surface active solvent-mediated self-assembly of charged gold and silver nanoparticles at water-air and water-oil interfaces." Physical Chemistry Chemical Physics Cambridge Royal Society of Chemistry.
Xu, J., *et al.* (2022). "Investigation of the Contact Angle and Packing Density of Silica Nanoparticles at a Pickering Emulsion Interface Fixed by UV Polymerization." Langmuir.
Xu, X., *et al.* (2020). "Layering of bidisperse charged nanoparticles in sedimentation." Soft matter **16**(20): 4718-4722.
Yaghoobi, H. and M. Torabi (2012). "Analytical solution for settling of non-spherical particles in incompressible Newtonian media." Powder Technology **221**(none): 453-463.
Yang, G. C., *et al.* (2018). "A comprehensive study of coupled LBM-DEM with immersed moving boundary."
Yin, X. and D. L. Koch (2007). "Hindered settling velocity and microstructure in suspensions of solid spheres with moderate Reynolds numbers." Physics of Fluids **19**(9): 093302.
Yka, B., *et al.* "Numerical study on the formations of gas channels and subsequent bubbles in unconsolidated sandy seabed sediment using a coupled LBM-DEM method." Journal of Natural Gas Science and Engineering **74**.
Yuan, P. and L. Schaefer (2006). "Equations of state in a lattice Boltzmann model." Physics of Fluids **18**(4): 042101.
Yuan, Y., *et al.* (2018). "Effects of spontaneous nanoparticle adsorption on the bubble-liquid and bubble-bubble interactions in multi-dispersed bubbly systems – A review." International Journal of Heat and Mass Transfer **120**: 552-567.
Zaidi, A. A., *et al.* (2015). "Direct numerical simulations of inertial settling of non-Brownian particles." Korean Journal of Chemical Engineering **32**(4): 617-628.
Zaidi, A. A., *et al.* (2015). "Hindered Settling Velocity & Structure Formation during Particle Settling by Direct Numerical Simulation." Procedia Engineering **102**: 1656-1666.

Zhang, K. and A. Acrivos (1994). "Viscous resuspension in fully developed laminar pipe flows." International journal of multiphase flow **20**(3): 579-591.
Zhang, Y., *et al.* (2017). "Interfacial Activity of Nonamphiphilic Particles in Fluid–Fluid Interfaces." Langmuir: acs.langmuir.7b00599.
Zimmels, Y. (1983). "Theory of hindered sedimentation of polydisperse mixtures." AIChE journal **29**(4): 669-676.